Stiff vessels approached in a flexible way

Stiff vessels approached in a flexible way

Advancing quantification and interpretation of arterial stiffness

Bart Spronck

ISBN 978-94-6233-414-4

Cover design by B. Spronck

Printed by Gildeprint, The Netherlands

Stiff vessels approached in a flexible way

Advancing quantification and interpretation of arterial stiffness

PROEFSCHRIFT

ter verkrijging van de graad van doctor aan de Universiteit Maastricht,
op gezag van de Rector Magnificus, Prof. dr. Rianne M. Letschert,
volgens het besluit van het College van Decanen,
in het openbaar te verdedigen
op woensdag 19 oktober 2016 om 16:00 uur

door

Bart Spronck

geboren op 4 oktober 1987
te Maastricht, Nederland

Promotor
Prof. dr. T. Delhaas

Copromotores
Dr. R.T.A. Megens
Dr. ir. K.D. Reesink

Beoordelingscommissie
Prof. dr. H.A.J. Struijker-Boudier (voorzitter)
Prof. dr. L.M.A.B. van Bortel (Universiteit Gent)
Prof. dr. C.G. Schalkwijk
Prof. dr. ir. F.N. van de Vosse (Technische Universiteit Eindhoven)
Prof. dr. N. Westerhof (VU Medisch Centrum)

Financial support by the **Dutch Heart Foundation** for the publication of this thesis is gratefully acknowledged.

In addition, financial support for the publication of this thesis as provided by **Maastricht University** and by **Stichting Hartsvrienden RESCAR** is gratefully acknowledged.

Contents

Chapter 1

General introduction

1.1 Arterial stiffness

CARDIOVASCULAR disease constitutes an increasing burden on the western society. In 2014, cardiovascular disease was responsible for 27% of all deaths in the Netherlands (Centraal Bureau voor de Statistiek 2016a). As the occurrence of cardiovascular disease shows a strong correlation with age (Lakatta and Levy 2003a; Lakatta and Levy 2003b), it is expected that this percentage will rise even further in our ageing population (Centraal Bureau voor de Statistiek 2016b).

Hypertension, a sustained increase in blood pressure, is a key condition in cardiovascular disease and is present in more than half of the population aged 60 years and older (Blokstra et al. 2015; Lakatta and Levy 2003a; Smulyan et al. 2016). It is associated with stroke, myocardial infarction, sudden death, heart failure, peripheral artery disease, and end-stage renal disease (Mancia et al. 2013).

A key aspect in the development of cardiovascular disease is arterial stiffening (Laurent et al. 2006). With every beat the heart ejects blood into the arteries, causing them to expand. The more compliant the arteries are, the easier they expand, and the less force is required by the heart to eject blood into them. With stiffened, less compliant arteries, the load on the heart is increased, potentially leading to heart failure in the long term. Accelerated stiffening is hence a strong predictor of cardiovascular complications worldwide (Ben-Shlomo et al. 2014; Laurent et al. 2001; Van Bortel et al. 2012).

The arterial wall consists of three main components that bear the pressure load: collagen, elastin, and smooth muscle cells (O'Connell et al. 2008; Wolinsky and Glagov 1964). Elastin gives the arteries their large compliance, while collagen ensures that at higher pressures, the arteries remain intact. Smooth muscle cells enable the arteries to contract, an effect that is more pronounced in more distal, muscular (e.g., femoral and brachial) arteries than in the larger elastic vessels such as the aorta and carotid arteries. Arterial stiffness is the result of the *interplay* between these three components. For example, with ageing, the elastin fibres become fragmented, leading to an increased role of the stiffer collagen in pressure load bearing, resulting in increased arterial stiffness (O'Rourke and Hashimoto 2007).

Arterial stiffening and hypertension, although both being independently associated with cardiovascular risk, are closely intertwined for two reasons (Humphrey et al. 2016; Mitchell 2014). First, an increase in arterial stiffness is associated with increased pulse pressure (the pressure difference between systole and diastole). With constant peripheral resistance (the resistance to blood flow that the end-organs pose) and mean arterial pressure, this increased pulse pressure will increase systolic blood pressure (Laurent et al. 2006; Westerhof et al. 2010). Second, as will be elaborated in section 1.2, the most commonly used clinical measure of arterial stiffness (pulse wave velocity) is *inherently* dependent on blood pressure (Bramwell et al. 1923; Laurent et al. 2006). Therefore, measured pulse wave velocity in hypertensive subjects will be inherently increased and does not directly indicate a stiffened arterial wall.

In the long term, a sustained increase in blood pressure is thought to stimulate matrix synthesis and thereby to increase vascular thickness and structural stiffness (pressure $\uparrow \rightarrow$ stiffness $\uparrow$). At the population level, increased arterial stiffness has been shown to precede increased blood pressure (stiffness $\uparrow \rightarrow$ pressure $\uparrow$; Dernellis and Panaretou 2005; Kaess et al. 2012; Liao et al. 1999), a finding that has also been observed in sponta-

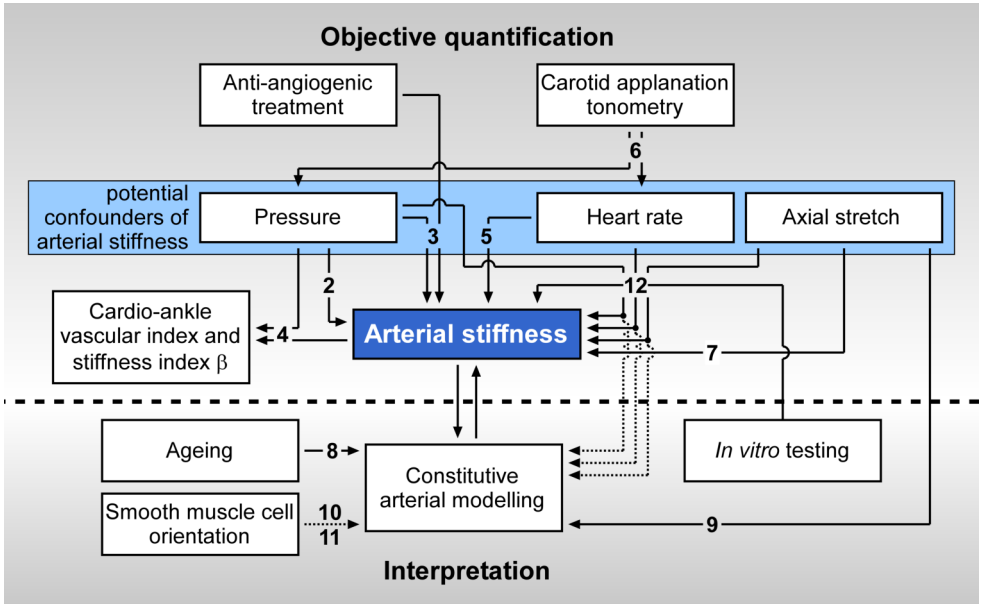

Figure 1.1: Overview of this thesis. Numbers indicate thesis chapters. The top part of the chart pertains to the objective quantification of arterial stiffness (thesis aim 1), the bottom part pertains to the interpretation of arterial stiffness changes (thesis aim 2).

neously hypertensive rats (Van Gorp et al. 2000). Hypertension and arterial stiffening are suggested to form a positive feedback loop (Humphrey et al. 2016), with hypertension increasing local wall stress, which induces remodelling and stiffening, in turn increasing blood pressure.

1.1.1 Aims

Although arterial stiffness is commonly measured in clinical studies, several confounding factors inherently impede its independent quantification. Furthermore, establishing whether an artery is stiffened or not does not inform a researcher or clinician on the *cause* of the stiffening. Therefore, this thesis is centred around two aims:

1. To advance the objective, independent quantification of arterial stiffness.
2. To advance the interpretation of observed differences and changes in arterial stiffness.

These aims, together with the associated chapters and their coherence, are visualised in Fig. 1.1. Throughout this thesis, these aims are approached from *clinical* as well as *engineering* perspectives.

1.2 Objective quantification of arterial stiffness

The gold standard method for the assessment of arterial stiffness in patients is the measurement of carotid-femoral pulse wave velocity (PWV; Laurent et al. 2006; Townsend et al. 2015). This measurement is performed by measuring the pressure or distension waveform at carotid and femoral sites. The time difference between the feet of these waveforms (transit time) is inversely related to PWV. By measuring the effective travel distance between the carotid and femoral sites using a caliper or a tape measure, and dividing this distance by the carotid-femoral time difference, an estimate of the PWV in the carotid-femoral arterial bed is obtained. PWV can also be measured locally, assessing only a small arterial segment (e.g., the carotid artery). This can either be performed by assessing transit time over a short segment (Hermeling et al. 2007; Hermeling et al. 2008; Pernot et al. 2007), or by combining locally measured pressure and diameter waveforms (Bramwell and Hill 1922a). The latter technique is based on estimating circumferential strain and pulse pressure, defining distensibility, which is intrinsically related to PWV by the Bramwell-Hill relation (Bramwell and Hill 1922a).

Although PWV is positively related to arterial stiffness, this relationship is confounded by several factors. Blood pressure and heart rate are the most commonly described physiological confounders of PWV (Townsend et al. 2015). Another, less studied confounder is axial stretch of the studied artery segment, which may influence the assessment of local PWV. The effects of blood pressure, heart rate, and axial stretch on measured arterial stiffness are discussed below, with reference to the first six chapters in this thesis.

1.2.1 Blood pressure as a confounder of arterial stiffness

Bramwell et al. (1923) already showed that PWV is directly dependent on blood pressure at the time of measurement. In clinical studies, PWV is commonly corrected for blood pressure by means of a statistical approach. However, statistical correction is not feasible in individual subjects. The Reference Values for Arterial Stiffness' Collaboration (2010) published a large multi-centre study that provided reference values for PWV in healthy and diseased subjects as a function of blood pressure. These values can be used as a reference for individual PWV measurements. However, in The Reference Values for Arterial Stiffness' Collaboration (2010) study, each subject is measured only at a single blood pressure. Therefore, the blood pressure dependence of PWV as quantified using such a study is of a cross-sectional nature, and has two potential causes. First, PWV *acutely* changes with blood pressure (e.g., Bramwell et al. 1923). Second, in a hypertensive subject, arterial remodelling may have occurred due to the chronically increased blood pressure, changing the *intrinsic* stiffness of the arterial wall. Using a cross-sectional study, these two causes are indistinguishable. In this thesis, we will focus on and try to correct for the first (acute) cause of pressure dependence (chapters 2 to 5). This will yield techniques to perform *independent* assessment of arterial stiffness.

In **chapter 2**, we present a technique to quantify the acute pressure dependence of PWV, which can be used to correct measured PWVs. We assessed the performance of this technique in **chapter 3**, by applying it to a data set of patients undergoing anti-angiogenic cancer treatment.

To overcome the problem of pressure dependence of PWV, alternative measures of ar-

terial stiffness have been proposed that are advocated as being intrinsically pressure-independent. Two of these measures are cardio-ankle vascular index (CAVI, Shirai et al. 2006), and stiffness index β (Hayashi et al. 1980). In **chapter 4**, we critically assess the assumptions made in the mathematical derivation of CAVI and β as pressure-independent measures.

1.2.2 Heart rate as a confounder of arterial stiffness

The relationship between heart rate and carotid-femoral PWV is controversial. A small number of acute pacing studies, specifically investigating the association between heart rate and PWV, found an independent effect of heart rate on PWV (Haesler et al. 2004; Lantelme et al. 2002). Others, however, found no change in PWV with heart rate (Albaladejo et al. 2001) or were unable to discriminate the measured increase in PWV from the concomitant pacing-induced increase in blood pressure (Liang et al. 1999; Millasseau et al. 2005). A potential influence of heart rate on PWV is important, as white-coat hypertension often coincides with an increased heart rate (Mancia et al. 1983). Therefore, if heart rate indeed influences PWV independent of blood pressure, the PWV measured in the doctor's office may be artificially increased by *both* an increased heart rate and an increased actual blood pressure. In **chapter 5**, we report the largest study to date to assess the confounding effect of heart rate on PWV using acute pacing, whilst rigorously correcting for variations in actual blood pressure.

Measurement of carotid-femoral PWV often involves applanation tonometry of the carotid artery. Excessive force on the carotid baroreceptors may induce a baroreceptor response, changing heart rate (Courand et al. 2014; Schweitzer and Teichholz 1985). If this is the case, PWV measurements involving applanation tonometry may not be taken at a subject's intrinsic resting heart rate. The presence or absence of a baroreceptor effect induced by applanation tonometry, however, remains unclear. Therefore, we assess the effect of carotid artery applanation tonometry on heart rate in **chapter 6**.

1.2.3 Axial stretch as a confounder of arterial stiffness

During assessment of local carotid artery stiffness, the head may be rotated upwards and backwards to optimise visibility of the carotid artery segment. This may cause stretching of the carotid artery to a greater-than-physiological length. Longitudinal stretching of an artery will affect arterial diameter and shift the relationship between pressure and diameter (Sommer et al. 2010). Therefore, in addition to blood pressure and heart rate, axial arterial stretch may confound local carotid artery stiffness measurements. In **chapter 7**, we study the effect of head rotation on arterial distension and local arterial stiffness.

1.3 Interpretation of changes in arterial stiffness

Whereas the previous section focussed on advancements in the objective *quantification* of arterial stiffness ("Does the artery stiffen?"), the present section focusses on the *interpretation* of arterial stiffening ("What makes the artery stiffer?").

1.3.1 *In vivo* quantification of constitutive properties

Measuring the mechanical behaviour of an artery as a whole (e.g., its stiffness) does not directly yield information about the individual structural components (collagen, elastin, and smooth muscle cells; O'Connell et al. 2008; Wolinsky and Glagov 1964) of the artery. To assess mechanical changes in the load-bearing individual components, the mechanical contributions of the individual components have to be disentangled. This can be accomplished by fitting a computer model that explicitly implements the individual components (a constitutive model) to the measurement data (Ferruzzi et al. 2013; Holzapfel and Ogden 2010a). Using such a model, observed changes in arterial stiffness can be ascribed to changes in one or more of the load-bearing components. In **chapter 8**, we implement a constitutive computer model of the arterial wall and use this to study the effects of ageing on the arterial wall components.

Fitting constitutive models to data obtained *in vivo* poses a challenge, since only data from a limited pressure range is available and measurements are typically taken at only one axial stretch state. In **chapter 9**, we propose a strategy to improve the quantification of constitutive model parameters, taking advantage of the effect of head rotation on arterial distension as presented in chapter 7.

1.3.2 Smooth muscle orientation

Implementing realistic constitutive models requires detailed structural knowledge of the individual wall components. For realistic constitutive modelling, (volume) content of the components, but also their orientation within the arterial wall are required. In constitutive modelling, the orientation of the smooth muscle cells in the arterial wall is often assumed to be perfectly circumferential (e.g., Masson et al. 2011; Zulliger et al. 2004b). However, experimental evidence for this assumption, obtained under controlled conditions, is lacking. In **chapter 10**, we develop a method to determine two-dimensional smooth muscle cell orientation in tubular structures, and use this method to quantify smooth muscle cell orientation in rat ureters. We extend this method to a three-dimensional method in **chapter 11**, and use it to quantify smooth muscle cell orientation in viable murine carotid arteries. In both chapters 10 and 11, two-photon laser scanning microscopy is used for imaging. This technique is inherently capable of optical sectioning (Helmchen and Denk 2005), allowing us to study arteries mounted between micropipettes under intact, viable conditions, without the need for histological sectioning. Furthermore, its high depth penetration allows us to image the entire thickness of the arterial wall (Megens et al. 2007).

1.3.3 *In vitro* assessment of arteries under pulsatile conditions

In order to optimally study the constitutive properties of arteries while taking into account the effects of heart rate, isolated arteries should be studied under pulsatile conditions. Commonly, arteries are mounted between cannulae and pressurised while measuring diameter and axial force at different axial stretches (Ferruzzi et al. 2013; Sommer et al. 2010). Typically, experiments are performed statically. In **chapter 12**, we present a newly developed, custom-built experimental measurement setup to measure arterial stiffness in murine carotid arteries under static as well as dynamic conditions.

1.4 Structure of this thesis

Chapters 2 to 12 constitute the body of this thesis, as visualised in Fig. 1.1. The general discussion of this thesis is presented in chapter 13.

Chapter 2

Blood pressure dependence of arterial stiffness: Potential clinical implications

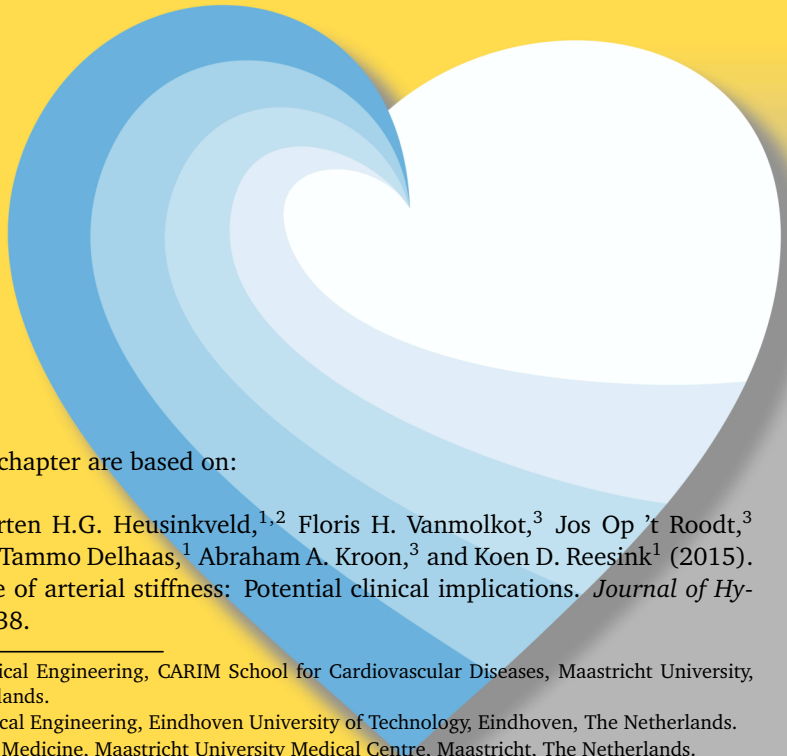

The contents of this chapter are based on:

Bart Spronck,[1] Maarten H.G. Heusinkveld,[1,2] Floris H. Vanmolkot,[3] Jos Op 't Roodt,[3] Evelien Hermeling,[4] Tammo Delhaas,[1] Abraham A. Kroon,[3] and Koen D. Reesink[1] (2015). Pressure-dependence of arterial stiffness: Potential clinical implications. *Journal of Hypertension* 33:330–338.

[1] Department of Biomedical Engineering, CARIM School for Cardiovascular Diseases, Maastricht University, Maastricht, The Netherlands.
[2] Department of Biomedical Engineering, Eindhoven University of Technology, Eindhoven, The Netherlands.
[3] Department of Internal Medicine, Maastricht University Medical Centre, Maastricht, The Netherlands.
[4] Department of Radiology, Maastricht University Medical Centre, Maastricht, The Netherlands.

Abstract

Arterial stiffness measures such as pulse wave velocity (PWV) have a known dependence on actual blood pressure, requiring consideration in cardiovascular risk assessment and management. Given the impact of ageing on arterial wall structure, the pressure dependence of PWV may vary with age. Using a non-invasive model-based approach, combining carotid artery echo-tracking and tonometry waveforms, we obtained pressure-area curves in 23 hypertensive patients at baseline and after three months of anti-hypertensive treatment. We predicted the follow-up PWV decrease using modelled baseline curves and follow-up pressures. In addition, based on these curves, we estimated PWV values for two age groups (mean ages 41 and 64 yrs) at predefined hypertensive (160/90 mmHg) and normotensive (120/80 mmHg) pressure ranges. Follow-up measurements showed a near 1 m/s decrease in carotid PWV when compared to baseline, which fully agreed with our model prediction given the roughly 10 mmHg decrease in diastolic pressure. The stiffness-blood pressure-age pattern was in close agreement with corresponding data from the "Reference Values for Arterial Stiffness' Collaboration" study, linking the physical and empirical bases of our findings. Our study demonstrates that the innate pressure dependence of arterial stiffness may have implications for the clinical use of arterial stiffness measurements, both in risk assessment and in treatment monitoring of individual patients. We propose a number of clinically feasible approaches to account for the blood pressure effect on PWV measurements.

2.1 Introduction

BEYOND blood pressure (BP), arterial wall stiffness measurements have emerged as guidance to target arterial wall structure in anti-hypertensive treatment and vascular risk management (Karalliedde et al. 2008; Ong et al. 2011; Shahin et al. 2012). Although the field is well aware of the fact that arterial wall stiffness is intrinsically pressure dependent (Laurent et al. 2006; Wolinsky and Glagov 1964), a clinically applicable method to disentangle BP and arterial stiffness is currently lacking. As a consequence, the order of magnitude and relevance of the pressure dependence of stiffness in the clinical context has not been established.

We previously showed by combining carotid artery ultrasound and tonometry, that arterial stiffness, expressed in terms of pulse wave velocity (PWV), may vary about 0.7–4.0 m/s within individuals due to the cyclic diastolic-systolic BP variation (Hermeling et al. 2012a; Hermeling et al. 2010). These cyclic stiffness changes clearly do not reflect any change in structural wall properties (Fig. 2.1; along curve A), but do suggest that the contribution of actual BP to the stiffness measurement in clinical practice may be considerable. In this light, the fixed threshold of 10 m/s for increased arterial stiffness, as advocated in the 2013 ESH/ESC guidelines (Mancia et al. 2013), requires a critical approach in (individual) patient management.

From a treatment perspective, the pharmacological modification of arterial wall struc-

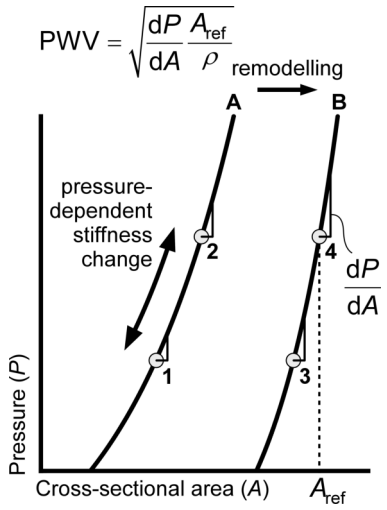

Figure 2.1: Study scope: quantitative influences of blood pressure and age on measured stiffness. Given a curvilinear pressure-area (*P-A*) relationship, short term changes in pressure will directly lead to changes in cross-sectional area and incremental slope (as indicated for curve A). The related changes in pulse wave velocity (PWV) in this case are not due to a change in the *P-A* relationship (cf. point 1 vs. 2). The stiffness assessed at the same pressure level in a remodelled vessel, illustrated by curve B, will be different due to a real change in the *P-A* relationship, as is known to occur with e.g., ageing (cf. point 1 vs. 3). Then ageing is expected to also modulate the pressure-related change in measured stiffness (consider the difference between 1 vs. 2 and 3 vs. 4). ρ, blood mass density.

ture has gained interest, with a particular focus on pressure-independent changes in PWV (Boutouyrie et al. 2011; Van Bortel et al. 2011; Wagenseil and Mecham 2012). An exploratory review of the literature shows that significant differences in PWV between groups or changes with treatment are accompanied by significant BP changes (Hermeling et al. 2010; Kithas and Supiano 2010; Ong et al. 2011). Thus, the extent to which observed changes in stiffness concurrent with BP changes reflect structural alterations in the arterial wall remains to be established (Boutouyrie et al. 2011; Van Bortel et al. 1999; Van Bortel et al. 2011).

Next to BP, age is the other major factor influencing arterial stiffness, as established by robust meta-analyses (Cecelja and Chowienczyk 2009; The Reference Values for Arterial Stiffness' Collaboration 2010). The structural alterations in the arterial wall related to ageing are well-known and clearly reflected by increased stiffness values found in older subjects (Langewouters et al. 1984; O'Rourke and Hashimoto 2007; Wagenseil and Mecham 2012). We previously observed that the pressure dependence itself may vary with age (Hermeling et al. 2010), which raises the question whether the BP effect on arterial stiffness measurements is as large in young subjects as in elderly (Fig. 2.1; compare curvature of curves A and B).

In the present study, we obtained more quantitative insight into the abovementioned aspects of the pressure dependence of arterial stiffness. To this end, we conducted an observational study in a sample of hypertensive subjects consecutively attending our out-

patient hypertension clinic.

We obtained non-invasive data on the carotid artery pressure-area relationship at baseline and at 3-month follow-up (Fig. 2.2A). At baseline, anti-hypertensive medication was discontinued. Shortly after the baseline measurement, anti-hypertensive medication was increased. At both visits, we calculated carotid pulse wave velocity (cPWV, Fig. 2.2A) using the Bramwell-Hill equation (Bramwell and Hill 1922a). In addition, baseline measurements were also used to obtain a pressure-area (*P-A*) curve model. If it is assumed that the *P-A* curve does not change, follow-up cPWV can be predicted (cPWVpred) using the baseline *P-A* curve and follow-up blood pressures (Fig. 2.2A). The feasibility of this assumption was verified by comparing the measured change in cPWV (ΔcPWV) with the predicted change (ΔcPWVpred).

In order to disentangle pressure and age effects on cPWV, we additionally calculated arterial stiffness at defined pressure levels for a young as well as an old subgroup of our population. We discuss our quantitative findings from a clinical perspective, focusing on their relevance in the cardiovascular risk management of individual patients.

2.2 Methods

2.2.1 Study population

The study was approved by the ethical committee of Maastricht University and conducted in accordance with the Declaration of Helsinki (Seoul 2008). All subjects provided written informed consent prior to participation. Thirty consecutive subjects were recruited from patients referred to our outpatient hypertension clinic for a two-day clinical assessment. Participants underwent extensive arterial function and hemodynamic measurements (detailed below) at inclusion and at three-months (3.0 ± 0.6 months) follow-up (Fig. 2.2A). Baseline characteristics and medication profile in units of daily defined dose (DDD, Wessling and Boethius 1990) are shown in Table 2.1. After baseline measurements, blood pressure was managed according to European Society of Hypertension (ESH) guidelines (Mancia et al. 2013), while treating physicians were blinded for (intermediate) study results. Seven subjects were excluded due to incomplete follow-up data ($n = 3$ no show; $n = 2$ missing carotid ultrasound) or inconsistent data quality ($n = 2$, see Discussion). Baseline and follow-up measurements obtained in 23 patients are used in the present analyses (Fig. 2.2B).

2.2.2 Measurements

Arterial function measurements (total duration 30–45 min) were performed in a quiet, temperature-controlled room (22 °C) after a resting period of 15 min with subjects in supine position. Throughout the session four to eight repeated oscillometric BP readings were obtained at the left upper arm (Omron 705IT, Omron Healthcare Europe B.V., Hoofddorp, The Netherlands). Additionally, continuous pulsatile finger BP, heart rate (HR) and an estimated cardiac output (CO), were obtained from the right middle finger by the Peñáz method (Nexfin, BMEYE B.V., Amsterdam, The Netherlands; Peñáz 1973).

Left common carotid artery diameter waveforms were obtained using a 7.5 MHz vascular ultrasound scanner (MyLab70, Esaote Europe, Maastricht, the Netherlands) operated

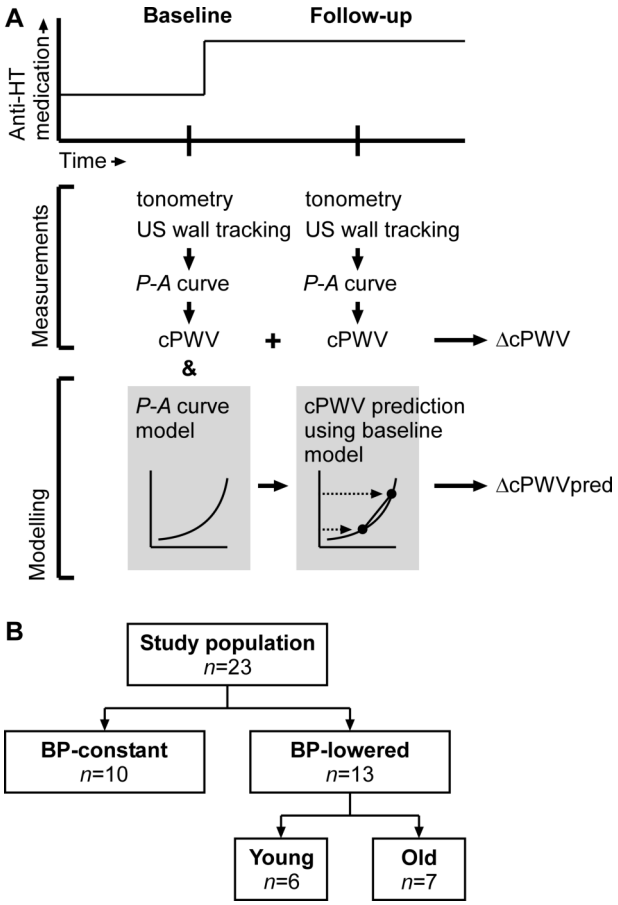

Figure 2.2: Study set-up and derivation of measured and predicted changes in carotid stiffness. **A**: The change in measured carotid pulse wave velocity (cPWV) from baseline to follow-up is termed ΔcPWV. The baseline pressure-area (*P-A*) curve of each subject was modelled by an exponential function. Using this baseline model and follow-up blood pressures, the change in cPWV with respect to baseline could be predicted (ΔcPWVpred), assuming that the *P-A* relationship did not change between baseline and follow-up. **B**: Stratification for analyses of blood pressure (BP) and age effects on measured stiffness. Young, subjects < 50 yrs; Old, subjects > 50 yrs; US, ultrasound.

Table 2.1: Baseline characteristics of study population

Parameter	Unit	$n = 23$
Age	yrs	56±15
Sex	# m/f	11/12
Height	cm	172±8
BMI	kg/m^2	27±4
aSBP	mmHg	140±15[a]
aDBP	mmHg	91±11[a]
aHR	1/min	73±9[a]
Dipper	# y/n	8/14[a]
	n[b]	DDD[b]
Anti-HT meds	9	2.6±1.6
ACEi/ARB	7	2.0±0.5
BB	7	0.6±0.3
CCB	1	2.0
Diuretics	5	0.7±0.3

Mean ± SD. aSBP and aDBP, 24-hour average systolic and diastolic blood pressures, respectively; aHR, 24-hour average heart rate. Dipper defined as night SBP < 85% of day SBP. ACEi, angiotensin-converting enzyme inhibitors; ARB, angiotensin receptor blockers; BB, beta blockers; CCB, calcium channel blockers. [a]$n = 22$. [b]Numbers (n) and daily defined doses (DDDs) pertain to only those receiving medication at baseline. Most of those not taking antihypertensive (anti-HT) drugs at baseline had discontinued medication prior to clinical blood pressure profiling.

at high frame rate as previously described (Hermeling et al. 2012b). Diastolic diameter and distension values over 6 consecutive heartbeats and a real-time distension waveform display were used to judge quality of the recordings ([RF]QAS utility, Esaote Europe). Subsequently, left common carotid artery tonometric pressure waveforms were obtained (SphygmoCor, AtCor Medical, Sydney, NSW, Australia). Raw carotid artery tonometry waveforms were used to obtain calibrated local left common carotid artery BP waveforms (Van Bortel et al. 2001). Signal processing was performed using proprietary MATLAB code (MATLAB R2013b, The MathWorks Inc, Natick, Massachusetts, USA). Carotid ultrasound and arterial tonometry measurements were obtained in triplet by a single experienced operator (JOR). Ambulatory (i.e., 24 h) BP was assessed from clinic assessment day one onto day two (Mobil-o-Graph, IEM, Stolberg, Germany).

2.2.3 Data processing

Waveform analysis and data processing

To enable quantitative assessment of the curvilinearity of the carotid artery pressure-area (P-A) relation at individual subject level, we followed procedures similar to those described previously (Hermeling et al. 2012b). Briefly, systolic (peak), dicrotic notch and diastolic (minimum) points were identified in the diameter (by manual cursor reading, using [RF]QAS) and pressure (automatic) waveforms. For diameter typically 9–12 and for pressure 18–30 heartbeats were included for each subject in each session.

To suppress variability related to echo and tonometry tracking artefacts, we applied the following averaging schemes for processing the acquired diameters (D). Diastolic diameter was averaged over acquired beats to obtain a recording average and subsequently over recordings to obtain a session average. Relative distensions (i.e., $\left(D_{\text{systolic}} - D_{\text{diastolic}}\right)/D_{\text{diastolic}}$) were averaged over beats and recordings, yielding a session average of relative distension. The session average of systolic diameter was then obtained by multiplying relative distension by the corresponding diastolic diameter and adding the diastolic diameter. Similarly, the relative distensions of the dicrotic notch point (i.e., $(D_{\text{notch}} - D_{\text{diastolic}})/\left(D_{\text{systolic}} - D_{\text{diastolic}}\right)$) were averaged for further analysis, rather than absolute dicrotic notch values. Exactly the same scheme was applied for carotid systolic, notch and diastolic blood pressures. Median averaging was used throughout.

Reproducibility

Intra-session measurement variability was quantified as follows. Differences of the three ($m = 3$) recording averages with the session mean were calculated for the entire study group ($n = 23$). The SD of these values from all subjects ($m \cdot n = 3 \cdot 23 = 69$) is a measure of intra-session variability.

Carotid stiffness calculation

Carotid artery cross-sectional areas were calculated at diastole (A_{d}), dicrotic notch (A_{n}) and systole (A_{s}) using $A = \pi (D/2)^2$. Local carotid PWVs (cPWV) were calculated using the Bramwell-Hill relationship (Bramwell and Hill 1922a):

$$\text{cPWV} = \sqrt{\frac{1}{\rho}\frac{\text{SBP} - \text{DBP}}{A_{\text{s}} - A_{\text{d}}} A_{\text{d}}}\,, \tag{2.1}$$

with $\rho = 1.050\,\text{kg/L}$ the blood mass density, and SBP and DBP the calibrated local systolic and diastolic carotid blood pressures, respectively.

Pressure-area curve description

In each individual and session, the three (diastolic, notch and systolic) *P-A* points obtained were used to fit an established mathematical description of the *P-A* relation, i.e., a single-exponential model (Meinders and Hoeks 2004):

$$P(A) = \text{DBP} \cdot e^{\gamma \cdot \left(\frac{A}{A_{\text{d}}} - 1\right)}\,. \tag{2.2}$$

γ is obtained by minimising the sum-of-squares of differences between measured and modelled notch and systolic pressures. The line is forced through the diastolic point. As a line with one free parameter (γ) is fitted through two points, the line will, in general, not pass exactly through the notch and systolic points.

Model prediction of stiffness at follow-up

Based on the above descriptive model (Eq. 2.2) and baseline *P-A* data, we predicted cPWV at follow-up (cPWVpred), using BP at follow-up as input. This was done under the explicit assumption that between baseline and follow-up the *P-A* relationship had remained unaltered. To verify whether this assumption was valid, we calculated stiffness for a prescribed, normotensive BP level of 120/80 mmHg by using the modelled *P-A* curves from baseline and follow-up ($\text{cPWVmod}_{120/80}$).

Stratification according to BP lowering at follow-up

To investigate whether measured changes in arterial stiffness were related to changes in BP observed in our study population, we stratified patients to a BP-lowered group ($n = 13$) if the reduction in DBP at three-month follow-up was more than twice the intra-session SD (i.e., 7 mmHg) and to a BP-constant control group ($n = 10$) if the reduction was less than 7 mmHg (Fig. 2.2B).

Stratification of BP lowering group to age

To identify age-related differences in hemodynamic and stiffness changes, we divided the BP-lowered group into a young group (< 50 yrs, $n = 6$) and an old group (> 50 yrs, $n = 7$) (Fig. 2.2B).

Age group data averaging and stiffness calculations for comparison with the "Reference Values for Arterial Stiffness' Collaboration"

For both the young BP-lowered group and the old BP-lowered group, we calculated an average *P-A* relationship by averaging the individual baseline *P-A* curves in *A*-direction. To enable comparison with reference values from The Reference Values for Arterial Stiffness' Collaboration (2010) study, we estimated cPWV values on these average baseline *P-A* curves, similar to described above. We applied pre-defined normotensive (120/80 mmHg; $\text{cPWVmod}_{120/80}$) as mentioned above) and hypertensive (160/90 mmHg; $\text{cPWVmod}_{160/90}$) blood pressure profiles for this analysis.

2.2.4 Statistical analysis

Statistical analyses were performed using MATLAB (MATLAB R2013b, The MathWorks Inc, Natick, Massachusetts, USA). Unless otherwise indicated, non-parametric Wilcoxon signed-rank or rank-sum tests were performed to evaluate statistical differences within patients and between groups, respectively. p-values ≤ 0.05 were considered statistically significant. Unless otherwise indicated, values are given as mean ± SD.

Agreement (bias and limits of agreement) between cPWV and cPWVpred changes at follow-up was assessed by Bland-Altman analysis.

Table 2.2: Changes in blood pressure and arterial properties without and with blood pressure lowering

Parameter	Unit	All individuals			
		Baseline		Change at 3-month follow-up	
		BP-constant	BP-lowered	BP-constant	BP-lowered
n		10	13	10	13
Age	yrs	59±17	53±14		
meds	DDD	1.2±1.9	0.8±1.2	0.3±0.6	1.6±0.8*,**
SBP	mmHg	154±24	163±29	1±14	−25±10*,**
DBP	mmHg	87±10	94±9	1±5	−12±6*,**
PP	mmHg	67±22	69±29	−0±13	−13±9*,**
cPWV	m/s	10.8±2.3	10.7±3.1	0.1±1.5	−0.9±1.1*
cPWVpred	m/s			0.1±0.4	−0.9±0.4*,**

Mean ± SD. meds denotes antihypertensive medication in daily defined dose (DDD). Sex differences were not statistically significant ($p = 0.21$, Fisher's exact test). BP, blood pressure; SBP and DBP, systolic and diastolic blood pressures, respectively; PP, pulse pressure; cPWV, carotid pulse wave velocity; cPWVpred, carotid pulse wave velocity predicted from the baseline pressure-area model curve and follow-up BP; meds, antihypertensive medication; PP, pulse pressure. $^{*}p < 0.05$ for change at follow-up compared with baseline (Wilcoxon signed-rank test). $^{**}p < 0.05$ for difference between BP-constant and BP-lowered groups (Wilcoxon rank-sum test).

2.3 Results

2.3.1 Reproducibility

Intra-session SDs were 2% for diastolic diameter, 13% for relative distension, and 7% for relative notch amplitude. Intra-session SDs (post calibration) were 4% for local carotid diastolic pressure, 10% for pulse pressure and 5% for relative notch amplitude. The absolute intra-session SD for diastolic blood pressure (DBP) was 3.5 mmHg.

2.3.2 Effect of BP lowering

At baseline, there were no significant differences in patient characteristics, BP, and arterial properties between the BP-lowered and BP-constant groups (Table 2.2).

Compared to the control group, the BP-lowered group tended to have less anti-hypertensive medication at baseline (0.8 ± 1.2 vs. 1.2 ± 1.9 DDD; Table 2.2) and had a more intensified regime at three-month follow-up (2.4 ± 1.4 vs. 1.5 ± 1.9 DDD, of which mainly renin-angiotensin-aldosterone system inhibitors: 1.4 ± 1.0 vs. 0.6 ± 0.9 DDD; not shown in table).

The anti-hypertensive treatment particularly decreased SBP, showing a decrease twice that of DBP (Table 2.2), although HR, CO and stroke volume (SV) did not change significantly (data not shown).

Carotid stiffness as expressed by pulse wave velocity (cPWV) significantly decreased in the BP-lowered group (Table 2.2). The change in cPWV, however, was not significantly dif-

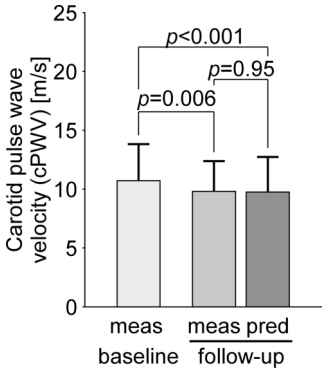

Figure 2.3: Measured (meas) carotid artery stiffness (carotid pulse wave velocity, cPWV; Bramwell-Hill) in the blood pressure-lowered group ($n = 13$) at baseline and at follow-up, in comparison with predicted (pred) changes based on follow-up blood pressures and using the single exponential model fitted to individual pressure-area data obtained at baseline. Whiskers indicate standard deviation.

ferent between the BP-lowered and BP-constant groups. Model predictions of the change in cPWV at follow-up (cPWVpred) were of the same order of magnitude (-0.9 ± 0.4 m/s) as the measured change (-0.9 ± 1.1 m/s; $p = 0.95$; Fig. 2.3). Bias and limits of agreement (Bland-Altman) between measured and predicted changes in cPWV were 0.0 ± 2.0 m/s.

2.3.3 Age-associated differences with BP lowering

Table 2.3 discriminates baseline BP and arterial properties as well as their changes at follow-up for the young and old subjects with BP lowering. There were no differences in sex, height, weight or BMI between age-groups. Differences in BP profiles and carotid cross-sectional area were noted at baseline but these did not reach statistical significance. Baseline values and follow-up changes in DBP and A_d were not significantly different between age groups. The old group tended to have less anti-hypertensive medication at baseline (0.6 ± 1.2 vs. 1.0 ± 1.4 DDD; Table 2.3) and had a more intensified regime at three-month follow-up (2.6 ± 1.5 vs. 2.2 ± 1.4 DDD, of which mainly renin-angiotensin-aldosterone system inhibitors: 1.7 ± 1.1 vs. 1.0 ± 0.9 DDD; not shown in table).

Both age groups with BP lowering showed significant reductions in SBP (-21 ± 9 mmHg, $p = 0.03$ and -29 ± 9 mmHg, $p = 0.02$ for < 50 and > 50 yrs, respectively; $p = 0.18$ for inter-group).

Pulse pressure (PP) showed a significant decrease at follow-up in the old group only (-17 ± 7 mmHg, $p = 0.01$; $p = 0.04$ for inter-group difference). SV was unchanged (no difference between age groups; data not shown).

Baseline cPWV differed significantly between age groups (Table 2.3). The measured change in cPWV was significant only in the old, amounting to -1.2 ± 1.0 m/s, and similar to cPWV changes predicted by the patient-specific single-exponential model (cPWVpred; -1.1 ± 0.4 m/s).

Baseline $\text{cPWVmod}_{120/80}$ was significantly different between age groups (Table 2.3). However, changes in $\text{cPWVmod}_{120/80}$ at 3-month follow-up were not significant within

Table 2.3: Blood pressure lowering related changes in arterial properties in younger and older patients

Parameter	Unit	BP-lowered patients			
		Baseline		Change at 3-month follow-up	
		Age < 50 yrs	Age > 50 yrs	Age < 50 yrs	Age > 50 yrs
n		6	7	6	7
Age	yrs	41±6	64±9**		
meds	DDD	1.0±1.4	0.6±1.1	1.2±0.8	2.0±0.7*
SBP	mmHg	149±17	174±34	−21±9*	−29±9*
DBP	mmHg	95±12	92±4	−13±4*	−12±8*
PP	mmHg	54±14	82±33	−8±9	−17±7*,**
A_d	mm^2	46.3±9.0	58.5±16.7	−1.5±0.9	−2.9±5.5
cPWV	m/s	8.4±1.2	12.7±2.9**	−0.5±1.1	−1.2±1.0*
cPWVpred	m/s			−0.7±0.3*	−1.1±0.4*
cPWVmod$_{120/80}$	m/s	7.4±1.0	11.0±2.1**	0.2±0.9	−0.2±1.0

Mean ± SD. meds denotes antihypertensive medication in daily defined dose (DDD). Sex differences were not statistically significant ($p = 0.59$, Fisher's exact test). SBP and DBP, systolic and diastolic blood pressures, respectively; PP, pulse pressure; A_d, diastolic cross-sectional area; BP, blood pressure; cPWV, carotid pulse wave velocity; cPWVpred, cPWV predicted from baseline *P-A* relationship and follow-up blood pressures; cPWVmod$_{120/80}$, cPWV calculated for standardised BP of 120/80mmHg; meds, antihypertensive medication; PP, pulse pressure. $^{*}p < 0.05$ for change (Wilcoxon signed-rank test). $^{**}p < 0.05$ for difference between age groups (Wilcoxon rank-sum test).

the age groups and the changes at follow-up were not significantly different between age groups.

2.3.4 Differences in pressure-area relationships between age groups

Fig. 2.4A shows the group-average of the single-exponential *P-A* curves of the individuals in both the young and old groups. With respect to the young group's curve, the old group's *P-A* curve is not only shifted rightward to larger areas but is also steeper, reflecting greater stiffness at corresponding to blood pressure levels.

Fig. 2.4A also indicates the normotensive and hypertensive pressure ranges we defined to assess more generically age-related differences in the *P-A* relationships (shaded areas). We calculated PWVs for these ranges (PWVs indicated in the figure and in Fig. 2.5A). These group-averaged PWVs suggest that for a given acute decrease in SBP and DBP of 40 and 10 mmHg respectively, measured arterial stiffness may decrease more in older hypertensive patients (−1.3 m/s; mean age 64 yrs) than in the younger (−0.9 m/s; mean age 41 yrs). These changes are clearly visible in Fig. 2.4B, where PWV is plotted as a function of DBP.

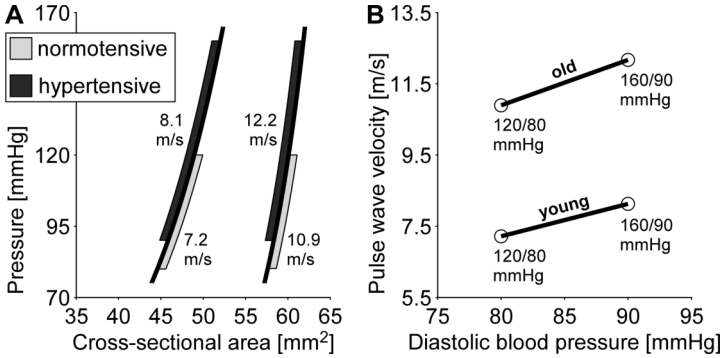

Figure 2.4: Relationship between age, blood pressure, and pulse wave velocity. **A**: Comparison of the young and old groups' pressure-area relationships. Note that the old group operates at a greater average cross-sectional area than the young group. To study the stiffness–pressure–age relationship more generically, we pre-defined normotensive and hypertensive blood pressure ranges, as indicated by the shaded areas. Pulse wave velocities for these ranges are indicated in the figure, and replicated in Fig. 2.5A. **B**: Pressure dependence of pulse wave velocity. Pulse wave velocities for normotensive and hypertensive groups in **A** as a function of diastolic blood pressure. Systolic and diastolic pressures are indicated in the figure as systolic/diastolic blood pressure. Note that in the old group, the pulse wave velocity increase with diastolic blood pressure is larger than in the young group (steeper slope of the lines).

A **This study**

Estimated pulse wave velocities for predefined pressure ranges [m/s]

		Age [yrs]	
		41	64
SBP/DBP [mmHg]	120/80	**7.2**	**10.9**
	160/90	**8.1**	**12.2**
	Δ	**0.9**	**1.3**

- Intra-subject
- Physical relationship
- 13 subjects

B **The "Reference Values for Arterial Stiffness' Collaboration"**

Pulse wave velocity [m/s]

		Age [yrs]	
		41	64
SBP/DBP [mmHg]	120/80	**7.1**	**10.0**
	160/90	**8.4**	**11.5**
	Δ	**1.2**	**1.6**

- Inter-subject
- Statistical association
- 11 092 subjects

Figure 2.5: Arterial stiffness, blood pressure and age patterns of the present study and the "Reference Values for Arterial Stiffness' Collaboration" are strikingly similar. Stiffness, as indicated by pulse wave velocity (PWV) is shown for the mean ages of the two age groups in the present study (baseline visit) and pre-defined normotensive (120/80 mmHg) and hypertensive (160/90 mmHg) pressure ranges. Δ: difference in PWV between hypertensive and normotensive conditions. **A**: Carotid artery PWV values derived from the modelled pressure-area curves ($cPWVmod_{120/80}$ and $cPWVmod_{160/90}$) via Bramwell-Hill for young and old groups. **B**: Carotid-femoral PWVs derived from published data from the "Reference Values for Arterial Stiffness' Collaboration" (The Reference Values for Arterial Stiffness' Collaboration 2010: Fig. 4, bottom and Table 6, bottom; PWVs linearly interpolated between age categories and at corresponding mean arterial pressures ($MAP = 0.4 \cdot SBP + 0.6 \cdot DBP$), i.e., hypertensive 118 and normotensive 96 mmHg). DBP, diastolic blood pressure; SBP, systolic blood pressure.

2.3.5 Comparison with the "Reference Values for Arterial Stiffness' Collaboration"

Fig. 2.5 compares the stiffness–BP–age pattern found in our mechanistic study (A) with those found on statistical grounds in the reference population (B) (The Reference Values for Arterial Stiffness' Collaboration 2010). Overall, the arterial stiffness patterns are very similar but their pressure dependence at a given age appears greater in the reference population (between groups) than within our patients. Interestingly, the difference in pressure dependence, i.e., the influence of the assumed BP change on measured stiffness, is the same for both: $(1.3-0.9)=(1.6-1.2)=0.4\,\mathrm{m/s}$.

2.4 Discussion

The present study shows that clinically observable changes in arterial stiffness and BP are linked through the non-linear arterial *P-A* relationship, the effect of which appears modified with age. Our findings show that a short-term decrease in DBP of about 10 mmHg leads to a decrease in measured carotid PWV of about 1 m/s. This decrease is not caused by a change in the *P-A* relationship, since we were able to predict this decrease by imputing BP values at follow-up onto the (modelled) *P-A* curve at baseline. We did observe a difference in the carotid artery *P-A* relationship between young (41 yrs) and old (64 yrs) subgroups, the old group having greater cross-sectional area and increased stiffness at comparable DBP. Based on these age-stratified *P-A* data, we estimated generalised carotid PWV values for predefined normotensive (120/80 mmHg) and hypertensive (160/90 mmHg) BP ranges. Our clinical measurements and the generalised data indicate that, for comparable changes in BP, PWV changes more in older subjects due to a higher degree of non-linearity of the *P-A* relationship. The resultant stiffness–BP–age pattern proved strikingly similar to the pattern we read from The Reference Values for Arterial Stiffness' Collaboration (2010) study, though it should be noted that this reference values study is based on transit time PWVs instead of carotid PWVs. These findings indicate that the innate pressure dependence of arterial stiffness could have implications regarding patient vascular risk stratification and treatment monitoring.

2.4.1 Influence of blood pressure on arterial stiffness measurements

To quantitatively assess the impact of BP level on PWV measurements and corresponding risk scoring, we approached the BP dependence of stiffness at the individual/small group level, using an established descriptive model (Meinders and Hoeks 2004). This model was used to derive PWV at well-defined and comparable BP levels, as opposed to a statistical approach. Adjustment for mean arterial pressure in multiple linear regression models is only possible in moderate to large populations (Schillaci et al. 2011), whereas our approach allows individual quantification of the BP effect on stiffness.

With our individualised 3-point *P-A* measurements and model fitting approach, we predicted cPWV changes following three months of anti-hypertensive treatment, under the assumption that no real change occurs in the *P-A* relationship (cPWVpred). The observation that the changes in cPWV and cPWVpred with BP lowering were of similar magnitude suggests that short-term anti-hypertensive treatment has no effect on intrinsic arterial wall

stiffness, but reduces measured stiffness mainly via the nonlinear *P-A* relationship (exemplified with curve A; Fig. 2.1). The hypothesis of no real change in the *P-A* relationship could not be rejected, as the measured *P-A* curves at follow-up and their standardised stiffness values ($cPWVmod_{120/80}$) were not significantly different.

The measured 1 m/s PWV decrease exceeds measurement variability, which is typically of the order of 0.5 m/s. Therefore, the pressure dependence appears relevant when considering fixed cut-off values to triage individual patients based on PWV measurements. As such, our study specifically links part of the uncertainty in PWV determinations to actual BP levels, which is an issue both in initial risk stratification and in monitoring treatment effects.

It is well known that the white-coat effect can cause office BPs to show higher values than a patient's actual BP as measured using ambulatory BP measurement. We assessed the effect of this artificially elevated measured BP on the measured arterial stiffness in the office (Appendix 2.A1). Our analysis of the white-coat effect on arterial stiffness measurements showed a similar 1 m/s difference in stiffness linked to a 10 mmHg difference between mean ambulatory and study DBP.

Taken together, our quantitative findings indicate that the (physically well-established) pressure dependence is relevant to consider in initial risk assessment and in monitoring treatment in individual patients.

2.4.2 Influence of ageing on arterial stiffness and its pressure dependence

Based on the stratification to age and on modelled *P-A* data, we consistently found a larger dependence of PWV on BP in older subjects than in younger. This difference with age is directly related to the steeper slope of the *P-A* relation, as notable from the modelled curves in Fig. 2.4. Our analysis based on predefined BP ranges (Fig. 2.5) further supports the notion of an age-related difference in pressure dependence and that this observation is not a by-effect of the differing BP (ranges) between age groups. Rather, the intrinsically different *P-A* relationship explains the age-related difference in elastic behaviour. In addition to the increased slope, a greater average cross-sectional area with age is evident from our data (Fig. 2.4), which is in line with *ex vivo* data (Virmani et al. 1991). It should however be noted, given discrepant observations in cross-sectional cohorts (Reneman et al. 2005; Virmani et al. 1991), that longitudinal data on changes in arterial structure with ageing are much needed. Both the stiffening (increase in slope) and dilatory (increase in mean area) aspects are biomechanically consistent with the established concept of age-related degradation of the elastin structure in the wall and the resulting transfer of mechanical stress to the stiffer collagen network (Bénétos et al. 1993; O'Rourke and Hashimoto 2007; Wagenseil and Mecham 2012).

2.4.3 Stiffness, blood pressure and age as a pattern

We found that the (modelled) within-age-group changes in carotid stiffness with BP lowering match well with the aortic stiffness–BP–age pattern observed in the reference values population (Fig. 2.5). This match existed despite the obvious methodological differences,

such as physical/statistical approach, number of subjects, intra-/inter-subject comparison, carotid/aortic measurements and stiffness calculations, and outpatients/population characteristics. This prompts critical consideration of the pressure dependence of stiffness measurements as advocated in clinical-epidemiological research (Kaess et al. 2012; Laurent et al. 2001; The Reference Values for Arterial Stiffness' Collaboration 2010) and practice guidelines (Laurent et al. 2006; Mancia et al. 2013).

Our study provides a physical underpinning of the epidemiological stiffness–BP–age data pattern, implying that at given age a considerable part of the arterial stiffness spread in the population may be simply explained by the non-linear elastic behaviour of arteries, having not so much to do with adaptive hypertrophy or hypertensive remodelling (Bots et al. 1997; Boutouyrie et al. 2000). The structural remodelling that does occur with ageing (Fig. 2.4) appears to accentuate the BP-related arterial stiffness spread in the older population (The Reference Values for Arterial Stiffness' Collaboration 2010).

In current clinical practice, treatment of hypertension is predominantly focussed on lowering blood pressure and much less on arterial wall stiffening as a potential cause for hypertension. However, current (2013) ESH guidelines (Mancia et al. 2013) do state a carotid-femoral PWV above 10 m/s as an additional risk factor. Our study shows that, if the BP effect is not accounted for, consideration of arterial stiffness (as quantified by PWV) in risk scoring may introduce a spurious double scoring of high BP (Mancia et al. 2013). In this regard, our findings suggest that the arterial stiffness of patient A with a PWV of 9 m/s and diastolic BP of 70 mmHg may be considered equivalent to that of patient B with respective readings of 11 m/s and 90 mmHg. Hence, it may not be justified physically to score patient B +1 for increased arterial stiffness (cf. Table 4 in (Mancia et al. 2013)).

The agreement between reference values data and our findings in clinical patients suggests that risk stratification on the basis of combined BP–age cut-off values would do more justice to the physical and practical aspects of arterial stiffness measurements. Alternative approaches to improve risk stratification would be 1) to use the individual patient's *P-A* data and calculate from a modelled curve the stiffness value at a fixed or normative (e.g., age-specific) BP level or, as a thumb-rule; or 2) to adjust PWV values for concurrently measured DBP at a rate of 1 m/s per 10 mmHg.

2.4.4 Limitations

Our study did not include a long-term follow-up. Therefore, we could not evaluate whether on the long-term the *P-A* relationship was modified by the anti-hypertensive treatment, as a sign of structural (re-)remodelling. Moreover, our observational study design and number of subjects do not allow a well-powered drug-specific analysis. In future studies, both short- and long-term follow-up measurements should be performed to be able to fully discriminate and quantify the pressure-dependent and -independent effects of (anti-hypertensive) drugs on arterial wall structure (Boutouyrie et al. 2011; Ong et al. 2011; Van Bortel et al. 1999; Van Bortel et al. 2011).

We found zero bias between measured and predicted changes in cPWV. The limits of agreement, however, were substantial. With our sample size we could have detected a significant difference of > 0.8 m/s at a power of 80%. A large part of the variability is explained by the fact that the measured changes in cPWV were subject to variability in both pressure and area measurements, whereas the model-predicted changes were only

subject to variability in pressure.

Our study was set up as an observational study in consecutive patients, which, given non-compliance with the protocol ($n = 3$) and missing data ($n = 2$), led to basic exclusion of subjects (see Study population). Additionally, two subjects were excluded. One subject showed a convex *P-A* relationship at one visit, which is physically not plausible and very likely a measurement error. In the other subject, we did not obtain sufficiently stable pressure and area waveforms due to vessel movement.

We calculated PWV values not from transit time based measurements but from distensibility based on *P-A* data (Fig. 2.1). Cross-sectional arterial distensibility is physically related to PWV via the Bramwell-Hill relationship (Bramwell and Hill 1922a). This approach is required, because transit time PWV measurement does not allow discrimination of stiffness within the diastolic-systolic range, to which the non-invasive assessment of large artery stiffness is practically limited to. Moreover, our aim was to get a feeling of the order of magnitude of the pressure dependence, not to establish absolute agreement between the two approaches.

The approach presented in this study requires the assumption of an exponential relationship between P and A. Although Meinders and Hoeks (2004) showed that this is a reasonable assumption, in individual cases, it may not hold. When full pressure and diameter waveforms are available (as is the case in the present study), one could also obtain pressure-independent, isobaric stiffness measurements without the exponential curve assumption. This is exemplified by studies by Balkestein et al. (1999) and De Hoon et al. (2001), in which isobaric distensibility and compliance coefficients were determined for a fixed pressure interval. Although this approach has the advantage of not relying on the assumption of an exponential *P-A* relationship, it is more sensitive to measurement noise, as only a small part of the measured relationship is used for stiffness quantification (Van Bortel et al. 2002).

It should be stressed that our 3-point *P-A* approach is not affected by apparent hysteresis caused by phase errors or time-delays between pressure and area waveform signals (Hermeling et al. 2012a), given that we only consider corresponding P and A amplitudes. Hysteresis due to viscous behaviour of the arterial wall *in vivo* using a well-characterised measurement set-up is negligible (Alghatrif et al. 2013; Hermeling et al. 2010).

Our measurements included carotid artery applanation tonometry, which requires substantial applied pressure to applanate the vessel. Consequently, baroreflex modulation may have potentially affected hemodynamic conditions. Using the continuous finger blood pressure and HR data acquired (Nexfin), we tested whether HR and relative dicrotic notch height (in the finger pressure waveform) were different between carotid (potential baroreflex effect) and femoral (no baroreflex effect) tonometry recordings. Three repeated and alternating carotid and femoral tonometry acquisitions were performed in all subjects ($n = 23$). We found no difference in HR (62.5 bpm carotid vs. 63.1 bpm femoral, $p = 0.24$) and no difference in relative dicrotic notch height (0.39 carotid vs. 0.38 femoral, $p = 0.24$). Moreover, the tonometric pressure waveform was calibrated to absolute values using session-averaged brachial blood pressures, hence potential baroreflex-mediated noise or bias in mean or pulse pressure during tonometry will not have propagated into our *P-A* data. Taken together, it appears unlikely that the tonometry measurements in our study affected proper correspondence between P and A datapoints.

We approached ageing by cross-sectional data. Ideally, ageing effects should be as-

sessed longitudinally, following patients over time, as for example in the recently published study by Alghatrif et al. (2013). Unfortunately, AlGhatrif et al. did not include information on the BP change between baseline and follow-up, i.e., only BP category at baseline was used as a statistical model determinant. Additionally, the question can be asked whether our small study in hypertensives is sufficiently powered and representative. While our stiffness–BP–age pattern agrees well with the reference values data as well as with current mechanistic concepts of arterial wall elastic behaviour and remodelling, we conclude that there is strong mechanistic and epidemiological evidence corroborating our present findings (Langewouters et al. 1984; O'Rourke and Hashimoto 2007; The Reference Values for Arterial Stiffness' Collaboration 2010; Virmani et al. 1991; Wagenseil and Mecham 2012; Wolinsky and Glagov 1964).

2.4.5 Perspectives

We conclude that short-term changes in carotid artery stiffness (in PWV terms) concurrent with BP lowering can be deemed BP-dependent, at a rate of about 1 m/s per 10 mmHg DBP. We also found that this pressure dependence appears greater in older subjects, which is consistent with changes in the arterial pressure-area relationship due to age-related structural remodelling. Both these BP and age influences are responsible for the clinical and epidemiological patterns observed between stiffness (PWV), BP and age. While current treatment of hypertension is focussed on lowering BP, ESH guidelines (2013) include the option to score a carotid-femoral PWV above 10 m/s as an additional risk factor. Based on the physically underpinned insights that our study yields, combined BP–age specific PWV thresholds seem more justified for use in vascular risk management than the current absolute threshold of 10 m/s for carotid-femoral PWV. Our non-invasive model-based methodology is feasible in a vascular clinic setting and could improve identification of treatment effects on arterial wall structure, by discriminating BP-dependent and -independent changes in arterial wall elastic properties.

2.5 Acknowledgements

This study was supported by a Kootstra Talent Fellowship awarded to B. Spronck by Maastricht University and by grant Veni-STW10261 for K.D. Reesink from the Innovational Research Incentives Scheme of the Dutch Organisation for Scientific Research (NWO).

2.A1 Appendix: Potential white-coat effect on arterial stiffness measurements

2.A1.1 Introduction

It is well known that the white-coat effect can cause office BPs to show higher values than a patient's actual BP as measured using ambulatory BP measurement (Parati and Valentini

2007). As PWV is dependent on BP, the white-coat effect potentially also has an influence on measured PWVs. In this appendix, we will assess the white-coat effect of BP on PWV.

2.A1.2 Methods

Baseline modelled *P-A* curves were used to calculate cPWVmod values for ambulatory BP values. These values were used to assess the white-coat effect on arterial stiffness measurements.

2.A1.3 Results

Table 2.A1 shows for both age-groups the differences in cPWV as measured during the study and the calculated cPWVmod, based on ambulatory BP values and the (individual) baseline *P-A* curves. A roughly similar 1 m/s difference in stiffness linked to a 10 mmHg difference between night-time ambulatory and study DBP was noted, corroborating the pressure dependence rate described above.

2.A1.4 Discussion

Our analysis of the white-coat effect on carotid artery stiffness measurements showed a similar 1 m/s difference in stiffness linked to a 10 mmHg difference between mean ambulatory and study DBP. It should be noted 1) that for the young the effect was smaller than in the older group, and 2) that in our white-coat PWV illustration, only the BP effect is included (Van Bortel et al. 2002), whereas it is known that the white-coat effect may also increase vessel tone (Van Bortel et al. 2011; Wagenseil and Mecham 2012), which would increase PWV beyond the mere BP effect. Schillaci et al. (2011) established the effect of white-coat hypertension on (office) arterial stiffness measurements, using a statistical approach at clinical population level. They concluded that stiffness values should be adjusted based on the office versus ambulatory BP difference. This, however, is only possible at individual patient level either using our model-based approach or using a 1 m/s per 10 mmHg thumb-rule.

Table 2.A1: Potential white-coat effect on arterial stiffness measurements

Parameter	Unit	BP-lowered patients							
		Age < 50 yrs				Age > 50 yrs			
		Study baseline ($n = 6$)	Ambulatory ($n = 6$)			Study baseline ($n = 6$*)	Ambulatory ($n = 6$*)		
			Day	Mean	Night		Day	Mean	Night
SBP	mmHg	149±17	143±17	137±16	124±14	164±22	147±14	142±14	133±18
DBP	mmHg	95±12	99±10	93±10	80±10	92±5	94±12	89±11	80±13
PP	mmHg	54±4	44±10	44±8	44±5	72±22	53±11	53±11	53±11
cPWV	m/s	8.4±1.2				12.0±2.4			
cPWVmod	m/s		8.4±1.2	8.1±1.2	7.5±1.2		11.6±1.9	11.4±2.0	10.9±2.2

Mean ± SD. *For one subject, ambulatory data were unavailable. BP, blood pressure; SBP and DBP, systolic and diastolic blood pressures; PP, pulse pressure; cPWV, carotid pulse wave velocity; cPWVmod, cPWV calculated from baseline, study *P-A* relationship and ambulatory blood pressures.

Chapter 3

Blood pressure correction of arterial stiffness in a cohort on anti-angiogenic medication

The contents of this chapter are based on:

Bart Spronck,[1] Tammo Delhaas,[1] Anouk G.W. de Lepper,[1] Julie Giroux,[2] François Goldwasser,[2] Pierre Boutouyrie,[3] Maureen Alivon,[3] and Koen D. Reesink[1] (2016). Patient-specific blood pressure correction technique for arterial stiffness: Evaluation in a cohort on anti-angiogenic medication [submitted].

[1] Department of Biomedical Engineering, CARIM School for Cardiovascular Diseases, Maastricht University, Maastricht, The Netherlands.
[2] CERIA, Cochin Hospital, Assistance Publique - Hôpitaux de Paris, Paris, France.
[3] Department of Pharmacology, Université Paris Descartes, INSERM U970, European Georges Pompidou Hospital, Assistance Publique - Hôpitaux de Paris, Paris, France.

Abstract

Anti-angiogenic drugs (AADs) are increasingly used in anti-cancer therapy, with hypertension as a frequent side effect. Furthermore, arterial pulse wave velocity (PWV) increases with AAD treatment. PWV, however, depends on blood pressure (BP). Therefore, using PWV to assess intrinsic arterial stiffness requires consideration of BP. We recently developed a mechanistic, model predictive approach to assess BP-independent changes in carotid PWV (cPWV). In the present study, we used this approach to assess the BP-independent effect of AADs on cPWV, and compared it to a conventional statistical correction approach. We obtained carotid artery systolic and diastolic cross-sectional areas (echo-tracking) and corresponding BPs (tonometry) in 48 patients before starting AAD treatment (sorafenib/sunitinib), and at four follow-up visits spaced two weeks apart. For each patient, we derived cPWV and a baseline single-exponential BP-cross sectional area curve. Based on these baseline curves and follow-up BPs, we predicted cPWV at follow-up due to BP. By comparing predicted and measured cPWVs at follow-up, we assessed the BP-independent cPWV increase. In the same way, we assessed whether diastolic cross-sectional area (A_d) changed beyond the BP-induced amount. The AAD-induced BP-independent increase in cPWV was $0.43[0.09, 0.77]\,m/s$ (mean[95%CI], $p = 0.014$, mechanistic approach) and $0.48[0.14, 0.82]\,m/s$ ($p = 0.006$, statistical approach). A_d increased with $1.92[0.93, 2.92]\,mm^2$ ($p < 0.001$) and $2.14[1.06, 3.23]\,mm^2$ ($p < 0.001$), respectively. In conclusion, the present study demonstrates the feasibility and potential of our mechanistic, model predictive approach to quantify BP-independent effects on arterial stiffness at the level of the individual, in a clinically relevant setting of AAD therapy.

3.1 Introduction

ANTI-ANGIOGENIC drugs (AADs) are increasingly used in anti-cancer therapy (Cao and Langer 2010). We recently showed that AADs lead to an increase in local carotid pulse wave velocity (cPWV) (Alivon et al. 2015), a measure of large artery stiffening. Furthermore, AAD treatment frequently leads to hypertension (Wu et al. 2008). Since pulse wave velocity is known to depend on blood pressure (BP) (Bramwell et al. 1923), the increased cPWV does not directly reflect intrinsic large artery stiffening. Therefore, using PWV to assess intrinsic arterial stiffness requires consideration of BP.

In a recent study, we demonstrated that by using distensibility measurements at carotid level and a mechanistic approach, it is possible to assess the blood pressure effect on cPWV in the individual patient, rather than adjusting for BP at the group level (Spronck et al. 2015b). This approach is based on a single-exponential relationship that is fitted to arterial pressure-area measurements, and allows estimation of any changes in stiffness due to changes in wall material and not due to BP.

In the present study, we will use our novel mechanistic approach to quantify the BP-independent effect of AADs on large artery stiffness. We will compare this novel mechanistic approach to the conventional, exclusively statistical correction for BP effects, and

discuss the differences between these two methods.

3.2 Methods

3.2.1 Study population and measurements

The population and measurements used in this study were elaborately described previously (Alivon et al. 2015). Briefly, patients in whom treatment with AADs (sorafenib or sunitinib) was indicated were recruited at a secondary unit dedicated to care of metastatic cancer patients (Fig. 1 in Alivon et al. (2015)). Patients were investigated during day hospitalisation for chemotherapy administration, at baseline, after 7–10 days of AADs (follow-up 1) and then every 2 weeks for 6 weeks (follow-ups 2–4). At each visit, brachial diastolic (DBP), mean (MAP) and systolic (SBP) blood pressures were recorded in triplicate using an oscillometric device (Dinamap, GE Medical, Tampa, Florida, USA). If AADs induced hypertension, the consulting physician put patients on anti-hypertensive drugs (AHDs). Systolic, mean and diastolic pressures were averaged over the three acquired measurements by calculating the average. In addition, carotid artery ultrasonic wall tracking was performed (ART.LAB; Esaote Pie-Medical, Maastricht, the Netherlands) (Alivon et al. 2015). Local carotid artery pulse pressure was calculated using the carotid applanation tonometry waveform recorded with a SphygmoCor device (AtCor Medical, Sydney, NSW, Australia) (Alivon et al. 2015). This approach assumes carotid DBP and MAP to equal brachial DBP and MAP (Van Bortel et al. 2001). Patients provided written informed consent before baseline testing. The study protocol was performed within the Angiogenesis Inhibitors Study and Research Centre (CERIA) and was approved by the Cochin Ethics committee (approval number 12804766).

3.2.2 Data processing

Data processing was performed using the software R, version 3.2.3 (R Core Team 2014).

Carotid stiffness calculation

Cross-sectional areas of the carotid artery lumen were calculated from the media-adventitia echo diameter using $A = \pi \cdot (\text{diameter}/2)^2$ at diastole (A_d) and systole (A_s). cPWV was calculated using the Bramwell-Hill relationship (Bramwell and Hill 1922a):

$$\text{cPWV} = \sqrt{\frac{1}{\rho}\frac{\text{SBP}-\text{DBP}}{A_\text{s}-A_\text{d}}A_\text{d}}\,, \tag{3.1}$$

with $\rho = 1.050\,\text{kg/L}$ the blood mass density, and SBP and DBP the systolic and diastolic brachial blood pressures, respectively.

Uncorrected effect of AADs on blood pressures, cPWV, and A_d

The uncorrected effect of AADs on blood pressures, cPWV, and A_d was assessed using mixed-effects models (R nlme package version 3.1-125) (Pinheiro et al. 2014) of the

form:

$$par = \beta_0 + \beta_1 \text{AAD} \,, \tag{3.2}$$

where par is brachial SBP, carotid SBP, MAP, DBP, cPWV, or A_d, respectively. AAD is a Boolean variable indicating the use of anti-angiogenic drugs, and is therefore coded 0 for the baseline visit and 1 for all follow-up visits. Therefore, β_0 represents the average value of par at baseline, and β_1 represents the average AAD-induced change in par over all follow-up visits.

Mixed-effects modelling has the distinct advantage over e.g., repeated-measures analysis of variance (ANOVA) that it can handle missing data points, maximising the use of all available data. Furthermore, mixed-effects modelling has proven to be very robust against non-normality of residuals (Gelman and Hill 2006). The most appropriate covariance structure was determined for each model by likelihood-ratio comparison of 8 models with different covariance structures (Walavalkar et al. 2016). Likelihood-ratio tests were used to compare the different covariance structures (Walavalkar et al. 2016; Zuur et al. 2009). After the most suitable covariance structure was found, significance of fixed model terms was assessed by likelihood-ratio comparison of successively more complicated models.

Mechanistic approach

Pressure-area curve description The diastolic and systolic pressure-area (*P-A*) points obtained at baseline (before anti-angiogenic treatment) were used to fit an established mathematical description of the *P-A* relation, i.e., a single-exponential model (Meinders and Hoeks 2004):

$$P(A) = \text{DBP}_\text{bl} \cdot e^{\gamma\left(\frac{A}{A_\text{d,bl}}-1\right)} \,, \text{ or equivalently} \tag{3.3}$$

$$A(P) = A_\text{d,bl}\left(\frac{\ln\left(\frac{P}{\text{DBP}_\text{bl}}\right)}{\gamma}+1\right) \,, \tag{3.4}$$

where DBP_bl and $A_\text{d,bl}$ indicate baseline diastolic blood pressure and cross-sectional area, respectively.

Model predictions of cPWV and A_d at follow-up For each individual patient, we predicted A_d ($A_\text{d}$pred) and A_s ($A_\text{s}$pred) at follow-up based on the baseline *P-A* curves (Eq. 3.3) and follow-up BPs (Fig. 3.1). Subsequently, predicted cPWV (cPWVpred) was obtained from Eq. 3.1, using follow-up BPs and predicted cross-sectional areas ($A_\text{d}$pred and $A_\text{s}$pred). This was done under the explicit assumption that between baseline and follow-up the *P-A* relationship had remained unaltered. Therefore, any difference between measured and predicted cPWV or A_d signifies a change in intrinsic wall properties and is not a BP effect.

Mixed-effects modelling to assess statistical significance of cPWV and A_d predictions The BP-independent effect of AADs on carotid artery stiffness was analysed by calculating the difference between predicted (cPWVpred) and measured cPWV at each follow-up visit,

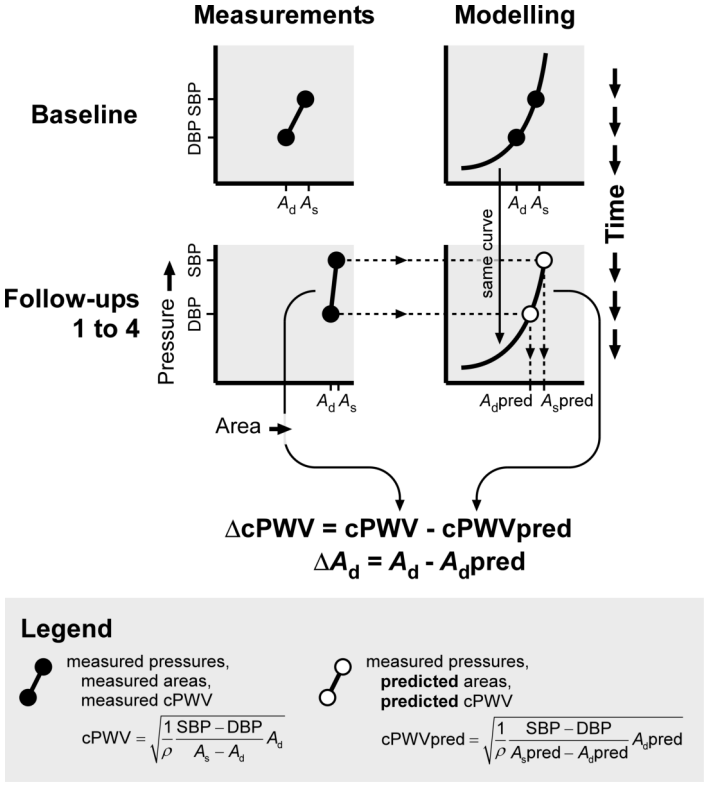

Figure 3.1: Study set-up. At baseline (top row), subjects were measured before onset of anti-angiogenic drugs (AADs). Directly after the baseline measurement, and before follow-up visits (bottom row) subjects were put on AADs. During both baseline and follow-up visits, measurements (left column) were performed which included carotid artery tonometry and ultrasound (US) wall tracking. These yielded diastolic (DBP, A_d) and systolic (SBP, A_s) pressure-area points (left column). At baseline, an exponential pressure-area curve was modelled through these points (top right) for each subject individually. At follow-up, this (unchanged) curve, together with follow-up pressures, was used to predict diastolic and systolic cross-sectional areas ($A_d$pred and $A_s$pred, bottom right). Measured carotid pulse wave velocity (cPWV) was calculated using measured *A*s, whereas predicted cPWV (cPWVpred) was calculated using predicted *A*s (legend). In both cases the Bramwell-Hill equation is used (Bramwell and Hill 1922a). The difference between measured and predicted cPWVs (ΔcPWV) was calculated by subtracting cPWVpred from cPWV. Similarly, ΔA_d was calculated by subtracting $A_d$pred from A_d. ρ refers to blood mass density; "area" refers to the artery lumen cross-sectional area.

which was termed ΔcPWV. An initial mixed-effects model with ΔcPWV as dependent variable was fitted to the data:

$$\Delta\text{cPWV} = \beta_0 + \beta_1 d_{n_{\text{visit}},1} + \beta_2 d_{n_{\text{visit}},2} + \beta_3 d_{n_{\text{visit}},3} + \beta_4 \text{AHD} \,, \tag{3.5}$$

containing:

1. An intercept (parameter β_0).
2. The visit number as a categorical variable (parameters β_1 – β_3), which was added by means of three dummy variables ($d_{n_{\text{visit}},1}$–$d_{n_{\text{visit}},3}$), for which deviation coding was used. As there are four follow-up visits, there are three dummy variables.
3. Use of anti-hypertensive drugs (parameter β_4), as a Boolean variable (AHD), which was also deviation-coded.

Baseline data points were not used in fitting the models, since these per definition only contain zeroes ($\Delta\text{cPWV} = 0$ at baseline) and lead to numerical problems in model fitting. Notably, the use of deviation coding for the categorical and Boolean variables ensures that the model's intercept term corresponds to the grand mean of the model. Therefore, in the current formulation, a (positive) significant intercept term indicates that ΔcPWV is significantly larger than 0. The latter implies that measured cPWV is significantly larger than predicted cPWV, indicating a BP-independent increase in cPWV at follow-up. Using the fixed model terms as described in Eq. 3.5, the most appropriate covariance structure was determined (Walavalkar et al. 2016; Zuur et al. 2009).

Difference between A_d prediction and measurement The BP-independent effect of AAD treatment on carotid diastolic cross-sectional area ($\Delta A_\text{d} = A_\text{d} - A_\text{d}\text{pred}$) was analysed using the same scheme as for the ΔcPWV analysis (see above).

Conventional, entirely statistical approach

Correcting for the BP dependence of cPWV Conventionally, PWV is corrected for blood pressure using a statistical model. In the present study, we replicated such an approach. We fitted the following initial mixed-effects model to the data:

$$\begin{aligned}\text{cPWV} = \beta_0 + \beta_1 \text{AAD} + \beta_2 \text{DBP} + \beta_3 \text{DBP}^2 \\ + \beta_4 d_{n_{\text{visit}},1} + \beta_5 d_{n_{\text{visit}},2} + \beta_6 d_{n_{\text{visit}},3} + \beta_7 \text{AHD} \,.\end{aligned} \tag{3.6}$$

In contrast to the mixed-effects models used in our mechanistic approach, cPWV (Eq. 3.6) is fitted to all five visits, including the baseline visit. Note that the dependent parameter is now cPWV instead of ΔcPWV as in Eq. 3.5. AAD is a Boolean variable indicating the use of anti-angiogenic drugs, and is therefore coded 0 for the baseline visit and 1 for all follow-up visits. Note that while each patient has five visits, there are only three visit dummy parameters present. This is necessary, as AAD also functions as a visit dummy variable, effectively distinguishing between baseline and follow-up visits. For the coding of AAD and $d_{n_{\text{visit}},1} - d_{n_{\text{visit}},3}$, see supplemental Table 3.A4. The most suitable covariance structure was again estimated from 8 potential candidates (Walavalkar et al. 2016).

Table 3.1: Study population characteristics

Parameter	Unit	$n = 48$
Sex	# m/f	30/18
Age	yrs	56±15
Height	m	1.72±0.11
Weight	kg	75±13
BMI	kg/m^2	25±4

Mean ± standard deviation. BMI, body mass index.

Correcting for the BP dependence of A_d Exactly the same, entirely statistical approach that was used to estimate the BP-independent effect of AADs on cPWV (see previous paragraph) was used to estimate the BP-independent effect of AADs on A_d.

3.3 Results

3.3.1 Patient population

The same patient data as in Alivon et al. (2015) were used. In the present study, only subjects with complete baseline measurements (echo-tracking, carotid tonometry, and blood pressure; see below) were included ($n = 48$). General characteristics of this group are outlined in Table 3.1. At the follow-up visits, $n = 39$ (follow-up 1), $n = 30$ (follow-up 2), $n = 31$ (follow-up 3), and $n = 23$ (follow-up 4) measurements were included.

3.3.2 Uncorrected effects of AADs on blood pressures, cPWV, and A_d

Table 3.2 shows the estimated, uncorrected effects of AADs on blood pressures, cPWV, and A_d. AADs increased cPWV and A_d by 0.75 m/s and 2.7 mm^2 on average, respectively (both $p < 0.001$). However, all BP measures also significantly increased ($p \leq 0.006$). This could potentially explain the increased cPWV and A_d that were measured, and emphasises the need for a method to correct for BP.

3.3.3 Main findings of mechanistic and conventional, statistical BP correction approaches

Using our mechanistic approach, for each subject, the difference between measured and predicted cPWV (ΔcPWV) was calculated. For the predicted cPWV values, strictly no change in wall behaviour is assumed, i.e., the *P-A* relationship remains unaltered. All differences between measured and predicted cPWVs are therefore assumed to be caused by intrinsic wall changes. Mixed-effects modelling was used to investigate the statistical significance of ΔcPWV. We found that AADs lead to a BP-independent increase in ΔcPWV of $0.43[0.09, 0.77]$ m/s ($p = 0.014$, Table 3.3). The change in cPWV was also assessed by an exclusively statistical approach, which resulted in a cPWV change of $0.48[0.14, 0.82]$ m/s ($p = 0.006$, Table 3.3).

Table 3.2: Estimated first-order effects of AADs on blood pressures, cPWV, and A_d

Parameter	Unit	Baseline		Change at follow-up		p
SBP, brachial	mmHg	123.2	[118.0,128.4]	8.3	[4.6,12.0]	< 0.001
SBP, carotid	mmHg	117.1	[111.1,123.1]	8.6	[3.7,13.4]	< 0.001
MAP	mmHg	92.7	[88.1,97.2]	5.3	[1.6,9.1]	0.006
DBP	mmHg	73.3	[70.1,76.5]	6.2	[4.0,8.5]	< 0.001
cPWV	m/s	6.82	[6.39,7.26]	0.75	[0.52,0.98]	< 0.001
A_d	mm^2	42.0	[38.9,44.9]	2.7	[1.7,3.6]	< 0.001

Mean [95% confidence interval] values of mixed-effects model (Eq. 3.4) intercept term (β_0, baseline) and AAD term (β_1, change at follow-up). Note that the changes in cPWV and A_d presented in this table have not been corrected for blood pressure effects yet. AAD, anti-angiogenic drug; SBP and DBP systolic and diastolic blood pressures, respectively; MAP, mean arterial pressure; cPWV, local carotid pulse wave velocity; A_d, diastolic carotid lumen cross-sectional area.

Table 3.3: Summary of blood pressure-independent effects of AADs on cPWV and A_d

	Mechanistic correction				Exclusively statistical correction			
	Effect of AADs (β_0)			Ref.	Effect of AADs (β_1)			Ref.
	Mean	CI	p		Mean	CI	p	
cPWV [m/s]	0.43	[0.09,0.77]	0.014	3.A1, #1	0.48	[0.14,0.82]	0.006	3.A5, #5
A_d [mm^2]	1.92	[0.93,2.92]	< 0.001	3.A2, #1	2.14	[1.06,3.23]	< 0.001	3.A6, #3

Summary of blood pressure-independent effects of AADs on cPWV and A_d, as assessed by our novel mechanistic correction approach (left part of table) and by an exclusively statistical approach (right part of table). Values are given as mean [95% confidence interval (CI)]. Ref., table references. AAD, anti-angiogenic drug; cPWV, local carotid pulse wave velocity; A_d, diastolic carotid lumen cross-sectional area.

Our mechanistic approach was also used to investigate the BP-independent effect of AADs on diastolic cross-sectional area (A_d). We found that AADs lead to an increase in ΔA_d of $1.92[0.93, 2.92]\,mm^2$ ($p < 0.001$, Table 3.3). Using the exclusively statistical approach, this change was estimated at $2.14[1.06, 3.23]\,mm^2$ ($p < 0.001$, Table 3.3).

3.3.4 Mechanistic approach: Changes in intrinsic carotid artery stiffness with the use of anti-angiogenic medication

Table 3.A1 contains the full analysis results discussed in this section. Mixed-effects modelling was used to investigate the effect of AADs on ΔcPWV, as well as the potential effects of anti-hypertensive medication and the potential difference in ΔcPWV between follow-up visits. Model 1 in Table 3.A1 (of which β_0 is reproduced in Table 3.3) represents the mixed-effects model with the simplest fixed-effects structure, i.e., only an intercept. The magnitude of the intercept term indicates that measured cPWVs are on average 0.43 m/s higher than predicted cPWVs, at $p = 0.014$. Addition of other model terms (distinguishing between follow-up visits and/or between the use of anti-hypertensive medication) did

not significantly improve the statistical model (Table 3.A1, right column: likelihood-ratio tests are all non-significant).

3.3.5 Mechanistic approach: Changes in intrinsic carotid artery diameter with the use of anti-angiogenic medication

Table 3.A2 contains the full analysis results discussed in this section. Again, for the predicted A_d values, strictly no change in wall behaviour is assumed. The same mixed-effects modelling approach as for cPWV was used. Model 1 in Table 3.A2 (of which β_0 is reproduced in Table 3.3) represents the mixed-effects model with the simplest fixed-effects structure, i.e., only an intercept. The magnitude of the intercept term indicates that measured A_ds are on average 1.9 mm^2 higher than predicted from the blood pressure increase, at $p < 0.001$. Addition of other model terms (distinguishing between follow-up visits and/or between the use of anti-hypertensive medication) again did not significantly improve the statistical model.

3.3.6 Changes in diastolic blood pressure with the use of anti-angiogenic medication

Table 3.A3 contains the full analysis results discussed in this section. As an internal check, we assessed whether DBP did indeed increase with AAD, and whether this increase differed between follow-up visits and between people that did or did not use anti-hypertensive drugs. Table 3.A3 shows mixed-effects models comparing DBP at each of the follow-up visits to baseline. Model #1 shows that at the follow-up visits, DBP was 6.0 mmHg higher than at baseline ($p < 0.001$). Addition of other model terms (distinguishing between follow-up visits and/or between the use of anti-hypertensive medication) did not significantly improve the statistical model.

3.3.7 Conventional, entirely statistical approach: Correcting for the BP dependence of cPWV

Table 3.A5 contains the full analysis results discussed in this section. In addition to our novel mechanistic methodology, we assessed the effects of anti-angiogenic drugs on cPWV by means of a statistical approach, without prediction of follow-up cPWVs. Table 3.A5 shows the results of a series of mixed-effects model fits. As expected, DBP had a significant influence on cPWV (addition of a DBP term improved the model, $p = 0.010$, model #2 vs. #1). Additional inclusion of a quadratic DBP term did not statistically significantly improve the model ($p = 0.288$, model #3 vs. #2). Nevertheless, we chose to continue statistical modelling with (models #5 and #7) and without (models #4 and #6) a quadratic DBP term. Distinguishing between visits improved the model ($p = 0.002$, model #4 vs. #2 and $p = 0.003$, model #5 vs. #3). Addition of a term accounting for the presence of anti-hypertensive medication did not improve the model, whether it was to a model without a quadratic DBP term ($p = 0.468$, models #6 vs. #4), or to a model with a quadratic DBP term ($p = 0.568$, models #7 vs. #5).

From a strictly statistical point of view (only keeping model terms that significantly improve the statistical model), model #4 (Table 3.A5) best describes our results. This

model indicates an AAD-induced increase in cPWV of 0.52 m/s. However, as there is a known nonlinear dependence of cPWV on DBP, using a model that corrects for DBP quadratically provides additional BP correction (model #5, of which β_1 is reproduced in Table 3.3). This model indicates an AAD-induced increase in cPWV of 0.48 m/s.

3.3.8 Conventional, entirely statistical approach: Correcting for the BP dependence of A_d

Table 3.A6 contains the full analysis results discussed in this section. Table 3.A6 shows the results of a series of mixed-effects model fits that assess the AAD-induced change in A_d on a statistical basis. The influence of DBP on A_d is statistically non-significant ($p = 0.105$, model #2 vs. #1). However, there is a clear, direct, mechanical relationship between pressure and lumen cross-sectional area. Addition of a quadratic term is again statistically non-significant ($p = 0.168$, model #3 vs. #2), albeit that physiologically, the relationship between A_d and pressure is known to be nonlinear (see e.g., Eq. 3.2). We have chosen to continue our statistical modelling again on "physiological grounds", keeping in both the DBP and DBP^2 terms (models #5 and #7), as well as performing parameter inclusion strictly statistically, omitting DBP terms altogether (models #4 and #6). Neither distinguishing between visits ($p = 0.553$, model #4 vs. #1 and $p = 0.673$, model #5 vs. #3) nor accounting for the presence of anti-hypertensive medication ($p = 0.584$, model #6 vs. #1 and $p = 0.584$, model #7 vs. #3) improved our models.

From a strictly statistical point of view (only keeping model terms that significantly improve it), model #1 (Table 3.A6) best describes our results. This model indicates an AAD-induced, BP-corrected increase in A_d of 2.67 mm^2. However, to obtain a physically warranted BP correction, a model should be used that corrects for the nonlinear dependence of A_d on DBP (model #3, of which β_1 is reproduced in Table 3.3). The latter model indicated an AAD-induced, BP-corrected increase in A_d of 2.14 mm^2.

3.4 Discussion

In the present study, we investigated the effect of AADs on arterial stiffness as quantified by cPWV. As cPWV is known to vary heavily with BP (Bramwell and Hill 1922a), one has to correct cPWV for this potential confounder. Recently, we published a study in which we quantified the BP effect on cPWV on a mechanistic basis, and proposed a way of correcting for this effect (Spronck et al. 2015b). We applied this mechanistic correction approach to the data in the present study, and found that AAD treatment leads to a BP-independent increase in cPWV of 0.43 m/s. With AAD treatment, arterial lumen cross-sectional area showed a BP-independent increase of 1.9 mm^2. We compared these findings obtained using our mechanistic approach to the results of the conventional approach of statistical correction. When correcting for a quadratic dependence of cPWV and A_d on DBP, we found an AAD-induced increase of 0.48 m/s in cPWV and 2.1 mm^2 in A_d. These numbers are similar to those obtained using our mechanistic approach, confirming that our mechanistic, model-driven methodology yields BP-corrected estimates of cPWV and A_d that are very similar to their statistically predicted counterparts. The advantage of our

mechanistic methodology, however, is that it provides a pressure-independent estimation of cPWV and A_d at the level of the individual, which is crucial for clinical management.

In our previous paper (Spronck et al. 2015b), we used three pressure-area points (diastolic, dicrotic notch, and systolic) to fit the curvilinear relationship between pressure and area. In the present study, dicrotic notch detection in the pressure and diameter signals was unavailable due to technical limitations, and therefore we resorted to a two-point approach. Our results show that the pressure dependence of cPWV can also be reasonably captured using a two-point approach, although we could not establish the possible quantitative consequences in the present study.

While mean arterial pressure is often used in correcting for blood pressure, from a physical point of view, it is the diastolic blood pressure that influences the velocity of the blood pressure wave (Bramwell et al. 1923; Nichols et al. 2011). In the present study, we therefore chose to base our statistical blood pressure corrections on diastolic blood pressure.

The structural changes underlying the increased stiffness and cross-sectional area of the carotid artery wall with AAD use are largely unknown. Several potential causes are discussed in our previous paper (Alivon et al. 2015), which include potential vasoactive properties of sorafenib and sunitinib (Papadopoulou et al. 2009) or their interaction with integrins, but also a potential effect of the AADs on the vasa vasorum, the microscopic arterial network that supply the artery wall with nutrients (Stefanadis et al. 1995). It is beyond the scope of the present study to structurally explain the observed changes in carotid artery stiffness and diameter.

The carotid blood pressure measurements used in this study are obtained by scaling the carotid artery applanation tonometry waveform, assuming that carotid diastolic and mean pressures are equal to brachial diastolic and mean pressures (Van Bortel et al. 2001). This scaling method has two potential disadvantages: 1) it introduces additional measurement noise, and 2) it requires additional tonometry measurements by an experienced research nurse (Spronck et al. 2016b), complicating the measurement protocol. In addition to the present analyses, we additionally re-performed our mechanistic correction technique using brachial systolic and diastolic pressures. All results were essentially the same, except for the observation that the pressure-independent increase in ΔcPWV with AAD got smaller and lost statistical significance ($\beta_0 = 0.314\,\mathrm{m/s}$, $p = 0.075$). This suggests that using brachial pressures instead of carotid yields an under-estimation of ΔcPWV.

In conclusion, the present study demonstrates the feasibility and potential of our mechanistic, model predictive approach to quantify BP-independent effects on arterial stiffness at the level of the individual, in a clinically relevant setting of AAD therapy.

3.4.1 Perspectives

Our study shows that AADs significantly increase stiffness of the carotid artery, independently of blood pressure. We show that the correction of cPWV for BP can be performed on a mechanistic basis and that this correction can therefore be applied to data of the individual, which is crucial for clinical management in daily practice.

3.5 Acknowledgements

Typesetting assistance by Elien Engels is gratefully acknowledged.

Table 3.A1: Mechanistic correction: mixed-effects models of ΔcPWV

Model #	Parameter	Regression coefficient [m/s]	p [-]	LR p [-]
1	Intercept	0.431	0.014	-
2	Intercept n_{visit}	0.422 multiple	0.016 multiple	0.157 (vs. #1)
3	Intercept AHD	0.431 −0.098	0.016 0.734	0.266 (vs. #1)
4	Intercept n_{visit} AHD	0.422 multiple −0.027	0.017 multiple 0.926	0.928 (vs. #2) 0.163 (vs. #3)

ΔcPWV, difference in local carotid pulse wave velocity between measurements and predictions; n_{visit}, follow-up number implemented as a categorical, dummy-coded variable; AHD, antihypertensive drugs, coded as a Boolean (yes/no) variable; LR, likelihood-ratio.

Table 3.A2: Mechanistic correction: mixed-effects models of ΔA_{d}

Model #	Parameter	Regression coefficient [mm^2]	p [-]	LR p [-]
1	Intercept	1.923	< 0.001	-
2	Intercept n_{visit}	2.036 multiple	< 0.001 multiple	0.445 (vs. #1)
3	Intercept AHD	1.926 0.402	< 0.001 0.612	0.620 (vs. #1)
4	Intercept n_{visit} AHD	2.035 multiple 0.082	< 0.001 multiple 0.921	0.919 (vs. #2) 0.487 (vs. #3)

ΔA_{d}, difference in diastolic carotid lumen cross-sectional area between measurements and predictions; n_{visit}, follow-up number implemented as a categorical, dummy-coded variable; AHD, antihypertensive drugs, coded as a Boolean (yes/no) variable; LR, likelihood-ratio.

Table 3.A3: Mixed-effects models of ΔDBP

Model #	Parameter	Regression coefficient [mmHg]	p [-]	LR p [-]
1	Intercept	6.007	< 0.001	-
2	Intercept	5.975	< 0.001	0.792 (vs. #1)
	n_{visit}	multiple	multiple	
3	Intercept	5.958	< 0.001	0.088 (vs. #1)
	AHD	−3.305	0.081	
4	Intercept	5.984	< 0.001	0.101 (vs. #2)
	n_{visit}	multiple	multiple	0.847 (vs. #3)
	AHD	−3.254	0.104	

ΔDBP, difference in diastolic blood pressure between follow-up measurements and baseline; n_{visit}, follow-up number implemented as a categorical, dummy-coded variable; AHD, anti-hypertensive drugs, coded as a Boolean (yes/no) variable; LR, likelihood-ratio.

Table 3.A4: Categorical variable coding used in exclusively statistical correction models with cPWV and A_{d} as dependent parameters

Visit	Intercept	AAD	n_{visit} dummy variables		
			1	2	3
Baseline	1	0	0	0	0
FU 1	1	1	1	0	0
FU 2	1	1	0	1	0
FU 3	1	1	0	0	1
FU 4	1	1	−1	−1	−1

AAD, anti-angiogenic drug; FU, follow-up.

Table 3.A5: Exclusively statistical correction: mixed-effects models of cPWV

Model #	Parameter	Regression coefficient		p [-]	LR p [-]
1	Intercept	6.822	m/s	< 0.001	-
	AAD	0.755	m/s	< 0.001	
2	Intercept	4.943	m/s	< 0.001	
	AAD	0.509	m/s	< 0.001	0.010 (vs. #1)
	DBP	0.027	m/s/mmHg	0.003	
3	Intercept	1.826	m/s	0.520	
	AAD	0.435	m/s	0.004	0.020 (vs. #1)
	DBP	0.108	m/s/mmHg	0.137	0.288 (vs. #2)
	DBP^2	−0.00051	$m/s/mmHg^2$	0.255	
4	Intercept	5.592	m/s	< 0.001	
	AAD	0.523	m/s	0.002	0.002 (vs. #2)
	DBP	0.022	m/s/mmHg	0.011	
	n_{visit}	multiple	m/s	multiple	
5	Intercept	3.088	m/s	0.275	
	AAD	0.481	m/s	0.006	0.003 (vs. #3)
	DBP	0.086	m/s/mmHg	0.226	0.392 (vs. #4)
	DBP^2	−0.00041	$m/s/mmHg^2$	0.362	
	n_{visit}	multiple	m/s	multiple	
6	Intercept	5.557	m/s	< 0.001	
	AAD	0.503	m/s	0.004	<0.001 (vs. #1)
	DBP	0.022	m/s/mmHg	0.011	0.005 (vs. #2)
	n_{visit}	multiple	m/s	multiple	0.468 (vs. #4)
	AHD	0.144	m/s	0.472	
7	Intercept	3.324	m/s	0.245	
	AAD	0.468	m/s	0.009	
	DBP	0.079	m/s/mmHg	0.273	0.568 (vs. #5)
	DBP^2	−0.00036	$m/s/mmHg^2$	0.423	0.466 (vs. #6)
	n_{visit}	multiple	m/s	multiple	
	AHD	0.114	m/s	0.578	

cPWV, carotid pulse wave velocity; AAD, anti-angiogenic drugs, coded as a Boolean (yes/no) variable; DBP, diastolic blood pressure; n_{visit}, follow-up number implemented as a categorical, dummy-coded variable; AHD, anti-hypertensive drugs, coded as a Boolean (yes/no) variable; LR, likelihood-ratio.

Table 3.A6: Exclusively statistical correction: mixed-effects models of A_d

Model #	Parameter	Regression coefficient		p [-]	LR p [-]
1	Intercept	41.91	mm^2	< 0.001	-
	AAD	2.67	mm^2	< 0.001	
2	Intercept	37.53	mm^2	< 0.001	
	AAD	2.30	mm^2	< 0.001	0.105 (vs. #1)
	DBP	0.0597	$mm^2/mmHg$	0.109	
3	Intercept	22.73	mm^2	0.046	
	AAD	2.14	mm^2	< 0.001	0.104 (vs. #1)
	DBP	0.440	$mm^2/mmHg$	0.119	0.168 (vs. #2)
	DBP^2	−0.00237	$mm^2/mmHg^2$	0.174	
4	Intercept	41.91	mm^2	< 0.001	
	AAD	2.76	mm^2	< 0.001	0.553 (vs. #1)
	n_{visit}	multiple	mm^2	multiple	
5	Intercept	25.09	mm^2	0.031	
	AAD	2.25	mm^2	0.001	0.673 (vs. #3)
	DBP	0.38	$mm^2/mmHg$	0.189	0.137 (vs. #4)
	DBP^2	−0.0020	$mm^2/mmHg^2$	0.264	
	n_{visit}	multiple	mm^2	multiple	
6	Intercept	41.74	mm^2	< 0.001	
	AAD	0.52	mm^2	0.588	0.584 (vs. #1)
	AHD	2.61	mm^2	< 0.001	
7	Intercept	23.07	mm^2	0.044	
	AAD	2.08	mm^2	< 0.001	0.584 (vs. #3)
	DBP	0.42	$mm^2/mmHg$	0.136	0.104 (vs. #6)
	DBP^2	−0.0023	$mm^2/mmHg^2$	0.198	
	AHD	0.525	mm^2	0.586	

A_d, diastolic carotid lumen cross-sectional area; AAD, anti-angiogenic drugs, coded as a Boolean (yes/no) variable; DBP, diastolic blood pressure; n_{visit}, follow-up number implemented as a categorical, dummy-coded variable; AHD, anti-hypertensive drugs, coded as a Boolean (yes/no) variable; LR, likelihood-ratio.

Chapter 4

Blood pressure dependence of stiffness index β and cardio-ankle vascular index

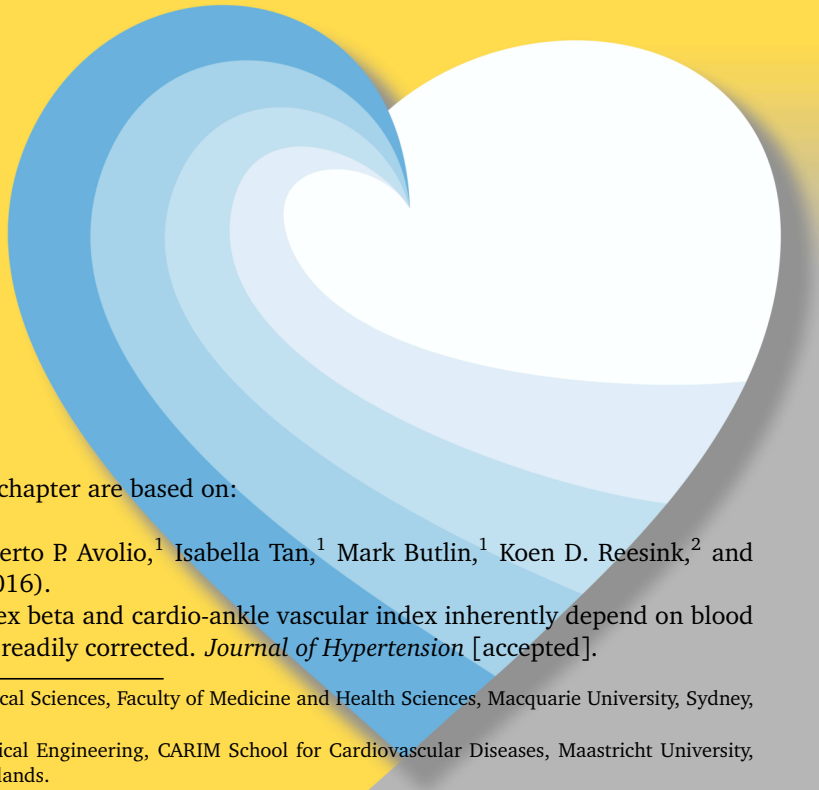

The contents of this chapter are based on:

Bart Spronck,[1,2] Alberto P. Avolio,[1] Isabella Tan,[1] Mark Butlin,[1] Koen D. Reesink,[2] and Tammo Delhaas[2] (2016).
Arterial stiffness index beta and cardio-ankle vascular index inherently depend on blood pressure, but can be readily corrected. *Journal of Hypertension* [accepted].

[1] Department of Biomedical Sciences, Faculty of Medicine and Health Sciences, Macquarie University, Sydney, NSW, Australia.
[2] Department of Biomedical Engineering, CARIM School for Cardiovascular Diseases, Maastricht University, Maastricht, The Netherlands.

Abstract

Arterial stiffness index β and cardio-ankle vascular index (CAVI) are widely accepted to quantify the intrinsic exponent (β_0) of the blood pressure (BP)-diameter relationship. CAVI and β assume an exponential relationship between pressure (P) and diameter (D). We aim 1) to demonstrate that, under this assumption, β and CAVI as currently implemented are inherently BP-dependent; and 2) to provide corrected, BP-independent forms of CAVI and β. In $P = P_{\text{ref}} e^{\beta_0\left(\frac{D}{D_{\text{ref}}}-1\right)}$, usually reference pressure (P_{ref}) and reference diameter (D_{ref}) are substituted with diastolic BP and diameter to accommodate measurements. Consequently, the resulting exponent is not equal to the pressure-independent β_0. CAVI does not only suffer from this "reference pressure" effect, but also from the linear approximation of $\frac{dP}{dD}$. For example, assuming $\beta_0 = 7$, an increase of systolic/diastolic BP from 110/70 to 170/120 mmHg increased β by 8.1% and CAVI by 14.3%. We derived corrected forms of β and of CAVI (CAVI_0) that indeed did not change with BP and represent the pressure-independent β_0. To substantiate the BP effect on CAVI in a typical follow-up study, we realistically simulated patients ($n = 161$) before and following BP-lowering "treatment" (assuming no follow-up change in intrinsic β_0 and therefore in actual P-D relationship). Lowering BP from $160 \pm 14/111 \pm 11$ to $120 \pm 15/79 \pm 11$ mmHg ($p < 0.001$) resulted in a significant CAVI decrease (8.1 ± 2.0 to 7.7 ± 2.1, $p = 0.008$); CAVI_0 clearly did not change (9.8 ± 2.4 and 9.9 ± 2.6, $p = 0.499$). β and CAVI as currently implemented are inherently BP-dependent, potentially leading to erroneous conclusions in arterial stiffness trials. BP-independent forms are presented to readily overcome this problem.

4.1 Introduction

ARTERIAL stiffness, as assessed by pulse wave velocity (PWV), is an important independent predictor for cardiovascular disease. PWV, however, is known to depend intrinsically on arterial blood pressure (BP) (Bramwell and Hill 1922a; Spronck et al. 2015b). This BP dependence has led to the search for BP-independent measures of arterial stiffness.

As shown by Hayashi et al. (1980), the relationship between arterial pressure and diameter can be described by an exponential function in the physiological range (Fig. 4.1A). Throughout the present paper, this exponential relationship between arterial pressure and diameter with pressure-independent exponent β_0, is assumed as a "ground truth" on which all other derivations are based. Of note, this paper has no intention to prove the validity of this basic assumption.

Kawasaki et al. (1987) proposed a clinically usable stiffness index β that is based on the exponential relationship as demonstrated by Hayashi et al. (1980). In the present paper, we will demonstrate that β is only an approximation of β_0, and that β is in fact pressure-dependent.

Cardio-ankle vascular index (CAVI) is being increasingly used in small and large population studies (Saiki et al. 2015), and is advocated as a pressure-independent index of

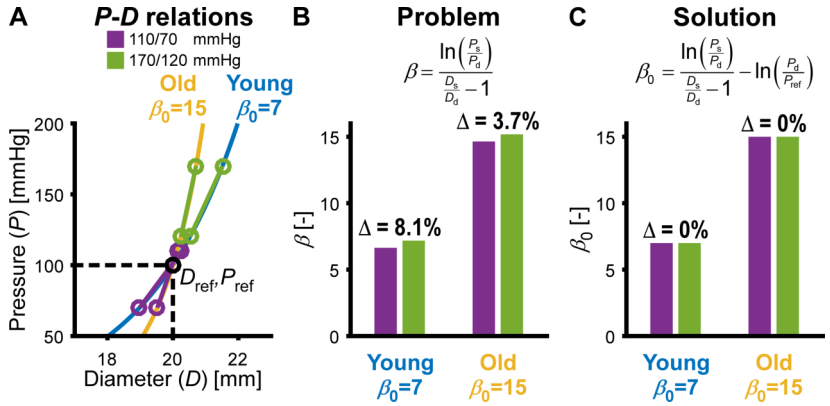

Figure 4.1: Pressure dependence of stiffness index beta (β). **A**: Intrinsic relationship between arterial pressure and diameter (Eq. 4.1). Hayashi et al. (1980) showed that in the physiological pressure range, this relationship is exponential (Hayashi et al. 1980). The exponential nature of this relationship is assumed as a "ground truth" in this paper, serving as the basis for all other derivations. Pressure ranges (systolic/diastolic blood pressure) indicated in this panel are used for calculating stiffness parameters in panels **B** and **C**. $P_{ref} = 100$ mmHg is a reference pressure (Eq. 4.1). D_{ref} is the diameter corresponding to the reference pressure. D_{ref} is kept fixed at 20 mm to illustrate solely the effect of a change in β_0 on the pressure-diameter relationship. **B**: Measured stiffness index β as computed from systolic and diastolic pressures (P_s, P_d) and diameters (D_s, D_d) on panel **A**'s curves, is blood pressure-dependent. Because the pressure dependence of β can be shown to exist mathematically (Eq. 4.4), β can be corrected using $\ln(P_d/P_{ref})$, obtaining the intrinsic, pressure-independent stiffness index beta (β_0, panel **C**). P_{ref} and D_{ref}, reference blood pressure and diameter corresponding to Eq. 4.1.

arterial stiffness (Shirai et al. 2006). CAVI is closely related to stiffness index β, and is also an approximation of the exponent of the pressure-diameter relationship. Whereas β is used for local characterisation of small artery segments, CAVI is derived as a summary measure for the heart-to-ankle arterial trajectory. CAVI is obtained by measuring PWV and converting it to an index using the Bramwell-Hill equation (Bramwell and Hill 1922a).

In the present paper, we will:

1. Show that β, as commonly calculated in biomedical literature, is not equal to the actual, intrinsic stiffness index of the pressure-diameter relationship (β_0), but instead varies with BP.
2. Show that the BP dependence of β can be corrected for, yielding a formula to obtain the true, intrinsic stiffness index β_0 from the same measurements.
3. Show that CAVI, which essentially is a form of stiffness index β, is also BP-dependent.
4. Show that a straightforward modification of the formula for calculating CAVI yields a pressure-independent version, i.e., CAVI_0.
5. Illustrate the scientific and clinical relevance of our analysis and proposed corrected β_0 and CAVI_0 formulas.

4.2 Methods

4.2.1 Behaviour of the arterial wall: *Intrinsic* stiffness index beta

Hayashi et al. (1980) showed experimentally that, in the physiological BP range, arterial pressure (P) and diameter (D) relate exponentially:

$$P = P_{\text{ref}} e^{\beta_0 \left(\frac{D}{D_{\text{ref}}} - 1\right)} . \tag{4.1}$$

Throughout this paper, this equation serves as our "ground truth". β_0 in this relationship is an intrinsic, pressure-independent measure of arterial stiffness. Note the use of P_{ref} (a "reference", or "standard" pressure) in this equation. D_{ref} is the diameter corresponding to the reference pressure. Fig. 4.1A shows two pressure-diameter relationships, obtained using Eq. 4.1 at $\beta_0 = 7$ and $\beta_0 = 15$. Each curve corresponds to one β_0 value. $P_{\text{ref}} = 100\,\text{mmHg}$ was used throughout the present study (Hayashi et al. 1980).

4.2.2 Assessment of arterial wall mechanics: *Measured* stiffness index beta

Stiffness index β as commonly reported is calculated using a slightly different equation than Eq. 4.1:

$$P_{\text{s}} = P_{\text{d}} e^{\beta \left(\frac{D_{\text{s}}}{D_{\text{d}}} - 1\right)} , \tag{4.2}$$

in which P_{s}, D_{s}, P_{d}, and D_{d} denote systolic and diastolic pressures and diameters, respectively. Note the following differences between Eq. 4.1 and 4.2: a) reference pressure and diameter have been changed to diastolic pressure and diameter; b) instantaneous, variable pressure has been changed to systolic pressure; and c) intrinsic stiffness index β_0 has been changed to measured stiffness β. Eq. 4.2 can be rearranged to obtain the commonly-used expression for β:

$$\beta = \frac{\ln\left(\frac{P_{\text{s}}}{P_{\text{d}}}\right)}{\frac{D_{\text{s}}}{D_{\text{d}}} - 1} . \tag{4.3}$$

If this equation is used to quantify β in an exponentially-distending wall (Eq. 4.1) with a given $\beta_0 = 7$ and $P_{\text{ref}} = 100\,\text{mmHg}$, calculated βs will be dependent on the pressure ranges (Fig. 4.1B). This can be understood as follows.

4.2.3 Pressure dependence of measured stiffness index β

Suppose that two pressure-diameter points are measured on the intrinsic pressure-diameter relationship (Eq. 4.1): a systolic (P_{s},D_{s}) and a diastolic (P_{d},D_{d}) point. From Eq. 4.3 and rearranging the result (see Appendix 4.A1), we obtain

$$\beta = \beta_0 + \ln\left(\frac{P_{\text{d}}}{P_{\text{ref}}}\right) . \tag{4.4}$$

This equation shows that β, the measured stiffness index, differs from the intrinsic stiffness index β_0, by an amount of $\ln\left(\frac{P_d}{P_{ref}}\right)$. This also implies that we can readily obtain the intrinsic, pressure-independent stiffness index β_0 by rearranging Eq. 4.4:

$$\beta_0 = \beta - \ln\left(\frac{P_d}{P_{ref}}\right) . \tag{4.5}$$

Note that if P_d is equal to P_{ref}, $\ln\left(\frac{P_d}{P_{ref}}\right) = 0$ and β_0 equals β. However, in general, this is not the case. Substituting the initial expression for β (Eq. 4.3) into Eq. 4.5 yields

$$\beta_0 = \frac{\ln\left(\frac{P_s}{P_d}\right)}{\frac{D_s}{D_d} - 1} - \ln\left(\frac{P_d}{P_{ref}}\right) , \tag{4.6}$$

which is a formulation that can be used to obtain the intrinsic, pressure-independent stiffness index β_0 from measured systolic and diastolic pressures and diameters.

4.2.4 The value of P_{ref}

The previous sections demonstrate that the pressure (either P_d or P_{ref}) that is used to multiply the exponential function influences the value of β or β_0 that is obtained. It is important to realise that a value of β_0 corresponds to a P_{ref} value. Therefore, one should choose one, fixed P_{ref} value for all subjects in a study, in order to be able to compare the β_0 values among these subjects. The numerical value of P_{ref} that is chosen is a matter of standardisation or consensus. P_{ref} does not represent a physiological pressure. Different values of P_{ref} (and the corresponding D_{ref}) lead to different values of β_0. However, the *P-D* curves that are described using these different combinations of $P_{ref}/D_{ref}/\beta_0$ perfectly and analytically overlap. Therefore, P_{ref} values should be taken equal between studies (irrespective of the patient cohort studied), if β_0-values are to be compared between those studies. Arbitrarily, in the present study, we have chosen $P_{ref} = 100\,\text{mmHg}$.

4.2.5 Cardio-ankle vascular index (CAVI)

Stiffness index β, (Eq. 4.3), which is a function of pressures (P_d and P_s) and diameters (D_d and D_s), can also be expressed as a function of pressures and PWV. This is accomplished by combining Eq. 4.3 with a simplified version of the Bramwell-Hill equation (Eq. 4.A10) (Bramwell and Hill 1922a). When PWV in this equation is determined from the heart-to-ankle arterial bed, the resulting quantity (in fact a β index) is termed cardio-vascular index (CAVI):

$$\text{CAVI} = \ln\left(\frac{P_s}{P_d}\right) \cdot \frac{\text{PWV}^2 \cdot 2\rho}{P_s - P_d} . \tag{4.7}$$

PWV from the heart to the ankle is obtained using a combination of phonocardiography, electrocardiography, and brachial and ankle cuff measurements (Shirai et al. 2006).

For the same reasons outlined in the previous section (the use of diastolic BP instead of a reference BP), CAVI is pressure-dependent. However, CAVI also depends on BP for another reason, as explained below.

The derivation of CAVI (Shirai et al. 2006) is based on a simplified version of the Bramwell-Hill equation (Fig. 4.2B), in which the derivative of pressure to diameter ($\frac{dP}{dD}$) is replaced by a linear approximation over the diastolic-to-systolic pressure range. This approximation introduces an error in the obtained CAVI value. The magnitude of this error can be quantified using the true PWV, i.e., the PWV based on the true $\frac{dP}{dD}$ in the diastolic point (Eq. 4.A11). Using this PWV to calculate CAVI by means of Eq. 4.7 yields:

$$\mathrm{CAVI} = \left(\beta_0 + \ln\left(\frac{P_\mathrm{d}}{P_\mathrm{ref}}\right)\right) \cdot \ln\left(\frac{P_\mathrm{s}}{P_\mathrm{d}}\right) \cdot \frac{P_\mathrm{d}}{P_\mathrm{s} - P_\mathrm{d}} \,. \tag{4.8}$$

The extra terms beside β_0 in the right hand side of this equation indicate the pressure dependence of CAVI (Fig. 4.2C).

4.2.6 Finding a pressure-independent CAVI

A pressure-independent CAVI formula should provide an index equivalent to the intrinsic stiffness index β_0. Such an index can be derived by squaring and rearranging the relationship between true PWV (obtained from the exact, analytic derivative of the *P-D* relationship) and β_0 (Eq. 4.A13):

$$\mathrm{CAVI}_0 = \beta_0 = \frac{\mathrm{PWV}^2 \cdot 2\rho}{P_\mathrm{d}} - \ln\left(\frac{P_\mathrm{d}}{P_\mathrm{ref}}\right) \,. \tag{4.9}$$

This equation can be used to obtain the pressure-independent CAVI_0 from PWV, ρ, and P_d (Fig. 4.2D).

4.2.7 Simulation

Residual BP dependence of stiffness index β and CAVI

In order to quantify the BP dependence of stiffness index β, we calculated β (Eq. 4.4) at two clearly distinct BP ranges (normotensive 110/70 mmHg systolic/diastolic BP (SBP/DBP) and hypertensive 170/120 mmHg). We did so for two values of intrinsic stiffness: $\beta_0 = 7$ and $\beta_0 = 15$, corresponding to a normal young subject and an older subject with a stiffened artery, respectively. The reference diameter (D_ref) was kept constant at 20 mm. The quantitative effect of BP on CAVI was determined for the same BP ranges and β_0 values (Eq. 4.8).

BP dependence of CAVI in a simulated population study

In order to gain insight into the magnitude of the BP dependence of CAVI and how this could affect a typical study's results, we computer-simulated a BP-lowering treatment in a population with an average intrinsic stiffness of $\beta_0 = 10$. For a detailed description of the protocol for data generation and randomisation, we refer the reader to Appendix 4.A2.

In short, we simulated a baseline and a follow-up measurement between which BP decreased on average from about 160/110 (SBP/DBP) to about 120/80 mmHg. Importantly, we assumed wall behaviour to remain unchanged. That is, with the BP change

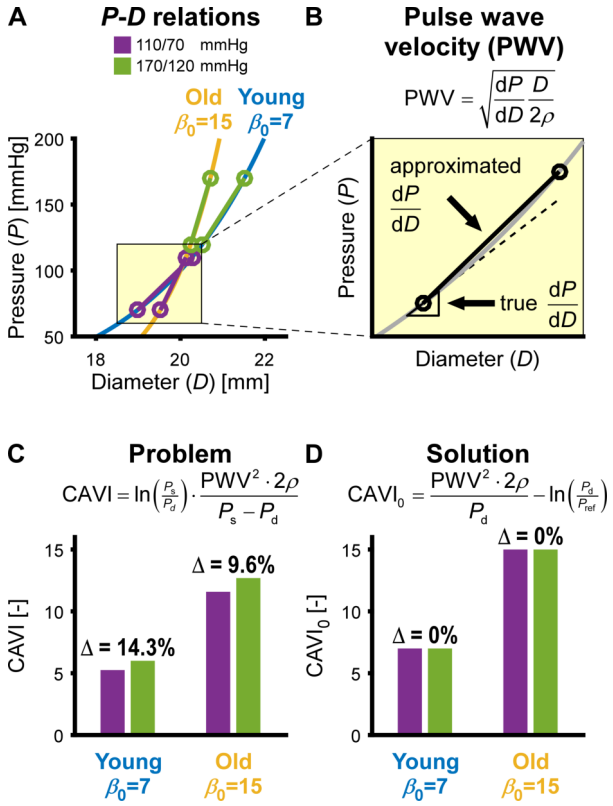

Figure 4.2: Pressure dependence of cardio-ankle vascular index (CAVI). **A**: Intrinsic P-D relations (Eq. 4.1) and pressure ranges (systolic/diastolic blood pressure) used for calculating CAVI in panels **C** and **D**. $P_{\text{ref}} = 100\,\text{mmHg}$ and $D_{\text{ref}} = 20\,\text{mm}$. **B**: As CAVI is essentially a form of stiffness index beta, the pressure dependence as shown in Fig. 4.1 also holds for CAVI. In CAVI, however, there is a second source of pressure dependence, which arises as follows. In the normal CAVI formula, an approximation of the Bramwell-Hill equation is used, effectively substituting $\frac{dP}{dD}$ with $\frac{\Delta P}{\Delta D}$. Therefore, if CAVI is determined using measured PWV and the standard equation (Eq. 4.7) (Shirai et al. 2006), CAVI shows a blood pressure dependence (panel **C**). **D**: As CAVI assumes an exponential pressure-diameter relationship (Eq. 4.1), one can analytically determine the true $\frac{dP}{dD}$. By using this analytic expression, one can find a pressure-independent formulation of CAVI ($CAVI_0$). Note the presence of the $\ln\left(\frac{P_d}{P_{\text{ref}}}\right)$ term, which is also present in the corrected form of stiffness index beta (Eq. 4.6 and Fig. 4.1C).

for each subject, the exponential *P-D* relationship (Eq. 4.1) and, hence, β_0 remained unchanged. DBP, SBP, and PWV values before and following "treatment" were drawn from normal distributions, simulating biological variation. Subsequently, measurements were simulated by adding normally-distributed measurement noise. CAVI and CAVI_0 were calculated from these simulated measurements.

Using the simulated population data, we calculated the sample size at which, for a power of 80% and $\alpha = 0.05$, the BP lowering would lead to a statistically significant change in CAVI. Subsequently, we simulated a study in the number of subjects obtained from the sample size calculation to illustrate a typical study's results.

4.3 Results

4.3.1 Residual BP dependence of stiffness index β and CAVI

Fig. 4.1B shows the quantitative effect of BP on stiffness index β. With increasing BP from 110/70 mmHg to 170/120 mmHg (SBP/DBP), β increased by 8.1% (from 6.6 to 7.2) in a young individual's artery with $\beta_0 = 7$. In an older individual's artery with $\beta_0 = 15$, β increased by 3.7% (from 14.6 to 15.2).

Pressure dependence of β was markedly smaller than that of PWV. PWV changed to a much larger extent with BP; from 5.4 to 7.4 m/s in the young artery (36% change) and from 8.1 to 10.8 m/s in the older artery (33% change). Stiffness index β as determined using the corrected equation (Eq. 4.6, yielding β_0) was independent of pressure (Fig. 4.1C).

Fig. 4.2C shows the quantitative effect of BP on CAVI. With increasing BP from 110/70 mmHg to 170/120 mmHg (SBP/DBP), CAVI increased from 5.3 to 6.0 (14.3% increase) in a young individual and from 11.6 to 12.7 (9.6% change) in an older individual. Furthermore, using the standard CAVI formula leads to much lower values for β than the actual, intrinsic β_0s of 7 and 15.

CAVI as determined using the corrected equation (Eq. 4.9, yielding CAVI_0) was independent of pressure (Fig. 4.2D).

Fig. 4.3 shows how stiffness index β (A) and CAVI (B) depend on diastolic and systolic BPs. Comparing Fig. 4.3A and 4.3B, one sees that 1) β only depends on DBP, whereas CAVI depends on DBP and SBP; and that 2) the BP dependence of CAVI is much larger than that of β (viz., compare the different colour scales of panes A and B). The larger BP dependence of CAVI is caused by the use of an approximated derivative in the CAVI formula (Fig. 4.2B), in addition to the "reference pressure" effect that affects both β and CAVI.

4.3.2 Simulated impact of the BP dependence of CAVI in a population study

For our simulated population, we determined that a sample size of 161 subjects would give an 80% chance of finding a statistically significant difference in CAVI due to BP lowering. Table 4.1 shows the results of a simulated set of measurements in 161 subjects. Values throughout are expressed as mean±standard deviation.

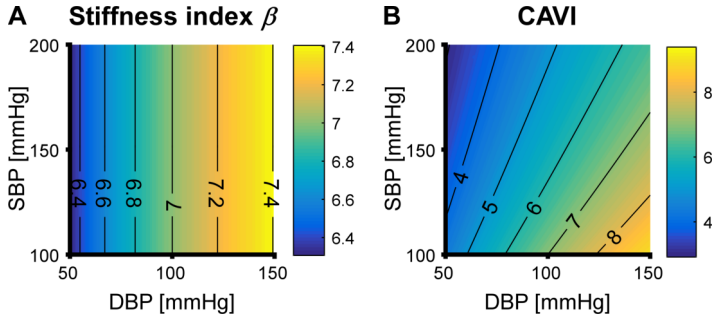

Figure 4.3: Dependence of stiffness index β and CAVI on diastolic and systolic blood pressures (DBP and SBP). **A**: β depends on DBP due to the "reference point" effect (cf. the difference between Eq. 4.1 and Eq. 4.2). **B**: The "reference point" effect also influences CAVI, causing a dependence of CAVI on DBP. CAVI is additionally blood pressure-dependent due to the use of an approximated derivative in the Bramwell-Hill equation (Fig. 4.2B), also introducing a dependence on SBP. Plots were generated for $P_{\text{ref}} = 100\,\text{mmHg}$ and $\beta_0 = 7$ (see text).

Table 4.1: Uncorrected cardio-ankle vascular index (CAVI) leads to misinterpretation

Parameter	Unit	Baseline	Follow-up	p^*
SBP	mmHg	161±14	120±15	< 0.001
DBP	mmHg	111±11	79±11	< 0.001
PWV	m/s	8.2±1.1	6.9±1.0	< 0.001
CAVI	-	8.1±2.0	7.7±2.1	0.008
CAVI_0	-	9.8±2.4	9.9±2.6	0.499

Pressure dependence of CAVI in a simulated data set ($n = 161$). Values denote mean ± standard deviation. SBP, systolic blood pressure; DBP, diastolic blood pressure; PWV, pulse wave velocity; CAVI, standard, pressure-dependent cardio-ankle vascular index (Eq. 4.7); CAVI_0, corrected, pressure-independent cardio-ankle vascular index (Eq. 4.9); $^*p$-value of two-sided paired t-test comparing baseline to follow-up values. Intrinsic stiffness index β_0 was 9.8 ± 1.9, and was equal at baseline and follow-up.

For the lowering of systolic BP from 160 ± 14 mmHg to 120 ± 15 mmHg ($p < 0.001$) and diastolic BP from 110 ± 11 mmHg to 79 ± 11 mmHg ($p < 0.001$), PWV significantly decreased from 8.2 ± 1.1 to 6.9 ± 1.0 m/s ($p < 0.001$). CAVI as calculated from the standard equation (Eq. 4.7) significantly decreased from 8.1 ± 2.0 to 7.7 ± 2.1 ($p = 0.008$) with lowering BP, as expected for the sample size.

The corrected CAVI as proposed and calculated from Eq. 4.9 (CAVI_0) showed no change with BP ($p = 0.499$).

4.4 Discussion

CAVI and β assume an exponential relationship between pressure and diameter. In this study, we have demonstrated that, under this assumption and contrary to the often made claim (Shirai et al. 2006), stiffness index β and CAVI are BP-dependent. This confirms findings by Lim et al. (2015), who showed a BP dependence of CAVI in an experimental setting. However, the BP dependence of other artery stiffness parameters, such as PWV (Spronck et al. 2015b), is greater than that of β and CAVI.

Using CAVI under the assumption of it being fully BP-independent may confound conclusions, especially in large population studies investigating relatively small changes in CAVI. For example, several studies have reported that arterial stiffness, as measured with CAVI, decreases with BP-lowering medication (Saiki et al. 2015; Shirai et al. 2011). However, our simulations show that even in a study with relatively few participants ($n = 161$) where intrinsic wall parameters (β_0) were explicitly kept constant, the BP effect on CAVI may emerge as statistically significant.

In our simulation study, the BP effect on PWV (1.3 m/s) is much larger than the within-subject standard deviation of 0.5 m/s (Salvi et al. 2008). The BP-induced change of CAVI of 0.4 in our simulation study is of the same order as the CAVI within-subject standard deviation of 0.5 (Kubozono et al. 2007). This comparison 1) underlines the much smaller BP dependence of CAVI when compared to PWV, and 2) emphasises that CAVI as usually implemented may lead to erroneous conclusions.

As mentioned in the Introduction, Kawasaki et al. (1987) previously derived β from β_0 (Hirai et al. 1989; Kawasaki et al. 1987). In their derivation, they correctly mentioned that clinically, it is difficult to measure diameter at a standard pressure of e.g., 100 mmHg. After this notice, they simplified Eq. 4.1 to Eq. 4.2, thereby neglecting the underlying BP dependence emerging from substituting diastolic BP and diastolic diameter for P_{ref} and D_{ref} in Eq. 4.1.

Note that CAVI as reported by the VaSera device by Fukuda Denshi, Co. LTD (CAVI_{VS}) is a scaled version of CAVI as used in this paper: $\text{CAVI}_{\text{VS}} = a \cdot \text{CAVI} + b$ (Shirai et al. 2006). The constants a and b are considered proprietary information by the company and therefore are not publicly available. However, as a and b constants, the BP dependence of CAVI is equally applicable to CAVI_{VS}.

The present study relies on the assumption that the *in vivo* arterial wall pressure-diameter relationship is exponential. The underlying arterial wall mechanics of the exponential behaviour are complex. At lower pressures, mainly elastin bears the load, whereas at higher pressures, this load bearing is gradually shifted to collagen (O'Rourke and Hashimoto 2007; Spronck et al. 2015a). This shift leads to the typical form of the full

P-D relationship, which, starting from $P = 0$ first shows an increase in compliance, then has a maximum, and subsequently decreases with increasing pressure (Langewouters et al. 1984). The maximum compliance, corresponding to an inflection point in the *P-D* relationship, occurs at a pressure of around 45 mmHg in individuals aged 30 years. With increasing age, the pressure at which the maximum compliance occurs decreases and becomes 0 mmHg at the age of 80 (Langewouters et al. 1980). If this full *P-D* relationship with an inflection point is to be described, a single-exponential *P-D* relationship is clearly insufficient; an arctangent-type model may be more suitable in this case (Langewouters et al. 1984). Because young subjects have an inflection point at relatively high pressures of ≈ 45 mmHg, the assumption of a single-exponential relationship may not hold when they are hypotensive. In this case, their low diastolic BPs may be close to their inflection point. However, in all other subjects, physiological BPs are normally well above the inflection point. Therefore, a single-exponential relationship provides an appropriate approximation of the true *P-D* relationship. The exponential shape of the *P-D* relationship as shown in vitro by Hayashi et al. (1980) was confirmed *in vivo* in humans by Stefanadis et al. (1997). They reported that "the pressure-diameter data fitted excellently to the monoexponential function $P = b \times e^{a \cdot D}$, ($r = .97$ to $.99$, $p < .001$), ..." in the human aorta, both in normotensive and hypertensive subjects. Later studies by these investigators again confirmed this finding (Stefanadis et al. 1998; Toutouzas et al. 2000). The choice of an exponential *P-D* relationship has a pragmatic reason. Models that are more complicated than the single-exponential model cannot be uniquely parameterised using a set of two pressures (systolic and diastolic) and two diameters or a PWV. This limits their use to very specific research studies in which the full pressure-diameter relationship is measured, or in which more than two *P-D* points are measured (e.g., by adding an additional dicrotic notch point, Hermeling et al. 2010). In our opinion, this limitation, together with the *in vivo* validations by Stefanadis et al. (1997), makes a strong case for using an exponential model to characterise *in vivo* arterial *P-D* relationships.

4.4.1 Conclusions

CAVI and stiffness index β rely on the assumption of an exponential relationship between pressure and diameter. In this paper we have shown that, under this assumption, stiffness index β and CAVI as commonly implemented, depend on BP. This dependence can potentially lead to erroneous conclusions in studies that use β and CAVI to estimate changes in stiffness of the artery wall. We have presented corrected stiffness indices, β_0 and CAVI_0, that readily overcome this problem.

4.4.2 Perspectives

The findings presented in this manuscript have direct implications for all studies that incorporate β and/or CAVI measurements. We have shown that due care should be taken in interpreting β and CAVI as strictly pressure-independent measures of arterial stiffness. In a moderately-sized study, a BP decrease from a hypertensive to a normotensive range may lead to a significant decrease in CAVI as calculated from the standard equation, merely due to the change in BP. CAVI_0 as derived in the present study, does not exhibit this pressure dependence. Our new formulations (β_0 and CAVI_0) allow even retrospective data

analysis for improved interpretation of arterial stiffness trials. Recently, we have shown that the degree of BP dependence of PWV is clinically relevant (Spronck et al. 2015b), and that the BP dependence is apparent from the PWV reference values (The Reference Values for Arterial Stiffness' Collaboration 2010). Based on the reference values for PWV, and considering the approach proposed in the present paper, pressure-independent reference values for β_0/CAVI_0 could be obtained.

4.5 Acknowledgements

This study was supported by a Kootstra Talent Fellowship awarded to B. Spronck by Maastricht University. Typesetting assistance by Elien Engels is gratefully acknowledged.

4.A1 Appendix: Detailed methods

4.A1.1 Derivation of Eq. 4.4

Eq. 4.1 of the main article can be re-arranged to

$$D = D_{\mathrm{ref}}\left(1+\frac{\ln\left(\frac{P}{P_{\mathrm{ref}}}\right)}{\beta_0}\right). \tag{4.A1}$$

Using this equation, we find an expression for systolic (D_s) and diastolic diameter (D_d):

$$D_\mathrm{s} = D_{\mathrm{ref}}\left(1+\frac{\ln\left(\frac{P_\mathrm{s}}{P_{\mathrm{ref}}}\right)}{\beta_0}\right) \text{ and } D_\mathrm{d} = D_{\mathrm{ref}}\left(1+\frac{\ln\left(\frac{P_\mathrm{d}}{P_{\mathrm{ref}}}\right)}{\beta_0}\right); \tag{4.A2}$$

and fill these in into Eq. 4.3 of the main article:

$$\beta = \frac{\ln\left(\frac{P_\mathrm{s}}{P_\mathrm{d}}\right)}{\frac{D_{\mathrm{ref}}\left(1+\frac{\ln\left(\frac{P_\mathrm{s}}{P_{\mathrm{ref}}}\right)}{\beta_0}\right)}{D_{\mathrm{ref}}\left(1+\frac{\ln\left(\frac{P_\mathrm{d}}{P_{\mathrm{ref}}}\right)}{\beta_0}\right)}-1}. \tag{4.A3}$$

Simplification of the denominator leads to

$$\beta = \frac{\ln\left(\frac{P_\mathrm{s}}{P_\mathrm{d}}\right)}{\frac{1+\frac{\ln\left(\frac{P_\mathrm{s}}{P_{\mathrm{ref}}}\right)}{\beta_0}}{1+\frac{\ln\left(\frac{P_\mathrm{d}}{P_{\mathrm{ref}}}\right)}{\beta_0}}-1} = \frac{\ln\left(\frac{P_\mathrm{s}}{P_\mathrm{d}}\right)}{\frac{\beta_0+\ln\left(\frac{P_\mathrm{s}}{P_{\mathrm{ref}}}\right)}{\beta_0+\ln\left(\frac{P_\mathrm{d}}{P_{\mathrm{ref}}}\right)}-1} = \frac{\ln\left(\frac{P_\mathrm{s}}{P_\mathrm{d}}\right)}{\frac{\beta_0+\ln\left(\frac{P_\mathrm{s}}{P_{\mathrm{ref}}}\right)}{\beta_0+\ln\left(\frac{P_\mathrm{d}}{P_{\mathrm{ref}}}\right)}-1}, \tag{4.A4}$$

and further to

$$\begin{aligned}\beta &= \frac{\ln\left(\frac{P_\mathrm{s}}{P_\mathrm{d}}\right)}{\frac{\beta_0+\ln\left(\frac{P_\mathrm{s}}{P_\mathrm{ref}}\right)}{\beta_0+\ln\left(\frac{P_\mathrm{d}}{P_\mathrm{ref}}\right)} - \frac{\beta_0+\ln\left(\frac{P_\mathrm{d}}{P_\mathrm{ref}}\right)}{\beta_0+\ln\left(\frac{P_\mathrm{d}}{P_\mathrm{ref}}\right)}} = \frac{\ln\left(\frac{P_\mathrm{s}}{P_\mathrm{d}}\right)}{\frac{\ln\left(\frac{P_\mathrm{s}}{P_\mathrm{ref}}\right)-\ln\left(\frac{P_\mathrm{d}}{P_\mathrm{ref}}\right)}{\ln\left(\frac{P_\mathrm{d}}{P_\mathrm{ref}}\right)+\beta_0}} \\ &= \frac{\left(\ln\left(\frac{P_\mathrm{d}}{P_\mathrm{ref}}\right)+\beta_0\right)\ln\left(\frac{P_\mathrm{s}}{P_\mathrm{d}}\right)}{\ln\left(\frac{P_\mathrm{s}}{P_\mathrm{ref}}\right)-\ln\left(\frac{P_\mathrm{d}}{P_\mathrm{ref}}\right)} .\end{aligned} \tag{4.A5}$$

Using the identity $\ln\frac{a}{b} = \ln a - \ln b$ to further simplify the denominator, we obtain

$$\beta = \frac{\left(\ln\left(\frac{P_\mathrm{d}}{P_\mathrm{ref}}\right)+\beta_0\right)\ln\left(\frac{P_\mathrm{s}}{P_\mathrm{d}}\right)}{\ln(P_\mathrm{s})-\ln(P_\mathrm{ref})-\ln(P_\mathrm{d})+\ln(P_\mathrm{ref})} = \frac{\left(\ln\left(\frac{P_\mathrm{d}}{P_\mathrm{ref}}\right)+\beta_0\right)\ln\left(\frac{P_\mathrm{s}}{P_\mathrm{d}}\right)}{\ln\left(\frac{P_\mathrm{s}}{P_\mathrm{d}}\right)} , \tag{4.A6}$$

and finally

$$\beta = \ln\left(\frac{P_\mathrm{d}}{P_\mathrm{ref}}\right)+\beta_0 . \tag{4.A7}$$

4.A1.2 Bramwell-Hill relationship

Bramwell and Hill (1922a) derived the relationship between local pressure (P) and cross-sectional area (A) and PWV:

$$\mathrm{PWV} = \sqrt{\frac{\mathrm{d}P}{\mathrm{d}A}\frac{A}{\rho}} , \tag{4.A8}$$

in which $\rho = 1050\,\mathrm{kg}\cdot\mathrm{m}^{-3}$ is the blood mass density. This equation can be re-written in terms of diameter (D):

$$\mathrm{PWV} = \sqrt{\frac{\mathrm{d}P}{\mathrm{d}D}\frac{D}{2\rho}} . \tag{4.A9}$$

For use in the conventional CAVI formula, this equation is approximated by (Shirai et al. 2006):

$$\mathrm{PWV} \approx \sqrt{\frac{P_\mathrm{s}-P_\mathrm{d}}{D_\mathrm{s}-D_\mathrm{d}}\frac{D_\mathrm{d}}{2\rho}} . \tag{4.A10}$$

4.A1.3 Derivation of the true pulse wave velocity at points on an exponential pressure-diameter curve (Eq. 4.1) and obtaining a pressure-independent formula for CAVI

The Bramwell-Hill equation contains a derivative of pressure to area ($\frac{\mathrm{d}P}{\mathrm{d}A}$, Eq. 4.A8) or to diameter ($\frac{\mathrm{d}P}{\mathrm{d}D}$, Eq. 4.A9). This derivative can be readily obtained by differentiating Eq. 4.1 with respect to D:

$$\frac{\mathrm{d}P}{\mathrm{d}D} = \frac{\beta_0}{D_\mathrm{ref}}P_\mathrm{ref}e^{\beta_0\left(\frac{D}{D_\mathrm{ref}}-1\right)} = \frac{\beta_0}{D_\mathrm{ref}}P . \tag{4.A11}$$

Combining this equation with Eq. 4.A9 for $P = P_d$ yields (Bramwell et al. 1923)

$$\mathrm{PWV} = \sqrt{P_d \frac{D_d}{D_{ref}} \frac{\beta_0}{2\rho}} \,. \tag{4.A12}$$

Filling in D_d from Eq. 4.A2 yields

$$\mathrm{PWV} = \sqrt{\frac{P_d}{2\rho}\left(\ln\left(\frac{P_d}{P_{ref}}\right) + \beta_0\right)} \,. \tag{4.A13}$$

Squaring this equation and rearranging yields Eq. 4.9 of the main article.

4.A2 Appendix: Generation of example dataset

In order to gain insight into the magnitude of the BP dependence of CAVI, we computer-generated measurement data. In the simulated subjects, an anti-hypertensive treatment-induced BP lowering was simulated, while assuming that the artery wall structure and function remained unaltered. I.e., subjects remained on their exponential *P*-*D* relationship (Eq. 4.1), and β_0 did not change. Measurement data were generated by (i) drawing numbers from normal distributions (assuming biological spread but no measurement noise) and (ii) subsequently adding measurement noise.

4.A2.1 Method for generation of measurement data

In this section $N(\mu, \sigma)$ denotes independent samples drawn from a normal distribution with mean μ and standard deviation σ. Subscripts bl and fu indicate baseline and follow-up, respectively. Subscript nf indicates "noise-free" values, i.e., these do not contain measurement noise. The following data were generated:

- An intrinsic stiffness index (β_0) for each subject was drawn from $N(10, 2)$.
- Baseline diastolic BPs ($P_{d,bl,nf}$) were drawn from $N(110\,\mathrm{mmHg}, 10\,\mathrm{mmHg})$. Baseline pulse pressures ($P_{p,bl,nf}$) were drawn from $N(50\,\mathrm{mmHg}, 10\,\mathrm{mmHg})$. Systolic pressure ($P_{s,bl,nf}$) was calculated as the sum of diastolic and pulse pressures. Baseline PWV ($\mathrm{PWV}_{bl,nf}$) was subsequently calculated from $P_{d,bl,nf}$, and β_0 by means of Eq. 4.A13. Note that PWV is calculated (or "measured") using the equation that is based on the true, non-approximated $\frac{dP}{dD}$.
- Follow-up diastolic BPs ($P_{d,fu,nf}$) were drawn from $N(80\,\mathrm{mmHg}, 10\,\mathrm{mmHg})$. Follow-up pulse pressures ($P_{p,fu,nf}$) were drawn from $N(40\,\mathrm{mmHg}, 10\,\mathrm{mmHg})$. Systolic pressure ($P_{s,fu,nf}$) was calculated as the sum of diastolic and pulse pressures. Follow-up PWV ($\mathrm{PWV}_{fu,nf}$) was again calculated using Eq. 4.A13.

Normally-distributed, additive, random measurement noise was added to DBP, SBP, and PWV at both baseline and follow-up. Noise on DBP and SBP measurements was assumed to be zero-mean and independent. Using data from a previous study (Spronck et al. 2015b), we calculated intra-subject SD of DBP as the square root of the mean of all individual variances (Bland and Altman 1996), resulting in an intra-subject SD of 5.0 mmHg.

If measurement noise is assumed to be the sole source of the repeatability variation, one can generate BP noise by drawing independent samples from $N(0, 5.0\,\mathrm{mmHg})$.

Repeatability of PWV measurements was assessed by Salvi et al. (2008). For their reference method, the SphygmoCor (AtCor, Sydney, NSW, Australia) device, they report a repeatability of 1.44 m/s. Salvi et al. (2008) defined repeatability as two times the standard deviation of the difference between two measurements. This led to a standard deviation in one measurement of $\frac{1.44}{2\sqrt{2}}$ m/s. Therefore, we generated PWV measurement noise by drawing samples from $N(0, \frac{1.44}{2\sqrt{2}}\,\mathrm{m/s})$.

Measured CAVI and CAVI_0 were calculated using Eq. 4.7 and 4.9, respectively, filling in SBP, DBP, and PWV including measurement noise.

4.A2.2 Simulation protocol

First, we generated measurement data as described above for a large number of subjects ($n = 10^6$). This yields robust estimates of the mean and standard deviation of CAVI in this simulated population, before and after simulated BP lowering. Using these values, we performed a sample size calculation, determining the number of subjects that, at a probability (power) of 0.8, would lead to a statistically significant difference ($\alpha = 0.05$) in CAVI between baseline and follow-up.

Second, we generated measurement data in the number of subjects that resulted from the sample size calculation. Results from this simulation are reported.

Chapter 5

Heart rate dependence of arterial stiffness

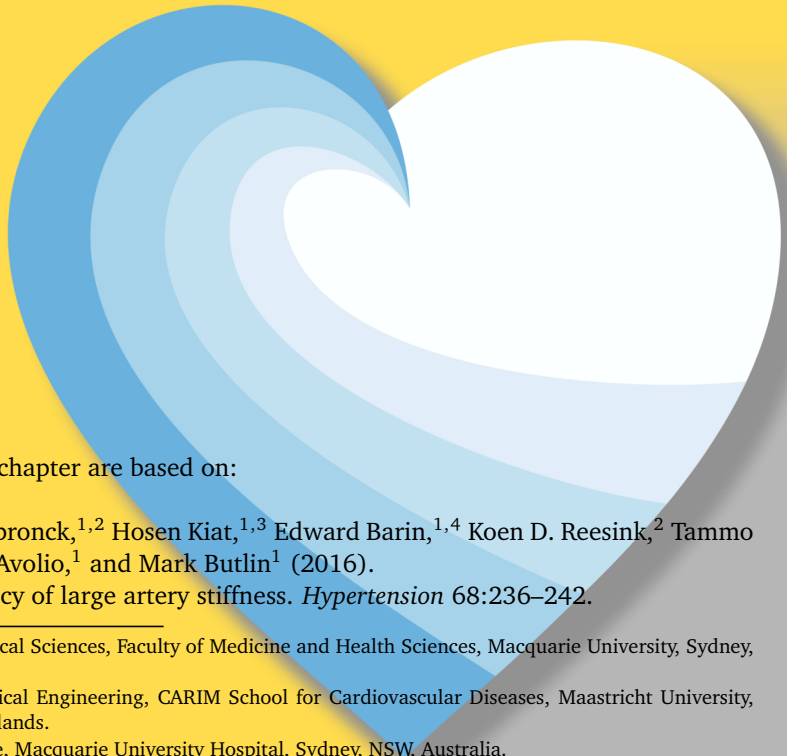

The contents of this chapter are based on:

Isabella Tan,[1] Bart Spronck,[1,2] Hosen Kiat,[1,3] Edward Barin,[1,4] Koen D. Reesink,[2] Tammo Delhaas,[2] Alberto P. Avolio,[1] and Mark Butlin[1] (2016).
Heart rate dependency of large artery stiffness. *Hypertension* 68:236–242.

[1] Department of Biomedical Sciences, Faculty of Medicine and Health Sciences, Macquarie University, Sydney, NSW, Australia.
[2] Department of Biomedical Engineering, CARIM School for Cardiovascular Diseases, Maastricht University, Maastricht, The Netherlands.
[3] Cardiac Health Institute, Macquarie University Hospital, Sydney, NSW, Australia.
[4] Macquarie Heart, Macquarie University Hospital, Sydney, NSW, Australia.

Abstract

Carotid-femoral pulse wave velocity (cfPWV) quantifies large artery stiffness, is used in haemodynamic research and is considered a useful cardiovascular clinical marker. cfPWV is blood pressure (BP)-dependent. Intrinsic heart rate (HR) dependence of cfPWV is unknown as increasing HR is commonly accompanied by increasing BP. This study aims to quantify cfPWV dependence on acute, sympathovagal-independent changes in HR, independent of BP. Individuals ($n = 52$, age 40–93 yrs, 11 female) with *in situ* cardiac pacemakers or cardioverter defibrillators were paced at 60, 70, 80, 90, and 100 bpm. BP and cfPWV were measured at each HR. Both cfPWV ($0.31[0.26, 0.37]$ m/s/(10 bpm), $p < 0.001$ mean[95%CI]) and central aortic diastolic pressure ($3.78[3.40, 4.17]$ mmHg/(10 bpm), $p < 0.001$) increased with HR. The HR effect on cfPWV was isolated by correcting for BP effects by three different methods: 1) statistically, by a linear mixed model; 2) mathematically, using an exponential relationship between BP and cross-sectional lumen area; and 3) using measured BP dependence of cfPWV derived from changes in BP induced by position changes (seated and supine) in a subset of subjects ($n = 17$). BP-independent effects of HR on cfPWV were quantified as $0.20[0.11, 0.28]$ m/s/(10 bpm) ($p < 0.001$, method 1), $0.16[0.11, 0.22]$ m/s/(10 bpm) ($p < 0.001$, method 2), and $0.16[0.11, 0.21]$ m/s/(10 bpm) ($p < 0.001$, method 3). With a mean HR dependence in the range of 0.16 to 0.20 m/s/(10 bpm), cfPWV may be considered to have minimal physiologically relevant changes for small changes in HR, but larger differences in HR must be considered as contributing to significant differences in cfPWV.

5.1 Introduction

CAROTID-FEMORAL pulse wave velocity (cfPWV), a surrogate measure for aortic stiffness, is an independent marker for all-cause and cardiovascular mortality (Laurent et al. 2001; Laurent et al. 2003). It is widely used in haemodynamic research and is increasingly being recognised as an important parameter in the clinical assessment of patients at risk for cardiovascular disease (Mancia et al. 2007). However, the uptake of cfPWV as part of the clinical routine has been slow despite the large amount of evidence supporting its relevance as a cardiovascular clinical marker (Brunner-La Rocca 2010), as well as being recommended as a clinical tool in current guidelines (Mancia et al. 2007). A potential reason for this is the lack of standardisation of cfPWV methodology and reference values (Brunner-La Rocca 2010). Although this has recently been addressed by the investigators of the Arterial Stiffness' Collaboration, whereby normative and reference values were determined for age, mean arterial pressure (MAP) and cardiovascular risk factors (The Reference Values for Arterial Stiffness' Collaboration 2010), other less well-established potential confounders of cfPWV were not considered. One such factor is heart rate (HR).

Despite studies that have investigated effects of HR on arterial stiffness in the past, the

relationship between the two has remained controversial. Although a few acute, pacing studies specifically investigating the association between HR and cfPWV found an independent HR effect on cfPWV (Haesler et al. 2004; Lantelme et al. 2002), others found no significant change in cfPWV with HR (Albaladejo et al. 2001) or were unable to discriminate the measured increase in cfPWV from the concomitant pacing-induced increase in blood pressure (BP) (Liang et al. 1999; Millasseau et al. 2005). In cross-sectional studies, only half of those that included HR as a parameter for predicting cfPWV in their model found a significant association (Cecelja and Chowienczyk 2009). As cfPWV is known to be pressure-dependent (Avolio et al. 1983; Bramwell and Hill 1922a; Pruett et al. 1988; Spronck et al. 2015b), any change in cfPWV accompanied by a change in BP needs to be corrected for BP in order to isolate the true effect of the factor being investigated. The present study aims to quantify the acute, BP-independent effect of HR on cfPWV.

5.2 Methods

Patients with implanted pacemakers or implantable cardioverter defibrillators (ICDs) with pacing function were recruited from the Cardiac Health Institute and Macquarie Heart clinics. Exclusion criteria included unstable angina, prior myocardial infarction within the last twelve months of the study, and uncontrolled congestive heart failure. A total of 52 subjects (age 40–93 yrs, 11 female) entered the study, and all were included in the analysis. The study protocol was approved by Macquarie University's Human Ethics Committee and written consent to participate in the study was obtained from all subjects.

5.2.1 Haemodynamic measurements

Brachial BP, central aortic BP, and cfPWV were determined by cuff-based pulse wave analysis (SphygmoCor XCEL, AtCor, Sydney, NSW, Australia). Brachial BP was obtained by oscillometric method with a brachial cuff positioned on the right arm, and central aortic waveform was derived from the brachial BP volume displacement waveform using a validated transfer function (Butlin et al. 2012). For measurement of cfPWV, the carotid and femoral pulse waveforms were obtained by tonometry on the skin above the right carotid artery and by a cuff placed on the right upper thigh, respectively (Butlin et al. 2013; Hwang et al. 2014). Subtraction method for path length was used to calculate cfPWV, whereby the path length was calculated as the distance between the sternal notch and the carotid site subtracted from the distance between the sternal notch and top of the thigh cuff (Butlin et al. 2013).

In a subset of the study's cohort ($n = 45$), beat-to-beat stroke volume (SV), cardiac output (CO), and total peripheral resistance (TPR) were determined from the finger arterial pressure waveform using the Modelflow method (Finometer PRO, Finapres Medical Systems, Amsterdam, Netherlands; Wesseling et al. 1993).

5.2.2 Study protocol

Subjects were advised to refrain from caffeine and fatty meals 4 hours prior to their study appointment, but to continue with their prescribed medications. There were no current

tobacco users in the cohort. After 10 minutes of seated rest, seated brachial BP was measured in duplicate (SphygmoCor XCEL). After a further 10 minutes of supine rest, finger arterial pressure waveform was measured from the left middle finger (Finometer PRO) to obtain SV, CO, and TPR. Brachial and central aortic BP and cfPWV were then obtained (SphygmoCor XCEL). Subjects were then paced in a randomised sequence at 60, 70, 80, 90, and 100 bpm using their prescribed pacemaker settings, with BP and cfPWV measurements repeated at each pacing step after 3 minutes of stabilisation. ECG was also acquired continuously for the duration of the study for monitoring of HR (PowerLab acquisition system, LabChart software, ADInstruments, Dunedin, New Zealand), and SV, CO, and TPR from the Finometer PRO device were also recorded via PowerLab and LabChart. The average duration for study protocol completion was 60 minutes.

5.2.3 Data analysis

For pulse wave analysis, brachial and central aortic BP waveforms were averaged over 5 seconds, and cfPWV was averaged over 10 seconds. Observations with measured HR differing from the paced rate by more than 5 bpm were excluded from the analysis, and the lowest pace rates of 60 and 70 bpm were not achievable in some subjects due to a higher unpaced resting heart rate. A linear mixed model with maximum likelihood was used to determine the effects of HR on each measured variable, with paced HR modelled as the fixed effect and the random effect modelled as the intercept for each individual:

$$Y_{ij} = \beta_0 + \beta_1 \cdot \mathrm{HR} + \epsilon_{ij} + u_j \,, \tag{5.1}$$

where Y_{ij} denotes the outcome measure at a particular paced HR for one individual, ϵ_{ij} denotes the residual of variances and u_j is the random effect due to individual subject variances, i.e., variance of the random intercepts. The correlation between repeated measures from the same subject is accounted for via the random effect. Linear mixed modelling was chosen because, as opposed to analysis of variance (ANOVA), it accounts for unbalanced data (Cnaan et al. 1997), which in the present study resulted from the lowest paced rates of 60 bpm and 70 bpm being unachievable in some individuals. Descriptive statistics are presented as mean±standard deviation (SD) unless otherwise stated. A p-value of less than 0.05 was considered as statistically significant. Data analysis was performed using the software R (R Core Team 2014) and mixed modelling was performed using R's NLME package (Pinheiro et al. 2014).

5.2.4 Blood pressure correction

In order to isolate HR effects on cfPWV from any influence of BP, three methods were used to correct for BP.

Method 1: Blood pressure correction through statistical methods

Central aortic diastolic BP (cDBP), as well as the interaction term between cDBP and HR, were added as fixed effects to the mixed model in Eq. 5.1:

$$\mathrm{cfPWV}_{ij} = \beta_0 + \beta_1 \cdot \mathrm{HR} + \beta_2 \cdot \mathrm{cDBP} + \beta_3 \cdot \mathrm{HR} \cdot \mathrm{cDBP} + \epsilon_{ij} + u_j \,. \tag{5.2}$$

In the case of a significant interaction term (β_3) between HR and cDBP, the HR dependence of cfPWV would be dependent on cDBP, such that at any given fixed cDBP level:

$$\text{cfPWV} = \beta_0 + (\beta_1 + \beta_3 \cdot \text{cDBP}) \cdot \text{HR} + \beta_2 \cdot \text{cDBP} \ . \tag{5.3}$$

Thus, the HR dependence of cfPWV is denoted by $(\beta_1 + \beta_3 \cdot \text{cDBP})$ at any given fixed cDBP level. For this present study, the reported HR dependence of cfPWV was calculated for the sample average of cDBP.

Method 2: Blood pressure correction through mathematical modelling

Based on the principle that in the physiological range, pressure (P) and arterial lumen cross-sectional area (A) relate exponentially (Meinders and Hoeks 2004), the *P-A* relationship is formulated as

$$P = P_{\text{ref}} e^{\alpha\left(\frac{A}{A_{\text{ref}}}-1\right)} \ . \tag{5.4}$$

PWV is also related to pressure and cross-sectional area changes, as defined by the Bramwell-Hill equation (Bramwell and Hill 1922b). By combining Eq. 5.4 and the Bramwell-Hill equation (Eq. 5.A2 in Appendix 5.A1), an expression for exponent α can be derived as a function of systolic and diastolic BP and PWV (Eq. 5.A4 in Appendix 5.A1), and denotes the BP dependence of PWV.

By using cfPWV and BP values at the lowest paced HR for each subject, α can be calculated. Subsequently, these α values can be used to calculate the predicted PWV values in each subject given the change in systolic and diastolic BP, compared to the reference level, at each higher paced rate (Eq. 5.A3 in Appendix 5.A1). Thus, for each subject at each HR, the difference (ΔcfPWV) between measured cfPWV ($\text{cfPWV}_{\text{meas}}$) and predicted cfPWV ($\text{cfPWV}_{\text{pred}}$) was calculated as:

$$\Delta\text{cfPWV} = \text{cfPWV}_{\text{meas}} - \text{cfPWV}_{\text{pred}} \ . \tag{5.5}$$

The following mixed statistical model was then fitted to the data:

$$\Delta\text{cfPWV}_{ij} = \beta_0 + \beta_1 \cdot \text{HR} + \epsilon_{ij} + u_j \ , \tag{5.6}$$

where β_1 is the estimate of the BP-independent HR effect on cfPWV.

Method 3: Empirical blood pressure correction from experimental data

As PWV varies with BP, individual variations in PWV with BP changes can be determined experimentally by varying a subject's BP through different body positions and measuring PWV at each position (Butlin et al. 2015). A subset of this study's cohort ($n = 17$) had their BP and cfPWV measured in both the seated and supine positions. In the seated position, a hydrostatic pressure gradient is present along the aorta and carotid artery due to gravity (Fig. 5.1A). In the supine position, this gradient is absent (Fig. 5.1B). In the seated position, hydrostatic pressure varies with height relative to the position of the aortic arch (Eq. 5.A6 in Appendix 5.A1), thus cfPWV also varies. On the contrary, cfPWV remains constant along the aortic trunk in the supine position. Assuming a linear relationship between PWV and BP, the measured differences in cfPWV between the seated and supine

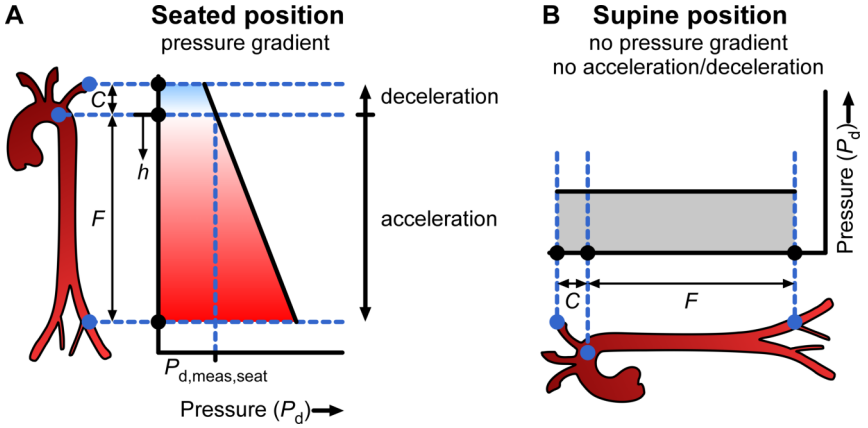

Figure 5.1: Empirical BP correction method using experimental data. In the seated position (**A**), a pressure gradient is present along the arteries due to gravity, causing PWV to vary with position h along the arterial tree, with pressure change being negative above the aortic arch and positive below. On the other hand, in the supine position (**B**), no such pressure gradient is present. Assuming PWV to be scaled linearly with diastolic pressure (P_d): $\text{PWV} = a \cdot P_d + b$, one can integrate incremental transit times (dt) along the arteries and calculate the transit time between the carotid and femoral sites as a function of parameters a and b in both seated (Eq. 5.A15 in Appendix 5.A1) and supine positions (Eq. 5.A17 in Appendix 5.A1). By solving both equations, a, the pressure dependence of PWV, can be calculated and used to correct for BP in measured cfPWV in the main study.

positions were used to calculate the BP dependence of cfPWV for each individual (see Appendix 5.A1). The averaged BP dependence across the 17 subjects was then used to calculate the BP-corrected cfPWV (cfPWVc, Eq. 5.A18 in Appendix 5.A1), and the effect of HR on cfPWVc was determined (Eq. 5.A19 in Appendix 5.A1).

5.3 Results

Clinical characteristics of the study cohort are outlined in Table 5.1. Baseline haemodynamic measurements, which did not differ with pacing modality (data not shown), are shown in Table 5.2. cfPWV increased significantly with HR, but brachial and central aortic BP parameters, except for central aortic systolic BP, also increased significantly (Table 5.3). SV and TPR decreased significantly and CO increased with increasing HR (Table 5.3).

5.3.1 Results from blood pressure correction for cfPWV

After correction for BP, the effect of HR on cfPWV remained significant regardless of the correction method used. The average BP-independent HR dependence of cfPWV across the three methods was 0.17 m/s/(10 bpm).

Table 5.1: Clinical characteristics of study cohort

	n
Implant indications	
SSS	10
Bradycardia	17
Irregular heart rate	4
Heart block	11
Syncope	2
Atrial fibrillation	11
Ventricular tachycardia	1
Cardiomyopathy	4
Other	7
Pacemaker mode	
AAI/DDD	6
DDD	34
VVI	11
VVD	1
Medications	
α blocker	3
β blocker	24
Calcium antagonists	11
Nitrates	5
ACE-inhibitors	14
AngII-blockers	16
Diuretics	13
Antiarrhythmics	16
Anticoagulants	24
Antiplatelets	10
Statins	31
Aspirin	10

SSS, sick sinus syndrome; AAI, atrial pacing and sensing; DDD, dual chamber (atrium and ventricle) pacing and sensing; VVI, ventricular sensing and pacing; VVD, ventricular pacing and atrial tracking; ACE, angiotensin-converting enzyme; AngII, angiotensin II.

Table 5.2: Baseline haemodynamic measurements of study cohort

Parameter	Unit	Mean±SD
HR	bpm	64±7
cfPWV	m/s	9.5±1.6
Brachial SBP	mmHg	126±15
Brachial DBP	mmHg	72±9
Central aortic SBP	mmHg	115±13
Central aortic DBP	mmHg	72±8
MAP	mmHg	88±9

cfPWV, carotid-femoral pulse wave velocity; SBP and DBP, systolic and diastolic blood pressure, respectively; MAP, mean arterial pressure; SD, standard deviation.

Table 5.3: Estimated effect of HR on all measured variables

Dependent variable	Unit	Estimated values for effect of HR per 10 bpm increase		p
		Mean	[95% CI]	
cfPWV	m/s	0.31	[0.26,0.37]	< 0.001
bSBP	mmHg	1.03	[0.56,1.50]	< 0.001
bDBP	mmHg	3.55	[3.18,3.92]	< 0.001
cSBP	mmHg	0.33	[−0.09,0.75]	0.120
cDBP	mmHg	3.78	[3.40,4.17]	< 0.001
MAP	mmHg	3.71	[3.33,4.08]	< 0.001
SV	mL	−6.10	[−6.85,−5.36]	< 0.001
CO	L/min	0.21	[0.16,0.26]	< 0.001
TPR	$\mathrm{dyn \cdot s \cdot cm^{-5}}$	−30.33	[−51.00,−9.65]	0.005

HR, heart rate; cfPWV, carotid-femoral pulse wave velocity; bSBP and bDBP, brachial systolic and diastolic blood pressure, respectively; cSBP and cDBP, carotid systolic and diastolic blood pressure, respectively; MAP, mean arterial pressure; SV, stroke volume; CO, cardiac output; TPR, total peripheral resistance; CI, confidence interval.

Table 5.4: Model parameters for model used for BP correction in method 1

Model parameter	Unit	β		p
		Mean	[95% CI]	
Intercept (β_0)	m/s	0.73	[−2.79,4.25]	0.685
HR (β_1)	m/s/bpm	0.09	[0.05,0.13]	< 0.001
cDBP (β_2)	m/s/mmHg	0.10	[0.05,0.15]	< 0.001
HR·cDBP (β_3)	m/s/(mmHg·bpm)	−0.0009	[−0.0013,−0.0004]	< 0.001

Mixed model was defined as $\mathrm{cfPWV}_{ij} = \beta_0 + \beta_1 \cdot \mathrm{HR} + \beta_2 \cdot \mathrm{cDBP} + \beta_3 \cdot \mathrm{HR} \cdot \mathrm{cDBP} + \epsilon_{ij} + u_j$. HR, heart rate; cfPWV, carotid-femoral pulse wave velocity; BP, blood pressure; cDBP, carotid diastolic BP, CI, confidence interval.

Blood pressure correction using statistical methods

The parameters of the statistical model are shown in Table 5.4. Adding cDBP ($\chi^2(2) = 108.66$, $p = 0.008$) and the interaction between HR and cDBP ($\chi^2(2) = 10.71$, $p = 0.001$) significantly improved the model as compared to a model with HR as the sole predictor. Due to the significant negative interaction between HR and cDBP, the HR dependence of cfPWV decreased with increasing BP (Fig. 5.2A). At the mean cDBP of this cohort (80 ± 12 mmHg), the HR dependence of cfPWV was calculated as $0.20[0.11, 0.28]$ m/s/(10 bpm) ($p < 0.001$).

Blood pressure correction using mathematical modelling

Fig. 5.2B shows the predicted and actual measured cfPWV values using mathematical modelling for each paced HR. The resulting BP-independent HR dependence of cfPWV was $0.16[0.11, 0.22]$ m/s/(10 bpm) ($p < 0.001$).

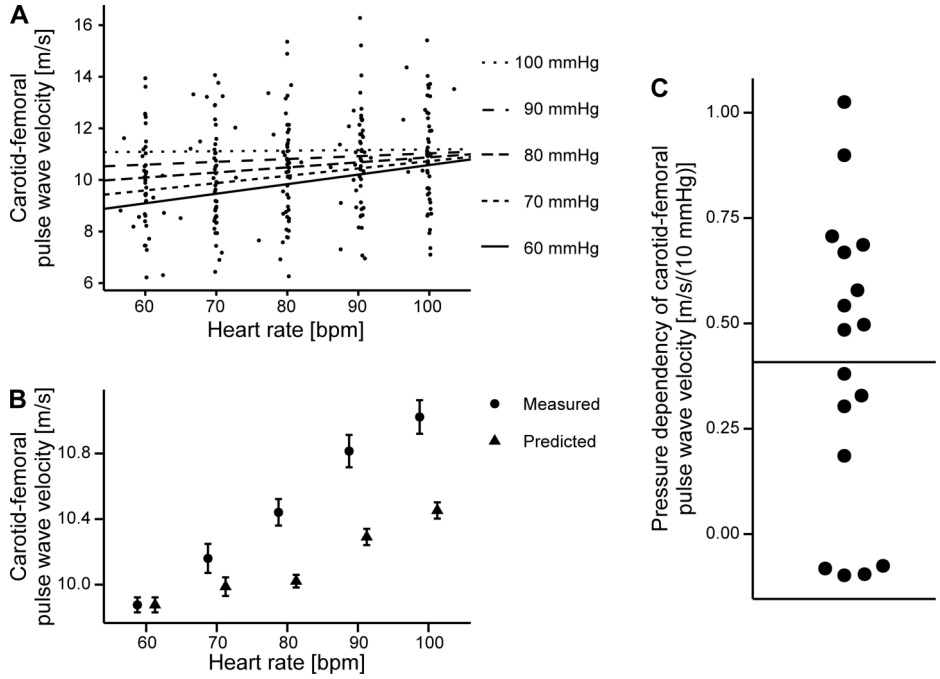

Figure 5.2: **A**: cfPWV increased with HR, but there was a significant negative interaction between HR and BP, as shown by the decreasing slope of PWV with HR at different central diastolic BP (cDBP) levels. **B**: Measured cfPWV at each paced HR level and predicted cfPWV using BP correction method with mathematical modelling. **C**: BP dependence of cfPWV calculated from experimental data in a subset of this study's cohort ($n = 17$). Horizontal line indicates mean.

Empirical blood pressure correction using experimental data

From the seated-supine experimental data (Fig. 5.2C), the average BP dependence of cfPWV was $0.04[0.02, 0.06]$ m/s/mmHg ($p < 0.001$, one-sample two-sided t-test). The resulting BP-independent HR dependence of cfPWV was $0.16[0.11, 0.21]$ m/s/(10 bpm) ($p < 0.001$).

5.4 Discussion

To the best of our knowledge, this is the first study to quantify the intrinsic effect of HR on cfPWV independent of observed BP changes with acute changes in HR.

Evidence from previous studies investigating the effects of HR on arterial stiffness in the past has been inconclusive. In acute studies, where HR was manipulated pharmacologically (Liang et al. 1999; Rhee et al. 2004) or through pacing (Albaladejo et al. 2001; Haesler et al. 2004; Lantelme et al. 2002; Millasseau et al. 2005), most observed an increase in measured cfPWV with increasing HR (Haesler et al. 2004; Lantelme et al. 2002; Liang et al. 1999; Millasseau et al. 2005). However, whilst some studies did show an

increase in arterial stiffness in the absence of significant BP changes (Haesler et al. 2004; Lantelme et al. 2002), other studies observed a concurrent increase in BP with increasing HR (Liang et al. 1999; Millasseau et al. 2005), making it difficult to determine whether HR contributed to the increase in cfPWV in addition to the BP contribution.

In the current study, cardiac pacing was used to induce HR changes as pacing allowed HR to be controlled directly and independently without introducing systemic changes to modify HR. However, the increase in HR led to a decrease in SV, resulting from reduced diastolic filling time (Noble et al. 1966; Weissler et al. 1961) and ejection duration (Weissler et al. 1961). Despite the decrease in SV and TPR, CO increased due to the large increases in HR, which likely drove the increase in MAP in addition to the increase in both peripheral and central diastolic BP. As cfPWV is highly influenced by BP (Avolio et al. 1983; Bramwell and Hill 1922b; Pruett et al. 1988; Spronck et al. 2015b), much of the increase in cfPWV observed in the present study can be attributed to the increase in pressure. In order to determine whether HR further influenced cfPWV changes, we employed three different methods to correct for BP; similar correction procedures were not conducted in previous studies.

The first correction method we used was a straightforward statistical method, with the effect of BP accounted for by including cDBP and the interaction between cDBP and HR in the mixed model. Diastolic BP was chosen as cfPWV was measured at the diastolic point of the cardiac cycle. As expected, the additional predictors significantly improved the model, indicating a significant effect of BP on cfPWV. The effect of HR remained significant, but the significant negative interaction between HR and cDBP indicated that the influence of HR on cfPWV decreased as BP increased. This is contrary to our previous study in the rat aorta, whereby, when compared at the same MAP, aortic PWV increased more with HR at higher mean pressures (Tan et al. 2012). The difference in observations may be due to the difference in arterial wall structure in humans and rats, with the rat aorta being more muscular than human aorta (Wolinsky and Glagov 1967), hence in rats, even at higher pressures where collagen fibres take the load bearing, the smooth muscle may have contributed further to the increase in stiffness with HR (Cox 1975). At the averaged cDBP level of this study's cohort, HR effect on cfPWV remained significant.

The second correction method employed mathematical modelling to predict the changes in PWV given a known change in pressure. The dependence of PWV on pressure was derived by assuming an exponential relationship between artery cross-sectional area and BP (Meinders and Hoeks 2004). Using this relationship, we predicted the BP-induced change in cfPWV with respect to the measured cfPWV at the lowest paced HR. As with the statistical correction method, we found that there remained a HR effect on cfPWV even after correction for BP.

The third correction method, similar to the correction of BP by mathematical modelling, individualised each subject's BP dependence of cfPWV by measuring cfPWV at different positions (Butlin et al. 2015). However, as only a subset of the cohort underwent the additional experimental protocol, the averaged BP dependence from the individuals was applied to the whole cohort to obtain a BP-independent HR effect on cfPWV. The resulting HR dependence of cfPWV obtained via this method was of the same order as both the statistical and mathematical modelling method.

From the study establishing normal and reference values for PWV in a large European cohort of over 11,000 subjects (The Reference Values for Arterial Stiffness' Collabora-

tion 2010), a regression model found that for individuals aged 70 yrs or above, there was a mean BP dependence of PWV of 0.0676 m/s/mmHg, which was similar to the BP dependence we obtained when fitting a mixed model predicting cfPWV using MAP only (0.0613 m/s/mmHg, $p < 0.001$). The BP change observed in the present study was 3.71 mmHg/(10 bpm), which, if using the reference BP dependence, would equate to an approximate increase in cfPWV of 0.25 m/s/(10 bpm). As the total increase in cfPWV with HR was 0.31 m/s/(10 bpm) in the present study (Table 5.3), the expected HR contribution to cfPWV would be $0.31 - 0.25 = 0.06$ m/s/(10 bpm). However, from the three different BP correction methods, the average BP-independent HR dependence of cfPWV obtained was much higher at 0.17 m/s/(10 bpm). This difference may be due to the fact that reference values were established from a cross-sectional study, as opposed to the present study where the acute effects of HR on cfPWV were investigated. Interestingly, although the reference values study did not include HR in the final regression model, it was stated that PWV was in fact significantly dependent on HR, albeit with much smaller influence compared to MAP and age (The Reference Values for Arterial Stiffness' Collaboration 2010).

It has previously been shown that an increase in HR of 10 bpm is equivalent to an increase in systolic BP of 10 mmHg in terms of associated cardiovascular risk (Perret-Guillaume et al. 2009). In the present study, cfPWV increased on average 0.17 m/s/(10 bpm) increase in HR, independent of BP changes. This was equivalent to a 1.8% increase in cfPWV, slightly lower than but of the same order as the 2.5% in cfPWV observed by Lantelme et al. (2002) for the same increase in HR, where the investigators reported no change in BP with HR. Another study found an increase in cfPWV of almost 6% with 10 bpm increase in HR in the absence of significant BP changes (Haesler et al. 2004). The moderate increase in cfPWV observed in the present study is equivalent to a 6% increase in the risk of all-cause mortality in end-stage renal disease patients per 10 bpm increase in HR, as it has been shown that 1 m/s increase in PWV translates to a 39% increase in risk in this population (Blacher et al. 1999). Thus, although the influence of HR on large artery stiffness may be small, it cannot be ignored when a large change in HR is present.

The mechanism behind the influence of HR on arterial stiffness is still largely unknown. Investigators have often attributed the change in arterial stiffness with HR to the viscoelasticity of the arterial wall (Lantelme et al. 2002; Wilkinson et al. 2002). Previous studies in both animals and humans have shown a frequency dependence of elastic modulus (Antonov et al. 2008; Bergel 1961; Imura et al. 1990). Other investigators explained the effect by the reduced time for the artery to recoil at increased HRs, thus resulting in a stiffer artery (Armentano et al. 1995; Mangoni et al. 1996). This is consistent with the presence of viscoelasticity. However, no studies to date have been able to conclusively determine whether viscoelasticity per se is indeed the mechanism involved.

Another potential mechanism for the change in arterial stiffness may be a change in smooth muscle tone in the large arteries, induced by a change in sympathetic activity. Although cardiac pacing, as performed in the present study, does not directly influence the sympathetic nervous system, indirect effects due to the changed haemodynamics, such as baroreceptor activation due to the increased BP, cannot be excluded. However, baroreceptor activation in response to increased BP would cause a decrease in sympathetic activity, potentially decreasing smooth muscle recruitment and reducing arterial

wall stiffness. Finally, the HR dependence of cfPWV could be a measurement artefact, caused by a change in pulse waveform due to the increased HR at either the carotid or femoral site, influencing the detected location of the diastolic foot. However, a previous study by Millasseau et al. (2005) demonstrated a significant HR effect on cfPWV regardless of whether the pulse propagation time was referenced to the diastolic foot or to the point of maximum systolic upstroke. In the present study, a post hoc analysis of a subset of 10 subjects comparing cfPWV calculated with two different algorithms for determining pulse transit time, one referencing the foot of the wave (Asmar et al. 1995) and the other referencing the point of maximum slope of the systolic upstroke (Chiu et al. 1991), also showed that the effect of HR on cfPWV was independent of the timing algorithm used (see Appendix 5.A2). It is beyond the current study's scope to provide additional explanatory evidence of how HR affects arterial stiffness, but our results further support previous observations whereby HR was shown to have a significant effect on measured large artery stiffness.

The current study has potential limitations. The study cohort consisted of subjects with *in situ* cardiac pacemakers who were heterogeneous in their cardiac function and indication for pacemaker implantation. Over half of the cohort were on antihypertensives, but treatment was not homogenous across the cohort. As cardiac dysfunction and hypertensive treatment have been shown to influence PWV (Asmar et al. 2001; Giannattasio et al. 1995), and as the cohort consisted of mainly elderly male subjects, results from the current study cannot be extrapolated to the general population nor beyond the HR range studied. In addition, responses to acute changes in HR by means of cardiac pacing may not be reflective of long term HR changes caused by pathological tachycardia, which involve numerous factors including neural and hormonal influences. In addition, the BP correction methods involved several assumptions. For the statistical BP correction, it was assumed that for the BP changes observed in this study, cfPWV changed linearly with BP, HR, and their interaction. This assumption also holds for the empirical correction method. It has been shown in studies where MAP was changed pharmacologically, that cfPWV and BP exhibited a curvilinear relationship (Kelly et al. 2001; Perkins et al. 2006; Stewart et al. 2003). However, as other empirical data have shown the two to be linearly associated (Avolio et al. 1983; The Reference Values for Arterial Stiffness' Collaboration 2010), it is not unreasonable to assume a linear relationship between cfPWV and BP in the present study. Our BP correction method using mathematical modelling incorporates the non-linear relationship between BP and cfPWV, and is based on an assumed exponential *P-A* relationship (Meinders and Hoeks 2004). However, the exact exponential nature of this relationship can be debated, as other descriptives (Langewouters et al. 1984) as well as *P-A* relationships based on the actual wall constituents (Holzapfel et al. 2000; Roccabianca et al. 2014; Spronck et al. 2015a) have also been proposed. Nevertheless, the exponential relationship provides an acceptable compromise between accuracy and practical utility.

In conclusion, although the effect of acute changes in HR on large arterial stiffness may not be of the same order as that of BP, it cannot be dismissed. In particular, in addition to correction for BP, cfPWV should be corrected for large changes in HR.

5.4.1 Perspectives

Our study quantified the intrinsic effect of HR on large artery stiffness independent of BP effects whereby there was a concurrent change in BP with HR. The HR effect, though moderate at 0.17 m/s/(10 bpm) increase in HR, can still translate to a moderate increase in risk of stroke and all-cause mortality. Our results show that HR is a relevant parameter that needs to be accounted for when large changes in HR are present in the measurement of cfPWV, both in research and in a clinical setting.

5.5 Acknowledgments

We would like to express our gratitude to all the pacemaker technicians from Medtronic, Biotronik, Boston Scientific, and St. Jude Medical who provided technical assistance in this study. Typesetting assistance by Elien Engels is gratefully acknowledged. This study was supported by the Australian Postgraduate Award (to I.T.), Australian Research Council (ARC) Discovery grant DP11010134 (to A.A. and M.B.), and ARC Linkage grant LP120100463 (to A.A. and M.B.).

5.A1 Appendix: Additional details on methods

5.A1.1 Method 2: Blood pressures correction through mathematical modelling

The pressure (P) and arterial lumen area (A) relationship as formulated in Eq. 5.4 of the main manuscript can be expressed as

$$A = A_{\text{ref}} \left(\frac{\ln\left(\frac{P}{P_{\text{ref}}}\right)}{\alpha} + 1 \right) , \tag{5.A1}$$

where P_{ref} denotes a reference pressure with corresponding cross-sectional area A_{ref}. PWV is also related to pressure and cross-sectional area changes, as defined by the Bramwell-Hill equation (Bramwell and Hill 1922b):

$$\text{PWV} = \sqrt{\frac{1}{\rho} \frac{P_{\text{s}} - P_{\text{d}}}{A_{\text{s}} - A_{\text{d}}} A_{\text{d}}} , \tag{5.A2}$$

with ρ being the mass density of blood, taken to be 1050 kg/m^3, and subscripts s and d denoting systolic and diastolic, respectively. Eq. 5.A1 can be used to obtain an expression for A_{d} as a function of P_{d}, and equivalently to obtain an expression for A_{s} as a function of P_{s}. These expressions can be entered into Eq. 5.A2, which yields

$$\text{PWV} = \sqrt{\frac{P_{\text{s}} - P_{\text{d}}}{\rho} \frac{\ln\left(\frac{P_{\text{d}}}{P_{\text{ref}}}\right) + \alpha}{\ln\left(\frac{P_{\text{s}}}{P_{\text{d}}}\right)}} . \tag{5.A3}$$

Note that no cross-sectional area terms are present in this equation as these terms cancel out. Rearranging Eq. 5.A3 yields an expression for exponent α as a function of systolic and diastolic BP and PWV:

$$\alpha = \ln\left(\frac{P_s}{P_d}\right)\frac{\rho}{P_s - P_d}\mathrm{PWV}^2 - \ln\left(\frac{P_d}{P_{ref}}\right) . \tag{5.A4}$$

5.A1.2 Method 3: Empirical blood pressure correction through experimental data

PWV in each small arterial segment was assumed to scale linearly with local diastolic BP (P_d), i.e.,

$$\mathrm{PWV} = a \cdot P_d + b . \tag{5.A5}$$

In the seated position, hydrostatic pressure P_{hyd} varies along the arteries with height h in metres relative to the position of the aortic arch given the blood mass density (ρ) and gravitational constant ($g = 9.81\,\mathrm{m/s^2}$):

$$P_{hyd} = \rho g h . \tag{5.A6}$$

Note that P_{hyd} is positive relative to the pressure at the aortic arch at levels below the arch, and negative at levels above it (Fig. 5.1A). P_d along height h is therefore

$$P_d = \rho g h + P_{d,seated} , \tag{5.A7}$$

where $P_{d,seated}$ is the central aortic diastolic BP (cDBP) measured in the seated position. By combining equations Eq. 5.A5 and Eq. 5.A7, PWV along the aortic trunk can be expressed as

$$\mathrm{PWV} = a\left(\rho g h + P_{d,seated}\right) + b = a\rho g h + aP_{d,seated} + b . \tag{5.A8}$$

As velocity is the derivative of distance with respect to time, PWV can be denoted as

$$\mathrm{PWV} = \frac{\mathrm{d}h}{\mathrm{d}t} , \tag{5.A9}$$

and thus, transit time can de denoted as

$$\mathrm{d}t = \frac{\mathrm{d}h}{\mathrm{PWV}} . \tag{5.A10}$$

The total transit time from the aortic arch to the carotid artery (t_C, along distance C in Fig. 5.1A) can be found by integrating $\mathrm{d}t$ along that distance:

$$t_C = \int_{-C}^{0} \frac{1}{\mathrm{PWV}}\mathrm{d}h = \int_{-C}^{0} \frac{1}{a\rho g h + \left(aP_{d,seated} + b\right)}\mathrm{d}h , \tag{5.A11}$$

which can be evaluated to

$$\begin{aligned} t_C &= \left.\frac{\ln\left|a\rho g h + aP_{d,seated} + b\right|}{a\rho g}\right|_{-C}^{0} \\ &= \frac{1}{a\rho g}\ln\left(\frac{aP_{d,seated} + b}{a\left(P_{d,seated} - \rho g C\right) + b}\right) . \end{aligned} \tag{5.A12}$$

Similarly, the total transit time from the aortic arch to the femoral artery (t_F) can be evaluated to

$$t_F = \left.\frac{\ln\left|a\rho gh + aP_{d,seated} + b\right|}{a\rho g}\right|_0^F$$
$$= \frac{1}{a\rho g}\ln\left(\frac{a\left(\rho gF + P_{d,seated}\right) + b}{aP_{d,seated} + b}\right) . \quad (5.A13)$$

The total transit time from the carotid to femoral artery (t_{seated}) using the subtraction method for path length is

$$t_{seated} = t_F - t_C , \quad (5.A14)$$

thus, by substitution,

$$t_{seated} = \frac{1}{a\rho g}\Big[\ln\left(a\left(P_{d,seated} + \rho gF\right) + b\right) + \ln\left(a\left(P_{d,seated} - \rho gC\right) + b\right) - 2\ln\left(aP_{d,seated} + b\right)\Big] . \quad (5.A15)$$

In the supine case, no pressure gradient is present and PWV is assumed to be constant along the aorta for supine diastolic BP ($P_{d,supine}$):

$$PWV = a \cdot P_{d,supine} + b . \quad (5.A16)$$

Given that PWV is distance divided by transit time (t_{supine}),

$$t_{supine} = \frac{F - C}{PWV} = \frac{F - C}{a \cdot P_{d,supine} + b} . \quad (5.A17)$$

Using the two equations for t_{seated} and t_{supine} (Eq. 5.A15 and Eq. 5.A17), the two unknown coefficients a and b can be evaluated for each subject, and a represents the BP dependence of cfPWV for each subject. The averaged a ($\bar{a}$) across the 17 subjects was used to calculate the BP corrected cfPWV ($cfPWV_c$):

$$cfPWV_c = cfPWV - \bar{a} \cdot (cDBP - cDBP_{ref}) , \quad (5.A18)$$

where $cDBP_{ref}$ denotes cDBP at the lowest paced HR for the individual. The following mixed model was then fitted to the BP-corrected PWV values:

$$cfPWV_c = \beta_0 + \beta_1 \cdot HR + \epsilon_{ij} + u_j , \quad (5.A19)$$

where β_1 denotes the BP-independent effect of HR on cfPWV.

5.A2 Appendix: Effect of using different algorithms for determination of the pressure wave foot

In order to determine whether the heart rate (HR) effect on carotid-femoral pulse wave velocity (cfPWV) observed in the current study was a measurement artefact due to possible changes in the foot of the pressure wave with HR, a post hoc analysis was run on

a subset of 10 subjects to compare cfPWV determined from two different pulse transit time algorithms. One method used the intersecting tangent method to identify the foot of the pressure wave (Asmar et al. 1995) (default algorithm of SphygmoCor). The other method used the point of maximum slope of the systolic upstroke on the pressure wave as the timing point of reference (Chiu et al. 1991) (as used in the Complior device).

5.A2.1 Methods

Carotid and femoral blood pressure waveforms measured from the SphygmoCor XCEL (AtCor Medical, Sydney, NSW, Australia) device were re-analysed with the SphygmoCor SCOR software (AtCor Medical) using the two different algorithms, both provided as options in the software. A linear mixed model, with HR and timing algorithm modelled as fixed effects and with random effect modelled as the intercept for each individual, was fitted to the cfPWV data as follows:

$$\text{cfPWV}_{ij} = \beta_0 + \beta_1 \cdot \text{Method} + \beta_2 \cdot \text{HR} + \beta_3 \cdot \text{Method} \cdot \text{HR} + \epsilon_{ij} + u_j \,, \tag{5.A20}$$

where "Method" was a dummy coded variable indicating the timing algorithm used for calculation of cfPWV, coded 0 for the intersecting tangent method and 1 for the maximum systolic upstroke method. β_2 represented the effect of HR on cfPWV for the intersecting tangent method; β_3 represented the difference in the effect of HR on cfPWV between the two methods, thus $\beta_2 + \beta_3$ represented the effect of HR on cfPWV for the maximum systolic upstroke method.

5.A2.2 Results

The results from the mixed model indicated that the effect of HR was significant regardless of the transit time algorithm used (for the intersecting tangent method, $\beta_2 = 0.05[0.03, 0.06]$ m/s/bpm, $t = 4.94$, $p < 0.0001$; for the maximum systolic upslope method, $\beta_2 + \beta_3 = 0.03[0.01, 0.05]$ m/s/bpm, $t = 3.09$, $p = 0.03$). The values obtained were identical to those obtained by Millasseau et al. (2005) in their study of 11 subjects, where there was a 0.05 m/s/bpm change in cfPWV with HR (2.1 m/s change in cfPWV from 80 bpm to 120 bpm) using the intersecting tangent method, and a 0.03 m/s/bpm change in cfPWV with HR (1.1 m/s change in cfPWV from 80 bpm to 120 bpm) using the maximum slope of systolic upstroke algorithm. The absence of a significant interaction term between HR and the timing algorithm ($\beta_3 = -0.02[-0.04, 0.01]$, $t = 1.33$, $p = 0.19$) indicated that the effect of HR on cfPWV was not dependent of the algorithm employed for determination of pulse transit time.

Chapter 6

Carotid artery applanation tonometry does not cause significant baroreceptor activation

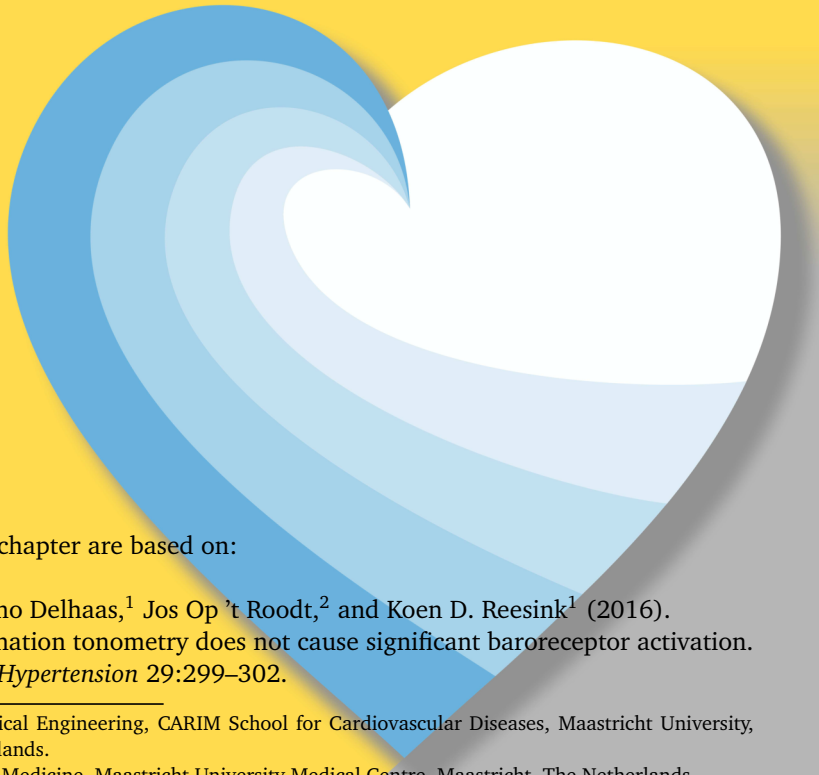

The contents of this chapter are based on:

Bart Spronck,[1] Tammo Delhaas,[1] Jos Op 't Roodt,[2] and Koen D. Reesink[1] (2016). Carotid artery applanation tonometry does not cause significant baroreceptor activation. *American Journal of Hypertension* 29:299–302.

[1] Department of Biomedical Engineering, CARIM School for Cardiovascular Diseases, Maastricht University, Maastricht, The Netherlands.
[2] Department of Internal Medicine, Maastricht University Medical Centre, Maastricht, The Netherlands.

Abstract

Carotid artery applanation tonometry is widely used in estimating local carotid artery pressure waveforms and carotid-femoral pulse wave velocity. However, the substantial pressure applied locally to the carotid artery with applanation tonometry might well evoke a baroreceptor response, resulting in bradycardia and hypotension. Therefore, when carotid and femoral tonometry are performed sequentially, baroreceptor activation could lead to different hemodynamic conditions between carotid and femoral acquisitions. Combining those acquisitions into one pulse wave velocity measure would be erroneous. In this study, we assessed whether carotid applanation tonometry has an influence on heart rate and blood pressure. In 26 hypertensive subjects, heart rate and blood pressure were assessed by continuous finger pulse waveform recording during carotid as well as femoral applanation tonometry. Both carotid and femoral acquisitions were measured in alternation and in triplicate. Median averaging over the three carotid and femoral measurements, respectively, was used to obtain a subject's median heart rate and blood pressure during carotid as well as femoral tonometry. Difference in heart rate during carotid and femoral tonometry was -0.7 ± 2.2 bpm. Differences in systolic, pulse, and diastolic blood pressure were -0.7 ± 6.8 mmHg, -0.1 ± 3.8 mmHg, and -0.3 ± 3.5 mmHg, respectively. All differences were statistically non-significant. Confidence intervals were used to calculate the maximum absolute difference at 95% certainty, which was 1.6 bpm for heart rate and ≤ 3.5 mmHg for all blood pressures. We conclude that in our study, carotid artery applanation tonometry as performed by an experienced researcher did not cause clinically significant baroreceptor activation.

6.1 Introduction

CAROTID-FEMORAL pulse wave velocity (cfPWV) is currently the gold standard measure for arterial stiffness (Laurent et al. 2001), and an increased cfPWV is considered an independent cardiovascular risk factor (Mancia et al. 2013). To measure cfPWV, mostly applanation tonometry is performed at the carotid and subsequently at the femoral artery. For proper applanation, substantial pressure is locally applied to the artery, compressing the vessel towards a firm background (typically bone), causing the artery to deform locally (Drzewiecki et al. 1983). Due to altered wall distension and receptor stretch, applanation tonometry might therefore induce a baroreceptor response (Courand et al. 2014; Schweitzer and Teichholz 1985). This effect is deliberately triggered during a Czermak-Hering test to assess autonomic nervous function, exerting bradycardia and hypotension (Takino et al. 1964). During applanation tonometry, however, it is unwanted. Because femoral applanation tonometry will not evoke baroreceptor responses, any baroreceptor activation during carotid applanation tonometry could cause a difference in blood pressure and heart rate between applanation at these two sites. Since pulse wave velocity notably depends on heart rate (Lantelme et al. 2002; Millasseau et al. 2005) and blood pressure (Spronck et al. 2015b), any effect of

tonometry on blood pressure and heart rate would lead to a difference in pulse wave velocity during carotid and femoral acquisitions. Clearly, combining both acquisitions into one cfPWV measure would be erroneous. In this study, we assessed the potential influence of carotid artery applanation tonometry on blood pressure and heart rate. To the best of our knowledge, there haven't been analytical reports on blood pressure during carotid and femoral tonometry measurements. In a previous expert consensus statement (Laurent et al. 2006), sequential recording of pulse waves for cfPWV assessment was discussed as follows: "Since the measurements are made a short time apart, the change in the isovolumic period of the LV or heart rate variability has little or no effect on measured pulse transit times." Potential baroreflex activation, however, is not mentioned.

6.2 Methods

6.2.1 Study population

Data obtained in a recently published study (Spronck et al. 2015b) were used for the present analysis. The study was approved by the ethical committee of Maastricht University Medical Center and conducted in accordance with the Declaration of Helsinki (Seoul 2008). All subjects provided written informed consent prior to participation. Thirty consecutive subjects were recruited from patients referred to our outpatient hypertension clinic. Four subjects were excluded due to missing data ($n = 3$) or severe ventricular extrasystoles ($n = 1$), yielding a group of 26 included subjects.

6.2.2 Measurements

Carotid and femoral tonometry were performed in alternation and in triplicate (Fig. 6.1A) using an applanation tonometer (SphygmoCor, AtCor Medical, Sydney, NSW, Australia). Simultaneous with the six tonometry acquisitions, finger blood pressure-derived parameters were acquired by the Peñáz method (Nexfin, BMEYE B.V., Amsterdam, The Netherlands) (Peñáz 1973). Parameters included systolic, diastolic, and pulse pressure, as well as heart rate. The three repeated measurements were averaged using median processing, giving one carotid and one femoral value for each parameter per subject. Measurements were performed by an experienced research nurse (JOR) in a quiet, temperature-controlled room (22 °C) after a resting period of 15 min with subjects in supine position.

6.2.3 Processing and statistics

Carotid-femoral differences in finger pressure parameters and heart rate were calculated and reported as mean ± standard deviation, as well as a 95%-confidence interval for the mean. A paired t-test was used to assess significant difference from zero ($\alpha = 0.05$).

6.3 Results

Results are presented in Fig. 6.1B–D. For none of the variables a significant carotid-femoral difference was detected. For heart rate, the maximum absolute difference (95%)

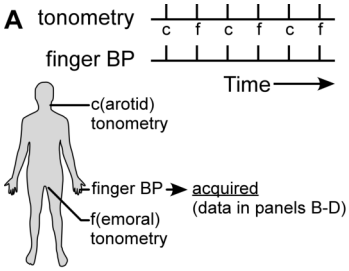

B

		Difference (carotid-femoral)		
		mean±SD	95% CI	*p**
HR	bpm	-0.7±2.2	-1.6,0.2	0.113
PP	mmHg	-0.1±3.8	-1.7,1.4	0.852
DBP	mmHg	-0.3±3.5	-1.7,1.1	0.657
SBP	mmHg	-0.7±6.8	-3.5,2.0	0.589

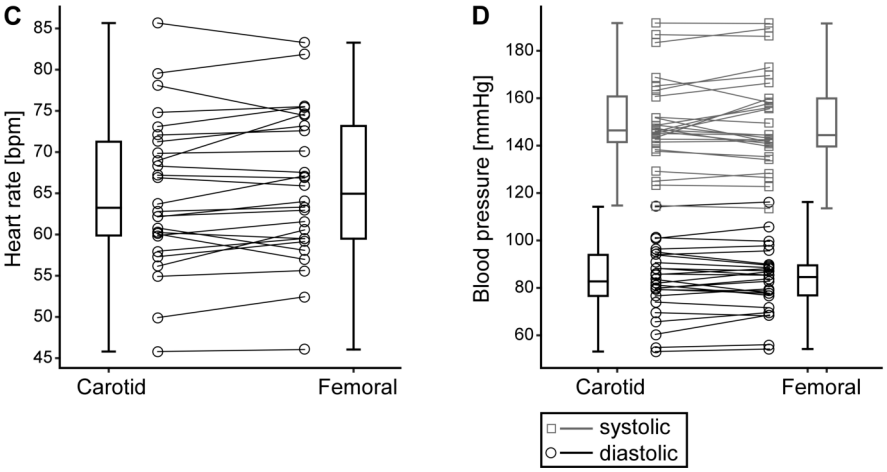

Figure 6.1: Study set-up and results. **A**: Carotid and femoral tonometry were performed in alternation and in triplicate. During each tonometry measurement, finger blood pressure (BP) was acquired. **B**: Differences in finger blood pressure parameters during carotid and femoral applanation tonometry. *paired student t-test; HR, heart rate; PP, pulse pressure; DBP, diastolic blood pressure; SBP, systolic blood pressure; SD, standard deviation; CI, confidence interval. **C**: Heart rate for each subject during carotid and femoral applanation tonometry, respectively. Whiskers indicate range. **D**: Systolic (squares, gray) and diastolic (circles, black) blood pressures for each subject during carotid and femoral applanation tonometry, respectively. Whiskers indicate range.

was 1.6 bpm. For the blood pressures, this difference was 3.5 mmHg (systolic) which is of the order of the measurement noise of 3.5 mmHg (Spronck et al. 2015b).

6.4 Discussion

In this study, we assessed the potential baroreflex-mediated effect of carotid applanation tonometry on blood pressure and heart rate. We found no statistically significant differences. Given the power of our study, the observed differences wouldn't be clinically relevant either.

In a Czermak-Hering test, baroreflex activation is deliberately triggered by applying external pressure to a subject's left and right carotid sinuses. Why applanation tonometry does not cause baroreceptor activation, whereas a Czermak-Hering test does, can be explained as follows. First, tonometry is typically performed on the common carotid artery, whereas during the Czermak-Hering test, pressure is applied to the carotid sinus, which is located more distally. Second, tonometry is performed unilaterally (as opposed to bilateral application of pressure in the Czermak-Hering test). However, it should be noted that unilateral carotid sinus massage is also known to activate a baroreceptor response, a technique used to treat supraventricular tachycardia (Schweitzer and Teichholz 1985).

It has to be mentioned that applanation tonometry was performed by an experienced research nurse in our study, using only minimal applanation force. Care was taken to perform applanation at a site about 2 cm proximal to the carotid sinus. In addition, pressure on the carotid sinus by e.g., resting the researcher's hand there, was avoided. Less-experienced researchers are likely to use more force, thereby imaginably increasing the probability of unwanted baroreceptor activation. Regardless of the cause, the researcher performing transit time pulse wave velocity measurements should assert that tonometry measurements taken at the different measurement sites are obtained at equal hemodynamic conditions.

Our protocol consistently started with carotid tonometry followed by femoral tonometry (see timeline, Fig. 6.1A). As subjects were in supine position, typically for 10–15 min, a further acclimatisation over time could have occurred. Because, on average, the carotid tonometry acquisitions were taken at an earlier time than the femoral tonometry acquisitions, this might have influenced our results. To assess this potential error, we re-processed all our results, excluding the first carotid (c) and last femoral (f) acquisition. The sequence of measurements now read "f-c-f-c", as compared to "c-f-c-f-c-f" originally (Fig. 6.1A). Re-processed results remained comparable: differences in heart rate, pulse, diastolic, and systolic pressures were -0.3 ± 2.1 bpm, -2.4 ± 6.1 mmHg, 0.5 ± 3.9 mmHg, and -1.5 ± 6.6 mmHg, respectively (all $p > 0.05$). Maximum absolute differences were 1.1 bpm for heart rate and ≤ 4.9 mmHg for blood pressures.

Methods for cfPWV assessment can be divided into sequential and simultaneous ones. Using a sequential method (typical device: SphygmoCor, AtCor Medical), carotid and femoral tonometry are not performed simultaneously. In the case of carotid baroreceptor activation as investigated here, the use of such a method would lead to the combination of two acquisitions at different hemodynamic conditions into one pulse wave velocity measure as discussed previously. Using a simultaneous method (typical device: Complior, Alam Medical, Vincennes, France), carotid and femoral tonometry are performed

simultaneously. In this case, hemodynamic conditions are, by their nature, equal during carotid and femoral tonometry. Millasseau et al. (2005) have compared cfPWVs acquired using both methods and found no statistical differences when signals were processed equally. Their finding that differences in hemodynamic conditions during carotid and femoral tonometry are indeed small corroborates our findings.

6.4.1 Conclusions

We conclude that in our study, carotid artery tonometry as performed by an experienced researcher did not cause significant baroreceptor activation. Carotid artery tonometry influenced heart rate by at most 1.6 bpm and peripheral blood pressure by no more than 3.5 mmHg, which both appear clinically insignificant.

6.5 Acknowledgements

This work was supported by grant Veni-STW10261 for K.D. Reesink from the Innovational Research Incentives Scheme of the Dutch Organisation for Scientific Research (NWO).

Chapter 7

Axial stretch dependence of arterial stiffness

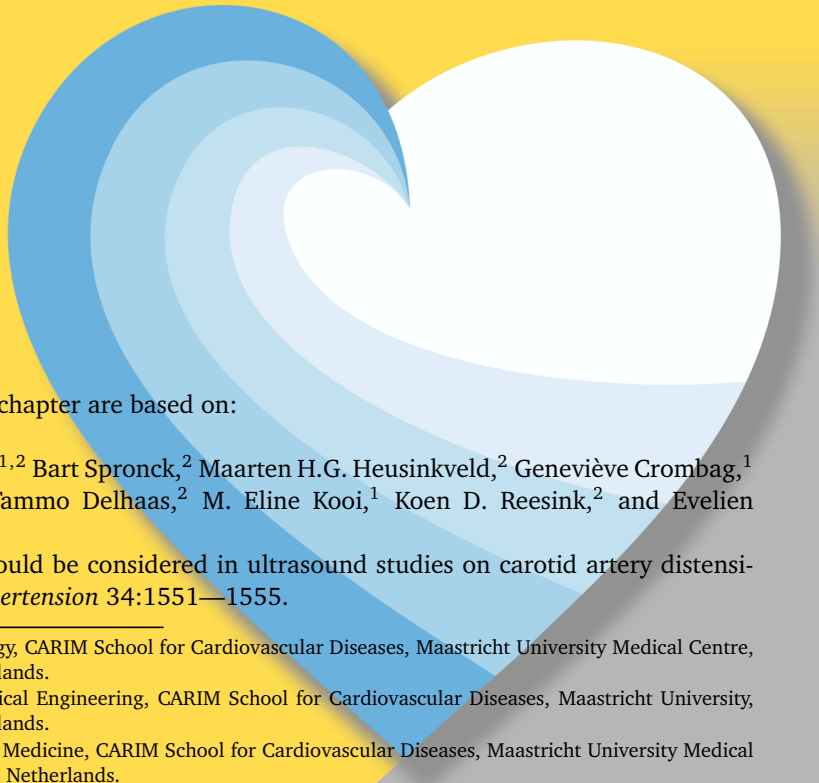

The contents of this chapter are based on:

Robert J. Holtackers,[1,2] Bart Spronck,[2] Maarten H.G. Heusinkveld,[2] Geneviève Crombag,[1] Jos Op 't Roodt,[3] Tammo Delhaas,[2] M. Eline Kooi,[1] Koen D. Reesink,[2] and Evelien Hermeling[1] (2016).
Head orientation should be considered in ultrasound studies on carotid artery distensibility. *Journal of Hypertension* 34:1551—1555.

[1] Department of Radiology, CARIM School for Cardiovascular Diseases, Maastricht University Medical Centre, Maastricht, The Netherlands.
[2] Department of Biomedical Engineering, CARIM School for Cardiovascular Diseases, Maastricht University, Maastricht, The Netherlands.
[3] Department of Internal Medicine, CARIM School for Cardiovascular Diseases, Maastricht University Medical Centre, Maastricht, The Netherlands.

Abstract

During ultrasound distensibility assessment of the carotid artery, the patient's head is usually rotated sidewards and slightly upwards to optimise visibility of the carotid segment. Head rotation may affect vessel length and thus the longitudinal strain of the arterial segment. Because the longitudinal and circumferential mechanical behaviour of an artery are intrinsically related, head rotation may influence circumferential mechanics and thereby measured distensibility. In twelve apparently healthy volunteers (age 22 ± 3 yrs (mean $\pm$ SD), 6 male/6 female), we investigated whether head rotation led to a change in absolute and relative distension of the common carotid artery by performing ultrasound examinations with the head in two orientations. Additionally, common carotid artery length was measured in both orientations with magnetic resonance imaging to assess whether indeed a change in length occurred due to head rotation. Rotation-induced longitudinal strain was calculated from these lengths. We found a significant decrease of 0.054 mm (6.8%, $p = 0.001$) and 0.007 (5.6%, $p = 0.019$) in absolute and relative distension with head rotation, respectively. Magnetic resonance imaging measurements showed a significant rotation-induced longitudinal strain of $1.7 \pm 2.3\%$ ($p = 0.032$). We conclude that consistent head rotation during a common carotid artery ultrasound assessment causes a significant and clinically relevant bias in carotid artery distension measurements. The impact of unstandardised use of head rotation in studies with carotid distensibility as an outcome measure can therefore not be neglected; thus, standardisation is highly recommendable.

7.1 Introduction

CAROTID artery distensibility is a measure of vascular function in clinical-epidemiological research, specifically recommended for biomechanical investigations on vascular stiffness (Hoeks et al. 1990; Laurent et al. 2006). Recently, reference values for local carotid artery stiffness have been established (Engelen et al. 2015), supporting its clinical application as a diagnostic marker for vascular dysfunction.

During ultrasound (US) assessment of carotid artery distensibility, the patient's head is usually rotated sidewards and slightly upwards to optimise visibility of the carotid segment (Fig. 7.1). However, the extent of head rotation during these assessments is not explicitly standardised, introducing noise in the estimate. The head orientation may affect the vessel length and thus the longitudinal strain of the arterial segment. Because of the intrinsic relationship between longitudinal and circumferential mechanical behaviour of an artery, longitudinal strain may influence measured distensibility (Dobrin 1978; Humphrey 2002).

In the present study, we investigated whether head rotation led to a change in absolute and relative distension of the common carotid artery (CCA) by performing US assessments with the head in two orientations. In both orientations, CCA length was estimated using

magnetic resonance imaging (MRI) to assess whether indeed a change in length occurred due to head rotation.

7.2 Methods

7.2.1 Study population

Twelve young, apparently healthy volunteers (age 22 ± 3 yrs, mean $\pm$ standard deviation (SD), 6 male/6 female) were recruited for this study. The only exclusion criteria were the standard MRI contraindications (pacemaker, nerve stimulator, metallic devices/implants, and severe claustrophobia). The local ethics committee approved this study and written informed consent was obtained from all participants before enrolment. Due to logistic reasons, the MRI examination of one subject could not be performed.

7.2.2 MRI measurements

MRI measurements were acquired using a 3T whole-body MR system (Achieva TX; Philips Healthcare, Best, The Netherlands). Before the measurements, the subjects rested in supine position on the MRI examination table for at least 10 minutes. Three ink markers (Fig. 7.1) were drawn on the subjects' sternal notch (fossa jugularis sternalis), chin and right mandibular angle (angulus mandibulae dexter). The distances between these markers were measured in both orientations in order to reproduce both orientations during the US measurements, which were performed 15–30 minutes after the MRI measurements. After the resting period, the subjects were asked to rotate their head to the left (approximately 50°) and tilt it to the back, referred to as the rotated orientation (Fig. 7.2). If required, sand bags were added for additional support. The distances between the three applied markers were measured, after which the subject was inserted in the scanner and a single measurement in the rotated orientation was acquired. After this measurement, the subjects were asked to rotate their heads back to a natural orientation (nose pointing upwards and no tilting backwards) while inside the scanner, referred to as the normal orientation (Fig. 7.2). After the measurement in the normal orientation, the subjects were retracted from the scanner and the distances between the three markers were measured again.

For the MRI measurements, a standard multi-slice coronal phase-contrast angiography scan (3D T_1 fast field echo technique) was used. Scan parameters were as follows: repetition time 10 ms, echo time 3.8 ms, flip angle 15°, velocity encoding 70 cm/s, field of view $300 \times 150 \times 50$ mm, acquisition matrix 256×122, reconstructed voxel size $0.59 \times 0.59 \times 1.00$ mm, 50 overcontiguous slices of 2 mm thickness, and number of signal averages 2. The measurements were acquired with an integrated body coil.

After these measurements, the subjects walked approximately 200 m, accompanied by one of the researchers, to the US examination room. Both MRI and US measurements were performed on the same day and within one hour. The subjects were not allowed to drink, eat, or smoke in between the measurements.

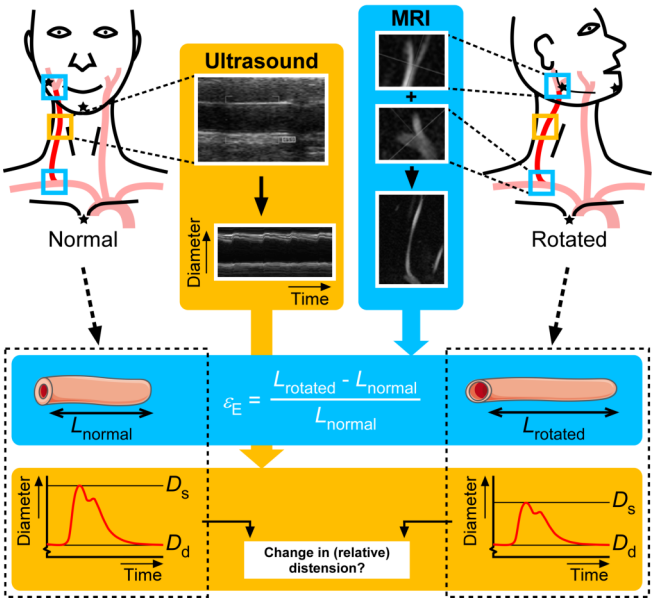

Figure 7.1: Common carotid artery ultrasound and magnetic resonance imaging (MRI) were performed with both the head in a normal and rotated orientation. MRI was used to assess a potential change in common carotid artery length, while ultrasound was used to measure the artery's cyclic diameter parameters. The black stars indicate the locations of the three applied markers used to reproduce the two head orientations. ϵ_E, longitudinal vessel strain; L, vessel segment length; D_s and D_d, systolic and diastolic diameter, respectively.

7.2.3 US and blood pressure measurements

After the subject rested at least 10 minutes in supine position, US measurements were performed using a MyLab 70 VGX ultrasound system (Esaote Europe; Maastricht, The Netherlands), equipped with an ART.LAB module and a 40 mm wide 7 – 13 MHz linear array transducer. US measurements were performed at the right CCA segment with the region of interest centred at 1.5 cm proximal to the start of the carotid bifurcation. Measurements of the two orientations were performed in alternation and in triplicate (scheme: rotated – normal – rotated – normal – rotated – normal) by an experienced vascular research technician (J.O.R.) in a quiet, temperature-controlled room (22°). Each orientation was reproduced before the US measurement by checking the measured distances between the three ink markers. Again, sand bags were used for support if required. Throughout the US session, three repeated oscillometric blood pressure readings were obtained at the right upper arm (Omron 705IT; Omron Healthcare Europe, Hoofddorp, The Netherlands).

The US system was operating in ART.LAB fast B-mode with electrocardiogram triggering, producing 31 M-mode lines spaced over a segment of about 29 mm. Maximal frame rate was approximately 300 Hz (temporal resolution 3.3 ms), determined by the number of M-lines and the pulse repetition frequency. The latter depends on the maximal depth

Figure 7.2: Overview of the normal (left) and rotated (right) head orientations, observed from a transversal (top row) and frontal (bottom row) point of view. The inclinometer indicates the degree of sidewards rotation, which was approximately 50° for all subjects.

range of the US measurement and was 9 kHz for superficial arteries like the carotid artery.

It should be noted that we could not perform MRI and US measurements simultaneously and in the same room due to the strong magnetic field of the MR system. Care was taken to measure in identical conditions during MRI and US measurements by having similar head positions as guided by ink markers and by keeping the time between the measurements as short as possible.

7.2.4 MRI analysis

MRI datasets were reformatted into curved 3D multi-planar reconstructions using the Osirix software package (Pixmeo; Bernex, Switzerland). This rendering technique enables one to measure the length of complex, tortuous structures such as blood vessels. Three trained observers (R.H., B.S. and G.C.), who where blinded to head orientation and to subject identity, independently identified and marked the flow divider of the brachiocephalic artery bifurcation (start point) and the flow divider of the right carotid artery bifurcation (end point; Fig. 7.1). Subsequently, they placed additional markers in the centre of the lumen of the right CCA in between start and end points. By calculating a 3D Bézier path through all these markers, the length of the right CCA was determined once by each observer for both orientations. The three measurements per orientation were averaged by taking the median over the three observers, giving one normal length (L_{normal}) and one rotated length (L_{rotated}) of the right CCA per subject. The rotation-induced longitudinal strain (ϵ_{E}) of the right CCA was then calculated as follows:

$$\epsilon_{\text{E}} = \frac{L_{\text{rotated}} - L_{\text{normal}}}{L_{\text{normal}}} \,. \tag{7.1}$$

7.2.5 US and blood pressure analyses

The three repeated blood pressure readings were averaged to obtain one, orientation-independent average value for systolic blood pressure (SBP) and diastolic blood pressure (DBP). Ultrasound radiofrequency data was processed with a MATLAB (The MathWorks, Natick, MA, USA) program, according to the technique developed and reported by Hoeks et al. (1999). The global positions of the near and far vessel walls at the proximal and distal end of the CCA segment in the acquired US images were manually indicated by the same experienced vascular research technician who performed the measurements (J.O.R.). The MATLAB program automatically (operator-independently) traced the exact location of the complete vessel wall for every timeframe by wall tracking. No manual interventions were performed during or after this analysis and thus no actual differences in processing exist between the two orientations. Based on the electrocardiogram, consecutive heartbeats were segmented to obtain beat-to-beat diastolic diameter, and absolute and relative distension values. Absolute distension (ΔD) was defined as the difference between systolic and diastolic arterial diameters (D_s and D_d):

$$\Delta D = D_\mathrm{s} - D_\mathrm{d} \; . \tag{7.2}$$

Relative distension was subsequently calculated as $\Delta D / D_\mathrm{d}$.

D_d, and ΔD and $\Delta D / D_\mathrm{d}$ were obtained for each M-line, spatially averaged over all lines, and then averaged over all heart beats by taking the median value, yielding a single value for these three parameters per measurement. Using these values combined with brachial SBP and DBP, the corresponding distensibility coefficient (DC) was calculated as (Hoeks et al. 2008):

$$\mathrm{DC} = \frac{\Delta A}{A_\mathrm{d}\,(\mathrm{SBP} - \mathrm{DBP})} = \frac{(D_\mathrm{d} + \Delta D)^2 - D_\mathrm{d}^2}{D_\mathrm{d}^2\,(\mathrm{SBP} - \mathrm{DBP})} \; , \tag{7.3}$$

with A_d the diastolic lumen cross-sectional area and ΔA the change in lumen cross-sectional area between diastole and systole. Local carotid pulse wave velocity (cPWV) is subsequently calculated as

$$\mathrm{cPWV} = \sqrt{\frac{1}{\rho \cdot \mathrm{DC}}} \; , \tag{7.4}$$

with $\rho = 1.050\,\mathrm{kg/L}$ the blood mass density.

The three repeated parameter values were subsequently averaged by taking the median value, yielding one value per orientation for each subject. Group averaged means ± SDs of the subject values are reported. Measurement variability was assessed as follows: The variance of the three repeated measurements was calculated per orientation for the entire study group; the square root of the average of these variances from the two orientations of all individuals is the measurement variability (intra-subject SD, Bland and Altman 1996).

7.3 Results

Table 7.1 shows the US and MRI parameters of the right CCA for both orientations, showing significant decreases of 0.054 mm (6.8%, $p = 0.001$) and 0.007 (5.6%, $p = 0.019$) in

Table 7.1: Ultrasound, blood pressure and magnetic resonance imaging parameters of the right common carotid artery (CCA) in normal and rotated orientations

Parameter	Unit	Head orientation		Intra-subject SD		p^*
		Normal	Rotated	Normal	Rotated	
Ultrasound and blood pressure ($n = 12$)						
ΔD	mm	0.789±0.123	0.735±0.115	0.035	0.047	0.001
$\Delta D/D_d$	-	0.124±0.018	0.117±0.021	0.007	0.011	0.019
D_d	mm	6.37±0.71	6.32±0.66	0.22	0.28	0.595
IMT	μm	539±64	510±46	40	31	0.053
SBP	mmHg	129.9 ± 13.1		2.9		
DBP	mmHg	71.8 ± 8.3		3.0		
DC	MPa^{-1}	34.8±6.1	32.8±7.1	2.3	3.1	0.018
cPWV	m/s	5.29±0.47	5.49±0.64	0.16	0.27	0.025
Magnetic resonance imaging ($n = 11$)						
L	cm	9.88±1.27	10.03±1.15	0.10	0.10	0.055
ϵ_E	%	1.7 ± 2.3		1.2		0.032

Values are given as mean ± standard deviation (SD), $^*p$-value, paired student t-test. ΔD, absolute distension; $\Delta D/D_d$, relative distension; D_d, diastolic diameter; IMT, intima-media thickness; SBP and DBP, brachial systolic and diastolic blood pressures, respectively; DC, distensibility coefficient; cPWV, carotid pulse wave velocity; L, common carotid artery length; ϵ_E, common carotid artery longitudinal strain.

absolute and relative distension with head rotation, respectively. Diastolic diameter and intima-media thickness did not change significantly with head rotation. The intra-subject SDs of 0.042 mm and 0.009 for absolute and relative distension, respectively, showed that the measurement variability was at least two times smaller than the variability between subjects (Table 7.1). The MRI measurements showed a significant rotation-induced longitudinal strain (ϵ_E) of the right CCA of $1.7 \pm 2.3\%$ ($p = 0.032$), with an intra-subject SD of 1.2%. DC showed a significant increase with head rotation, while cPWV showed a significant decrease. R-R interval did not vary with head rotation ($p = 0.961$).

7.4 Discussion

In this study, we assessed the potential bias in absolute and relative distension as a result of head rotation during ultrasound assessment of the CCA. The MRI measurement confirmed the presence of a rotation-induced longitudinal strain of the CCA segment.

The present study investigates the effect of consistent head rotation on carotid artery distension. In practice, positioning of the subject's head is performed at the discretion of the sonographer. The present findings suggest that unstandardised (or unrecorded) use of head manipulation introduces noise in distension measurements. Further standardisation of head orientation is highly recommendable, especially for smaller-scale intervention studies focussing on changes in carotid mechanics over time and with therapy.

The practical relevance of our findings becomes evident when considering the refer-

ence values for carotid artery distensibility (Engelen et al. 2015). Engelen et al. (2015) showed that the difference in carotid distension between the healthy sub-population and the sub-population with prior cardiovascular disease is about 0.10 mm. Engelen et al. (2015) also studied a subgroup of subjects without prior cardiovascular disease that are not treated using medication that lowers BP, lipids, and/or glucose. In this subgroup, distension in subjects with at least one cardiovascular risk factor (i.e., smoking and self-reported diabetes) was found to be 0.05 mm smaller than in subjects without risk factors.

Considering the rotation-induced change of 0.054 mm in absolute distension that we detected (Table 7.1), the impact of unstandardised head rotation in studies with carotid distensibility as an outcome measure cannot be neglected. The present findings suggest that standardisation of head rotation is needed to enable unbiased measurement of distension.

Pressure measurements were not taken at a specific head orientation. A systematic change in blood pressure between orientations is unlikely, as pulse pressure is determined by the stroke volume of the heart and the compliance of the complete arterial system. A change in stroke volume with head rotation is not to be expected, but carotid artery compliance may slightly change due to the extra longitudinal strain induced by head rotation. However, as the carotid artery compliance forms only a small part of the total arterial compliance, a change in pulse pressure is highly unlikely. Under the assumption that pulse pressure and diastolic blood pressure remain constant, the observed changes in distension with head rotation will propagate into changes in DC and cPWV (Table 7.1).

DC and cPWV as calculated in this study (Table 7.1) were based on brachial pressure measurements. Ideally, local carotid pressure measurements would be used to calculate DC and cPWV. These measurements were unavailable in this study. Generally, using a brachial pressure measurement as a surrogate for local carotid blood pressure overestimates pulse pressure and SBP. Therefore, the reported DC values may slightly underestimate true DC values, while the reported cPWV values may overestimate true cPWV values. However, as no change in blood pressure is expected with head rotation, the use of brachial instead of carotid pressures only influences the absolute values of cPWV and DC, and does not influence the observed *changes* in DC and cPWV with head rotation.

During an US assessment, no substantial force is exerted by the transducer on the skin, as this is not required for proper imaging. Even the larger force that would be applied when carotid applanation tonometry is performed does not cause significant baroreceptor activation (Spronck et al. 2016b). Therefore, we assume that US assessment did not cause baroreceptor activation either.

The substantial intra-subject SD of ϵ_{E} is likely due to the difficulty the three observers had to identify the reference point in the brachiocephalic bifurcation. A 3D isotropic MRI scan sequence could improve the accuracy of vessel segment length determination. More measurements might also improve the accuracy of the estimate, though at the expense of confounding memory effects of the observers.

The present study was performed in a relatively small study population of only young healthy individuals. However, the population was large enough to detect a significant change in carotid artery distension, due to the head rotation, that is also clinically significant. Because we only estimated the effect of head rotation on distension in young healthy individuals, no direct statements can be made about the magnitude of this effect in elderly subjects. The observed effect of head rotations on distension could potentially

be used to improve the quantification of age-related changes in mechanical properties of the arterial wall constituents, as follows. Previously, we have used pressure and diameter measurements (i.e., the pressure-diameter relation) to quantify age-related changes in mechanical properties of the collagen-elastin matrix in the carotid artery wall (Spronck et al. 2015a). These matrix properties were estimated by means of fitting a biomechanical model to the measurements. The present study implies that carotid pressure-diameter relations can effectively be measured at two *in vivo* lengths, instead of one, as is common in other studies including our previous work. Measuring in two experimental conditions would double the amount of information that can be obtained and may thus improve the accuracy of non-invasive assessment of arterial biomechanics.

We conclude that consistent head rotation during a common carotid artery US assessment causes a significant and clinically relevant bias in carotid artery distension. The impact of unstandardised use of head rotation in studies with carotid distensibility as an outcome measure can therefore not be neglected and thus standardisation is highly recommendable.

7.5 Acknowledgements

This study was supported by Stichting de Weijerhorst (R.J. Holtackers) and a Kootstra Talent Fellowship awarded to M.H.G. Heusinkveld by Maastricht University.

Chapter 8

Constitutive modelling interpretation of carotid artery ageing

The contents of this chapter are based on:

Bart Spronck,[1] Maarten H.G. Heusinkveld,[1,2] Wouter P. Donders,[2,3] Anouk G.W. de Lepper,[1] Jos Op 't Roodt,[4] Abraham A. Kroon,[4] Tammo Delhaas,[1] and Koen D. Reesink[1] (2015).
A constitutive modeling interpretation of the relationship between carotid artery stiffness, blood pressure and age in hypertensive subjects. *American Journal of Physiology - Heart and Circulatory Physiology* 308:H568–H582.

[1] Department of Biomedical Engineering, CARIM School for Cardiovascular Diseases, Maastricht University, Maastricht, The Netherlands.
[2] Department of Biomedical Engineering, Eindhoven University of Technology, Eindhoven, The Netherlands.
[3] Department of Biomedical Engineering, MHeNS School for Mental Health and Neuroscience, Maastricht University, Maastricht, The Netherlands.
[4] Department of Internal Medicine, CARIM School for Cardiovascular Diseases, Maastricht University Medical Centre, Maastricht, The Netherlands.

Abstract

Aging has a profound influence on arterial wall structure and function. We have previously reported the relationship between pulse wave velocity, age, and blood pressure in hypertensive subjects. In the present study, we aimed for a quantitative interpretation of the observed changes in wall behaviour with age using a constitutive modelling approach. We implemented a model of arterial wall biomechanics and fitted this to the group-averaged pressure-area (*P-A*) relationship of the "young" subgroup of our study population. Using this model as our take-off point, we assessed which parameters had to be changed to let the model describe the "old" subgroup's *P-A* relationship. We allowed elastin stiffness and collagen recruitment parameters to vary and adjusted residual stress parameters according to published age-related changes. We required wall stress to be homogeneously distributed over the arterial wall, and assumed wall stress normalisation with age by keeping average "old" wall stress at the "young" level. Additionally, we required axial force to remain constant over the cardiac cycle. Our simulations showed a shift in pressure load bearing from elastin to collagen, caused by a decrease in elastin stiffness and a considerable increase in collagen recruitment. Correspondingly, simulated diameter and wall thickness increased by about 20 % and 17 %, respectively. The latter compared well with a measured thickness increase of 21 %. We conclude that the physiologically realistic changes in constitutive properties we found under physiological constraints with respect to wall stress could well explain the influence of aging in the stiffness-pressure-age pattern observed.

8.1 Introduction

It is well established that aging has a profound influence on arterial wall structure and function. Previously, we non-invasively established that in clinical hypertension patients, the commonly observed increase in pulse wave velocity (PWV) with BP could be directly predicted from the nonlinearity of the pressure-area (*P-A*) relationship, and does not require a change of the *P-A* relationship itself (Spronck et al. 2015b, methods reproduced in Appendix 8.A1). With age, however, we did find a shift of the *P-A* relationship to larger areas and an increase in steepness of the relationship, together corresponding to an increase in PWVs (Spronck et al. 2015b, main findings reproduced in Table 8.1). The BP–age–stiffness pattern is merely descriptive and does not readily reveal any mechanistic insight. The BP dependence of arterial stiffness is known to be directly linked to arterial wall matrix constitution and actual distribution of mechanical load, while age-related changes also entail adaptive responses to load. In the present study, we used a constitutive modelling approach for a quantitative interpretation of the previously observed age- and pressure-related differences in arterial stiffness. Such an approach could potentially be applicable in a broad range of clinical studies focusing on arterial wall remodelling.

Constitutive modelling of the arterial wall has been used for a variety of applications

Table 8.1: Previously obtained pulse wave velocities for predefined pressure ranges in relation to age

SBP/DBP [mmHg]	Pulse wave velocity, m/s	
	Mean age: 41 yrs ("young")	Mean age: 64 yrs ("old")
120/80	7.2	10.9
160/90	8.1	12.2

Stiffness, as indicated by pulse wave velocity (PWV), is shown for normotensive (120/80 mmHg) and hypertensive (160/90 mmHg) pressure ranges for the 2 age groups studied. Carotid artery PWV values were derived from the exponentially modelled pressure-area curves via Bramwell-Hill for the "young" and "old" groups. SBP, systolic blood pressure; DBP, diastolic blood pressure.

(Holzapfel and Ogden 2010a) such as studies of aneurysm rupture or of arterial remodelling. However, the number of studies that apply constitutive modelling to *in vivo* measured data is limited.

In 2003, Schulze-Bauer and Holzapfel (2003) used a Fung-type combination of strain energy functions to describe the mechanical behaviour of the thoracic aorta of one normotensive and one hypertensive subject. Their model, however, does not explicitly model the three major constituents of the wall, i.e., collagen, elastin and vascular smooth muscle (VSM).

Stålhand et al. followed a similar approach in 2004–2006, using invasively measured pressure data from a healthy volunteer (Stålhand and Klarbring 2005; Stålhand and Klarbring 2006; Stålhand et al. 2004). In 2009, Stålhand expanded his model by including explicit isotropic and anisotropic parts, separating the anisotropic contribution of collagen from the other vascular constituents (Stålhand 2009).

In 2011, Åstrand et al. published a study (Åstrand et al. 2011) in which they used the approach described by Stålhand (2009) to assess constitutive parameters in thirty healthy volunteers divided into three age groups. One of their remarkable findings was an increase of the elastin structure stiffness with age. This finding could be explained ultrastructurally by the mechanism of elastocalcinosis. Although it is established that elastocalcinosis is associated with an increased overall artery stiffness (2), it can be questioned whether this increase is due to either an increased stiffness of the load-bearing elastin, or a shift in load bearing to the stiffer collagen due to elastin fibre rupture. The current paradigm of arterial aging, in which the elastin structure is thought to degrade or rupture with age (Wagenseil and Mecham 2012), suggests a decrease in stiffness of the elastin structure.

Masson et al. proposed a three-constituent model for clinical application in 2008 (Masson et al. 2008). The study by Masson et al. differs from the aforementioned studies (Åstrand et al. 2011; Schulze-Bauer and Holzapfel 2003; Stålhand 2009; Stålhand and Klarbring 2005; Stålhand and Klarbring 2006; Stålhand et al. 2004) in two ways. Firstly, Masson et al. measured blood pressure non-invasively using tonometry, whereas the earlier studies used invasive catheter measurements. This makes the entire data-acquisition non-invasive and increases the potential to include larger numbers of subjects. Secondly, Masson et al. assessed wall thickness patient-specifically by measuring intima-media thickness. The other studies used a population-based equation to estimate wall

thickness, ignoring potential patient- and group-specific differences.

In 2011, Masson et al. used their model to evaluate 16 normotensive and 25 hypertensive subjects (Masson et al. 2011). Although their results were promising in showing the potential of non-invasive assessment of age- and blood pressure-induced changes in wall constituents, their study had the limitation that fourteen parameters were estimated based on only the pressure-area curve. Therefore, the uniqueness of the obtained parameter values obtained is questionable.

In the present study, we modified a mathematical model developed by Zulliger et al. (2004b), and used this to quantitatively assess the constitutive changes with aging in the carotid artery that we became aware of due to the stiffness–BP–age pattern previously found (Table 8.1, Spronck et al. 2015b). The model considers the arterial wall to be composed of an extracellular matrix consisting of elastin and collagen embedded with VSM, with the three constituents homogeneously distributed in the wall. VSM is assumed to be oriented/acting in circumferential direction (i.e., anisotropically), while elastin is assumed to behave isotropically. Collagen is assumed to be anisotropic and oriented in two symmetric helices, as proposed by e.g., Holzapfel et al. (2000). The model also includes parameters to incorporate changes in residual stress as they occur with aging of the artery wall (Saini et al. 1995; Zulliger and Stergiopulos 2007).

We explicitly chose to:

1. focus on modelling the transition from “young” to “old” artery wall mechanics (i.e., “aging”), varying only five selected parameters, to avoid overfitting and related interpretation problems;
2. investigate changes in stiffness and recruitment of the different wall constituents and resulting changes in load bearing;
3. assess changes in wall geometry related to wall stress;
4. use clinically obtained measurements in hypertensive patients. We measured these patients under untreated (baseline) and treated (repeat) conditions. The data thus obtained at two distinct pressure ranges, allow evaluation of the consistency of the model outcomes; and
5. use non-invasive data, including echographic estimation of wall thickness, i.e., intima-media thickness.

Our approach addresses the limitations of previous work, in which either a very large number of parameters was fitted (e.g., (Masson et al. 2011)), the wall constituents were not explicitly modelled (e.g., (Åstrand et al. 2011), omitting VSM), or an estimated instead of a measured reference for wall thickness was used (Masson et al. 2011; Masson et al. 2008).

We evaluate our quantitative modelling approach and discuss the potential value of constitutive model-based interpretation of clinical patient data. Explicitly, we are not proposing a new model per se, but instead are focusing on interpreting clinical measurements using an established constitutive model with only minimal modifications. Such a model-based interpretation may offer insight into the individual patient’s arterial biomechanical state, as needed in e.g., stiffness-treatment studies targeting specific wall constituents.

Table 8.2: Study group characteristics

Parameter	Unit	Age group	
		"young" age <50 yrs	"old" age >50 yrs
n	-	6	7
Sex	# m/f	3/3	5/2
Age	yrs	41±6	64±9*
Height	cm	174±6	174±8
Weight	kg	82±18	85±9
BMI	kg/m^2	27±4	28±2
Meds	DDD	1.0±1.4	0.6±1.1
SBP (P_s)	mmHg	149±17	174±34
DBP (P_d)	mmHg	95±12	92±4
PP (P_p)	mmHg	54±14	82±33
A_d	mm^2	46±9	59±17
A_n	mm^2	50±11	61±17
A_s	mm^2	51±11	62±17
Carotid CC (C)	10^{-2} mm^2/mmHg	8.8±3.2	4.8±1.1*
IMT	mm	0.65±0.08	0.79±0.23
Carotid PWV (v_{car})	m/s	8.4±1.2	12.7±2.9*
Aortic PWV (v_{ao})	m/s	8.8±1.0	11.1±1.8*

Values are Mean ± SD. Meds denotes antihypertensive medication in daily defined dose (DDD). BMI, body mass index; PP, pulse pressure; A_d, A_n, and A_s, diastolic, dicrotic notch, and systolic carotid artery cross-sectional area, respectively (based on adventitia-adventitia distance); CC, compliance coefficient; IMT, intima-media thickness; v_{car}, local carotid PWV based on the Bramwell-Hill equation; v_{ao}, aortic PWV based on carotid-to-femoral transit time. Sex differences (f, female; m, male) were not statistically significant ($p = 0.59$, Fisher's exact test). $^*p < 0.05$, for difference between age groups (Wilcoxon rank-sum test).

8.2 Methods

8.2.1 Pressure-area curve data acquisition and processing

Data acquisition and patient data used for the present study are extensively described in Appendix 8.A1. The study protocol conformed to the Declaration of Helsinki (updated Seoul 2008) and was approved by the Maastricht University medical ethics committee. Study subjects were recruited from patients attending an outpatient hypertension clinic. Measurements were performed at inclusion (baseline) and repeated after three months (repeat) for each individual. *P-A* relationships were obtained at each visit (Spronck et al. 2015b, method summarised in Appendix 8.A1). Intima-media thickness was determined as described previously (Hoeks et al. 1997; Van Bortel et al. 2001; Willekes et al. 1999). To critically evaluate the consistency of our approach, we used baseline and repeat data from $n = 13$ patients whose blood pressure was clearly reduced at repeat. We divided the group into a "young" group (age < 50 yrs, $n = 6$) and an "old" group (age > 50 yrs, $n = 7$). Baseline characteristics of both groups are shown in Table 8.2. The present analysis focuses on the differences in carotid artery wall properties between the age groups.

8.2.2 Constitutive modelling

In order to interpret the differences in measured biomechanical behaviour between age groups, we implemented a constitutive model of the arterial wall (64). We approached the group-averaged curve of the "young" patients as the reference state and, accordingly, the "old" group's data as the result of age-related changes in arterial wall matrix properties and adaptation to wall stress. We specifically quantified to which extent elastin stiffness, collagen recruitment and VSM characteristics needed to be modified to explain the age-related differences in terms of pressure-area relation. We took into account long-term homeostasis of wall stress in the wall (Åstrand et al. 2011; Matsumoto and Hayashi 1994; Wolinsky 1972), independence of axial force on pressure (Avril et al. 2013; Brossollet and Vito 1995; Fung 1990; Humphrey 2002; Weizsäcker et al. 1983), as well as changes in residual strains with age (Saini et al. 1995; Zulliger and Stergiopulos 2007).

Model definition

A detailed description of the model used can be found in Appendix 8.A2. Our model, which largely follows the model published by Zulliger et al. (2004b), distinguishes three wall components: elastin, collagen and VSM. The mechanical behaviour of each of these components is described by a strain energy function (SEF). SEFs provide a relationship between stress and strain, and as such provide a convenient way of formulating constitutive behaviour of hyperelastic materials (Humphrey 2002).

Elastin, assumed to be mechanically isotropic, is described by a convex SEF (Eq. 8.A4) that is governed by parameter c_{elast}, which linearly scales the elastin stress-strain relationship.

Collagen is assumed to be oriented in two symmetric helices at an angle of $\pm\beta_0$ with respect to the circumferential orientation (Fig. 8.A1), similar to e.g., Holzapfel et al. (2000). The SEF of a single collagen fibre (Eq. 8.A8) increases quadratically with strain. The fibre SEF is convolved with a log-logistic engagement stretch distribution (Eq. 8.A5) to obtain the SEF of the collagen ensemble. The latter function describes the probability that, given a certain stretch, a collagen fibre is recruited. This distribution is governed by two parameters: 1) b, a scaling parameter which, for increasing values, shifts the log-logistic probability density function to the right, causing collagen to engage at higher strains. At the same time, probability density function height decreases and variance increases. 2) k, a shape parameter which, for increasing values, results in a higher maximum and a narrower distribution, thus causing collagen to engage more abruptly.

VSM is assumed to be oriented circumferentially (Hahn and Schwartz 2009; Rachev and Hayashi 1999). The VSM SEF (Eq. 8.A10) results in a linear stress-strain relationship when VSM is maximally contracted. Parameter c_{VSM} linearly scales this relationship, analogous to c_{elast} in the elastin SEF. Myogenic behaviour is implemented by means of a sigmoid-shaped scaling function (S_1, Eq. 8.A12). The location and dispersion of the curve are determined by parameters μ and σ, respectively.

Four additional model parameters, i.e., cross-sectional wall area (A_{w}), the zero-stress inner radius (R_{i}), the longitudinal stretch ratio (λ_z), and the opening angle (α) were used to fit the model to the "young" group data (Cowin and Humphrey 2001). Notably, we defined our opening angle from the center of the stress-free (cut open) configuration (Fig. 8.A1).

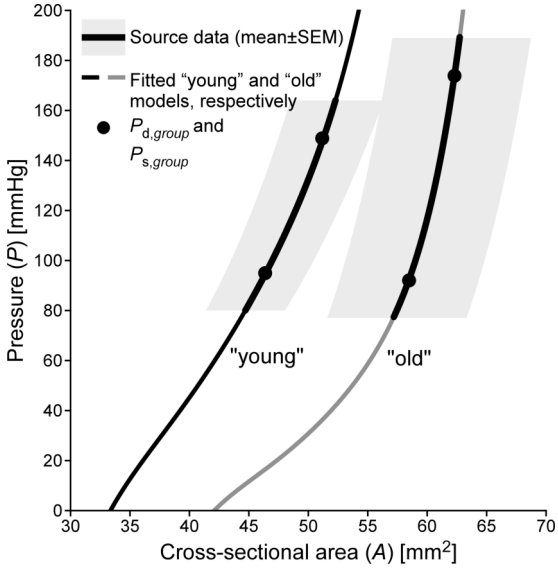

Figure 8.1: Resultant constitutive model curves (thin lines) based on measured age group-specific pressure-area (*P-A*) data (thick lines). Circles indicate diastolic ($P_{\mathrm{d,group}}$) and systolic ($P_{\mathrm{s,group}}$) pressures in both groups. Fitting considered a pressure range of $P_{\mathrm{d,group}} - 15\,\mathrm{mmHg}$ to $P_{\mathrm{s,group}} + 15\,\mathrm{mmHg}$. The "old" group curve shown was obtained by fitting the "young" constitutive model to the "old" *P-A* data under wall stress and axial force constraints (see Fig. 8.2B). Means ± SD in *A*-direction.

Age group data averaging for fitting

For each individual we fitted a single exponential (SE) function (Eq. 8.A3) to the measured *P-A* data, as further detailed in Appendix 8.A1. To obtain group averaged pressure-area relations for the "young" group (group="young", $n = 6$) as well as for the "old" group (group="old", $n = 7$), curves from individual SE models were averaged in *A*-direction:

$$A_{group}(P) = \frac{1}{n_{\mathrm{s}}} \sum_{j=1}^{n_{\mathrm{s}}} A_j(P) = \frac{1}{n_{\mathrm{s}}} \sum_{j=1}^{n_{\mathrm{s}}} \left[A_{\mathrm{d},j} \left(1 + \frac{1}{\gamma_j} \ln\left(\frac{P}{P_{\mathrm{d},j}} \right) \right) \right], \tag{8.1}$$

where n_{s} is the number of subjects in each group and j is the subject number. A_j is subject j's pressure-area relationship as given by the inverse of Eq. 8.A3.

For fitting purposes, we assumed that the group averaged SE models were valid for $P \in \left[P_{\mathrm{d},group} - 15\,\mathrm{mmHg},\, P_{\mathrm{s},group} + 15\,\mathrm{mmHg} \right]$, where $P_{\mathrm{d},group}$ and $P_{\mathrm{s},group}$ are the group-averaged diastolic and systolic pressures (Fig. 8.1). Fitting was performed using $r_{group} = \sqrt{\frac{A_{group}}{\pi}}$ instead of A_{group} for convenience.

Fit procedure

As the used echo tracking tool ($^{\mathrm{RF}}$QAS, Esaote Europe) considers the media-adventitia echoes of near and far walls, we assumed the measured r_{group} to reflect common carotid

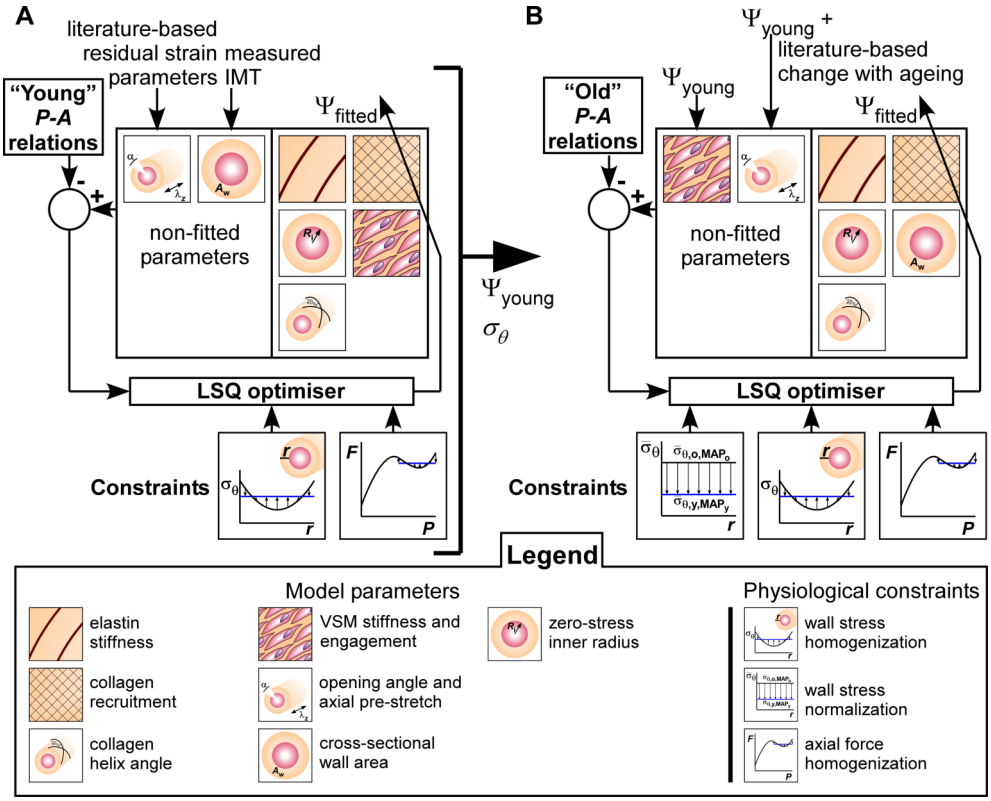

Figure 8.2: Block diagrams summarising the performed model fits on the *P-A* relations of the "young" (**A**) and "old" (**B**) patient groups. LSQ optimiser, nonlinear least-squares optimiser. A_w: cross-sectional wall area; λ_z: longitudinal stretch ratio; α: opening angle; R_i: zero stress inner radius, σ_θ: circumferential wall stress; $\bar{\sigma}_\theta$: average circumferential wall stress; $\sigma_{\theta,\mathrm{o,MAP_o}}$: "old" group average wall stress at mean arterial pressure (MAP); $\sigma_{\theta,\mathrm{y,MAP_y}}$: "young" group average wall stress at MAP; F: reduced axial force; IMT: intima-media thickness; VSM: vascular smooth muscle.

artery outer radius. Fitting was accomplished by varying model parameters (described below) while minimising the sum of squared differences between model and measurements (Fig. 8.2). The total sum of squares ($S_{\mathrm{S,t}}$) is the weighted sum of a radius term and one or two wall stress related terms, as explained below.

Circumferential wall stress was forced to be distributed homogeneously along each radial position of the wall at mean arterial pressure (MAP) (i.e., wall stress homogenisation), in both the "young" and "old" situations. MAP ($P_{\mathrm{m},group}$)) was defined as $P_{\mathrm{m},group} = 0.6P_{\mathrm{d},group} + 0.4P_{\mathrm{s},group}$. For the "old" group fits, average circumferential wall stress ($\sigma_{\theta,\mathrm{o,MAP_o}}$) at MAP could optionally be forced to remain at the "young" group level (i.e., wall stress normalisation).

The normalised radius sum of squares ($S_{\mathrm{S,r}}$) between measured (r_j) and modelled

($r_{\text{const},j}$) radii is given by

$$S_{\text{S},r} = \frac{1}{n_r}\frac{1}{r_{\text{y,d}}^2}\sum_{j=1}^{n_r}\left(r_{\text{const},j} - r_j\right)^2 , \tag{8.2}$$

with n_r the number of data points and $r_{\text{y,d}}$ the average diastolic radius for the "young" group.

Wall stress difference ($D_{\text{S},\sigma,n}$) is formulated as a squared difference between average wall stresses in "young" and "old" groups, both at their respective MAP:

$$D_{\text{S},\sigma,n} = \frac{1}{\bar{\sigma}_{\theta,\text{y,MAP}_\text{y}}^2}\left(\bar{\sigma}_{\theta,\text{o,MAP}_\text{o}} - \bar{\sigma}_{\theta,\text{y,MAP}_\text{y}}\right)^2 , \tag{8.3}$$

with $\bar{\sigma}_{\theta,\text{o,MAP}_\text{o}}$ the "old" group's average wall stress and $\bar{\sigma}_{\theta,\text{y,MAP}_\text{y}}$ the "young" group's average wall stress at MAP.

The degree of wall stress inhomogeneity is formulated as a sum of squares between local wall stress and the average wall stress:

$$S_{\text{S},\sigma,\text{h}} = \frac{1}{n_\text{e}}\frac{1}{\bar{\sigma}_{\theta,\text{MAP}}^2}\sum_{e=1}^{n_e}\left(\sigma_{\theta,\text{e,MAP}} - \bar{\sigma}_{\theta,\text{MAP}}\right)^2 , \tag{8.4}$$

with n_e the number of elements in which the wall is subdivided radially, $\sigma_{\theta,\text{e,MAP}}$ the local wall stress at MAP and $\bar{\sigma}_{\theta,\text{MAP}}$ the average wall stress at MAP.

Axial force was kept constant over the fitting pressure range via the degree of axial force inhomogeneity:

$$S_{\text{S},F} = \frac{1}{n_r}\frac{1}{F_{\text{target}}^2}\sum_{j=1}^{n_r}\left(F_j - F_{\text{target}}\right)^2 , \tag{8.5}$$

with F_j the reduced axial force at a given pressure (cf. Eq. 8.A23). Reduced axial force is clearly described by Holzapfel and Ogden (2010a) as the force applied in the axial direction additional to that generated by the pressure on the closed ends of the tube. For the "young" group, F_{target} was 0.5 N; a value based on a canine carotid artery (Patel et al. 1969). For the "old" group, F_{target} is defined as the mean F over the wall. In other words, in the young group, reduced axial force is forced to remain constant at 0.5 N over the fitting pressure range, whereas in the old group it is forced to remain constant, but at a non-fixed value.

The four sums of squares ($S_{\text{S,r}}$, $D_{\text{S},\sigma,n}$, $S_{\text{S},\sigma,\text{h}}$, and $S_{\text{S},F}$) are combined into the total sum of squares ($S_{\text{S},t}$) via

$$S_{\text{S},t} = w_r S_{\text{S},r} + w_{\sigma,\text{n}} D_{\text{S},\sigma,\text{n}} + w_{\sigma,\text{h}} S_{\text{S},\sigma,\text{h}} + w_F S_{\text{S},F} . \tag{8.6}$$

w_r, $w_{\sigma,\text{n}}$, $w_{\sigma,\text{h}}$, and w_F are dimensionless weighting parameters, as specified in Table 8.3. Fitting was performed using the trust-region-reflective algorithm, implemented in the MATLAB Optimization Toolbox function LSQNONLIN (MATLAB R2014b, The MathWorks Inc, Natick, Massachusetts, USA). Fitting was initiated from 100 random start points in the parameter space using the MATLAB Global Optimization Toolbox function MULTISTART.

Radius, wall stress, and axial force fit quality were assessed using their normalised mean squared errors:

$$E_r = 100\% \cdot \frac{1}{r_{\mathrm{y,d}}} \sqrt{\frac{1}{n_r} \sum_{j=1}^{n_r} \left(r_{\mathrm{const},j} - r_j\right)^2} = 100\% \cdot \sqrt{S_{\mathrm{S,r}}}\,, \tag{8.7}$$

$$E_{\sigma,\mathrm{n}} = 100\% \cdot \left| \frac{\bar{\sigma}_{\theta,\mathrm{o,MAP_o}} - \bar{\sigma}_{\theta,\mathrm{y,MAP_y}}}{\bar{\sigma}_{\theta,\mathrm{y,MAP_y}}} \right| = 100\% \cdot \sqrt{D_{\mathrm{S},\sigma,n}}\,, \tag{8.8}$$

$$E_{\sigma,\mathrm{h}} = 100\% \cdot \frac{1}{\bar{\sigma}_{\theta,\mathrm{MAP}}} \sqrt{\frac{1}{n_\mathrm{e}} \sum_{e=1}^{n_e} \left(\sigma_{\theta,\mathrm{e,MAP}} - \bar{\sigma}_{\theta,\mathrm{MAP}}\right)^2} = 100\% \cdot \sqrt{S_{\mathrm{S},\sigma,\mathrm{h}}}\,, \text{and} \tag{8.9}$$

$$E_F = 100\% \cdot \frac{1}{F_{\mathrm{target}}} \sqrt{\frac{1}{n_r} \sum_{j=1}^{n_r} \left(F_j - F_{\mathrm{target}}\right)^2} = 100\% \cdot \sqrt{S_{\mathrm{S},F}}\,. \tag{8.10}$$

Fitted model parameters

Constitutive model fitting was performed with various combinations of fixed and fitted parameters and constraints (Fig. 8.2 and Table 8.3). Fitting was first performed on the "young" pressure-area curve, yielding a take-off parameter set consisting of 8 parameters for subsequent fitting of the "old" *P-A* curve (Table 8.3).

Residual stretch related parameters (opening angle (α) and axial pre-stretch (λ_z)) were fixed in the "young" situation and estimated from literature. Opening angle and axial pre-stretch vary markedly along the vascular tree. In this study on the carotid artery, we chose to fix "young" opening angle to 100°, based on reported carotid artery opening angles of 110° (human, (14)) and 101.2° (non-human primates; Rhesus Macaques, Wang et al. 2014). We fixed our "young" pre-stretch to 1.20, based on Delfino et al. (1997) reporting $\lambda_z = 1.10$, and Wang et al. (2014) reporting $\lambda_z = 1.46$.

In the "old" model, wall stress normalisation was added as an additional constraint. Both the cross-sectional wall area and the zero-stress inner radius were fitted to yield the final formulation of the "old" pressure-area fitted model (Fig. 8.2B).

Arterial residual strain is known to change with age (Zulliger and Stergiopulos 2007). Zulliger and Stergiopulos (2007) derived population-based relations of aortic α and λ_z with age, based on data by Saini et al. (1995) Using these formulas, we calculated aortic opening angle and axial pre-stretch for our "young" ($\alpha = 373°$, $\lambda_z = 1.26$) and "old" group's ages ($\alpha = 407°$, $\lambda_z = 1.19$). Notably, these values are based on measurements of the aorta, and cannot be used directly when modelling the carotid artery. Therefore, subsequently, we calculated the percentage change with aging (α: +9%, λ_z: −6%), and imposed these percentage changes onto our "old" group fits.

To assess the consistency of our measurement and modelling approach, we repeated the fitting procedure using "young" and "old" data obtained under repeat, i.e., after anti-hypertensive treatment, conditions.

Statistical analyses

Statistical analyses were performed using MATLAB. Non-parametric Wilcoxon rank-sum tests were performed to evaluate statistical differences between patient groups. p-values ≤ 0.05 were considered statistically significant. Unless otherwise indicated, values are given as mean ± SD.

8.3 Results

8.3.1 Source data: Study population and pressure-area curves

Table 8.2 summarises "young" and "old" group characteristics. Both groups exhibit arterial hypertension at baseline. Age groups do not show statistical differences, except in age, PWV, and compliance coefficient. Both aortic and carotid PWV in the "old" group are increased with respect to the "young" group. However, pressures also differ between groups. Table 8.1 shows carotid PWV for predefined pressure ranges, thereby enabling BP-independent comparison of "young" and "old" carotid stiffness. As evident from this table, PWV increases with age and with BP independently.

Fig. 8.1 shows the *P-A* curves for the "young" and the "old" groups (thick lines). With respect to the "young" curve, the "old" curve is shifted to the right (higher cross-sectional area). Additionally, the "old" working range extends to higher pressures, effectively leading to a steeper effective *P-A* curve working area and therefore a stiffer vessel.

8.3.2 Constitutive modelling

"Young" *P-A* fitting results

Our model was fully able to describe the "young" *P-A* relationship (Table 8.3, "young" column). Fit errors were small (radial fit error $E_r = 2.8 \cdot 10^{-2}$%, wall stress homogenisation error $E_{\sigma,\mathrm{h}} = 0.34$%, and axial force error $E_F = 0.18$%; not shown). Note the difference in magnitude between those errors, which is caused by the difference in weighting of the radius and wall stress homogenization/axial force terms (Eq. 8.6). At MAP, elastin bears approximately 70% of the load, whereas collagen and VSM bear the remaining 5% and 25%, respectively. Average wall stress at MAP was 81 kPa, which is in line with physiological values (Carallo et al. 1999).

Preliminary "old" *P-A* fitting results

To investigate the performance of our constitutive modelling approach in describing aging, we assessed several combinations of parameter changes with respect to the "young" situation (not shown). Firstly, we tried to assess aging by varying only one component's parameters (i.e., only of elastin, only of collagen, or only of VSM) and not including the wall stress homogenisation constraint. Fitting was unsuccessful in all of these cases, leading to *P-A* curves that clearly deviated from the measured curves, with radial fit errors > 1.5%. We continued our study by varying the parameters of sets of two components, i.e., elastin and collagen; elastin and VSM; and collagen and VSM. Only the elastin-collagen combination yielded a successful fit. At this point, we decided to focus

Table 8.3: Relative changes in constituent parameters fitting "old" group pressure-area data with "young" group fit as take-off condition

Parameter [unit]	Fit range		"Young"	"Old"
	Lower	Upper		
Weighting				
w_r [-]			10	10
$w_{\sigma,\mathrm{n}}$ [-]			0	1
$w_{\sigma,\mathrm{h}}$ [-]			1	1
w_F [-]			1†	1
Parameter values				
Geometrical				
A_w [mm^2]	10	100	14.4	*+31%*
R_i [mm]	1	10	*4.0*	*+12%*
λ_z [-]			1.20	−6%
α [°]			100	+9%
Elastin				
c_elast [kPa]	5.0	400	*181*	*−14%*
Collagen				
k [-]	2.0	32.0	*6.7*	*0%*
b [-]	0.2	2.1	*0.4*	*−30%*
β_0 [°]	0	90	*40*	*−3%*
VSM				
c_VSM [kPa]	5	100	*77*	*
μ [-]	1	10.0	*3.2*	*
σ [-]	0.05	1.0	*0.14*	*
Mean arterial pressure (MAP)				
P_m [mmHg]			117	125
Wall loading at MAP				
Pressure load bearing				
P_elast [mmHg] (%)			82 (70%)	67 (54%)
P_coll [mmHg] (%)			5 (5%)	34 (28%)
P_VSM [mmHg] (%)			30 (25%)	23 (19%)
Collagen engagement				
Cumulative density function, %			0.58	3.5
Average wall stress				
$\bar{\sigma}$ [kPa]			81	81
Model wall thickness [mm]			0.63	0.75
Diastolic model wall thickness [mm]			0.65	0.76

Parameter percentages are 100% · ["old" fit value − "young" fit value] / ["young" fit value]. Residual strain related parameters (λ_z and α) were taken from literature for the young group, as were their changes with aging (see main text). Vascular smooth muscle (VSM) parameters were evaluated in initial fits and kept constant in the final analysis, because incorporation of vascular smooth muscle parameters would have led to overfitting. Parameter values and changes in italics were obtained by means of fitting. *Parameter was kept constant at the value of the "young" group. †In the "young" group, reduced axial force (F) was, in addition to being homogenised over the fitting pressure interval, kept at 0.5 N.

on using elastin-collagen changes in describing aging, and not to include any additional fitted parameters. The inclusion of additional (VSM) parameters would lead to an underdetermined problem (i.e., overfitting). As such, the resulting fit would be of little value.

"Old" *P-A* fitting results

As indicated, we focused on elastin and collagen as the two main structural substrates of arterial aging. We added the constraint of wall stress normalisation (i.e., requiring average wall stress in the "old" group to equal that in the "young" group), requiring both A_w and R_i to be included as fitting variables to yield a successful fit (Fig. 8.2B). Fitting results are given in Table 8.3 ("old"). Wall thickness showed a physiologically realistic increase from 0.65 to 0.76 mm (measured wall thicknesses: 0.65 and 0.79 mm). With aging, we observed a 14% reduction in elastin stiffness (c_{elast}), which, together with changes in collagen recruitment from 0.58 to 3.5%, caused load bearing to shift from elastin to collagen (elastin: from 70% to 54%, collagen: from 5% to 28%; Table 8.3).

Consistency of final model fitting results

The aforementioned results are based on *P-A* curves measured at baseline, with the patients on a less intensive anti-hypertensive regime (Spronck et al. 2015b). Though carotid arteries operated at clearly different operating points due to anti-hypertensive treatment in the repeat conditions, after 3.0 ± 0.6 months, we did not find significant *P-A* curve changes. Repeat measurement MAPs were 100 mmHg and 107 mmHg for "young" and "old", respectively (Table 8.A1), while corresponding baseline MAPs were 117 mmHg and 125 mmHg. We utilised these (apparently similar) *P-A* data under different hemodynamic conditions to check the consistency of our model outcomes. We obtained "young" and "old" model fits to the repeat data. Overall, results were similar to those obtained with the baseline data (Table 8.A1). Changes in A_w, R_i, and c_{elast} with aging were +27%, +11%, and −11%, respectively (as compared to +31%, +12%, and −14% at baseline; Table 8.3). Changes in collagen recruitment parameters k and b, however, were markedly different at −22% and −16% (as compared to 0% and −30%). The reader is referred to the Discussion section for further interpretation of these differences. In both "young" and "old" fits, at baseline and repeat, collagen fibre angle (β_0) remained within the range of $35-40°$, similar to Zulliger et al. 2004a.

Despite the difference in MAP between repeat and baseline, the age-related changes in wall loading were similar (for elastin, collagen, and VSM, respectively −16, +23 and −6 percent points at baseline and −15, +22, and −6 percent points at repeat; Table 8.3). Expectedly, collagen engagement in the "old" group at repeat (2.6%) was slightly lower than at the baseline visit (3.5%; Table 8.3), as was average wall stress ($\bar{\sigma}_{\theta,MAP}$) which was 68 kPa under repeat conditions as compared to 81 kPa at baseline.

8.4 Discussion

8.4.1 Key findings

In the present study, we used patient measurements to quantify age-related changes in carotid artery wall constituent properties and load bearing. Our model predicts that, from roughly the 5th into the 7th decade, a) elastin stiffness decreases, b) load bearing significantly shifts from elastin to collagen, and c) collagen recruitment increases considerably. Correspondingly, simulated diameter and wall thickness increased by about 20% and 17%, respectively. Due to the fitting regime, fitting the model's radius response to the measured radius response, the simulated diameter increase was equal to the measured increase. The increase in wall thickness compares reasonably well with a measured thickness increase of 21%. These geometrical changes were only consistent with patient data if wall stress regulation was considered in model fitting. Our quantitative findings remained consistent with those obtained based on repeated measurements in our patients, despite measurement noise and clear differences in blood pressure. Our findings are well in line with the existing aging paradigm and epidemiological findings and they do suggest that age-related changes in arterial wall structure can be understood and studied quantitatively, by integrating constitutive modelling and non-invasive patient data.

8.4.2 Previous findings from literature

The present study addresses key problems of previous clinically applied constitutive modelling studies. Contrary to Masson et al. (2011), who used 14 parameters for fitting, our findings with respect to aging are based on changes in only five model parameters. This significantly reduces the possible effects of overfitting. Our method uses clinically obtained, non-invasive data, and can therefore easily be applied in a broad context to quantitatively assess changes in arterial wall structure and function.

Our quantitative findings on the load shift from elastin to collagen are consistent with the classic paradigm as proposed by O'Rourke and Hashimoto (2007). They state that with aging the elastin sub-structure degrades due to wear, leading to a progressive transfer of mechanical load bearing to the collagen structure, which may be reinforced by increased cross-linking.

Comparing our findings regarding wall thickness with literature, the model-calculated wall thickness increase with aging from 41 yrs to 64 yrs (+0.11 mm) was comparable to the median increase in IMT for the same age range in the Reference Values for IMT Study (healthy sub-population; Table 8.3 in The Reference Values for Arterial Stiffness' Collaboration 2010; men: +0.131 mm, women: +0.124 mm).

With regard to vessel dilation, "young" and "old" group average vessel cross-sectional areas (50 and 60 mm^2; Fig. 8.1) roughly correspond to diameters of about 8.0 and 8.7 mm, respectively, supporting a near 10% increase in diameter. This compares well with the increase in proximal aortic diameter of about 13% from 23 mm at age 44 yrs to 26 mm at 64 yrs, as derived from data in post-mortem aortic specimens at 100 mmHg (Virmani et al. 1991). In our "old" fit, we forced wall stress to remain constant with age. We based this constraint on findings by Åstrand et al. (2011) and Matsumoto and Hayashi (1994). Åstrand et al. (2011) describe carotid wall stress to remain constant with age

in a human population. Matsumoto and Hayashi (1994) have shown that in rats, after inducing hypertension, wall remodelling is such that wall stress at in-situ blood pressure remains constant, a finding which was confirmed by Wolinsky (1972).

8.4.3 Influence of wall stress normalisation

Our "old" fit (Table 8.3) incorporates a wall stress normalisation constraint, i.e., we force average circumferential wall stress in the "old" situation to be equal to the "young" situation. Before we enforced this constraint, we tried fitting the "old" situation without wall stress normalisation, setting $w_{\sigma,\mathrm{n}} = 0$. The results are given in Table 8.A2. With $w_{\sigma,\mathrm{n}} = 0$, fitting is successful if either cross-sectional area (A_w) or zero-stress inner radius (R_i) is varied. Although these fits were successful with respect to their fit errors (E_r and $E_{\sigma,\mathrm{h}} < 1\%$ for both fits), these models showed non-physiological wall thickness changes. The fit in which A_w was fitted showed almost a doubling of wall thickness (diastolic wall thickness change from 0.65 to 1.13 mm). If R_i was fitted, wall thickness showed a decrease with age. The latter cannot be considered physiological. These results prompted us to add wall stress normalisation to our "old" fits, yielding the "old" fit in Table 8.3.

8.4.4 Influence of age-related changes in residual strain parameters

In our "old" fit (Table 8.3), we have chosen to change the residual strain parameters based on the relation of aortic residual strain parameters with age as described by Zulliger and Stergiopulos (2007) (see also Methods section). We assessed the influence of the age-related residual strain parameters by performing a number of additional fits. First, we fitted the "old" data while keeping λ_z and α at their "young" values (Table 8.A3, "old", $\lambda_z \leftrightarrow, \alpha \leftrightarrow$). In this case, age-related changes in load bearing are more pronounced than in the fit with changed λ_z and α (Table 8.3, "old"; Table 8.A3, "old", $\lambda_z \downarrow, \alpha \uparrow$). If only the increase of α is included (Table 8.A3, "old", $\lambda_z \leftrightarrow, \alpha \uparrow$), load bearing changes are even more pronounced. On the contrary, if only the decrease in λ_z is incorporated (Table 8.A3, "old", $\lambda_z \downarrow, \alpha \leftrightarrow$), a smaller shift in load bearing is required than in the case where both λ_z and α are varied. From the results in Table 8.A3, we conclude that the lowering of axial stretch with age "helps" in shifting the *P-A* curve from its young to its old shape.

8.4.5 Influence of age-related changes in vascular smooth muscle parameters

In our "old" fit (Table 8.3), we have chosen to keep VSM-related parameters constant to prevent overfitting. However, literature reports some changes in VSM with age. Hence, we evaluated the importance of these (potential) changes on our main findings.

One influential change in VSM that may occur with age, is that smooth muscle cells change their phenotype from contractile to synthetic (Lundberg and Crow 1999). Mechanically, this may translate into a smaller number of smooth muscle cells taking part in vasoconstriction, hypothetically leading to a smaller maximum contractive force. Some studies in rat aortas indeed confirm this decrease in maximum contractive force (Cohen and Berkowitz 1976; Tuttle 1966), whereas other studies in rat carotid artery show

no decrease in maximum contractive force (Duckles et al. 1985). In order to study the potential effect of a decrease in maximum contractive force on our aging findings, we assessed the effect of a 50% decrease in the c_{VSM} parameter with aging. Table 8.A4 ("old", $\lambda_z \downarrow, \alpha \uparrow, c_{\mathrm{VSM}} \downarrow$) shows that the 50% decrease in c_{VSM} removes the need for elastin de-stiffening. As expected, VSM load bearing in the "old" situation with reduced c_{VSM} is approximately halved when compared to the situation in which c_{VSM} is kept constant.

Another change in VSM that may occur with age is related to intrinsic, passive smooth muscle cell stiffness. Qiu et al. (2010) reported an increase in intrinsic smooth muscle cell stiffness of 223%, as measured by atomic force microscopy. This change may be linked to the aforementioned change to a more synthetic VSM phenotype with age. In order to study the effect of increased smooth muscle cell stiffness, we increased S_{basal} by a factor of 2, and assessed the influence on our aging findings. Table 8.A4 ("old", $\lambda_z \downarrow, \alpha \uparrow, S_{\mathrm{basal}} \uparrow$) shows that the effect of a decrease of S_{basal} on our findings is negligible, also with respect to the observed reproducibility (Table 8.A1). Overall, we conclude that the influence of age-related changes in VSM parameters on our constitutive finding (the shift to collagen load bearing) is relatively small, and that the error that we make by assuming constant VSM parameters with age is small.

8.4.6 Measurements, population

Our study setup was cross-sectional. Ideally, aging would be studied longitudinally. However, we found our stiffness–BP–age pattern (Table 8.1) to be strikingly similar to the findings in the Reference Values for Arterial Stiffness (The Reference Values for Arterial Stiffness' Collaboration 2010). This similarity indicates that the measured cross-sectional changes in *P-A* relationships do reflect normal aging. We based our results on a relatively small population ($n = 13$). Our study, however, did evaluate the reproducibility of our approach, based on repeated measurements in the same patient but under clinically significantly different blood pressure conditions.

We divided our study population into two, almost equally large, age groups by using an age cut-off value of 50 yrs. As evident from e.g., The Reference Values for Arterial Stiffness' Collaboration (2010) study, vascular stiffening with age is a gradual, progressive phenomenon. In this light, the use of an absolute age cut-off defining "young" and "old" is inappropriate. However, given our small population, is was not feasible to use multiple age groups, which would have caused an unacceptably large measurement uncertainty.

8.4.7 Constitutive modelling assumptions

The volume fractions of collagen, elastin, and VSM in the wall were taken from literature (Fridez et al. 2003; Zulliger et al. 2004a). Ideally, these values would be measured patient-specifically. However, using the non-invasive techniques we employed, this is not feasible. We did not fit these parameters since, in our formulation, this would lead to overfitting (see also section 8.4.8 below). For example, an increase in elastin content is mechanically indistinguishable from an increase in elastin stiffness. The same holds for the other components. Therefore, the decrease in elastin stiffness that we reported could (mechanically) also reflect a decrease in elastin content.

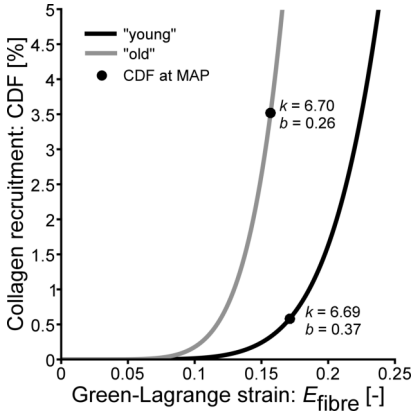

Figure 8.3: Log-logistic cumulative density function (CDF) describing the cumulative collagen engagement strain distribution of the constitutive model fitted to the "young" patient group and the "old" patient group. Circles indicate the percentage of collagen engaged for the Green-Lagrange strain (E_{fibre}) at MAP. k, b: log-logistic shape (k) and scale (b) parameters.

The mechanical response of each constituent was assumed to be hyperelastic and could therefore be described by a strain energy function (SEF). This approach neglects eventually present viscoelastic effects. Previously, we have shown that viscous behaviour and the associated hysteresis in *P-A* relationships of the carotid arterial wall is negligible *in vivo* when using a well-characterised measurement set-up (Boutouyrie et al. 1998; Hermeling et al. 2010).

Our collagen recruitment model requires some additional attention. Collagen was modelled to engage in load bearing with increased stretch. This engagement is characterised by a statistical probability density function (PDF) of the log-logistic type with a shape (k) and a scale (b) parameter. Collagen recruitment in our study, however, was (in absolute sense) very low at 0.5–3%. This means that the only part of the PDF used is a very small part of the upslope. A shift in upslope to a lower strain (as shown in Fig. 8.3 when comparing the "old" and "young" curves) can, to a large extent, be accomplished both by changing k and b. In other words, k and b are not independent parameters and are therefore not uniquely identified by parameter fitting. This explains the more inconsistent behaviour of k and b with the various fits.

In our fits, we have constrained circumferential wall stress to be homogeneous over the artery wall. This constraint is based on reports that incorporation of residual stresses in a constitutive model greatly reduces the transmural gradient in circumferential wall stress (Fung 1990; Lundberg and Crow 1999). We have assumed that there is a full transmural homogenisation. In reality, it can be questioned whether this state is reached in an artery at working pressure. In this light, it is important to realise that we assume all wall constituents to be homogeneously distributed in the wall. Under this assumption, and given the fact that a living artery "does not know its zero-stress state" (i.e., it has, during its life span, always been subjected to the blood pressure), it is quite likely that artery structure is such that all material contributes approximately equally to the total

circumferential wall stress (Fung 1990; Westerhof et al. 2010). In our opinion, assuming a non-homogeneous distribution of wall stress at working pressure, in a model with a homogeneous distribution of constituents, is therefore unrealistic.

As just mentioned, in our model, we assume all mechanical wall constituents to be homogeneously distributed in the wall. This means e.g., that there are no separate intimal, medial, and adventitial layers, and that elastin is not concentrated in layers. In a layered constitutive model (Cardamone et al. 2009; Holzapfel and Ogden 2010b), however, wall stress distribution at working pressure would not necessarily be uniform across the wall, and our assumption of wall stress homogenisation would be invalid.

Another related assumption is that the law of mixtures is obeyed in our model, which means that all wall components act mechanically in parallel. A consequence of this assumption is e.g., that VSM contraction unloads elastin and collagen. However, it is well possible that locally, matrix-attached smooth muscle cells load/stretch the matrix components. Modelling such effects requires highly complex models, which is beyond the scope of this paper.

8.4.8 Fitting approach

In nonlinear parameter fitting of (relatively) large numbers of parameters there are two important difficulties to consider, as clearly described by Stålhand et al. (2004). Firstly, there can be several local minima in the parameter space. A gradient-based algorithm (like the algorithm we used) can end in such a minimum, thereby overlooking the global minimum. We reduced this limitation of the fitting algorithm by running the algorithm from multiple start points ($n = 100$ in this study) and selecting the fitted parameter set corresponding to the lowest minimum found. Another alternative would be sampling the entire parameter space using a Monte Carlo approach, which has the disadvantage of being computationally very heavy. Secondly, a much more fundamental problem is that of overparameterisation, or overfitting. In that case, the sum of squares at the optimum changes very little with varying parameters, meaning there is not a single optimal parameter combination, but a range of optimal solutions for varying parameter combinations. In this case, the number of fitted model parameters needs to be reduced.

Our "young" parameter fit (varying 10 parameters) is susceptible to overfitting. However, it is not the absolute "young" parameter values that were of interest, but rather the changes in an aging hypothesis-based subset of these parameters. As described in the Results section, when one of the constituents' parameters were fixed, fitting was unsuccessful. This is a strong indication that the young-to-old fits were not overparameterised. As we found that the elastin-collagen combination yielded a successful fit, we decided not to include additional smooth muscle related parameters, which clearly would have led to overfitting.

8.4.9 Perspectives

Our study demonstrates that age-related changes in arterial wall structure can be understood and studied mechanistically at the quantitative level, by combining constitutive modelling and non-invasive clinical patient data. Our integrated methodology is potentially widely applicable in larger scale human studies into arterial wall remodelling. As

such, our approach could be of added value in mechanistic and clinical intervention studies. However, it should be stressed that, when patient specific assessment is considered, our approach explicitly will remain sensitive to measurement noise (as illustrated for our study in Fig. 8.1).

8.4.10 Conclusions

Our constitutive modelling approach suggests that the arterial elastic and geometric properties of older compared to younger hypertensive patients are directly linked to reduced elastin stiffness or content and advanced collagen engagement in the arterial wall, as well as to modulation of wall stress by vessel enlargement and wall thickening. We conclude that these findings could well explain the influence of aging in the stiffness-pressure-age pattern observed.

8.5 Acknowledgments

This study was supported by a Kootstra talent fellowship awarded to B. Spronck by Maastricht University and by grant Veni-STW10261 for K. Reesink from the Innovational Research Incentives Scheme of the Dutch Organisation for Scientific Research (NWO).

8.A1 Appendix: Pressure-area curve data acquisition and processing

The method of obtaining non-invasive pressure-area curves as summarised below is elaborated in Spronck et al. 2015b.

8.A1.1 Study population

The study was approved by the ethical committee of Maastricht University and conducted in accordance with the Declaration of Helsinki (updated Seoul 2008). All subjects provided written informed consent prior to participation. Subjects were recruited from patients referred to our outpatient hypertension clinic for a two-day clinical assessment. In most patients anti-hypertensive drugs were discontinued two weeks prior to the two-day clinical assessment. Participants underwent extensive arterial function and hemodynamic measurements (detailed below) at inclusion and at three-months (3.0±0.6 months) follow-up (repeat). Patients were managed according to European Society of Hypertension (ESH) guidelines (Mancia et al. 2013), and their treating physicians were blinded for (intermediate) study results. We identified $n = 13$ patients whose anti-hypertensive treatment led to a decrease in diastolic blood pressure of more than 7 mmHg, i.e., twice the a-posteriori observed BP measurement variability of 3.5 mmHg. In the present analysis we used the baseline and repeat *P-A* curves of these patients. We divided the group into a "young" group (age < 50 yrs, $n = 6$) and an "old" group (age > 50 yrs, $n = 7$). The baseline characteristics of both groups are shown in Table 8.2.

Table 8.A1: Reproducibility of findings based on repeat measurements

Parameter [unit]	Fit range		"Young" repeat	"Old" repeat
	Lower	Upper		
Weighting				
w_r [-]			10	10
$w_{\sigma,\mathrm{n}}$ [-]			0	1
$w_{\sigma,\mathrm{h}}$ [-]			1	1
w_F [-]			1†	1
Parameter values				
Geometrical				
A_w [mm^2]	10	100	14.2	*+27%*
R_i [mm]	1	10	*3.9*	*+11%*
λ_z [-]			1.20	−6%
α [°]			100	+9%
Elastin				
c_elast [kPa]	5.0	400	*169.7*	*−11%*
Collagen				
k [-]	2.0	32.0	*8.1*	*−22%*
b [-]	0.2	2.1	*0.3*	*−16%*
β_0 [°]	0	90	*35*	*+11%*
VSM				
c_VSM [kPa]	5	100	*33*	*
μ [-]	1	10.0	*3.2*	*
σ [-]	0.05	1.0	*0.06*	*
Mean arterial pressure (MAP)				
P_m [mmHg]			100	107
Wall loading at MAP				
Pressure load bearing				
P_elast [mmHg] (%)			79 (78%)	67 (63%)
P_coll [mmHg] (%)			3 (3%)	27 (25%)
P_VSM [mmHg] (%)			19 (19%)	13 (12%)
Collagen engagement				
Cumulative density function, %			0.34	2.6
Average wall stress				
$\bar{\sigma}$ [kPa]			68	68
Model wall thickness [mm]			0.64	0.74
Diastolic model wall thickness [mm]			0.65	0.75

This table shows the same data as Table 8.3 in the main text, except for the fact that "repeat" instead of "baseline" source data are used for fitting. Parameter percentages are 100% · ["old" fit value − "young" fit value] / ["young" fit value]. Residual strain related parameters (λ_z and α) were taken from literature for the young group, as were their changes with aging (see main text). Vascular smooth muscle (VSM) parameters were evaluated in initial fits and kept constant in the final analysis, because incorporation of vascular smooth muscle parameters would have led to overfitting. Parameter values and changes in italics were obtained by means of fitting. *Parameter was kept constant at the value of the "young" group. †In the "young" group, reduced axial force (F) was, in addition to being homogenised over the fitting pressure interval, kept at 0.5 N.

Table 8.A2: Necessity of wall stress normalisation with age

Parameter [unit]	Fit range		"Young"	"Old" $w_{\sigma,\mathrm{n}} = 0$, A_w ↻, R_i ↔	"Old" $w_{\sigma,\mathrm{n}} = 0$, A_w ↔, R_i ↻	"Old"
	Lower	Upper				
Weighting						
w_r [-]			10	10	10	10
$w_{\sigma,\mathrm{n}}$ [-]			0	0	0	1
$w_{\sigma,\mathrm{h}}$ [-]			1	1	1	1
w_F [-]			1†	1	1	1
Parameter values						
Geometrical						
A_w [mm^2]	10	100	14.4	*+85%*	*	*+31%*
R_i [mm]	1	10	*4.0*	*	*+18%*	*+12%*
λ_z [-]			1.20	−6%	−6%	−6%
α [°]			100	+9%	+9%	+9%
Elastin						
c_elast [kPa]	5.0	400	*181*	*−70%*	*+37%*	*−14%*
Collagen						
k [-]	2.0	32.0	*6.7*	*−42%*	*+23%*	*0%*
b [-]	0.2	2.1	*0.4*	*+13%*	*−40%*	*−30%*
β_0 [°]	0	90	*40*	*+4%*	*−6%*	*−3%*
VSM						
c_VSM [kPa]	5	100	*77*	*	*	*
μ [-]	1	10.0	*3.2*	*	*	*
σ [-]	0.05	1.0	*0.14*	*	*	*
Mean arterial pressure (MAP)						
P_m [mmHg]			117	125	125	125
Wall loading at MAP						
Pressure load bearing						
P_elast [mmHg] (%)			82 (70%)	38 (30%)	77 (62%)	67 (54%)
P_coll [mmHg] (%)			5 (5%)	50 (40%)	31 (25%)	34 (28%)
P_VSM [mmHg] (%)			30 (25%)	38 (30%)	17 (13%)	23 (19%)
Collagen engagement						
Cumulative density function [%]			0.58	2.2	5.2	3.5
Average wall stress						
$\bar{\sigma}$ [kPa]			81	49	115	81
Model wall thickness [mm]			0.63	1.11	0.56	0.75
Diastolic model wall thickness [mm]			0.65	1.13	0.57	0.76

"Young" and "Old" columns are reproduced from Table 8.3. Parameter percentages are 100% · ["old" fit value − "young" fit value] / ["young" fit value]. Residual strain related parameters (λ_z and α) were taken from literature for the young group, as were their changes with aging (see main text). Vascular smooth muscle (VSM) parameters were evaluated in initial fits and kept constant in the final analysis, because incorporation of vascular smooth muscle parameters would have led to overfitting. Parameter values and changes in italics were obtained by means of fitting. ↻ indicates a fitted parameter; ↔ indicates that the respective parameter is kept at its "young" value. *Parameter was kept constant at the value of the "young" group. †In the "young" group, reduced axial force (F) was, in addition to being homogenised over the fitting pressure interval, kept at 0.5 N. Parameter values and changes in italics were obtained by means of fitting.

Table 8.A3: Influence of age-related changes in residual strain parameters

Parameter [unit]	Fit range		"Young"	"Old" $\lambda_z \leftrightarrow$, $\alpha \leftrightarrow$	"Old" $\lambda_z \leftrightarrow$, $\alpha \uparrow$	"Old" $\lambda_z \downarrow$, $\alpha \leftrightarrow$	"Old" $\lambda_z \downarrow$, $\alpha \uparrow$
	Lower	Upper					
Weighting							
w_r [-]			10	10	10	10	10
$w_{\sigma,\mathrm{n}}$ [-]			0	1	1	1	1
$w_{\sigma,\mathrm{h}}$ [-]			1	1	1	1	1
w_F [-]			1†	1	1	1	1
Parameter values							
Geometrical							
A_w [mm^2]	10	100	14.4	*+31%*	*+31%*	*+31%*	*+31%*
R_i [mm]	1	10	*4.0*	*+13%*	*+15%*	*+10%*	*+12%*
λ_z [-]			1.20	*	*	−6%	−6%
α [°]			100	*	+9%	*	+9%
Elastin							
c_elast [kPa]	5.0	400	*181*	*−21%*	*−40%*	*+17%*	*−14%*
Collagen							
k [-]	2.0	32.0	*6.7*	*−22%*	*−17%*	*+7%*	*0%*
b [-]	0.2	2.1	*0.4*	*−28%*	*−23%*	*−38%*	*−30%*
β_0 [°]	0	90	*40*	*−13%*	*−10%*	*−7%*	*−3%*
VSM							
c_VSM [kPa]	5	100	*77*	*	*	*	*
μ [-]	1	10.0	*3.2*	*	*	*	*
σ [-]	0.05	1.0	*0.14*	*	*	*	*
Mean arterial pressure (MAP)							
P_m [mmHg]			117	125	125	125	125
Wall loading at MAP							
Pressure load bearing							
P_elast [mmHg] (%)			82 (70%)	56 (45%)	49 (39%)	78 (62%)	67 (54%)
P_coll [mmHg] (%)			5 (5%)	44 (35%)	46 (37%)	28 (23%)	34 (28%)
P_VSM [mmHg] (%)			30 (25%)	25 (20%)	30 (24%)	19 (15%)	23 (19%)
Collagen engagement							
Cumulative density function [%]			0.58	3.9	3.9	3.4	3.5
Average wall stress							
$\bar{\sigma}$ [kPa]			81	81	81	81	81
Model wall thickness [mm]			0.63	0.75	0.75	0.75	0.75
Diastolic model wall thickness [mm]			0.65	0.76	0.76	0.76	0.76

"Young" and "Old" $\lambda_z \downarrow$,$\alpha \uparrow$ columns are reproduced from Table 8.3. Parameter percentages are 100% · ["old" fit value − "young" fit value] / ["young" fit value]. Residual strain related parameters (λ_z and α) were taken from literature for the young group, as were their changes with aging (see main text). Vascular smooth muscle (VSM) parameters were evaluated in initial fits and kept constant in the final analysis, because incorporation of vascular smooth muscle parameters would have led to overfitting. $\lambda_z \downarrow$ indicates manual decrease of 6% in axial prestretch; $\alpha \uparrow$ indicates manual increase of 9% in opening angle; $\leftrightarrow$ indicates that the respective parameter is kept at its "young" value. Parameter values and changes in italics were obtained by means of fitting. *Parameter was kept constant at the value of the "young" group. †In the "young" group, reduced axial force (F) was, in addition to being homogenised over the fitting pressure interval, kept at 0.5 N.

Table 8.A4: Influence of potential age-related changes in vascular smooth muscle parameters

Parameter [unit]	Fit range		"Young"	"Old" $\lambda_z \downarrow$, $\alpha \uparrow$	"Old" $\lambda_z \downarrow$, $\alpha \uparrow$, $c_{\mathrm{VSM}} \downarrow$	"Old" $\lambda_z \downarrow$, $\alpha \uparrow$, $S_{\mathrm{basal}} \uparrow$
	Lower	Upper				
Weighting						
w_r [-]			10	10	10	10
$w_{\sigma,\mathrm{n}}$ [-]			0	1	1	1
$w_{\sigma,\mathrm{h}}$ [-]			1	1	1	1
w_F [-]			1†	1	1	1
Parameter values						
Geometrical						
A_{w} [mm^2]	10	100	14.4	*+31%*	*+31%*	*+31%*
R_{i} [mm]	1	10	*4.0*	*+12%*	*+12%*	*+12%*
λ_z [-]			1.20	−6%	−6%	−6%
α [°]			100	+9%	+9%	+9%
Elastin						
c_{elast} [kPa]	5.0	400	*181*	*−14%*	*+3%*	*−17%*
Collagen						
k [-]	2.0	32.0	*6.7*	*0%*	*+7%*	*+2%*
b [-]	0.2	2.1	*0.4*	*−30%*	*−32%*	*−31%*
β_0 [°]	0	90	*40*	*−3%*	*−6%*	*−3%*
VSM						
c_{VSM} [kPa]	5	100	*77*	*	−50%	*
μ [-]	1	10.0	*3.2*	*	*	*
σ [-]	0.05	1.0	*0.14*	*	*	*
Mean arterial pressure (MAP)						
P_{m} [mmHg]			117	125	125	125
Wall loading at MAP						
Pressure load bearing						
P_{elast} [mmHg] (%)			82 (70%)	67 (54%)	80 (64%)	65 (52%)
P_{coll} [mmHg] (%)			5 (5%)	34 (28%)	33 (27%)	35 (28%)
P_{VSM} [mmHg] (%)			30 (25%)	23 (19%)	12 (9%)	25 (20%)
Collagen engagement						
Cumulative density function, %			0.58	3.5	3.5	3.6
Average wall stress						
$\bar{\sigma}$ [kPa]			81	81	81	81
Model wall thickness [mm]			0.63	0.75	0.75	0.75
Diastolic model wall thickness [mm]			0.65	0.76	0.76	0.76

"Young" and "Old" $\lambda_z \downarrow$,$\alpha \uparrow$ columns are reproduced from Table 8.3. Parameter percentages are 100% · ["old" fit value − "young" fit value] / ["young" fit value]. Residual strain related parameters (λ_z and α) were taken from literature for the young group, as were their changes with aging (see main text). Parameter values and changes in italics were obtained by means of fitting. *Parameter was kept constant at the value of the "young" group. †In the "young" group, reduced axial force (F) was, in addition to being homogenised over the fitting pressure interval, kept at 0.5 N. $\lambda_z \downarrow$ indicates manual decrease of 6% in axial prestretch; $\alpha \uparrow$ indicates manual increase of 9% in opening angle; $\leftrightarrow$ indicates that the respective parameter is kept at its young value; $S_{\mathrm{basal}} \uparrow$ indicates manual increase of vascular smooth muscle (VSM) basal tone parameter (S_{basal}) by a factor of 2; $c_{\mathrm{VSM}} \downarrow$ indicates manual decrease in maximum VSM contraction parameter (c_{VSM}) by a factor of 2.

8.A1.2 Measurements

Arterial function measurements (total duration 30–45 min) were performed in a quiet room (22 °) after a resting period of 15 min with subjects in supine position. Throughout the session four to eight repeated oscillometric BP readings were obtained at the left upper arm (Omron 705IT, Omron Healthcare Europe B.V., Hoofddorp, The Netherlands). Additionally, continuous pulsatile finger BP, heart rate (HR) and an estimated cardiac output (CO), were obtained by the Peñáz method (Peñáz 1973) from the right middle finger (Nexfin, BMEYE B.V., Amsterdam, The Netherlands).

Left common carotid artery diameter waveforms were obtained using a 7.5 MHz vascular ultrasound scanner (MyLab70, Esaote Europe, Maastricht, the Netherlands) operated at high frame rate as previously described (Hermeling et al. 2012b). Diastolic diameter and distension values over 6 consecutive heartbeats and a real-time distension waveform display were used to judge quality of the recordings (^{RF}QAS utility, Esaote Europe). Subsequently, left common carotid and right femoral artery tonometric pressure waveforms were obtained to assess carotid-femoral transit time (SphygmoCor, AtCor Medical, Sydney, NSW, Australia). For the calculation of aortic PWV (v_{ao}, defined as ([carotid-femoral distance])/(transit time)), carotid-femoral distance was determined as sternal notch-to-femoral distance (distance as the crow flies, not over body surface) minus sternal notch-to-carotid distance as obtained by tape measure. Baseline distance was assumed at repeat to assess changes in v_{ao} after three months. Raw carotid artery tonometry waveforms were used to obtain calibrated local left common carotid artery BP waveforms (Van Bortel et al. 2001). Further processing was performed using proprietary MATLAB code (MATLAB R2013b, The MathWorks Inc, Natick, Massachusetts, USA). Carotid ultrasound and arterial tonometry measurements were obtained in triplicate by a single experienced operator (JOR).

8.A1.3 Waveform analysis and data processing

To enable quantitative assessment of the curvilinearity of the carotid artery pressure-area relation at individual subject level, we followed procedures similar to those described in (Hermeling et al. 2010). Briefly, systolic (peak), dicrotic notch and diastolic (minimum) points were identified in the diameter (by manual cursor reading, using ^{RF}QAS) and pressure (automatic) waveforms. For diameter typically 9–12 and for pressure 18–30 heartbeats were included for each subject in each session.

Diastolic diameter was averaged over beats as recording mean and over recordings as session mean. Relative cyclic diameter variations (i.e., ([systolic-diastolic])/diastolic) were averaged, rather than systolic diameters to avoid common noise. Accordingly, the relative amplitude of the dicrotic notch point (i.e., ([notch-diastolic])/([systolic-diastolic])) was averaged for further analysis, rather than absolute dicrotic notch values. For carotid systolic, notch and diastolic BP values the exact same scheme was applied. Median averaging was used throughout.

8.A1.4 Carotid linear stiffness and compliance calculations

Carotid cross-sectional area (A) values were calculated assuming circular cross-section, using $A = \pi\left(\frac{\text{diameter}}{2}\right)^2$, resulting in diastolic (A_d), notch (A_n) and systolic (A_s) cross-sectional areas. Local, linear carotid PWVs (v_car) were calculated using the Bramwell-Hill relationship (Bramwell and Hill 1922a):

$$v_\text{car} = \sqrt{\frac{1}{\rho_\text{b}} \frac{P_\text{s} - P_\text{d}}{A_\text{s} - A_\text{d}} A_\text{d}} \,, \tag{8.A1}$$

with $\rho_\text{b} = 1.050\text{kg/L}$ the blood mass density, and P_s and P_d the calibrated local systolic and diastolic carotid blood pressures. Accordingly, compliance coefficients (C) were calculated as

$$C = \frac{A_\text{s} - A_\text{d}}{P_\text{s} - P_\text{d}} \,. \tag{8.A2}$$

Pressure-area curve description

In each individual and session, the three (diastolic, notch and systolic) P-A points obtained were used to fit an established mathematical description of the P-A relation, i.e., a single-exponential (SE) curve (Meinders and Hoeks 2004):

$$P(A) = P_\text{d} e^{\gamma\left(\frac{A}{A_\text{d}} - 1\right)} \,. \tag{8.A3}$$

γ is obtained by minimising the sum-of-squares of differences between measured and curve notch and systolic pressures. As a line with one free parameter (γ) is fitted through two points, the line will, in general, not pass exactly through these two points.

8.A1.5 Intima-media thickness processing

Carotid ultrasound recordings were used to estimate intima-media thickness (IMT) as described previously (Hoeks et al. 1997; Van Bortel et al. 2001; Willekes et al. 1999). IMTs at diastolic blood pressure for all 19 ultrasound lines were averaged by taking the arithmetic mean for each acquisition. Subsequently, the median IMT of all acquisitions was calculated, resulting in one measured subject IMT. A group-averaged IMT was calculated by averaging (arithmetic mean) the IMTs of all subjects in one group.

8.A2 Appendix: Constitutive modelling

8.A2.1 Model assumptions

The influence of various material parameters on the pressure-area relation reconstructed by the model can give more insight into the influence of those parameters on the mechanical characteristics of the arterial wall. Throughout this study, it was assumed that the load-bearing components of an artery are elastin, collagen and VSM.

The human carotid artery was considered to be an incompressible, anisotropic thick-walled cylindrical tube (Holzapfel and Ogden 2010a). The elastic mechanical properties of separate elastic components of the arterial wall are expressed in terms of strain energy functions (SEFs), based on deformation gradients (Holzapfel and Ogden 2010a). Additionally, a pseudo-SEF is used to describe VSM mechanics (Zulliger et al. 2004b).

8.A2.2 Strain energy functions

We based our analysis on SEFs, expressed in a cylindrical coordinate system (e_r, e_θ, e_z), describing the passive and active mechanical behaviour of the arterial wall. Zulliger et al. propose SEFs that distinguish isotropic and orthotropic contributions representing respectively elastin and collagen (Zulliger et al. 2004a; Zulliger et al. 2004b).

Elastin

Elastin has been observed as a non-linear elastic material resulting in a convex SEF for increasing elastin fibre stretch (Milnor 1989; Zulliger et al. 2004a):

$$W_{\text{elast}} = c_{\text{elast}} \left(I_1 - 3\right)^{\frac{3}{2}} \ , \tag{8.A4}$$

in which c_{elast} is the elastin elastic modulus, $I_1 = 2E_r + 2E_\theta + 2E_z + 3$ is the first invariant of the Green-Lagrange strain tensor, which, via $E_i = \frac{1}{2}\left(\lambda_i^2 - 1\right), i \in \{r, \theta, z\}$ is coupled to the three principal stretch ratios λ_i.

Collagen

Collagen was assumed to be oriented in two symmetrical helices with angle $\pm\beta_0$ with respect to the circumferential direction. At low stretch values, collagen fibres appear to be in a wavy or coiled configuration in which case these fibres do not participate in load bearing (Clark and Glagov 1985). It is assumed that the engagement of collagen fibres when stretched is distributed in some statistical manner (Zulliger et al. 2004b). Zulliger et al. propose a log-logistic distribution (ρ_{fibre}) to describe the statistical distribution of the circumferential strain E_θ at which collagen starts bearing load. Following the method proposed by Zulliger et al., we have chosen the log-logistic probability density function to describe the engagement of collagen.

The engagement stretch probability density function (PDF) of collagen ρ_{fibre} is a piecewise function dependent on the Green-Lagrange strain in fibre direction (E_{fibre}):

$$\rho_{\text{fibre}} = \begin{cases} 0, & E_{\text{fibre}} \leq E_0 \\ \frac{b^k \cdot k \cdot (E_{\text{fibre}} - E_0)^{k-1}}{\left[b^k + (E_{\text{fibre}} - E_0)^k\right]^2}, & E_{\text{fibre}} > E_0 \end{cases} \ , \tag{8.A5}$$

where $b > 0$ is a scaling parameter which, for increasing values, shifts the PDF to the right, causing collagen to engage at higher strains (Tsamis and Stergiopulos 2007). At the same time, PDF height decreases and variance increases. Parameter k>0 is a shape parameter which, for increasing values, results in a higher maximum and a narrower distribution,

thus causing collagen to engage more abruptly (Tsamis and Stergiopulos 2007). E_{fibre} can be obtained from λ_{fibre} via

$$E_{\text{fibre}} = \frac{1}{2}\left(\lambda_{\text{fibre}}^2 - 1\right) \text{, with} \tag{8.A6}$$

$$\lambda_{\text{fibre}}^2 = \cos^2\beta_0\lambda_\theta^2 + \sin^2\beta_0\lambda_z^2 \,. \tag{8.A7}$$

Note that due to symmetry, E_{fibre} is equal for both collagen fibre families. The log-logistic PDF has a lower bound at value E_0, the Green-Lagrange strain at which collagen starts to change from a wavy configuration towards a straightened load-bearing configuration. Under the assumption that collagen is unable to withstand compressive forces, we set $E_0 = 0$.

In order to model collagen, we distinguish between the mechanical behaviour of a single collagen fibre and the mechanical behaviour of the ensemble of fibres. For a single collagen fibre, an SEF is proposed (Zulliger et al. 2004b):

$$W_{\text{fibre}} = \begin{cases} 0, & E_{\text{fibre}} \leq 0 \\ \frac{1}{2}c_{\text{coll}}E_{\text{fibre}}^2, & E_{\text{fibre}} > 0 \end{cases} \,, \tag{8.A8}$$

where c_{coll} is the collagen fibre elastic modulus and E_θ is the Green-Lagrange strain tensor in the fibre direction.

The collagen ensemble SEF for one fibre family (at either $+\beta_0$ or $-\beta_0$) is now obtained by convolving ρ_{fibre} and W_{fibre}:

$$W_{\text{coll}}(E_{\text{fibre}}) = \int_{-\infty}^{+\infty} W_{\text{fibre}}(x)\cdot\rho_{\text{fibre}}(E_{\text{fibre}} - x)\cdot \mathrm{d}x \,. \tag{8.A9}$$

Vascular smooth muscle

In this study, we assumed that VSM is orientated in circumferential direction (Hahn and Schwartz 2009; Matsumoto and Hayashi 1996). Zulliger et al. propose an SEF for VSM in which for fully contracted VSM a stress-strain relationship with Cauchy stress linear in stretch ratio $\lambda_\theta^{\text{VSM}}$ results. The SEF describing the mechanical behaviour of VSM is proposed as follows:

$$W_{\text{VSM}} = c_{\text{VSM}}\left[\lambda_\theta^{\text{VSM}} - \log(\lambda_\theta^{\text{VSM}}) - 1\right] \,, \tag{8.A10}$$

where c_{VSM} is the VSM elastic modulus and $\lambda_\theta^{\text{VSM}}$ is the stretch ratio of VSM. Following Zulliger et al.,

$$\lambda_\theta^{\text{VSM}} = \lambda_\theta\lambda_{\text{pre}} \,, \tag{8.A11}$$

with $\lambda_{\text{pre}} = \frac{L_{\text{r}}}{L_{\text{c}}} > 1$, accounting for the assumption that the length L_{c} of fully contracted VSM in the unpressurised state is shorter than the passive arterial components L_{r}. Following Zulliger et al., λ_{pre} is set to 1.83.

The contribution of VSM to wall mechanics is scaled by two functions, S_1 and S_2. S_1 implements strain-induced contractile behaviour by varying VSM tone with deformation of the arterial wall (Baek and Kim 2011; Zulliger et al. 2004b):

$$S_1 = S_{\text{basal}} + (1 - S_{\text{basal}})\frac{1}{2}\left[1 + \text{Erf}\frac{Q-\mu}{\sqrt{2}\sigma}\right] \,, \tag{8.A12}$$

where Erf is the error function and $S_{\text{basal}} \in [0,1]$ is the basal muscle tone. Q is a deformation which, following Zulliger et al., is set to $Q = I_1$, implying that VSM tone is isotropically dependent on stretching of the arterial wall (Seow 2000; Zulliger et al. 2002). σ is the half-width of the VSM tone distribution and μ is the mean VSM engagement deformation threshold. In case the artery is not deformed ($Q = 0$), basal tone (S_{basal}) remains (Bevan and Laher 1991; Zulliger et al. 2004b). In this study, S_{basal} was set to 0.052.

S_2 assures that the modelled VSM only exerts force between certain stretch limits (Zulliger et al. 2004b). Outside these bounds, VSM does not participate in load bearing:

$$S_2 = \begin{cases} 1, & 0.680 < \frac{\lambda_\theta^{\text{VSM}}}{\lambda_{\text{pre}}} < 1.505 \\ 0, & \text{otherwise} \end{cases} . \tag{8.A13}$$

Overall constitutive relationship

The three aforementioned SEFs are combined into a relation describing the local Cauchy stress for all three ($i \in \{r, \theta, z\}$ principal directions:

$$\sigma_i = -P_{\text{l}} + f_{\text{elast}} \lambda_i^2 \frac{\partial W_{\text{elast}}}{\partial E_i} + f_{\text{coll}} \lambda_i^2 \frac{1}{2} \sum_{i_{\text{f}}=1}^{2} \frac{\partial W_{\text{coll},i_{\text{f}}}}{\partial E_i} + S_1 S_2 f_{\text{VSM}} \left(\lambda_i^{\text{VSM}}\right)^2 \frac{\partial W_{\text{VSM}}}{\partial E_i^{\text{VSM}}} , \tag{8.A14}$$

with P_{l} the local hydrostatic pressure within the wall and $W_{\text{coll},i_{\text{f}}}$ the collagen SEF of fibre family i_{f}, with $i_{\text{f}} \in \{1,2\}$. Note that each component is multiplied by its respective volume fraction f_{elast}, f_{coll} and f_{VSM}. This leads to the following expressions for σ_r, σ_θ, and σ_z:

$$\sigma_r = -P_{\text{l}} + 3 f_{\text{elast}} \lambda_r^2 c_{\text{elast}} \sqrt{I_1 - 3} , \tag{8.A15}$$

$$\sigma_\theta = -P_{\text{l}} + 3 f_{\text{elast}} \lambda_\theta^2 c_{\text{elast}} \sqrt{I_1 - 3} + f_{\text{coll}} \frac{\lambda_\theta^2}{\lambda_{\text{fibre}}^2} \cos^2 \beta_0 \tau_{\text{fibre}} + f_{\text{VSM}} c_{\text{VSM}} S_1 S_2 \left(\lambda_\theta^{\text{VSM}} - 1\right) , \tag{8.A16}$$

$$\sigma_z = -P_{\text{l}} + 3 f_{\text{elast}} \lambda_z^2 c_{\text{elast}} \sqrt{I_1 - 3} + f_{\text{coll}} \frac{\lambda_z^2}{\lambda_{\text{fibre}}^2} \sin^2 \beta_0 \tau_{\text{fibre}} , \tag{8.A17}$$

with

$$\tau_{\text{fibre}} = \lambda_{\text{fibre}}^2 \frac{\mathrm{d}W_{\text{coll}}}{\mathrm{d}E_{\text{fibre}}} . \tag{8.A18}$$

Implementation

We distinguish four configurations of an artery (Fig. 8.A1): Ω_0 is the unstressed, opened, stress-free configuration. Ω_1 is the closed configuration, Ω_2 is the closed, pre-stretched configuration and Ω is the closed, pre-stretched and pressurised configuration.

Taking into account the incompressibility of the tissue, relations between deformed coordinates (r, θ, z) in Ω and reference coordinates (R,Θ,Z) in Ω_0 are given by:

$$r = \sqrt{r_{\text{o}}^2 - \frac{R_{\text{o}}^2 - R^2}{\lambda_z k_\alpha}} , \theta = k_\alpha \Theta , z = \frac{l}{L} Z , \tag{8.A19}$$

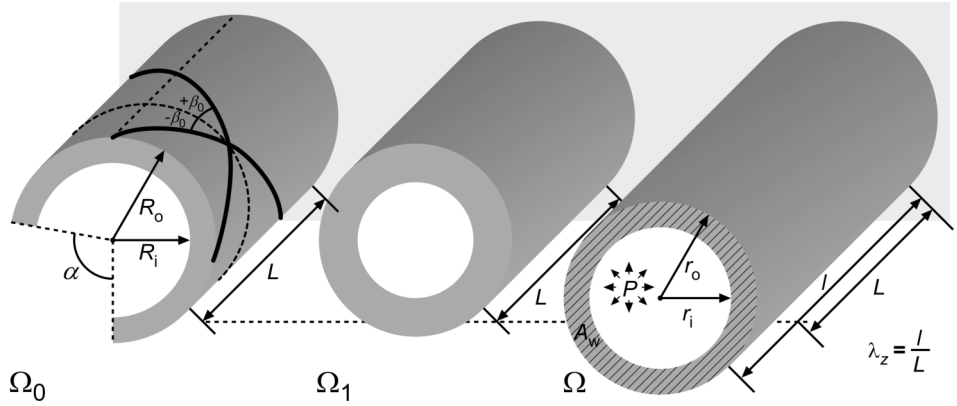

Figure 8.A1: Definitions of configurations. Ω_0: unstressed, opened, stress-free configuration with opening angle α, collagen fibre angle β_0, and inner and outer radii R_i and R_o, respectively. Ω_1: closed configuration. Ω: closed, prestretched and pressurised situation with cross-sectional wall A_w, luminal pressure P, and inner and outer radii r_i and r_o, respectively. Axial prestretch λ_z is defined as the quotient of unstretched (L) and stretched (l) lengths. Ω_2 (not depicted) can be obtained from Ω for $P = 0$. Note that in this study, α is defined from the center of the stress-free vessel, and that A_w is defined in Ω.

where R_o and r_o are the outer radii in Ω_0 and Ω, respectively, k_α is a parameter relating to the opening angle (α) via $k_\alpha = \frac{2\pi}{2\pi-\alpha}$, and L and l are the lengths of the vessel in Ω_0 and Ω, respectively. Note the definitions of α and A_w in our study (Fig. 8.A1), which may differ from other papers. The principal stretch ratios (λ_r,λ_θ,λ_z) with respect to the opened configuration are

$$\lambda_r = \frac{R}{r k_\alpha \lambda_z} \, , \, \lambda_\theta = \frac{k_\alpha r}{R} \, , \, \lambda_z = \frac{l}{L} \, . \tag{8.A20}$$

For the internal (r_i) and external artery radius (r_o) in Ω, we can write:

$$r_\mathrm{i} = \frac{\lambda_\theta R_\mathrm{i}}{k_\alpha} \, , \, r_\mathrm{o} = \sqrt{\frac{A_\mathrm{w}}{\pi} + r_\mathrm{i}^2} \, , \tag{8.A21}$$

where A_w is the cross-sectional area of the arterial wall and R_i is the zero-stress inner radius in Ω_0. The pressure within the lumen of the artery is finally obtained by solving the balance equation:

$$P = \int_{r_\mathrm{i}}^{r_\mathrm{o}} \frac{\sigma_\theta - \sigma_r}{r} \mathrm{d}r \, . \tag{8.A22}$$

Reduced axial force is found by solving

$$F = \pi \int_{r_\mathrm{i}}^{r_\mathrm{o}} (2\sigma_z - \sigma_r - \sigma_\theta) \, r \mathrm{d}r \, . \tag{8.A23}$$

Fixed model parameters

Fitted model parameters are described in the Methods section. Fixed model parameters are described here. Collagen stiffness, c_{coll}, was prescribed at all simulations to be 200 MPa, which is in the range of values found in literature (Langewouters 1982; Silver et al. 2003).

Area fractions f_{elast}, f_{coll}, f_{VSM} were taken as published by Fridez et al. (2003) for rat aorta and were respectively 0.306, 0.203 and 0.491 (Zulliger et al. 2004a).

Chapter 9

Non-invasive biaxial characterisation of carotid artery wall mechanics

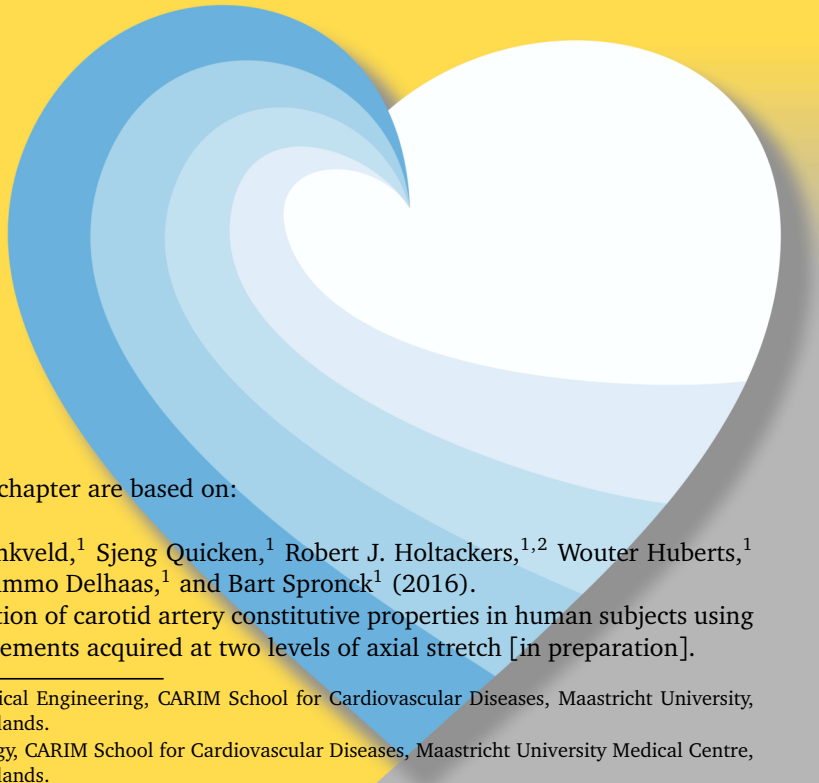

The contents of this chapter are based on:

Maarten H.G. Heusinkveld,[1] Sjeng Quicken,[1] Robert J. Holtackers,[1,2] Wouter Huberts,[1] Koen D. Reesink,[1] Tammo Delhaas,[1] and Bart Spronck[1] (2016).
Non-invasive estimation of carotid artery constitutive properties in human subjects using distensibility measurements acquired at two levels of axial stretch [in preparation].

[1] Department of Biomedical Engineering, CARIM School for Cardiovascular Diseases, Maastricht University, Maastricht, The Netherlands.
[2] Department of Radiology, CARIM School for Cardiovascular Diseases, Maastricht University Medical Centre, Maastricht, The Netherlands.

Abstract

Models describing arterial mechanics at the microstructural level (i.e., the elastin-collagen matrix), could be important in understanding and predicting the effects of drugs targeting specific wall structures when treating hypertension. Behaviour of wall constituents can be estimated *in vivo* by fitting a constitutive model to carotid artery pressure and diameter data. Although potentially valuable, non-invasive estimation of constitutive parameters remains cumbersome given the scarcity of clinically-measurable data available for model fitting. In this study, we aimed to investigate whether we could improve constitutive parameter estimation by increasing the amount of measurable mechanical information. We used a clinically feasible method to acquire distensibility data at two levels of axial stretch. Using MRI, the increase in axial stretch was estimated. Measurement noise was added to group-averaged distensibility data, creating a large virtual data set, used for parameter estimation. We found spread of the parameter representing collagen stiffness to be reduced by 43% in case the model was fitted to the full distensibility data set containing data from both levels of axial stretch, instead of one. Uncertainty in the parameter representing elastin stiffness remained equal when adding more distensibility data. Sensitivity analysis revealed that in further reducing the uncertainty of estimated constitutive parameters, it is most beneficial to increase the precision of ultrasound-based measurements of arterial diameter, distension and wall thickness. We conclude that distensibility measurements acquired at two levels of carotid artery stretch could be valuable for more accurate estimation of carotid artery wall properties.

9.1 Introduction

ARTERIAL stiffening is a major complication in hypertension and vice versa (Humphrey et al. 2016). Treatment options for arterial stiffening can roughly be divided into two categories (Townsend et al. 2015): 1) drugs that lower blood pressure, and thereby reverse the arterial remodelling that occurred due to hypertension, and 2) drugs that directly target one of the arterial wall components. The latter category includes cross-link breaking drugs that target the arterial collagen (Kass et al. 2001; Wolffenbuttel et al. 1998), but also matrix metalloproteinase (MMP) inhibitors that are thought to inhibit elastin fragmentation (Sun 2015; Wang et al. 2012).

In vivo assessment of the performance of these drugs is limited. Arterial stiffness is typically assessed by measuring carotid-femoral pulse wave velocity, or by local assessment of distensibility. However, such arterial stiffness measurement does not yield insight into the effect of a drug on the individual wall components.

A potential solution to this problem lies in the use of constitutive computer models of the artery wall (Holzapfel and Ogden 2010a). Such models explicitly incorporate elastin and collagen mechanical behaviour. If these models could be parameterised using non-invasive measurement data obtained through stiffness measurements, they could be used to obtain stiffness information of the individual wall components.

Several studies have attempted to use *in vivo* data to parameterise constitutive models of the arterial wall. An overview of these studies is given in Spronck et al. 2015a. Typically, pressure and diameter measurements at the carotid artery are used to fit such models. A major drawback is that the amount of measurement information that is available through *in vivo* measurements is limited. This hampers the unique identification of model parameters (Ogden et al. 2004). Therefore, any method to "extract" more mechanical information from the arterial wall would significantly benefit the non-invasive characterisation of arterial mechanics.

In *in vitro* testing set-ups found in the laboratory, arteries are commonly examined at multiple axial stretch states, improving model fitting and uniqueness of model parameters (Hayashi et al. 1980; Takamizawa and Hayashi 1987; Zulliger et al. 2004a; Zulliger et al. 2004b). If such a methodology would be applicable to *in vivo* measurements without harming the patient, it could well improve the *in vivo* characterisation of arterial mechanics.

In the present study, we propose a method to assess *in vivo* carotid artery mechanics at two distinct states of axial stretch. This was accomplished by performing supine measurements while subjects held their head 1: 1) in a normal orientation, facing forwards; and 2) in a rotated orientation, facing sidewards and upwards. In both positions, carotid artery diameter and distension were recorded; blood pressure was monitored throughout the experiment. Intima-media thickness (IMT) was recorded in the normal orientation. Additionally, the change in carotid artery length due to the change in orientation was estimated using magnetic resonance imaging (MRI). Measurement results were reported previously by Holtackers et al. (2016). A constitutive model was fitted to these results, directly incorporating information from the two states of axial stretch, yielding a method for *in vivo* biaxial assessment of the carotid artery.

To assess the robustness of our approach, we performed uncertainty quantification. This technique gives insight into how the uncertainty (noise) in measured variables affects the fitted constitutive model parameters. In addition, a sensitivity analysis was performed. This sensitivity analysis reveals how noise in the *individual* measured variables propagates into uncertainty in the constitutive model parameters. Sensitivity analysis thus yields a discrimination between variables that negligibly influence variance in estimated constitutive parameters, and variables that do influence this variance. In improving an overall measurement protocol, reducing measurement error of the influential measurements will benefit constitutive parameter quantification most (Saltelli et al. 2004).

9.2 Methods

9.2.1 Outline of approach

The approach outlined in this section is structured as follows (see also Fig. 9.1):

- **Measurements**. Carotid artery diameter, distension, intima-media thickness, blood pressure and rotation-induced extra axial stretch were measured in 12 subjects with their head in 1) a normal and 2) a rotated orientation (Holtackers et al. 2016).
- **Generation of data set for constitutive modelling**. By averaging among subjects, group-averaged measured variables were obtained for each orientation. Group-

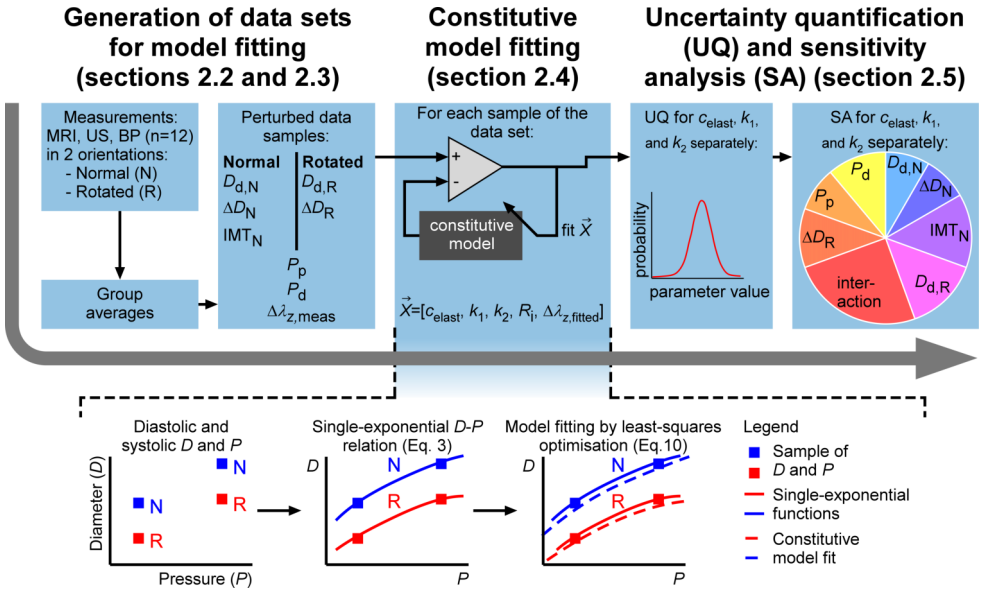

Figure 9.1: Outline of the current study (see text for details). D_d, diastolic diameter; ΔD, distension; P_d and P_p, diastolic and pulse pressure, respectively; $\Delta\lambda_{z,meas}$, extra axial stretch; IMT, intima-media thickness; c_{elast}, elastin stiffness modulus; k_1 and k_2, collagen stress-scaling and stress-curve shape parameters, respectively. Subscripts N and R refer to the normal and rotated orientations in which measurements were performed, respectively. R_i refers to the unstressed vessel inner radius and is an auxiliary model parameter (see Appendix 9.A1).

averaged variables were subsequently perturbed based on their measurement uncertainty, yielding a data set composed of 825 samples containing measured variables for both orientations. Next, for each sample, we used diastolic diameter and distension measurements in combination with associated blood pressure measurements to quantify an expected, exponential diameter-pressure relation (Meinders and Hoeks 2004). These exponential relationships will subsequently be used to fit the constitutive model to.

- **Constitutive modelling of carotid artery wall mechanics**. For each sample, we fitted the constitutive model to both the normal and rotated diameter-pressure relation simultaneously. As a result, each input sample finally results in one realisation of the constitutive parameters.
- **Uncertainty quantification and sensitivity analysis**. All constitutive model realisations together yield insight in the distribution of the constitutive parameters that results from the presence of measurement uncertainty. This distribution of constitutive parameters was therefore used to *quantify* the uncertainty in the different constitutive parameters. Subsequently, sensitivity analysis was performed to determine how *measurement* uncertainty in the different variables (diameter, distension, intima-media thickness, blood pressure and rotation-induced extra axial stretch) propagates to uncertainty in the different *constitutive* parameters. This is potentially useful for improving a future measurement protocol (Saltelli et al. 2004).
- **Presentation of results**. Finally, results were presented in the form of representative examples of model fits, plots of the distributions of the individual constitutive parameters, and tables that apportion constitutive model parameter uncertainty to measurement uncertainty.

9.2.2 Measurements

The measurement protocol and data used in the present study are elaborately described in Holtackers et al. 2016.

Study population

Twelve apparently healthy volunteers (22 ± 3 yrs, 6 male, 6 female) were recruited. The study was approved by the medical ethics committee of Maastricht University Medical Centre (Maastricht, The Netherlands) and written consent was obtained from all participants prior to enrolment.

Magnetic resonance imaging measurements

MRI measurements were performed while the subject's head was in two different orientations. Prior to acquisition, the subjects rested in supine position on the MRI examination table for 10 minutes. First, the subjects were instructed to rotate their head to the left and tilt their chin backwards, defined as the rotated (R) orientation. The imposed rotation was approximately 50° (Holtackers et al. 2016). Then, subjects were measured in a

supine position, with their head in a natural orientation (nose pointing upwards and no tilting backwards), defined as the normal (N) orientation.

For the MRI measurements, a standard multi-slice coronal phase-contrast angiography scan (three-dimensional (3D) T_1 fast field echo technique) was used (Achieva TX; Philips Healthcare, Best, The Netherlands). Data were visualised and carotid artery length was determined by three observers by marking the path between the flow divider of the brachiocephalic artery bifurcation and the flow divider of the right carotid artery bifurcation. From the centerline segment length, carotid artery lengths for the N orientation (defined L_{N}) and the R orientation (defined L_{R}) were obtained (Osirix; Pixmeo, Bernex, Switzerland).

Ultrasound measurements

Ultrasound (US) measurements were acquired at the same orientations as the MRI measurements. US acquisition was performed at the right common carotid artery (CCA) in the anterolateral plane for both orientations. Measurements were repeated three times for both the N and R orientations. Diastolic blood pressure and pulse pressure were measured three times within the US imaging protocol using an oscillometric device (Omron 705IT; Omron Healthcare Europe, Hoofddorp, The Netherlands). For a complete overview of the US protocol, the reader is referred to the work of Holtackers et al. (2016).

The acquired US measurements were analysed to determine the right CCA vessel distension for measurements at both orientations. Because the echo tracking tool used ($^{\mathrm{RF}}$QAS; Esaote, Maastricht, The Netherlands) utilises the media-adventitia echoes of near and far walls, we assumed the measured diameter signal over time to reflect the CCA *outer* diameter (Spronck et al. 2015b).

The work by Holtackers et al. (2016) contains a complete overview of the signal processing steps. For both N and R orientations, we obtained pairs of the following variables: diastolic vessel diameter (D_{d}), vessel wall distension (ΔD), diastolic blood pressure (P_{d}) and pulse pressure (P_{p}). Furthermore, we obtained IMT in the N orientation at P_{d} using an automated software tool (Hoeks et al. 1999).

MRI and US measurements were performed after one another and within one hour.

9.2.3 Generation of data set for constitutive modelling

From the performed measurements, we obtained an initial data set consisting of averaged values for D_{d} and ΔD for each orientation of the measured subjects. We assumed P_{d} and P_{p} to be equal for both orientations. IMT was determined for the N orientation. $\Delta\lambda_z$ was, as a first-order approximation, estimated by the relative change in carotid artery length between the N and R orientation, as measured by MRI.

In this study, uncertainties in the measured variables were accounted for by generating multiple samples within the uncertainty ranges of each measured metric. Each sample consisted of a vector $\vec{M}$ containing the following variables: $\vec{M} = [D_{\mathrm{d,N}},\ \Delta D_{\mathrm{N}},\ D_{\mathrm{d,R}},\ \Delta D_{\mathrm{R}},\ P_{\mathrm{d}},\ P_{\mathrm{p}},\ \mathrm{IMT}_{\mathrm{N}},\ \Delta\lambda_{z,\mathrm{meas}}]$. As the distributions of the parameter uncertainties were not known exactly, uniform distributions were assumed for all parameters, representing a "worst-case scenario" (Huberts et al. 2014). Within these distributions, quasi-random samples were drawn using Sobol's low discrepancy series (Sobol 1967). Based on the

Table 9.1: Overview of average values and intra-subject SDs per measured variable for each orientation (normal and rotated)

Parameter	Unit	Mean ($n = 12$)		Intra-subject SD ($n = 12$)	
		Normal	Rotated	Normal	Rotated
P_d	mmHg	72	72	3.0	3.0
P_p	mmHg	58	58	3.1	3.1
D_d	mm	6.37	6.32	0.22	0.28
ΔD	mm	0.789	0.735	0.035	0.047
IMT	μm	539	-	40	-
$\Delta\lambda_{z,\text{meas}}$	-	1.017		0.012	

Data from Holtackers et al. (2016). Diastolic diameter (D_d) and distension (ΔD) intra-subject standard deviations (SDs) were obtained for both orientations. Means and intra-subject SDs for diastolic blood pressure (P_d) and pulse pressure (P_p) were assumed to be equal for both orientations. Intima-media thickness (IMT) was only obtained for the normal orientation. $\Delta\lambda_{z,\text{meas}}$ represents the increase in axial stretch as a result of head rotation.

number of measured variables and the polynomial order of the meta-model, it was calculated that at least 330 samples were required for performing sensitivity analysis (see Section 9.2.5). Because of our enforced physiological constraint (Eq. 9.2), not all samples were eligible for model fitting. Therefore, a total of 825 samples were drawn.

The uncertainty domains for each measured variable M_i in $\vec{M}$ were defined as

$$M_i = \bar{M}_i \pm 1.96 \frac{\text{SD}_{\text{intra},M_i}}{\sqrt{N_{\text{rep}}}}\,, \tag{9.1}$$

where $\bar{M}_i$ represents the average measured value of parameter M_i and $\text{SD}_{\text{intra},M_i}$ represents the corresponding intra-subject standard deviation as given in Table 9.1.

The error in the estimation of a sample mean scales inversely with the square-root of the number of repeated measurements (Bland and Altman 1996). Therefore, $\text{SD}_{\text{intra},p}$ was divided by $\sqrt{N_{\text{rep}}}$, with N_{rep} the number of repeated measurements. In our case, $N_{\text{rep}} = 3$ (Holtackers et al. 2016). Systolic blood pressure (P_s) was calculated as $P_s = P_d + P_p$; systolic diameter (D_s) was calculated as $D_s = D_d + \Delta D$. All samples of D and P are shown in Fig. 9.2. Note the greater amount of scattering of systolic D and P data points compared to diastolic data points. This is caused by the fact that systolic pressure is defined as the sum of diastolic and pulse pressure. As diastolic and pulse pressure are assumed to be independent, their sum (systolic blood pressure) will have a larger spread than diastolic blood pressure. The larger spread in systolic diameter than in diastolic diameter has the same origin, as systolic diameter is defined as the sum of diastolic diameter and distension.

Given the overlap in uncertainty intervals for N and R diameters, it could occur that despite an increase in λ_z, a lower diameter was sampled for the N orientation compared to the R orientation (Fig. 9.2). It has been shown in many studies that for the physiological pressure range, arterial diameter decreases with increasing λ_z (Matsumoto and Hayashi 1996; Takamizawa and Hayashi 1987). Therefore, after sampling, the following condition

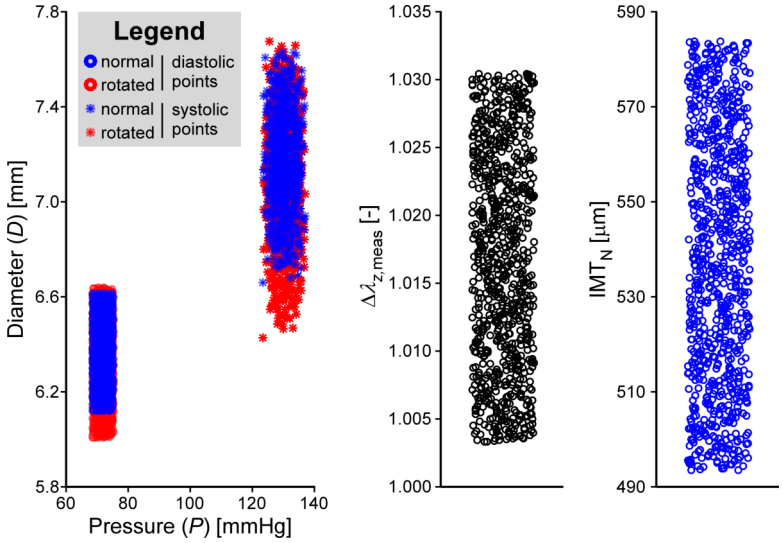

Figure 9.2: Overview of a total of 825 computer-generated samples for diastolic and systolic pressure and diameter for the normal and rotated orientations (left), rotation-induced extra axial stretch ($\Delta\lambda_{z,\mathrm{meas}}$, middle), and intima-media thickness (right). Note that for visualisation purposes, the $\Delta\lambda_{z,\mathrm{meas}}$ and $\mathrm{IMT_N}$ samples were randomly perturbed in horizontal direction.

was enforced for a sample to be included for model fitting:

$$D_{\mathrm{d,N}} > D_{\mathrm{d,R}} \quad \text{and} \quad D_{\mathrm{s,N}} > D_{\mathrm{s,R}} \,. \tag{9.2}$$

Inability of a sample to meet this condition resulted in removal of the sample from the data set.

For each sample in the data set, the following single-exponential function was used to obtain continuous D-P relations for the N and R orientations:

$$P(D) = P_{\mathrm{d}} \exp\left[\gamma\left(\frac{D^2}{D_{\mathrm{d}}^2} - 1\right)\right] . \tag{9.3}$$

This single-exponential function is considered an established function to describe the relation between pressure and diameters of the carotid artery within a large pressure range (i.e. 60 to 160 mmHg) (Hayashi et al. 1980; Meinders and Hoeks 2004). D is a continuous variable describing vessel diameter and γ is a dimensionless nonlinearity factor, which is calculated from systolic and diastolic pressures and diameters as:

$$\gamma = \frac{\log\left(\frac{P_{\mathrm{s}}}{P_{\mathrm{d}}}\right)}{\frac{D_{\mathrm{s}}^2}{D_{\mathrm{d}}^2} - 1} \,. \tag{9.4}$$

9.2.4 Constitutive modelling of carotid artery wall mechanics

Model description

To identify material properties of the carotid artery wall, we used a constitutive model describing passive carotid artery wall mechanics. Appendix 9.A1 gives a detailed description of this model. Our model follows the material laws proposed by Holzapfel and Ogden (2010a) and is implemented in the constitutive framework as previously described by Holzapfel et al. (2000) and Humphrey (2002). In the model, the carotid artery is considered a mono-layered thick-walled tubular structure composed of a mixture of two components: 1) elastin, assumed mechanically isotropic, and 2) collagen fibres, assumed mechanically orthotropic and arranged helically (Holzapfel and Ogden 2010a). Mechanical properties of the arterial wall components are expressed in terms of strain energy functions.

The strain energy function used for elastin (W_{elast}) was

$$W_{\text{elast}} = c_{\text{elast}}(I_1 - 3)\,, \tag{9.5}$$

where $I_1 = \lambda_r^2 + \lambda_\theta^2 + \lambda_z^2$, with r the radial direction, θ the circumferential direction, and z the axial direction, expressed in a cylindrical coordinate system. c_{elast} is the constitutive parameter for elastin (see Appendix 9.A1 for a detailed overview).

The strain energy function used for collagen (W_{coll}) was

$$W_{\text{coll}} = \frac{k_1}{k_2}\left[\exp\left[k_2\left(\lambda_{\text{fibre}}^2 - 1\right)^2\right] - 1\right]\,, \tag{9.6}$$

where k_1 and k_2 are constitutive parameters and λ_{fibre} denotes fibre stretch (Appendix 9.A1).

In W_{elast} and W_{coll}, the following parameters characterise constitutive behaviour of elastin and collagen:

- c_{elast}: stiffness modulus of elastin, units of Pa.
- k_1: stress-scaling parameter of collagen, units of Pa.
- k_2: collagen stress-curve shape parameter, dimensionless.

Following appropriate parameterisations of c_{elast}, k_1, and k_2, elastin acts as the predominant load bearer for low pressure loads. Collagen, which is modelled as an unstressed fibrous material for low pressure, starts bearing load at higher pressures (Holzapfel and Ogden 2010a; O'Rourke and Hashimoto 2007; Watton et al. 2009).

Based on literature reports on excised human and animal carotid arteries, we assumed that in the N orientation, the artery is subjected to an initial pre-stretch ($\lambda_{z,\text{N}}$) of 1.20 (Spronck et al. 2015b). Furthermore, an extra axial stretch ($\Delta\lambda_z$) resulting from head rotation was estimated from MRI measurements:

$$\Delta\lambda_z = \frac{L_{\text{R}}}{L_{\text{N}}}\,, \tag{9.7}$$

where L_{N} and L_{R} are MRI-estimates of carotid artery length for respectively the N and R orientations. Pre-stretch of the carotid artery at the R orientation ($\lambda_{z,\text{R}}$) can now be defined as:

$$\lambda_{z,\text{R}} = \Delta\lambda_z \lambda_{z,\text{N}}\,. \tag{9.8}$$

Two methods of determining $\Delta\lambda_z$ were evaluated: 1) using $\Delta\lambda_z$ as measured from MRI measurements ("$\Delta\lambda_{z,\text{meas}}$"), or 2) including $\Delta\lambda_z$ in the constitutive model fitting routine ("$\Delta\lambda_{z,\text{fitted}}$").

The angle between the two families of collagen fibres in our model (β_0) was assumed to be 35.3° in the unstressed configuration. This angle was chosen from an analytical solution resulting in a constant reduced axial force (F_z) over the cardiac cycle ($\mathrm{d}F_z/\mathrm{d}P = 0$, Humphrey 2002; Takamizawa and Hayashi 1987; Van Loon 1976; Weizsäcker et al. 1983) for a thin-walled, fibre-reinforced tube (Badel et al. 2012). F_z is defined as the force applied in the axial direction additional to that generated by the pressure on the closed ends of the vessel (Holzapfel and Ogden 2010a). In an earlier study, we have shown that for constitutive models describing thick-walled tubes, physiologically realistic behaviour of F_z exists for fibres helix angles ranging from 35° to 40° (Spronck et al. 2015b).

Three additional parameters define the constitutive model, and are used for mapping from a stress-free cut configuration of an artery, to an unloaded intact configuration, to a loaded configuration (Appendix Fig. 9.A1, Holzapfel et al. 2002; Humphrey 2002; Spronck et al. 2015b). These include an opening angle (α), unstressed inner vessel radius (R_i), and pressurised wall cross-sectional area (A_w). The value for α was taken from literature (100°, Spronck et al. 2015b). R_i was fitted using constitutive model fitting routine (see below). A_w was calculated for the normal orientation ($A_{\text{w,N}}$) from $D_{\text{d,N}}$ and IMT_N:

$$A_{\text{w,N}} = \pi\left(\frac{1}{4}D_{\text{d,N}}^2 - \left(\frac{1}{2}D_{\text{d,N}} - \text{IMT}_\text{N}\right)^2\right). \tag{9.9}$$

For the rotated orientation, $A_{\text{w,R}}$ was calculated using the value for $A_{\text{w,N}}$, while assuming incompressibility: $A_{\text{w,R}} = \frac{A_{\text{w,N}}}{\Delta\lambda_z}$.

D-P and F_z-*P* relations were obtained by applying the constitutive framework and by integration of strain energy functions (Appendix 9.A1).

Fitting procedure

The constitutive model was fitted to each data set by variation of constitutive parameters c_elast, k_1, k_2, and R_i. In addition, we evaluated whether fitting $\Delta\lambda_z$ ($\Delta\lambda_{z,\text{fitted}}$, Fig. 9.1) would improve the quality of the fit of the constitutive model to the data set. Lower and upper bounds of all fitted parameters are given in Appendix Table 9.A7.

For each sample in the data set, we assumed the single-exponential function to be valid within the range $P \in \{P_{\text{d,sample}} - 15\text{mmHg},\quad P_{\text{s,sample}} + 15\text{mmHg}\}$. In Fig. 9.2, $P_{\text{d,sample}}$ is represented by the blue circles (N orientation) and red circles (R orientation), and $P_{\text{s,sample}}$ is represented by blue (N orientation) and red asterisks (R orientation), respectively. This pressure range defines the fitting range.

Fitting was performed using the trust-region reflective algorithm (Moré and Sorensen 1983), implemented in the MATLAB Optimization Toolbox function LSQNONLIN (MATLAB R2015a; The MathWorks Natick, MA, USA) and was initiated from 10 random start points in the parameter space using the MATLAB Global Optimization Toolbox function MULTISTART. The same 10 start points were used for fitting all samples. Throughout model fitting, we aimed to minimise the sum of squares difference between measured

pressure from the single-exponential curve P_j and modelled $P_{\text{mod},j}$ for both the N and R orientations:

$$S_{S_P} = \sum_{i\in\{\text{N,R}\}} \left(\frac{1}{n_{P,i}} \frac{1}{P_{\text{p}}^2} \sum_{j=1}^{n_P} (P_{i,j} - P_{\text{mod},i,j})^2 \right) , \tag{9.10}$$

where, for each sample, n_P is the number of fitting points and P_{p} is the pulse pressure.

As a physiological constraint, F_z was forced to remain constant with varying pressure, at a target value defined $F_{\text{z,target},i}$. This was enforced by minimising the following expression:

$$S_{S_{F_z}} = \sum_{i\in\{\text{N,R}\}} \left(\frac{1}{n_{P,i}} \frac{1}{F_{z,\text{target},i}^2} \sum_{j=1}^{n_P} (F_{z,i,j} - F_{z,\text{target},i})^2 \right) , \tag{9.11}$$

where $F_{\text{z,target,N}}$ is assumed to be equal to 0.5 N (Spronck et al. 2015b). For the R orientation, F_z was forced to remain equal at a non-fixed value over the fitting pressure range (i.e., recalculating $F_{\text{z,target,R}}$ for each model evaluation).

S_{S_P} and $S_{S_{F_z}}$ are combined into the weighted total sum of squares ($S_{\text{S,T}}$):

$$S_{S_T} = w_P S_{S_P} + w_{F_z} S_{S_{F_z}} , \tag{9.12}$$

where w_P and w_{F_z} are non-dimensional weighting factors. Here, we chose $w_P = 10$ and $w_{F_z} = 1$. The S_{S_P} term was given a higher importance than the $S_{S_{F_z}}$ term, because of absence of F_z measurements in our study and uncertainty in the assumed target value for F_z.

The fitting error describing goodness-of-fit is expressed as a normalised root mean square error ($E_{\text{RMS},P}$ and E_{RMS,F_z}):

$$E_{\text{RMS},P} = 100\% \cdot \sqrt{S_{S_P}} , \quad \text{and} \tag{9.13}$$

$$E_{\text{RMS},F_z} = 100\% \cdot \sqrt{S_{S_{F_z}}} . \tag{9.14}$$

9.2.5 Uncertainty quantification and sensitivity analysis

All constitutive model realisations together yield insight in the distribution of the constitutive parameters that results from the presence of measurement uncertainty. This distribution of constitutive parameters was therefore used to *quantify* the uncertainty in the different constitutive parameters (uncertainty quantification, UQ).

Sensitivity analysis (SA) was subsequently used to apportion uncertainty in the model-predicted constitutive properties to uncertainty in specific measured variables (Huberts et al. 2014). A variance-based global SA was performed using regression-based generalised polynomial chaos expansion (gPCE), as detailed in Huberts et al. 2014.

The gPCE method captures the relation between constitutive parameters (X_i) and measured variables (M_i) by means of an infinite polynomial expansion. For practical reasons, an approximation of this relation, by means of a finite expansion of orthogonal polynomials (denoted f_{gPCE}) was used:

$$X_i = f^{X_i}(\vec{M}) \approx f_{\text{gPCE}}^{X_i}(\vec{M}) , \tag{9.15}$$

with $\vec{X} = [c_{\text{elast}}, k_1, k_2]$ and $\vec{M} = [M_1, M_2, ..., M_{N_{\text{vars}}}] = [D_{\text{d,N}}, \Delta D_{\text{N}}, D_{\text{d,R}}, \Delta D_{\text{R}}, P_{\text{d}}, P_{\text{p}}, \text{IMT}_{\text{N}}, \Delta\lambda_{z,\text{meas}}]$, and with N_{vars} the number of measured variables (Fig. 9.1).

Such a polynomial expansion acts as a meta-model of the constitutive parameter estimation method. After constructing the meta-model, the value of the leave-one-out cross-validation coefficient (Q^2) is computed. Q^2 is a quality measure of the meta-model, indicating its predictive properties (Sudret 2015). A Q^2-value close to one indicates an accurate meta-model. Throughout this study we assumed $Q^2 > 0.90$ to indicate an appropriate meta-model.

From the meta-model, the variance of a fitted constitutive parameter (a measure of its uncertainty) can be computed. The following sensitivity metrics were computed:

- **Main sensitivity indices**. The main sensitivity index of measured variable M_i represents the expected reduction in uncertainty of the constitutive parameter if M_i were known exactly. A graphical interpretation of main sensitivity indices is given in Fig. 9.1, right pane. Here, each portion of the disc represents the contribution of a specific measured variable (or interaction between more than one measured variable) to the total uncertainty of a constitutive parameter.
- **Total sensitivity indices**. The total sensitivity index of M_i representing the expected uncertainty in constitutive parameter that would remain if all other measured variables except M_i were known exactly.

The main sensitivity indices are used to determine which measured variables are most rewarding to be obtained more accurately, in order to reduce the uncertainty of estimated constitutive parameters. The total sensitivity indices are used to determine which measured variables could potentially be fixed within their uncertainty domain. We refer to Appendix 9.A2 for a detailed breakdown on calculating main and total sensitivity indices.

9.2.6 Presentation of results

Results are presented as follows. First, a representative example of fitting the constitutive model to a single sample from the generated data set is presented. Second, the results of the uncertainty quantification are presented. We use kernel density estimation (KDE) to visualise the distributions of estimated constitutive parameters. KDE estimates the probability density function, which in this context implies the probability density of finding a certain value of a constitutive parameter (Silverman 1986). Finally, results from the sensitivity analysis are reported, explaining the influence of measurement uncertainty on the obtained variance in estimated constitutive parameters.

9.3 Results

9.3.1 Measurements

Table 9.1 shows the MRI and US parameters, reported as group averages among subjects for both orientations, as also reported in the study by Holtackers et al. (2016). They found a 7% decrease in ΔD with head rotation, whereas only a 1% decrease in D_{d} was measured. Furthermore, $\Delta\lambda_{z,\text{meas}}$ resulting from head rotation was found to be 1.017. P_{d} and P_{p} (assumed equal for both orientations) were 72 and 58 mmHg, respectively.

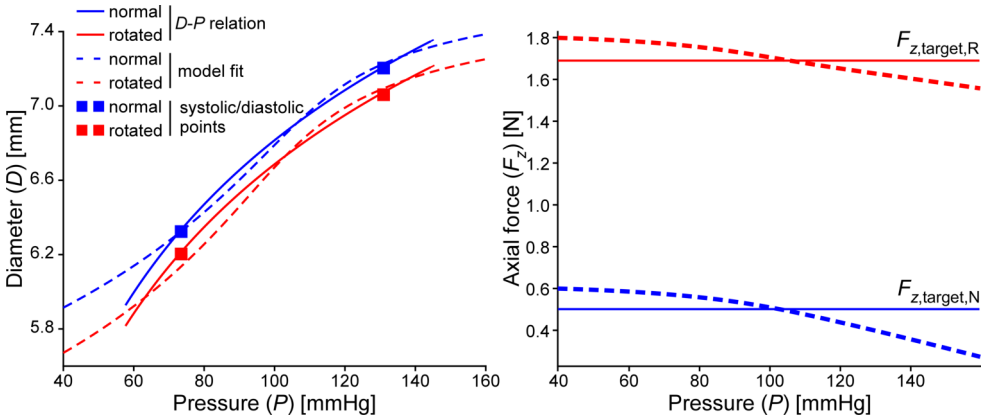

Figure 9.3: Model-predicted D-P curves and F_z-P curves (dashed lines). Solid lines indicate the data fitted upon. The difference between measured and model-predicted pressure was minimised over the pressure fitting range (i.e., $P_\mathrm{d}-15$mmHg to $P_\mathrm{s}+15$mmHg), whereas reduced axial force was fitted to a target value ($F_{z,\mathrm{target,N}}$ and $F_{z,\mathrm{target,R}}$ respectively). Note that $F_{z,\mathrm{target,N}}$ is a fixed value (0.5 N) and $F_{z,\mathrm{target,R}}$ is the average reduced axial force over the pressure range. This results in reduced axial force in the N orientation being forced to remain constant at 0.5 N over the pressure fitting range. Reduced axial force in the R orientation is also forced to remain constant over the pressure fitting range, but at an arbitrary value. Fitted parameters were $c_\mathrm{elast} = 49.6\,\mathrm{kPa}$, $k_1 = 1.80\,\mathrm{kPa}$, $k_2 = 7.97$, and $\Delta\lambda_{z,\mathrm{fitted}} = 1.10$. Fit errors, describing the goodness-of-fit were $E_{\mathrm{RMS},P} = 0.06\%$ and $E_{\mathrm{RMS},F_z} = 21.4\%$.

9.3.2 Representative example of a fitted constitutive model

A representative example of a model-based D-P relationship assessed by model fitting on data from both orientations is depicted in Fig. 9.3. The slope of the plotted curves ($\mathrm{d}D/\mathrm{d}P$) scales with vessel compliance. Low vascular compliance corresponds to high vascular stiffness and vice versa. Model fits (dashed lines, Fig. 9.3) show sigmoidal D-P behaviour over a 40–160 mmHg pressure range, suggesting low compliance for the lower part of pressure range followed by higher compliance in the physiological pressure range and again lower compliance for the upper part of the pressure range. Sigmoidal behaviour is also observed in *ex vivo* studies performing inflation tests on intact human aortic segments and rat carotid arteries (Fridez et al. 2003; Langewouters et al. 1986). For the example presented, the inflection point lies at a relatively high pressure as compared to data shown by Fridez et al. (2003) and Langewouters et al. (1986).

The best-fit constitutive parameters for this representative sample were $c_\mathrm{elast} = 49.6\,\mathrm{kPa}$, $k_1 = 1.80\,\mathrm{kPa}$, $k_2 = 7.97$, and $\Delta\lambda_{z,\mathrm{fitted}} = 1.10$. When $\Delta\lambda_z$ was not fitted but kept fixed at its measured value, an inferior fit was obtained corresponding to increases in $E_{\mathrm{RMS},P}$ and E_{RMS,F_z} of respectively +65% and +22%.

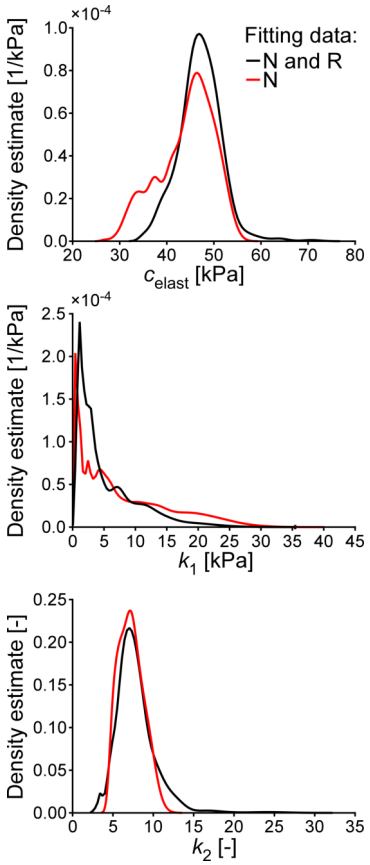

Figure 9.4: Kernel density estimates (KDE) of fitted constitutive parameters (c_{elast}, k_1, and k_2). Black line: KDE for model fitted to measurements acquired at both the normal (N) and rotated (R) orientations. Red line: KDE for model fitted to measurements acquired at the N orientation only.

9.3.3 Uncertainty quantification

Uncertainty quantification quantifies the uncertainty in constitutive parameters due to measurement uncertainty. In order to meet the physiological constraint as formulated in Eq. 9.2, when fitting both the N and R orientations, a total of 437 samples were removed from the initial data set of 825 samples, leaving 388 samples for uncertainty quantification.

In Fig. 9.4, the KDEs of constitutive parameters are shown for the model fitted to both the N and R orientation data of the generated data set (black lines), and for the model fitted to only the N orientation data (red lines).

An overview of medians and interquartile ranges (IQRs) resulting from fitting the samples is given in Table 9.2. For c_{elast} and k_2, IQRs were between 10–30% of their respective medians for parameters, regardless of whether the model was fitted to data

Table 9.2: Parameter values for c_{elast}, k_1, k_2, and $\Delta\lambda_{z,fitted}$

Orientation	c_{elast} [kPa]		k_1 [kPa]		k_2 [-]		$\Delta\lambda_{z,fitted}$		
	Median	IQR	Median	IQR	Median	IQR	Median	IQR	No. of fits
N and R	47.1	5.5	3.2	6.0	7.4	2.5	1.083	0.12	388
N	45.4	7.9	7.2	10.6	7.2	2.2	-		825

Results from fitting both normal (N) and rotated (R) orientations simultaneously and from fitting only the N orientation are shown.

obtained at the two orientations or only at the N orientation (Table 9.2). Collagen parameter k_1 showed a high degree of variation (IQR 190% for N and R and 150% for N of its corresponding median value respectively, Table 9.2). However, the absolute variance of k_1 was found to be much smaller when fitting the model to data acquired at both orientations (IQRs of 6.0 kPa for N and R and 10.6 kPa for N, Table 9.2).

The median value for $\Delta\lambda_{z,fitted}$, (1.083), exceeded the MRI-based value for $\Delta\lambda_{z,meas}$ (1.017, Table 9.2). Furthermore, the spread in $\Delta\lambda_{z,fitted}$ exceeded the intra-subject SD measured in our study (Tables 9.1 and 9.2).

9.3.4 Sensitivity analysis

Sensitivity analysis was performed to apportion uncertainty in measured variables to uncertainty in fitted constitutive parameters. A full overview of main and total sensitivity indices can be found in Tables 9.A1 to 9.A6. Table 9.A1 shows that distension and IMT are the variables for which it is most rewarding for the estimation of c_{elast} to be measured more accurately. Main sensitivity indices for distension are 0.12 for ΔD_R and 0.26 for ΔD_N, respectively. The main sensitivity index for IMT was 0.23 (Table 9.A1). For k_1, distension is the most important measured variable with main sensitivity indices of 0.18 and 0.19 for ΔD_N and ΔD_R respectively (Table 9.A2).

Considering our enforced threshold for Q^2 of 0.90, no appropriate meta-model was obtained for k_2 (Q^2=0.87, Table 9.A3). Therefore, no conclusions can be made regarding sensitivities of k_2 to measured variables.

Reducing uncertainty of blood pressure measurements seems of negligible importance in reducing uncertainty for any given constitutive parameter compared to ultrasound-based measurements of diameter and distension (Tables 9.A1 to 9.A3).

A large discrepancy between main and total sensitivity indices for a certain measured variable indicates there is a contribution of interaction between measured variables causing uncertainty in a constitutive parameter (Sudret 2008). We found that the uncertainty in estimating k_1 and k_2 was significantly dependent on interaction between distension (ΔD_N, ΔD_R) and diastolic diameter ($D_{d,N}$, $D_{d,R}$) as measured in both orientations (separate interaction indices are not reported in Tables 9.A1 to 9.A3).

We also performed a sensitivity analysis considering only measurements acquired at the N orientation. In this case, distension (ΔD_N) was the measured variable contributing the most to uncertainty in constitutive parameters (main sensitivity index between 0.79 and 0.94, Tables 9.A4 to 9.A6). Interaction between meta-model terms was negligible, as illustrated by the minor difference between main and total sensitivity indices (Tables

9.A4 to 9.A6). Meta-models for these data were significantly more accurate reporting Q^2-values between 0.97 and 0.99 (Tables 9.A4 to 9.A6).

9.4 Discussion

To our knowledge, this is the first study to use *in vivo* carotid artery distensibility data *measured under controlled manipulation of axial stretch*, for constitutive parameter estimation. Our aim was to investigate whether this approach, effectively doubling the amount of mechanical measurement data a model is fitted to, would reduce the variability in estimated constitutive parameters.

9.4.1 Key findings

Although we found a high variation in k_1, adding distensibility data of the R orientation reduced its variation (as quantified by the IQR) by almost a factor of two. An *in vitro* study by Sommer and Holzapfel (2012) also reported a large spread in this parameter, finding a k_1-value of 28.4 ± 30.8 kPa (mean ± SD). They performed model fitting on data obtained from inflation-deflation experiments (measuring pressure, radius and axial force) on 11 intact carotid arteries from a total of 8 human donors. Measurements were performed at λ_z-values ranging from 1.0 to 1.3 with 0.05 increments. The reduction of variation in estimating k_1 in the present study suggests, however, that uncertainty in this parameter, when assessed *in vivo*, can be reduced by using our method.

Results indicate that overall, estimations of c_{elast} and k_2 were not influenced significantly by adding distensibility data at the R orientation. This can be appreciated by the overlapping distributions (KDEs) of these parameters (Fig. 9.4).

9.4.2 Sensitivity analysis

Sensitivity analysis showed that the most important contributors to uncertainty in c_{elast} are variables measured by ultrasound (i.e., carotid artery diameter, distension and IMT). Uncertainty of collagen parameter k_1 was primarily caused by measurement uncertainty of carotid artery diameter and distension. Although our model-based approach still requires blood pressure to be measured, improving the precision of measurements of arterial diameter and wall thickness clearly appears to be most rewarding. Whereas the potential for improving the precision of a single ultrasound measure is practically limited, effective precision of ultrasound measurements could be improved by increasing the number of repeated measurements (N_{rep}, see Eq. 9.1).

9.4.3 Uniqueness of estimated parameters

In an earlier study, Ogden et al. (2004) carried out a detailed analysis of fitting strain energy functions to experimental data on mechanical testing of rubber-like materials. They compared the uniqueness of estimated parameters for multiple constitutive models with different numbers of parameters. Model parameters were estimated for several testing

protocols, including biaxial testing. Fitting a model containing only three material parameters on biaxial data sets did not result in multiplicity in fitted parameters, implying convergence to one unique solution (Gent 1996; Ogden et al. 2004). When fitting a more complex model to the same data (effectively estimating six parameters), Ogden et al. (2004) observed non-uniqueness of the fitted parameters.

In the present study we used a least squares-based parameter estimation method similar to the method used by Ogden et al. (2004). As detailed in Appendix 9.A4, our model fitting routine converged to a unique, global minimum, even if 10 randomly selected start points were used.

9.4.4 Limitations and future perspectives

The amount of extra axial stretch induced by head rotation ($\Delta\lambda_z$) is small when measured by MRI $\Delta\lambda_{z,\text{meas}}$. Our model approach predicts a much larger effect of head rotation on $\Delta\lambda_z$ than the estimations obtained from MRI measurements. In our study, $\Delta\lambda_z$ was used as an "aggregate" measure of extra axial stretch. This measure was based on the change in length of the centerline of the carotid artery segment between both orientations. This is a simplification, given the actual 3D geometry of the carotid artery segment. There could, however, be spatial inhomogeneity in the distribution of extra axial stretch along the axis of the carotid artery segment, caused by inhomogeneity in carotid artery wall stiffness along the segment, but also by inhomogeneity in the tethering of the artery by its surrounding tissue.

The observed difference in *D-P* relations between both orientations could be due to torsion of the carotid artery segment as well. Hence, the inferior model fits yielded by fixing $\Delta\lambda_{z,\text{meas}}$ to the MRI value could be explained by the fact that torsion was not accounted for in our model.

In future studies, it should be investigated whether head rotation results in a significant amount of torsion of the carotid artery. Subsequently, the extent to which torsion and axial stretch influence carotid artery distensibility should be evaluated. In this context, given the 3D structure and tethering of the carotid artery wall by surrounding tissue, a 3D finite element analysis would be a suitable method to evaluate the effects of head rotation on local variation in torsion and axial stretch. Such elaborate analysis could elucidate the magnitude of tethering and axial stretch on the fitted constitutive parameters, and could yield useful insight for improving the *in vivo* characterisation method proposed in the present study.

9.4.5 Conclusions

We conclude that our model-based approach, taking into account distensibility data from two levels of axial stretch, could reduce uncertainty in estimated constitutive parameters and, therefore, may improve the assessment of the effect of vascular drugs on wall components. Sensitivity analysis revealed that increasing the precision of ultrasound-based measurements of arterial diameter, distension, and wall thickness, would further benefit constitutive parameter estimation.

9.5 Acknowledgements

This study was supported by a Kootstra Talent Fellowship from Maastricht University Medical Centre to M.H.G. Heusinkveld and by Stichting de Weijerhorst (R.J. Holtackers).

9.A1 Appendix: Constitutive modelling

We considered the carotid artery wall to be an incompressible thick-walled cylindrical structure composed of hyperelastic material. Elastic mechanical properties of separate components of the arterial wall can be expressed in terms of strain energy functions, based on deformation gradients (Holzapfel and Ogden 2010a; Ogden 1972). We assumed that there is only deformation along the principal axes, i.e., we assumed no shear. Therefore, the relevant stretch components of deformation, expressed using cylindrical coordinates (Fig. 9.A1), are λ_r, λ_θ and λ_z, with r the radial direction, θ the circumferential direction, and z the axial direction.

On the structural level of the arterial wall, we distinguish between two types of material: elastin and collagen. For simplicity, we assume that there is no influence of vascular smooth muscle cells on wall mechanics.

9.A1.1 Elastin

Elastin was modelled as an isotropic material. Following the work by Watton et al. (2009) and Holzapfel and Ogden (2010a), the corresponding strain energy function for elastin under the assumption of neo-Hookean material behaviour was formulated as:

$$W_{\text{elast}} = c_{\text{elast}}(I_1 - 3)\,, \tag{9.A1}$$

where $I_1 = \lambda_r^2 + \lambda_\theta^2 + \lambda_z^2$ and c_{elast} is the constitutive parameter for elastin.

9.A1.2 Collagen

Collagen was assumed to be orientated in two equal fractions of fibres with a given helix angle $\pm\beta_0$ with respect to the circumferential direction (Holzapfel and Ogden 2010a, Fig. 9.A1). An expression for the two fibre families added reads:

$$W_{\text{coll}} = \frac{k_1}{k_2}\left[\exp\left[k_2\left(\lambda_{\text{fibre}}^2 - 1\right)^2\right] - 1\right]\,, \tag{9.A2}$$

where k_1 and k_2 are constitutive parameters. λ_{fibre} denotes fibre stretch, which was calculated according to $\lambda_{\text{fibre}}^2 = \cos^2(\beta_0)\lambda_\theta^2 + \sin^2(\beta_0)\lambda_z^2$.

9.A1.3 Constitutive relations

Under the assumption that both elastin and collagen act in parallel in terms of mechanical load bearing, the constituent-specific strain energy functions were combined into a

relation describing local Cauchy stress:

$$\sigma_i = -P_{\mathrm{h},i} + \lambda_i \frac{\partial W_{\mathrm{elast}}}{\partial \lambda_i} + \lambda_i \frac{\partial W_{\mathrm{coll}}}{\partial \lambda_i} \,, \tag{9.A3}$$

where $P_{\mathrm{h},i}$ denotes the local hydrostatic pressure within the wall. This results in the following expressions for σ_r, σ_θ and σ_z:

$$\sigma_r = -P_{\mathrm{h},i} + 2\lambda_r^2 c_{\mathrm{elast}} \,, \tag{9.A4}$$

$$\sigma_\theta = -P_{\mathrm{h},i} + 2\lambda_\theta^2 c_{\mathrm{elast}} + 4k_1\lambda_\theta^2(\lambda_{\mathrm{fibre}}^2 - 1)\cos^2(\beta_0)\left(\exp\left[k_2\left(\lambda_{\mathrm{fibre}}^2 - 1\right)^2\right]\right) \,, \text{ and} \tag{9.A5}$$

$$\sigma_z = -P_{\mathrm{h},i} + 2\lambda_z^2 c_{\mathrm{elast}} + 4k_1\lambda_z^2(\lambda_{\mathrm{fibre}}^2 - 1)\sin^2(\beta_0)\left(\exp\left[k_2\left(\lambda_{\mathrm{fibre}}^2 - 1\right)^2\right]\right) \,. \tag{9.A6}$$

9.A1.4 Constitutive framework

We distinguished between the unstressed and stressed states of an artery (Fig. 9.A1). Under the assumption of an incompressible wall tissue, a mapping of coordinates (r, θ, z) of the deformed, stressed configuration to coordinates (R, Θ, Z) of the unstressed configuration is given by:

$$r(R) = \sqrt{r_{\mathrm{o}}^2 - \frac{R_{\mathrm{o}}^2 - R^2}{\lambda_z k_\alpha}} \,,\ \theta = k_\alpha \Theta \,, \text{ and } z = \frac{l}{L} Z \,, \tag{9.A7}$$

where R_{o} and r_{o} are the outer radii of respectively the unstressed and stressed configuration (Fig. 9.A1). k_α is defined as $k_\alpha = \frac{2\pi}{2\pi - \alpha}$, with α the opening angle (Fig. 9.A1). L and l are vessel length of the unstressed and stressed configuration defining an initial prestretch of an artery λ_z (Fig. 9.A1). The principal stretch ratios $(\lambda_r, \lambda_\theta, \lambda_z)$ with respect to the opened configuration are:

$$\lambda_r = \frac{R}{r k_\alpha \lambda_z}, \quad \lambda_\theta = \frac{k_\alpha r}{R}, \quad \text{and} \quad \lambda_z = \frac{l}{L} \,. \tag{9.A8}$$

Inner and outer radii (r_{i} and r_{o}, respectively) in the stressed configuration can be written as follows:

$$r_{\mathrm{i}} = \frac{\lambda_\theta R_{\mathrm{i}}}{k_\alpha} \quad \text{and} \quad r_{\mathrm{o}} = \sqrt{\frac{A_{\mathrm{w}}}{\pi} + r_{\mathrm{i}}^2} \,, \tag{9.A9}$$

where A_{w} is the cross-sectional wall area in the stressed configuration (Fig. 9.A1). In practice, A_{w} can be determined by measuring IMT and vessel diameter using ultrasonography (Hoeks et al. 1999). We furthermore assumed $\lambda_z = 1.20$, $\alpha = 100°$, and $\beta_0 = 35.3°$.

9.A1.5 Balance equations

We obtained lumen pressure (P) by solving the balance equation:

$$P = \int_{r_i}^{r_o} \frac{\sigma_\theta - \sigma_r}{r} \mathrm{d}r \,. \tag{9.A10}$$

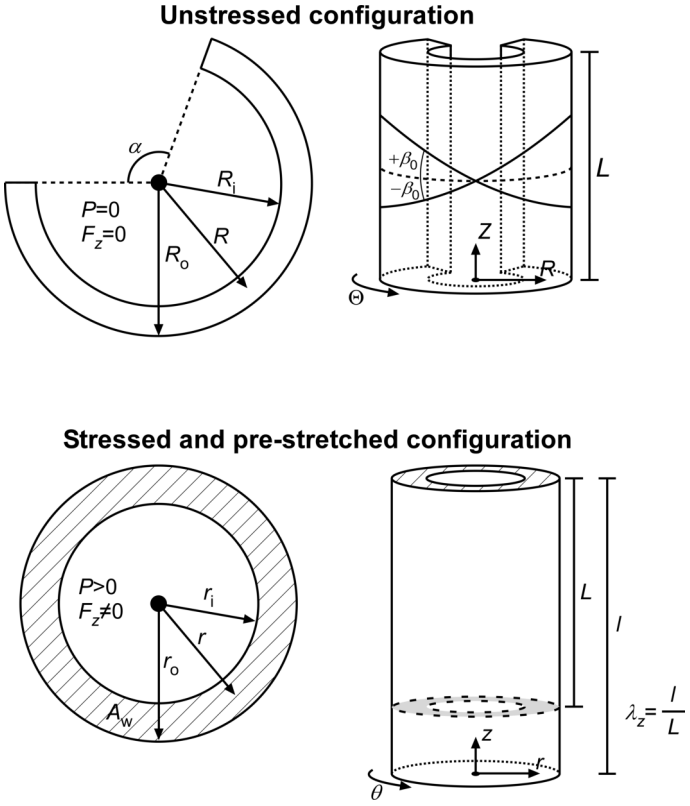

Figure 9.A1: Overview of two configurations of an artery. Top: R, unstressed radius; R_i, unstressed inner radius; R_o, unstressed outer radius; α, opening angle; L, unstressed vessel length. In the unstressed configuration, we consider two families of helically orientated collagen fibres, with an angle $\pm\beta_0$ with respect to the circumferential direction. Bottom: r, stressed radius; r_i, stressed inner radius; r_o, stressed outer radius; A_w, cross-sectional wall area in the stressed configuration; l, stressed vessel length. A pre-stretch of λ_z was imposed.

As a boundary condition, it was assumed that $\sigma_r(r_\mathrm{i}) = -P$ and $\sigma_r(r_\mathrm{o}) = 0$.

Reduced axial force was found by solving the following balance equation:

$$F_z = \int_{r_i}^{r_o} (2\sigma_z - \sigma_r - \sigma_\theta) r \mathrm{d}r \ . \tag{9.A11}$$

9.A2 Appendix: Uncertainty quantification and sensitivity analysis

In this appendix, a detailed mathematical overview of the derivation of main and total sensitivity indices is provided.

9.A2.1 Sobol decomposition

The fitting procedure that was used in the current study for obtaining estimates of the constitutive parameters is considered as an arbitrary function: $X = f(\vec{M})$. This function yields an uncertain constitutive parameter, X, as a function of its N_vars-number of uncertain input variables $\vec{M} = [M_1, M_2, \cdots, M_{N_\mathrm{vars}}]$.

For the purpose of uncertainty quantification and sensitivity analysis, a Sobol variance decomposition of $X = f(\vec{M})$ can be constructed. First, the function $f(\vec{M})$ is decomposed into summands of increasing dimensionality (Saltelli et al. 2008):

$$\begin{aligned} X = f(\vec{M}) = f_0 &+ \sum_{i_1=1}^{N_\mathrm{vars}} f_{i_1}(M_{i_1}) \\ &+ \sum_{i_1=1}^{N_\mathrm{meas}-1} \sum_{i_2>i_1}^{N_\mathrm{vars}} f_{i_1,i_2}(M_{i_1}, M_{i_2}) + \cdots + f_{i_1,i_2,\cdots,i_{N_\mathrm{vars}}}(M_{i_1}, M_{i_2}, \cdots, M_{i_{N_\mathrm{vars}}}) \ . \end{aligned} \tag{9.A12}$$

Here, f_0 represents the expected value of X: $E(X)$. All other terms have zero mean and are orthogonal.

It can be shown that the total variance of X, $V(X)$ is then equal to the sum of the variances of all the summands (Saltelli et al. 2008):

$$\begin{aligned} V(X) &= \sum_{i_1=1}^{N_\mathrm{vars}} V(f_{i_1}(M_{i_1})) \\ &\quad + \sum_{i_1=1}^{N_\mathrm{vars}-1} \sum_{i_2>i_1}^{N_\mathrm{vars}} V(f_{i_1,i_2}(M_{i_1}, M_{i_2}) + \cdots + V(f_{i_1,i_2,\cdots,i_{N_\mathrm{vars}}}(M_{i_1}, M_{i_2}, \cdots, M_{i_{N_\mathrm{vars}}})) \end{aligned} \tag{9.A13}$$

$$= \sum_{i_1=1}^{N_\mathrm{vars}} V_{i_1} + \sum_{i_1=1}^{N_\mathrm{vars}-1} \sum_{i_2>i_1}^{N_\mathrm{vars}} V_{i_1,i_2} + \cdots + V_{i_1,i_2,\cdots,i_{N_\mathrm{vars}}} \ . \tag{9.A14}$$

Sobol's sensitivity indices are obtained from this formulation after normalising with respect to the total variance, $V(X)$ (Saltelli et al. 2008):

$$\sum_{i_1=1}^{N_{\text{vars}}} S_{i_1} + \sum_{i_1=1}^{N_{\text{vars}}-1} \sum_{i_2>i_1}^{N_{\text{vars}}} S_{i_1,i_2} + \cdots + S_{i_1,i_2,\cdots,i_{N_{\text{vars}}}} = 1 \ . \tag{9.A15}$$

In this formulation, S_{i_1} represents the main sensitivity index of parameter M_{i_1}. The higher order sensitivity indices represent interaction terms. The total sensitivity index S_{T,i_1} of a parameter M_{i_1} is obtained by adding all Sobol indices in which parameter M_{i_1} is involved.

In the context of parameter fixing and prioritisation, the main sensitivity index, S_i, represents the expected reduction in $V(X)$ if M_i were known exactly. As such, the main sensitivity indices are used to determine which variables are most rewarding to measure more accurately (i.e., parameters with a high main sensitivity index), in order to reduce the variance of X (Huberts et al. 2014). The total sensitivity index, $S_{\text{T},i}$, represents the residual variance in X if all parameters except M_i were known exactly. Therefore the total sensitivity indices are used to determine which parameters have negligible impact on the variance of X (i.e., parameters with a low total sensitivity index).

9.A2.2 Generalised polynomial chaos expansion

The generalised polynomial chaos expansion (gPCE) can be used to compute the Sobol sensitivity indices. For this purpose, the gPCE was used to construct a meta-model of the function response of $X = f(\vec{M})$ by expanding it into an infinite sum of orthogonal polynomials:

$$X = f(\vec{M}) = f_{\text{gPCE}}(\vec{M}) = \sum_{\boldsymbol{\alpha}\in\mathbf{A}^{\infty}} c_{\boldsymbol{\alpha}} \Phi_{\boldsymbol{\alpha}}(\vec{M}) \ . \tag{9.A16}$$

Here, $\Phi_{\boldsymbol{\alpha}}(\vec{M})$ are orthogonal polynomials and $c_{\boldsymbol{\alpha}}$ are the expansion coefficients. The polynomials $\Phi_{\boldsymbol{\alpha}}(\vec{M})$ are defined as the product of univariate polynomials, $\phi_{\alpha_i}(M_i)$ that are of polynomial degree $\alpha_i \in \mathbb{N}_0$. The polynomial degree of each univariate polynomial is defined in the multi-index $\boldsymbol{\alpha} = [\alpha_1, \alpha_2, \cdots, \alpha_{N_{\text{vars}}}]$. The definition of $\Phi_{\boldsymbol{\alpha}}(\vec{M})$ given by:

$$\Phi_{\boldsymbol{\alpha}} = \prod_{i=1}^{N_{\text{vars}}} \phi_{\alpha_i}(M_i) \ . \tag{9.A17}$$

The set $\mathbf{A}^{\infty}$ contains all possible $\boldsymbol{\alpha}$. The total polynomial degree of $\Phi_{\boldsymbol{\alpha}}$ is defined as:

$$\text{degree}(\boldsymbol{\alpha}) = |\boldsymbol{\alpha}| = \sum_{i=1}^{N_{\text{vars}}} \alpha_i \ . \tag{9.A18}$$

The formulation of the gPCE in Eq. 9.A16 is unique and equivalent to the decomposition in Eq. 9.A12 (Sudret 2008).

The variance of the gPCE can be calculated analytically according to:

$$V(X) = V(f_{\text{gPCE}}(\vec{M})) = \sum_{\boldsymbol{\alpha}\in\mathbf{A}^{\infty}} c_{\boldsymbol{\alpha}}^2 H_{\boldsymbol{\alpha}} \ , \tag{9.A19}$$

where $H_{\boldsymbol{\alpha}}$ is a normalisation factor dependent on the used type of polynomial. In this study we used Legendre polynomials for the polynomial expansion, because it was shown that this type of polynomial gives the best convergence for uniformly distributed input parameters (Sudret 2008). $H_{\boldsymbol{\alpha}}$ is given by:

$$H_{\boldsymbol{\alpha}} = \prod_{i=1}^{N_{\text{vars}}} \frac{1}{2\alpha_i + 1} \ . \tag{9.A20}$$

Dividing the right hand side of Eq. 9.A19 by $V(f_{\text{gPCE}}(\vec{M}))$ yields Sobol's sensitivity indices. The main sensitivity index of X_i is obtained by:

$$S_i = \frac{1}{V(f_{\text{gPCE}}(\vec{M}))} \sum_{\boldsymbol{\alpha} \in \mathbf{A}_i} c_{\boldsymbol{\alpha}}^2 H_{\boldsymbol{\alpha}} \ , \tag{9.A21}$$

where $\mathbf{A}_i$ is the set of multi-indices where α_i is positive and all other indices of $\boldsymbol{\alpha}$ are zero. The total sensitivity index of X_i is calculated according to:

$$S_{\text{T},i} = \frac{1}{V(f_{\text{gPCE}}(\vec{M}))} \sum_{\boldsymbol{\alpha} \in \mathbf{A}_{\text{T,i}}} c_{\boldsymbol{\alpha}}^2 H_{\boldsymbol{\alpha}} \ , \tag{9.A22}$$

where $\mathbf{A_{T,i}}$ is the set that contains any multi-index in which α_i is positive.

In practice the infinite polynomial chaos expansion is truncated. This results in the fact that equations 9.A19, 9.A21, and 9.A22 represent *estimates* of the total variance, main sensitivity index, and total sensitivity index, respectively. In this study, only these polynomials were included in the meta-model that could be described by a multi-index with degree($\boldsymbol{\alpha}$) ≤ 3.

9.A3 Appendix: Sensitivity indices for all variables and parameters

In this appendix, an overview of main and total sensitivity indices is presented for each measured variable. Sensitivity indices were determined by fitting data from the normal (N) and rotated (R) orientations simultaneously and by fitting only data from the N orientation.

9.A3.1 Fitting the normal and rotated subsets of the data set

Table 9.A1: Main and total sensitivity indices for c_{elast}

Parameter: c_{elast}, $Q^2 = 0.93$			
Measured variable	Symbol	Main sensitivity index	Total sensitivity index
Diastolic blood pressure	P_{d}	0.013	0.024
Pulse pressure	P_{p}	0.0014	0.016
Diastolic diameter, normal	$D_{\text{d,N}}$	0.016	**0.12**
Distension, normal	ΔD_{N}	**0.26**	**0.37**
Intima-media thickness, normal	IMT_{N}	**0.23**	**0.26**
Diastolic diameter, rotated	$D_{\text{d,N}}$	0.09	**0.26**
Distension, rotated	ΔD_{R}	**0.12**	**0.27**

Sensitivity indices larger than 0.10 are indicated in bold. Q^2 indicates the accuracy of the meta-model.

Table 9.A2: Main and total sensitivity indices for k_1

Parameter: k_1, $Q^2 = 0.95$			
Measured variable	Symbol	Main sensitivity index	Total sensitivity index
Diastolic blood pressure	P_{d}	0.0012	0.010
Pulse pressure	P_{p}	0.037	0.062
Diastolic diameter, normal	$D_{\text{d,N}}$	0.051	**0.18**
Distension, normal	ΔD_{N}	**0.18**	**0.49**
Intima-media-thickness, normal	IMT_{N}	0.0030	0.029
Diastolic diameter, rotated	$D_{\text{d,N}}$	0.019	**0.22**
Distension, rotated	ΔD_{R}	**0.19**	**0.62**

Sensitivity indices larger than 0.10 are indicated in bold. Q^2 indicates the accuracy of the meta-model.

Table 9.A3: Main and total sensitivity indices for k_2

Parameter: k_2, $Q^2 = 0.87$			
Measured variable	Symbol	Main sensitivity index	Total sensitivity index
Diastolic blood pressure	P_{d}	0.0024	0.013
Pulse pressure	P_{p}	0.0051	0.019
Diastolic diameter, normal	$D_{\text{d,N}}$	0.014	**0.16**
Distension, normal	ΔD_{N}	**0.29**	**0.48**
Intima-media thickness, normal	IMT_{N}	0.0091	0.033
Diastolic diameter, rotated	$D_{\text{d,N}}$	**0.18**	**0.42**
Distension, rotated	ΔD_{R}	**0.19**	**0.27**

Sensitivity indices larger than 0.10 are indicated in bold. Q^2 indicates the accuracy of the meta-model.

9.A3.2 Fitting the normal subset of the data set

Table 9.A4: Main and total sensitivity indices for c_{elast}

Parameter: c_{elast}, $Q^2 = 0.99$			
Measured variable	Symbol	Main sensitivity index	Total sensitivity index
Diastolic blood pressure	P_{d}	0.012	0.013
Pulse pressure	P_{p}	0.0072	0.019
Diastolic diameter, normal	$D_{\text{d,N}}$	0.0077	0.021
Distension, normal	ΔD_{N}	**0.83**	**0.86**
Intima-media thickness, normal	IMT_{N}	**0.12**	**0.12**

Sensitivity indices larger than 0.10 are indicated in bold. Q^2 indicates the accuracy of the meta-model.

Table 9.A5: Main and total sensitivity indices for k_1

Parameter: k_1, $Q^2 = 0.99$			
Measured variable	Symbol	Main sensitivity index	Total sensitivity index
Diastolic blood pressure	P_{d}	0.0011	0.0016
Pulse pressure	P_{p}	0.030	0.041
Diastolic diameter, normal	$D_{\text{d,N}}$	0.022	0.030
Distension, normal	ΔD_{N}	**0.91**	**0.94**
Intima-media thickness, normal	IMT_{N}	0.0085	0.013

Sensitivity indices larger than 0.10 are indicated in bold. Q^2 indicates the accuracy of the meta-model.

Table 9.A6: Main and total sensitivity indices for k_2

Parameter: k_2, $Q^2 = 0.97$			
Measured variable	Symbol	Main sensitivity index	Total sensitivity index
Diastolic blood pressure	P_{d}	0.0064	0.015
Pulse pressure	P_{p}	0.089	0.10
Diastolic diameter, normal	$D_{\text{d,N}}$	**0.11**	**0.12**
Distension, normal	ΔD_{N}	**0.77**	**0.79**
Intima-media thickness, normal	IMT_{N}	0.0016	0.0095

Sensitivity indices larger than 0.10 are indicated in bold. Q^2 indicates the accuracy of the meta-model.

9.A4 Appendix: Uniqueness of best-fit model parameters

In this appendix, we propose a method to define the uniqueness of fitted parameters. As described in the Methods section, our constitutive model was fitted to each sample in the data set, departing from 10 random start points. To quantify the uniqueness of the

Table 9.A7: Complete overview of lower and upper bounds used in fitting of parameters c_{elast}, k_1, k_2, R_{i}, and $\Delta\lambda_{z,\text{fitted}}$

Parameter	Unit	Lower bound	Upper bound
c_{elast}	kPa	1	400
k_1	kPa	$0.1 \cdot 10^{-3}$	400
k_2	-	0	100
R_{i}	m	$0.5 \cdot 10^{-3}$	$10 \cdot 10^{-3}$
$\Delta\lambda_{z,\text{fitted}}$	-	0.7	1.3

estimated parameters, we calculated the range (minimum-maximum difference) of the series of parameter values found for all start points. Let the uniqueness (U_i) of a fitted parameter ($X_{i,j,k}$) be expressed as:

$$U_i = 100\% \cdot \frac{1}{X_{i,\text{scale}}} \left(\frac{1}{N} \sum_{j=1}^{N} \max\left(X_{i,j,1}, X_{i,j,2}, \ldots, X_{i,j,n_{\text{s}}}\right) - \min\left(X_{i,j,1}, X_{i,j,2}, \ldots, X_{i,j,n_{\text{s}}}\right) \right), \quad (9.\text{A}23)$$

where n_{s} denotes the number of start points, k denotes a start point index, j denotes a sample from the data set, i denotes the index of the fitted parameter within $\vec{X}$, and N_{samp} denotes the number of fitted samples. $X_{i,\text{scale}}$ is a scaling factor, defined for each fitted parameter as the absolute difference between its lower and upper bound (Table 9.A7).

On average, 6 of the 10 start points converged to a stable solution. Only those solutions that were considered to be converged to an optimal solution were included in this analysis. An optimal solution was defined as a solution for which $S_{S,\text{T},j} < 10$ (Eq. 9.12). By enforcing this criterion, 140 out of 2269 solutions were omitted.

Using this method, we found $U_{c_{\text{elast}}} = 2\%$, $U_{k_1} = 0.3\%$, $U_{k_2} = 1\%$, $U_{R_{\text{i}}} = 3\%$, and $U_{\Delta\lambda_{z,\text{fitted}}} = 19\%$. Note that $U_i = 0\%$ would indicate that for parameter i, for all 10 start points, identical best-fit parameter values would be found.

Chapter 10

2D method to quantify smooth muscle orientation in tubular structures

The contents of this chapter are based on:

Bart Spronck,[1,*] Jort J. Merken,[1,*] Koen D. Reesink,[1] Wilco Kroon,[1,2] and Tammo Delhaas[1]
(2014).
Ureter Smooth Muscle Cell Orientation in Rat Is Predominantly Longitudinal. *PLOS ONE* 9(1):e86207.

[*] Authors contributed equally.
[1] Department of Biomedical Engineering, CARIM School for Cardiovascular Diseases, Maastricht University, Maastricht, The Netherlands.
[2] Institute of Computational Science, University of Lugano, Lugano, Switzerland.

Abstract

In ureter peristalsis, the orientation of the contracting smooth muscle cells is essential, yet current descriptions of orientation and composition of the smooth muscle layer in human as well as in rat ureter are inconsistent. The present study aims to improve quantification of smooth muscle orientation in rat ureters as a basis for mechanistic understanding of peristalsis. A crucial step in our approach is to use two-photon laser scanning microscopy and image analysis providing objective, quantitative data on smooth muscle cell orientation in intact ureters, avoiding the usual sectioning artifacts. In 36 rat ureter segments, originating from a proximal, middle or distal site and from a left or right ureter, we found close to the adventitia a well-defined longitudinal smooth muscle orientation. Towards the lamina propria, the orientation gradually became slightly more disperse, yet the main orientation remained longitudinal. We conclude that smooth muscle cell orientation in rat ureter is predominantly longitudinal, though the orientation gradually becomes more disperse towards the proprial side. These findings do not support identification of separate layers. The observed longitudinal orientation suggests that smooth muscle contraction would rather cause local shortening of the ureter, than cause luminal constriction. However, the net-like connective tissue of the ureter wall may translate local longitudinal shortening into co-local luminal constriction, facilitating peristalsis. Our quantitative, minimally invasive approach is a crucial step towards more mechanistic insight into ureter peristalsis, and may also be used to study smooth muscle cell orientation in other tube-like structures like gut and blood vessels.

10.1 Introduction

CONTRACTION and relaxation of smooth muscle cells (SMCs) of the ureter are responsible for active propulsion of urine from the kidneys to the bladder by peristalsis. Although it is accepted that orientation of SMCs plays an important role in peristalsis (Brasseur et al. 2007), morphological reports on the lamina muscularis (LM) are inconsistent. Findings with respect to the number of layers that are distinguishable by orientation and with respect to the specific orientation of SMCs within the layers (circumferential, longitudinal, helical, disperse) differ between studies. For example, a number of investigators reported different layers in the LM of human ureters based on distinct SMC orientation patterns (Bouvin 1869; Ebner 1902; Henle 1866; Köllilker 1859; Maier 1881; Obersteiner 1871; Stevens and Lowe 1992; Toldt 1877), whereas others did not find a well-defined layering in SMC orientations (Disse 1896; Disselhorst 1894; Floyd et al. 2008; Gosling et al. 1983; Murnaghan 1957; Protopopow 1897; Sappey 1873; Satani 1919; von Möllendorff and Schröder 1930; Woodburne 1965). Moreover, some of the investigators found longitudinal and/or circumferential orientations (Bouvin 1869; Ebner 1902; Henle 1866; Köllilker 1859; Maier 1881; Obersteiner 1871; Protopopow 1897; Toldt 1877), while others observed helical/interwoven SMC orientations (Sappey 1873; Satani 1919; Schneider 1938; Stevens and Lowe 1992). In rat ureter, similar discrepan-

cies are found, i.e., some authors describe the rat ureter's LM as being layered with an outer longitudinal and an inner circular layer (Aragona et al. 1988; Hoyes et al. 1976; Lang et al. 2001), whereas other groups describe no clear layering (Disselhorst 1894; Wolf et al. 1996), or an inner longitudinal and outer circular layer (Hicks 1965). It is important to note that methodological aspects may play a role in these discrepancies. Most studies evaluated the LM's structure by histological sectioning methods, which may affect tissue morphology and provides limited capabilities for quantifying SMC orientation across the thickness of the LM.

The aim of the present study was to develop a quantitative approach to study SMC orientation 1) in intact ureters at approximate *in vivo* geometry, 2) throughout the entire thickness of the LM, 3) with sufficient (depth) resolution, and 4) with consideration of potential differences along the length of the ureter or between left and right ureters. Given that in rat ureter similar discrepancies in terms of SMC stratification and within-layer orientation as in human were found, we used whole ureters from wild type rats as a model. In order to avoid artifacts due to histological fixation and sectioning, we used two-photon laser scanning microscopy (TPLSM) to image intact ureters that were mounted between glass pipettes at approximate *in vivo* length and diameter. The adequate penetration depth of TPLSM allowed us to transverse the entire LM from out- to inside.

10.2 Concise methods

10.2.1 Ethics statement

Experiments and procedures were approved by the Maastricht University animal experiments committee.

10.2.2 Experimental procedures

Left and right ureters were excised from six Wistar rats, euthanised with CO_2. After removal of excessive fat, ureters were mounted between glass micropipettes and stained both intra- and extraluminally using 2 µM SYTO 13 (staining cell nuclei) in Hanks' Balanced Salt Solution (HBSS) for 30 minutes (Fig. 10.1A). Mounted ureters were imaged using a two-photon laser scanning microscope, acquiring a 3D stack of images traversing the ureter wall from out- to inside at an equal lateral and axial (i.e., in depth or z direction) resolution of 0.5 mm. Image stacks were acquired at proximal, middle and distal locations along each ureter, yielding a total of 36 stacks.

10.2.3 Processing and analysis

In summary, after assessment of ureter diameter, smooth muscle cell nuclei and their orientations were automatically identified in the acquired image stack. For each stack, a depth-dependent region of interest (ROI; see Fig. 10.1B) was calculated. This ROI was applied after delineation of SMC nuclei. SMC orientation was only calculated for nuclei within the ROI.

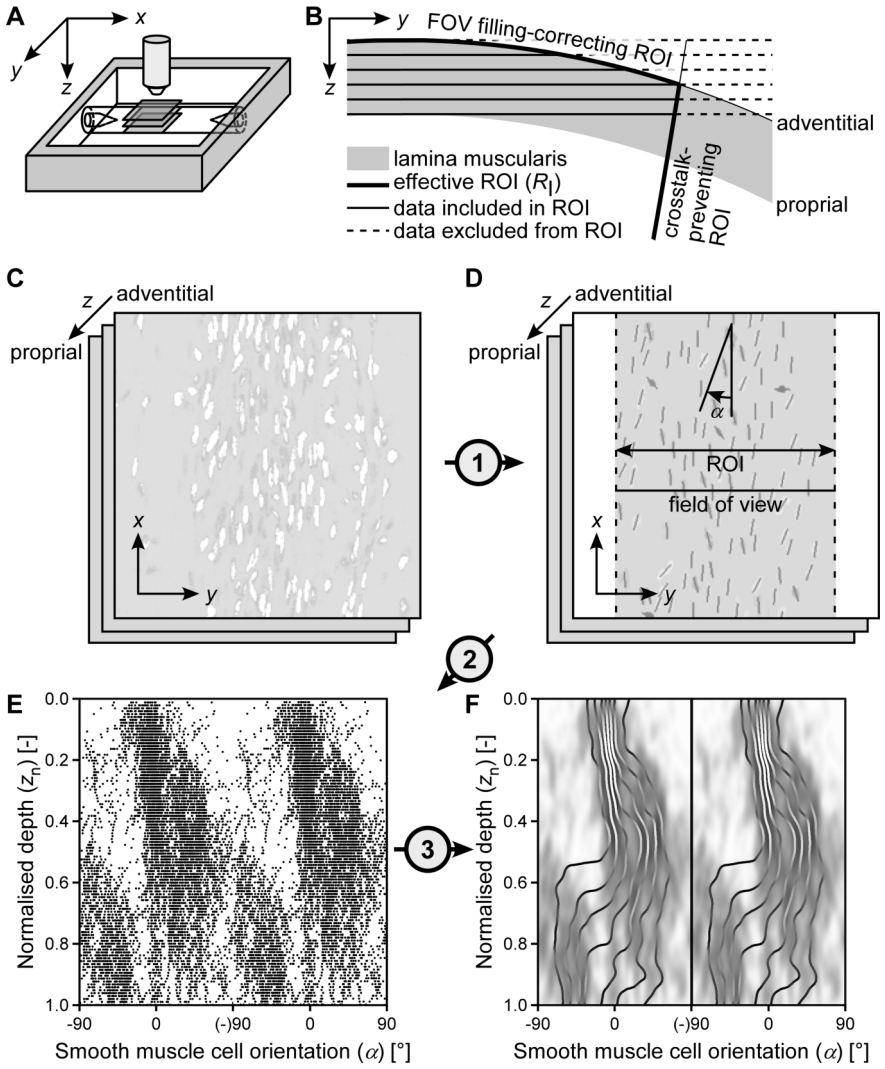

Figure 10.1: Image acquisition and processing workflow. **A**: Image stacks of the muscle layer (of the mounted, submerged ureter) were acquired at increasing depth (z) from the adventitial to the proprial side, at proximal, middle and distal locations (i.e., three segments per ureter). **B**: Given the curvature of the vessel, the region of interest (ROI) for quantitative analysis was adjusted to ensure reliable cell density estimation and to limit crosstalk of cells resident at other depths within the wall. **C**: A stack of raw images, showing smooth muscle cell (SMC) nuclei stained with SYTO 13. **D**: Raw images (panel **C**) were filtered using cellness filtering (step 1) to identify SMC nuclei. Subsequently, a ROI was applied and individual SMC angles (α) were determined. α was defined with reference to the longitudinal axis of the vessel (x-direction). **E**: SMC angles were plotted as a function of depth to evaluate transmural changes in orientation, taking circularity of the data into account. **F**: A kernel density estimation (KDE) plot was used to estimate the orientation distribution. On this KDE, octile lines were plotted to clarify changes in orientation dispersion with depth.

Cellness filtering and smooth muscle cell identification

Stack images were filtered using cellness filtering, in analogy to vesselness filtering (Frangi et al. 1998). Cellness filtering enhances elongated structures, e.g., SMC nuclei, in an image, and suppresses background noise, thereby resulting in a high-contrast image with clearly delineated cell nuclei. Cellness-filtered images were converted to binary images by means of thresholding. Pixels of value 1 were clustered and subsequently filtered based on their surface area, removing dye particles (area too small) or adjacent cells that are erroneously clustered as one (area too large). Each cluster now represents a nucleus and signifies an SMC.

Region of interest application

As flat image slices were acquired of a curved object, structures (clusters) at various depths of the wall could end up in one image slice, cf. Fig. 10.1B. This crosstalk among slices is reduced by narrowing the region of interest (ROI) used for quantification of SMC orientation (Fig. 10.1B). With increasing imaging depth, and with a decreasing radius of curvature of the ureter wall, the ROI is narrowed. Furthermore, for the outermost slices, the imaging field of view is not fully filled with the lamina muscularis (Fig. 10.1B). By assuming a cylindrically shaped ureter with a measured radius, the ROI can be chosen such that it is always completely filled with lamina muscularis, allowing cell densities to be calculated.

Angle calculation

Nuclear shape was assessed based on the eigenvalues of the structure tensor that was calculated for each identified cluster (Jähne 1993). The ratio of its eigenvalues is required to be larger than 1.5 to exclude cells with round-shaped nuclei. Principle cluster orientation for the included nuclei is represented by the eigenvector corresponding to the largest eigenvalue. SMC nuclear orientation is expressed by the angle a of this eigenvector with respect to the longitudinal ureter axis (Fig. 10.1C–E).

Probability density estimation

For each stack, imaging depth was normalised from 0 to 1, after which a two-dimensional kernel density estimate (KDE) (Silverman 1986) was calculated (Fig. 10.1F). Kernel density estimation allows for estimation and visualisation of the probability density from a set of data points. In our case, the KDE shows how often a certain SMC orientation is encountered at a certain imaging depth. In addition to the KDEs per stack, an overall KDE was calculated of all 36 imaged stacks. For each depth, eight quantiles (octiles) were calculated and displayed as lines on the KDE (Fig. 10.1F).

Cell density estimation

Cell density (having the unit “cells per cross-sectional area”) is calculated by dividing the number of detected nuclei in a slice by the area of the region of interest for that slice. The key difference between cell densities and the aforementioned probability densities is

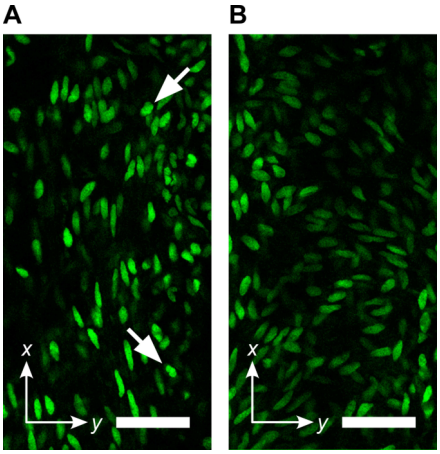

Figure 10.2: Example image slices from a single image stack. **A**: Image slice towards the adventitial side, showing predominantly longitudinally oriented smooth muscle cells (SMCs). **B**: Image slice towards the proprial side, showing a more disperse orientation. Scale bar: 50 μm. Arrows indicate relatively round cells which are excluded from further analysis.

that cell densities are corrected for the ROI and, thus, give a measure of the physical cell density.

For details on imaging and image analysis procedures and calculations, including parameter values, please see Appendix 10.A1.

10.3 Results

By visual inspection, the acquired TPLSM image stacks typically showed an outer, longitudinal layer of SMCs (Fig. 10.2A). With increasing imaging depth, SMC orientation generally dispersed but remained longitudinal (e.g., Fig. 10.2B). In the analysis of SMC orientation, we considered a normalised imaging depth to be able to compare LMs of different thicknesses. The unnormalised median (25th—75th percentile) thickness of the 36 SMC layers was 53 (41–70) μm.

Based on our image analysis methodology (Concise methods), we quantified SMC orientation, and indeed found a predominantly longitudinal orientation in the 36 rat ureter segments we studied (Fig. 10.3). From the adventitial side toward the proprial side we found a clear, but gradual transition from a narrowly longitudinal to a more dispersely longitudinal distribution (Fig. 10.3A and 10.3C). The broadening of the orientation distribution is also evident from its increasing standard deviation with depth (Fig. 10.3B). Average SMC density was between 8 cells per $10^4\,\mathrm{mm}^2$ (adventitial and proprial sides) and 25 cells per $10^4\,\mathrm{mm}^2$ (middle of the LM, Fig. 10.3A).

Whereas the main SMC orientation was uniformly longitudinal, individual ureter segments showed slight variability with respect to their dispersion (Fig. 10.4). The 50th percentile of the orientation standard deviation (SD) increased from 25° (adventitially) to 32° (proprially) (Table 10.1). Towards the proprial side (normalised depth 0.8), the SD

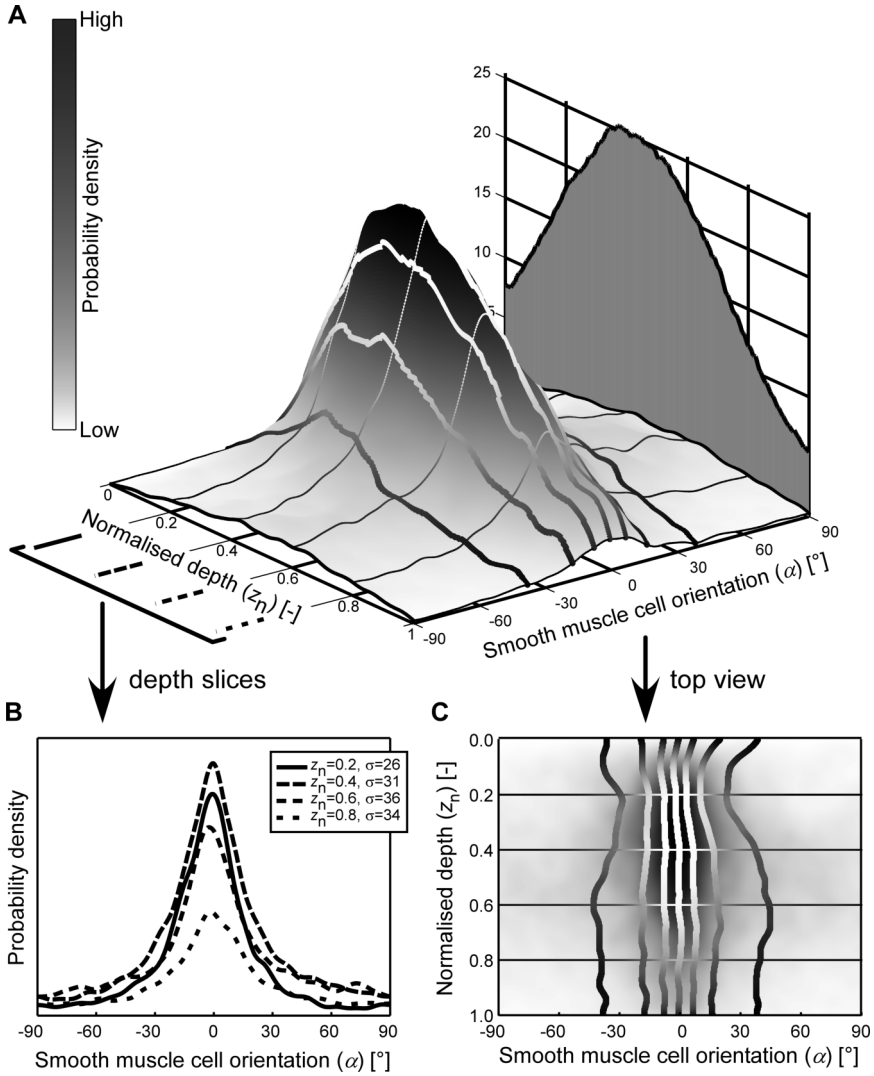

Figure 10.3: Smooth muscle cell (SMC) orientation in intact rat ureter is predominantly longitudinal. Panel **A** shows the orientation distribution (3D plot) and the cell density (2D graph) as function of depth, averaged over 36 rat ureter segments. Normalised depth 0 corresponds to the adventitial side of the muscle layer and 1 to the proprial side. At the adventitial side (normalised depth 0 to 0.5) there is a high probability that the angle of the SMCs with respect to the longitudinal axis of the ureter is about 0u. Towards the proprial side the SMC orientation gradually disperses but remains centred around 0°, as further illustrated in panel **B** by the distributions at four distinct normalised depths (z_n) as indicated. At these depths, standard deviations (σ) are given. In the distribution plot (**A**) and its top view (**C**) the curves delimit the octiles of the orientation distribution.

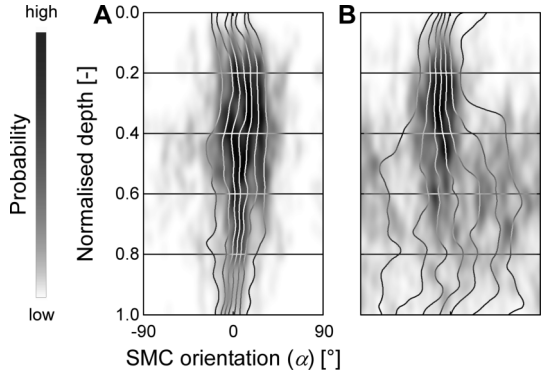

Figure 10.4: Example orientation patterns of two ureter segments. Panels **A** and **B** (view as defined in Fig. 10.3C) show two examples of orientation patterns acquired in different ureter segments. The pattern in **A** remains longitudinal from adventitial to proprial side, whereas the pattern in **B** disperses towards the proprial side.

showed a doubled variation among stacks (inter-quartile range (IQR) of $41^\circ - 25^\circ = 16^\circ$) than at the adventitial side (normalised depth 0.2, IQR of $29^\circ - 21^\circ = 8^\circ$) (Table 10.1).

10.4 Discussion

The present results, derived from our intact ureter high-resolution imaging technique, show that the LM of the ureter in rat is a single layer with predominantly longitudinally oriented SMCs. Although the dispersion of orientation did vary among individual segments, we found no particular differences between left and right ureters, nor between proximal, middle and distal sites. Since image analysis was fully automated, the quantitative differences among the ureter segments we studied are observer-independent.

The disparity among previous reports on LM structure with regard to SMC orientation and layering may have arisen because of insufficient sampling in the depth direction, apart from the potentially deleterious effects of sectioning. Unlike conventional histological approaches, our high-resolution data was obtained in intact ureters by using TPLSM, an imaging technique similar to confocal laser scanning microscopy (CLSM, Shotton 1989). In both techniques, a microscopic sample is scanned point-to-point by a focused laser beam. However, whereas in CLSM, a pinhole is used to accomplish optical sectioning, in TPLSM, optical sectioning is accomplished by the two-photon effect (Denk et al. 1990; Göppert-Mayer 1931; Helmchen and Denk 2005). As this effect only occurs in at very high light intensities, it only occurs at the laser's focus, and therefore intrinsically leads to optical sectioning (Denk and Svoboda 1997). The fact that no pinhole is required greatly increases detection sensitivity. Another advantage of TPLSM when compared to CLSM is the use of long-wavelength laser light, increasing penetration depth (Oheim et al. 2001) and limiting out-of-focus photo-bleaching. TPLSM has been applied to a wide variety of biological samples (Helmchen and Denk 2005). With our co-workers, we have used TPLSM to study the structure of large arteries in mice (Megens et al. 2007; Van Zandvoort et al. 2004). Because a rat ureter has approximately the same dimensions as

Table 10.1: Variability in dispersion among different stacks

Normalised depth	Percentile of segmental SDs at a given normalised depth		
	25th	50th	75th
0.2	21°	25°	29°
0.4	24°	29°	37°
0.6	25°	32°	48°
0.8	25°	32°	41°

To assess variability in dispersion between stacks, we calculated for each stack the orientation standard deviation (SD) at normalised depths 0.2, 0.4, 0.6 and 0.8, as we already did for the entire distribution in Fig. 10.3B. The 25th, 50th and 75th percentile of the SD values at each of these normalised depths are shown. Towards the proprial side (normalised depth 0.8), the SD showed a doubled variation among stacks (inter-quartile range (IQR) of $41°-25° = 16°$) than at the adventitial side (normalised depth 0.2, IQR of $29° - 21° = 8°$). Overall, observations between samples consistently show a longitudinal orientation.

these arteries, TPLSM is an ideal imaging modality to study the ultrastructure of these vessels.

By using TPLSM, we could show that SMC orientation dispersion changes gradually from the adventitial to proprial side. If we would have assessed SMC orientation at a limited number of depths across the LM, we could have (erroneously) identified the LM as a layered structure of a highly longitudinal outer layer and dispersely longitudinal inner layer. Unfortunately, most (older) studies on ureter wall and LM structure are rather narrative, lacking quantitative description, and as such may suffer from this pitfall (Aragona et al. 1988; Bouvin 1869; Disse 1896; Disselhorst 1894; Ebner 1902; Floyd et al. 2008; Henle 1866; Hicks 1965; Hoyes et al. 1976; Köllilker 1859; Lang et al. 2001; Maier 1881; Murnaghan 1957; Obersteiner 1871; Protopopow 1897; Sappey 1873; Satani 1919; Schneider 1938; Toldt 1877; von Möllendorff and Schröder 1930; Wolf et al. 1996; Woodburne 1965).

The predominant longitudinal orientation of SMCs in the LM requires some discussion when peristaltic function is considered. Because shortening of SMCs occurs along their long axis (Fay and Delise 1973), our results suggest that SMC contraction would rather locally shorten the ureter than cause luminal constriction. However, the role of the ureter wall matrix cannot be neglected. If the latter has a netlike structure throughout the wall, then shortening along the longitudinal axis in one segment will cause luminal constriction in a neighbouring segment, in analogy to e.g., a Chinese finger trap (Hayes et al. 1999). This concept of peristaltic bolus propulsion driven by longitudinally oriented SMCs is corroborated by a study of bolus propulsion in cat esophagus (Dodds et al. 1973), showing that bolus propulsion may be driven by the (coordinated) contraction of SMCs in a neighbouring esophageal wall segment. Further support for an active contribution to peristaltic function of longitudinally oriented SMC in the LM of the ureter is provided by the modelling study by Brasseur et al. (2007) who studied quantitatively the augmenting effect of longitudinal shortening on luminal constriction of the esophagus as caused primarily by contraction of circumferentially oriented SMCs. Taken together, our findings are not

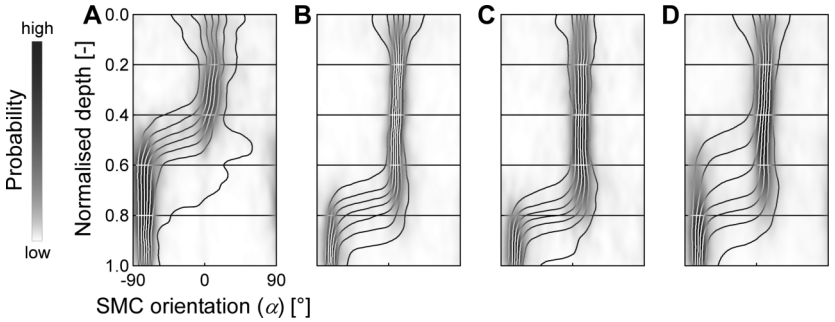

Figure 10.5: Control sample: By orientation distinguishable smooth muscle layers in the small intestine. In order to verify our image processing method, we applied the exact same preparation and staining method to a rat small intestine, an organ with clearly delineated longitudinal and circumferential smooth muscle layers (Disselhorst 1894; Maier 1881). Panels **A**—**C** show orientation distributions analogous to the panels in Fig. 10.4, at three different sites in the intestine. Panel **D** shows the average orientation distribution, calculated from panels **A**—**C**. All panels clearly show a transition from a superficial, longitudinal smooth muscle orientation to a circumferential orientation at the deep end. The patterns shown are all slightly shifted to the right by $\sim 10°$, which is caused by the fact that the two pipettes used to mount the intestine were not perfectly aligned (i.e., microscopy images were rotated by $\sim 10°$).

in conflict with the mechanics of peristalsis.

In order to validate our observation of a gradually dispersing SMC orientation across the ureter LM, in a pilot experiment, we imaged a rat small intestine, an organ known to possess clearly separated SMC layers (Disselhorst 1894; Maier 1881). In this organ, we indeed found distinct changes in orientation with depth (Fig. 10.5), confirming that the more gradual orientation change we observed in the ureters is unlikely caused by our methodology or by measurement artifacts.

Although our image acquisition and analysis approach provides compelling insight into SMC orientation in the LM of rat ureter, a number of methodological aspects should be considered. We assumed the SMC nucleus orientation to be representative of the orientation of its containing cell body, an assumption also made by Walmsley and Canham (1979) and Holzapfel et al. (2002). In an image, the cell nuclei appear separated in contrast to than the tightly packed smooth muscle cells and, therefore, are easier to delineate. Though Todd et al. (1983) state that nuclear orientation is not representative of cell orientation, it should be kept in mind that other studies describe the SMC to be clearly elongated (Rhodin 1967), whereas Todd et al. found cell shape to be irregular; a finding that could be indicative of artifacts due to histological sectioning and mechanical unloading.

A second point of attention is that, using SYTO 13 as a dye, we stained the nuclei of all cells in the ureter. By including only anisotropic nuclei in our analyses, we assumed to have assessed only SMCs. In order to verify this assumption, we performed an SMC-specific staining. From previous experiments, we know that staining entire organs (e.g., an artery) specifically for SMCs is very difficult due to the limited penetration depth of available dyes. Therefore, we chose to perform SMC-specific staining (alpha smooth

muscle actin) and bright field microscopy in one histologically fixed and sectioned ureter. In the acquired images (Fig. 10.A1), the adventitia, LM, lamina propria and urothelium are clearly visible. As the adventitia contains very few nuclei, possible crosstalk from non-SMC nuclei in the adventitia is limited. The urothelium, on the other hand, does contain large numbers of nuclei. Because these nuclei are isotropic, they are filtered out and therefore do not influence our quantification.

It is known that in the lamina propria, a layer of connective tissue, fibroblasts are present. Because of the aspecific nuclear dye that we used, also labelling fibroblast nuclei, our scans do not allow identification of the transition from LM to lamina propria. Therefore, with increasing imaging depth, the probability that we are imaging the lamina propria increases, and, hence, we cannot rule out a contribution of fibroblasts to the orientation distribution at the proprial side. This artifact may be partly responsible for the increased dispersion we observed towards this side. However, our data clearly shows that, despite this limitation, the predominant orientation is longitudinal.

Fig. 10.A1 shows that the LM also contains small blood vessels with SMCs. These SMCs could potentially influence our quantification of orientation. Therefore, we took care to acquire TPLSM stacks at such sites that all blood vessels were out of view.

Another methodological aspect to consider is that in our quantitative analysis of each image slice, when calculating the region of interest (ROI), we assumed the ureter wall to be perfectly round. However, because the ureters were not pressurised, their cross-section may have been slightly oval instead of circular. If this were the case, effective radius of curvature would have been larger and potential crosstalk among layers would have been less. Furthermore, the filling-corrected ROI function used is too conservative in case of oval ureters. This potentially removes nuclei of interest and, hence, decreases the signal-to-noise ratio.

Although our method provides quantitative data on (depth-dependent differences in) SMC orientation within the LM, application of our 2D imaging approach to a 3D cylindrical structure has its limitations. First, absolute SMC density is not quantifiable while cell nuclei appear in images at multiple depths (slice interspacing,nucleus dimensions). Second, transverse orientation (i.e., an SMC orientation not fully parallel to the ureter wall) is not measurable while transversely aligned nuclei appear foreshortened (i.e., round shaped) in the image, which may lead to elimination in the cellness filtering process (based on lack of anisotropy). In the future, 3D processing of the image stack could address these issues. For further mechanistic studies on ureter wall structure and peristaltic function, matrix composition and orientation should be further quantified and intra-vital imaging of actual ureter peristalsis should be performed.

In the present study, we imaged ureters of rats. It should be mentioned that although rat ureter structure and function cannot be directly translated to the human situation, our technique does offer an unprecedented view of the intact ureter ultrastructure. Presently, no techniques are available to accomplish this level of detail in larger (i.e., human) intact ureters.

From this study, we conclude that smooth muscle cell orientation in rat ureter is predominantly longitudinal. The observed gradual dispersion towards the proprial side does not support identification of separate layers. Our minimally invasive and quantitative image acquisition and analysis approach is a crucial step towards more quantitative insight into ureter peristaltic function, and can also be used to study smooth muscle cell

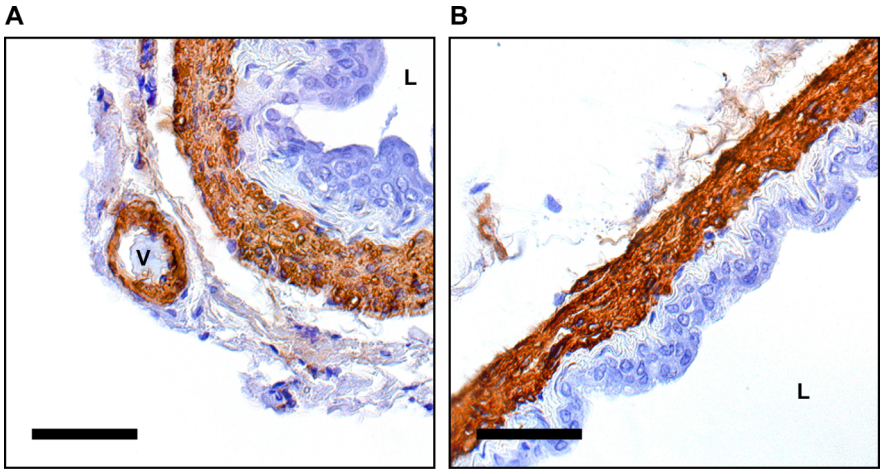

Figure 10.A1: Alpha smooth muscle actin staining in histological ureter sections. Panels **A** and **B** show cross-sectional and longitudinal sections of a rat ureter, stained for alpha smooth muscle actin (brown) and nuclei (purple). Scale bar: 50 µm. L, lumen; V, blood vessel. Histology was performed on a ureter fixed in 4% buffered paraformaldehyde, routinely processed, embedded in paraffin, and sectioned at 4 µm. Sections were labelled with monoclonal anti-alpha smooth muscle actin-fluorescein isothiocyanate (FITC) antibodies (Sigma-Aldrich, St. Louis, MO) and successively stained with anti-FITC horseradish peroxidase (HRP). Nuclei were stained using haematoxylin. Imaging was performed using a Nikon Eclipse 800 microscope (Nikon Instruments Inc., Melville, NY) equipped with a Nikon S Fluor 40x/1.30 oil immersion objective. Images were acquired using a Media Cybernetics Evolution VF camera (Media Cybernetics Inc., Rockville, MD).

orientation in other tube-like structures, e.g., in gut and in blood vessels.

10.5 Acknowledgements

We would like to thank Chantal Pöttgens and Timo Rademakers for assistance with histological staining. Furthermore, the help of Wim Engels, Jeroen Hameleers, Remco Megens, and Ward Vanagt is gratefully acknowledged.

10.A1 Appendix: Detailed methods

10.A1.1 Experimental procedures

Experiments and procedures were approved by the local ethics committee on use of laboratory animals. Our experimental animal group consisted of six Wistar rats, from the experimental animal center of Maastricht University. Animals were euthanised with CO_2. Within 5 minutes after euthanasia, the ureters were approached via a median incision, opening the abdominal cavity. Proximal and distal ends of the ureter were cut 1 mm from

the renal pelvis and 5 mm from the bladder, respectively. Identification of the proximal end was achieved by applying surgical wire to the proximal end. Distinction between left and right ureter samples was achieved by tying one wire on the proximal end of left-sided and two wires on the proximal end of right-sided ureters. Excessive fat surrounding the ureters was manually removed under a stereomicroscope. Next, the excised rat ureters were mounted between glass micropipettes in a custom-built ureter mounting chamber (Fig. 10.1A), containing Hanks' Balanced Salt Solution (HBSS; Life Technologies Europe BV, Bleiswijk, the Netherlands) in which the ureter remained immersed during the whole staining and imaging process. The HBSS we used had a pH of 7.4 and contained NaCl (137 mM), HEPES (15 mM), glucose (5.5 mM), KCl (5.3 mM), $CaCl_2$ (2.5 mM), Na_2HPO_4 (0.34 mM), KH_2PO_4 (0.44 mM) and $MgSO_4$ (1.1 mM). Specimens were stained with the DNA/RNA fluorescent dye SYTO 13 ($\lambda_{max,emission} = 520\,nm$; Life Technologies), diluted with HBSS to a final concentration of $2\,\mu M$. HBSS in the mounting chamber was replaced with the diluted SYTO 13, as was the intraluminal HBSS. To avoid bleaching of the staining solution by ambient light, the setup was covered with aluminum foil during staining. After 30 minutes, the staining solution was again replaced with pure HBSS. Imaging was performed with a two-photon laser scanning microscopy (TPLSM) system (Leica TCS SP5 MP, Leica Mikrosysteme Vertrieb GmbH, Wetzlar, Germany) equipped with an HCX APO L 20x/1.00W water dipping objective and a Hamamatsu R9624 (Hamamatsu Photonics, Hamamatsu city, Japan) photomultiplier tube (PMT). Two-photon excitation was achieved using a pulsed Ti-Sapphire laser (Chameleon Ultra II, Coherent Inc., Santa Clara, USA) at a wavelength of 800 nm. Laser power was kept as low as possible to avoid tissue damage. Scanning frequency was set to 600 lines per second. Resolution (1480×1480 pixels) and field of view size ($738 \times 738\,\mu m^2$) were kept constant throughout the imaging process, resulting in a pixel size of $0.5 \times 0.5\,\mu m^2$. Image stacks were acquired at 12 bits and with an inter-slice distance of $0.5\,\mu m$, traversing the ureter wall from out- to inside. Three image stacks were acquired along the length of the ureter at proximal, middle and distal positions. After acquisition, lateral field of view was reduced by cropping the images to a resolution of 512×512 pixels to ease further processing and limit computation time.

10.A1.2 Processing and analysis

Cropping and diameter assessment

In each acquired stack, ureter diameter was assessed by showing a transversal section through the stack and drawing a circle on screen using ImageJ 1.47v (National Institutes of Health, Bethesda, Maryland, USA). After diameter assessment, the lateral field of view was reduced by cropping the images to a resolution of 512×512 pixels to ease further processing and limit computation time. All further processing was performed using MATLAB R2013b (The MathWorks Inc, Natick, Massachusetts, USA).

Cellness filtering

Stack images were filtered using cellness filtering, in analogy to vesselness filtering (Frangi et al. 1998). This filtering is a technique originally developed to enhance blood

vessels in 2D or 3D image stacks (Frangi et al. 1998). Cellness filtering enhances elongated structures (in this case, SMC nuclei) in an image and suppresses background noise, thereby resulting in a high-contrast image with clearly delineated cell nuclei. First, for each pixel, a Hessian matrix $\mathbb{H}$ is computed:

$$\mathbb{H}(x,y) = \begin{bmatrix} \left.\frac{\partial^2 I}{\partial x^2}\right|_{x,y} & \left.\frac{\partial^2 I}{\partial x \partial y}\right|_{x,y} \\ \left.\frac{\partial^2 I}{\partial x \partial y}\right|_{x,y} & \left.\frac{\partial^2 I}{\partial y^2}\right|_{x,y} \end{bmatrix} , \tag{10.A1}$$

with $I(x,y)$ being the image intensity at a given point. Hessian terms are calculated by convolution of the image with the respective second-order derivatives of a 2D Gaussian kernel G:

$$G(x,y) = \frac{e^{-\frac{x^2+y^2}{2\sigma^2}}}{2\pi\sigma^2} , \tag{10.A2}$$

in which σ is the kernel standard deviation (Table 10.A1). Second, for each pixel, the eigenvalues ($\left|\lambda_{\mathbb{H},1}\right| \leq \left|\lambda_{\mathbb{H},2}\right|$)of $\mathbb{H}$ are computed, which are subsequently used to calculate blobness ($0 \leq R_B \leq 1$) and structureness ($S \geq 0$):

$$R_B = \left|\frac{\lambda_{\mathbb{H},1}}{\lambda_{\mathbb{H},2}}\right| , \text{ and} \tag{10.A3}$$

$$S = \sqrt{\lambda_{\mathbb{H},1}^2 + \lambda_{\mathbb{H},2}^2} . \tag{10.A4}$$

For pixels in an isotropic structure, in which the eigenvalues are approximately equal, $R_B = 1$; whereas for pixels in an anisotropic structure, $R_B \to 0$. Cell pixels can be distinguished from background pixels by S, because the magnitude of the derivatives (and thus of the eigenvalues) in background pixels is small (Frangi et al. 1998). R_B and S are combined into cellness ($0 \leq C \leq 0$) using

$$C = \begin{cases} 0, & \lambda_{\mathbb{H},2} > 0 \\ \left(e^{-\frac{R_B^2}{2\beta^2}}\right) \cdot \left(1 - e^{-\frac{S^2}{2\gamma^2}}\right), & \lambda_{\mathbb{H},2} \leq 0 \end{cases} , \tag{10.A5}$$

with β and γ being parameters weighing blobness and structureness, respectively (Table 10.A1).

Smooth muscle cell identification

Cellness-filtered images were thresholded at θ_C (Table 10.A1), yielding binary images. In these images, pixels of value 1 were clustered based on their 8-adjacency (Gonzalez and Woods 2008), each cluster signifying an SMC. Clusters were subsequently filtered based on the their surface area using lower and upper thresholds of $\theta_{A,\downarrow}$ and $\theta_{A,\uparrow}$, respectively (Table 10.A1).

Table 10.A1: Parameter values used in image analysis

Parameter	Unit	Value	Description
σ	µm	1.9	Cellness filtering kernel width (equals 4 pixels).
β	-	0.5	Cellness filtering parameter weighing blobness, which is used to distinguish blob-like from line-like structures.
γ	-	100	Cellness filtering parameter weighing image intensity.
θ_c	-	0.01	Threshold used to convert cellness images to binary images.
$\theta_{A,\downarrow}$	µm^2	23	Lower cross-sectional area threshold (equals 100 pixels). Clusters with a smaller cross-sectional area than $\theta_{A,\downarrow}$ are filtered out.
$\theta_{A,\uparrow}$	µm^2	230	Upper cross-sectional area threshold (equals 1000 pixels). Clusters with a larger cross-sectional area than $\theta_{A,\uparrow}$ are filtered out.
Δr_{max}	µm	6	Effective slice thickness, i.e., the maximum crosstalk depth.
$\theta_{\lambda_{\mathbb{M}}}$	-	1.5	Lower threshold for the ratio of eigenvalues ($\frac{\lambda_{\mathbb{M},2}}{\lambda_{\mathbb{M},1}}$; i.e., anisotropy) of a cluster. Clusters with a ratio below this value are filtered out.
σ_z	-	0.02	Probability density estimation kernel size in depth-direction.
κ	-	100	Probability density estimation kernel concentration parameter in angular direction.

Parameters were chosen to obtain optimal results. σ represents the standard deviation and therefore approximately half the width of the Gaussian derivative kernel used in cellness filtering. In order to optimally detect the SMC nuclei, the kernel width should be approximately equal to the width of the SMCs, which, in our case, was about 3–4 µm. $\beta = 0.5$ was known to give good results in other studies (Frangi et al. 1998). $\gamma = 100$ was determined empirically. It should be noted that the choice of γ depends on the intensity of the acquired images. The value of θ_c was not critical (cellness rapidly decreases to very low values outside nuclei). $\theta_{A,\downarrow}$ and $\theta_{A,\uparrow}$ were determined empirically, however, an estimate of the SMC cross-sectional area can be calculated from the SMC nucleus' mean short axis (mean ± SD, $l_1 = 3.1 \pm 0.8$ µm for an aortic SMC, O'Connell et al. 2008) and long axis ($l_2 = 19.0 \pm 3.3$ µm for an aortic SMC, O'Connell et al. 2008) lengths, assuming an elliptically shaped cross-section: $A_{ellipse} = \frac{\pi l_1 l_2}{4} = 46 \pm 15\,\mu m^2$. Therefore, $\theta_{A,\downarrow}$ and $\theta_{A,\uparrow}$ do include SMC nuclei of normal sizes. The choice of Δr_{max} was a tradeoff between minimisation of crosstalk (small Δr_{max}) and number of included nuclei (large Δr_{max}). $\theta_{\lambda_{\mathbb{M}}}$ was safely set to 1.5 (actual SMC anisotropy (e.g., $\frac{l_2}{l_1} = 6.1 \pm 1.2$, O'Connell et al. 2008) is much larger). σ_z and κ were chosen by assessing probability density estimates calculated using various combinations of σ_z and κ and choosing those values that gave the optimal trade-off between noise and detail.

Region of interest application

As flat image slices were acquired of a curved object, structures (clusters) at various depths of the wall could end up in one image slice. This crosstalk among slices can be reduced by narrowing the ROI used for quantification of SMC orientation (Fig. 10.1B). With increasing imaging depth (z), and thus with a decreasing radius of curvature of the ureter wall, the ROI should narrow. For a certain effective slice thickness ($\Delta r_{\max} = r_2 - r_1 = 6\,\mu\text{m}$, Fig. 10.1B and Table 10.A1), it can be shown that for the crosstalk-limiting ROI ($R_{\text{I,cl}}(z)$), it holds that:

$$R_{\text{I,cl}}(z) = 2\sqrt{(r_0 - z + \Delta r_{\max})^2 - (r_0 - z)^2}\,, \tag{10.A6}$$

with r_0 being the outer ureter radius, i.e., the distance from the ureter axis to the outermost muscle layer.

For the outermost slices, the crosstalk-limiting ROI is not fully filled with the lamina muscularis (Fig. 10.1B). In order to correctly estimate SMC density, which will be calculated by dividing the number of detected cells within a slice's ROI by the surface area of this ROI, a filling-corrected ROI ($R_{\text{I,fc}}(z)$) was defined:

$$R_{\text{I,fc}}(z) = 2\sqrt{r_0^2 - (r_0 - z)^2}\,. \tag{10.A7}$$

For $z = \Delta r_{\max}$, $R_{\text{I,cl}}(z) = R_{\text{I,fc}}(z)$. From this depth ($z = \Delta r_{\max}$), $R_{\text{I,cl}}(z)$ is again used as the normalising function. In summary, the overall ROI function ($R_{\text{I}}(z)$) can be formulated as

$$R_{\text{I}}(z) = \begin{cases} 2\sqrt{r_0^2 - (r_0 - z)^2}, & z \le \Delta r_{\max} \\ 2\sqrt{(r_0 - z + \Delta r_{\max})^2 - (r_0 - z)^2}, & z > \Delta r_{\max} \end{cases}\,. \tag{10.A8}$$

Orientation calculation

In order to obtain the principal axes of the clusters of interest (i.e., clusters that satisfy the area criteria $\theta_{\text{A},\downarrow}$ and $\theta_{\text{A},\uparrow}$, and that are within the ROI), for each of these clusters, a structure tensor ($\mathbb{M}$) was calculated (Jähne 1993; Vader et al. 2009):

$$\mathbb{M} = \begin{bmatrix} \sum (x - x_{\text{c}})^2 & \sum (x - x_{\text{c}})(y - y_{\text{c}}) \\ \sum (x - x_{\text{c}})(y - y_{\text{c}}) & \sum (y - y_{\text{c}})^2 \end{bmatrix}, \tag{10.A9}$$

with (x_{c},y_{c}) the cluster's center of mass. Nuclear shape can now be assessed based on the eigenvalues ($\lambda_{\mathbb{M},1} \le \lambda_{\mathbb{M},2}$) of $\mathbb{M}$. Only clearly elongated clusters ($\frac{\lambda_{\mathbb{M},2}}{\lambda_{\mathbb{M},1}} \ge \theta_{\lambda_{\mathbb{M}}}$, Table 10.A1) were considered in the analysis to include SMC nuclei but to exclude e.g., fibroblasts. For the included nuclei, the eigenvector corresponding to the largest eigenvalue ($\lambda_{\mathbb{M},2}$) of $\mathbb{M}$ represents the principal cluster orientation. Nuclear orientation is expressed by the angle α of this eigenvector with the longitudinal ureter axis (Fig. 10.1C–E).

Probability density estimation

For each stack, z was normalised to a range of $[0, 1]$, yielding z_{n}. Subsequently, a two-dimensional (α, z_{n}) kernel density estimate (KDE, Silverman 1986) was calculated[1] (Fig.

[1] Kernel density estimation is comparable to the calculation of a histogram, but, has an important advantage, since the mandatory choice of origin of the histogram (and, therefore, of the cutoff values for each bin, potentially influencing results) is avoided.

10.1F, Fisher 1989). Kernel density estimation allows for estimation and visualisation of the probability density from a set of data points, which, in our case, shows how often a certain SMC orientation is observed at a certain imaging depth. Briefly, the contribution of each data point $(\alpha_c, z_{n,c})$ is spread out over a (relatively small) area (Fisher 1989; Fisher 1995); the KDE at a given depth (z_n) in a given direction (α) is then the sum of the contributions of the smeared-out points at this (α,z_n), and equals 1 when integrated over the full (α,z_n)-plane. The contributions are described by a two-dimensional function, the so-called "kernel". In depth direction, this kernel was normally shaped, whereas in the angular direction, a Von-Mises shape is used:

$$K(\alpha, z_n) = \frac{1}{N} \frac{e^{\frac{-(z_n - z_{n,c})^2}{2\sigma_z^2}}}{\sqrt{2\pi}\sigma_z} \frac{e^{\kappa \cos(2(\alpha - \alpha_c))}}{2\pi I_0(\kappa)} , \tag{10.A10}$$

where N is the total number of data points per ureter segment, $(\alpha_c, z_{n,c})$ is the kernel center, σ_z is the kernel width in z-direction, κ is a measure of concentration in angular direction, and I_0 is a modified Bessel function of order 0. The at first sight unusual choice of a Von-Mises distribution is required since α describes a direction (ranging from, e.g., −90 to 90°) (Fisher 1995). A kernel in α-direction, therefore, must be π-periodic. σ_z and κ were set to 0.02 and 100, respectively (Table 10.A1).

In addition to the KDEs per ureter segment, an overall KDE was calculated of all 36 imaged ureters by essentially adding all 36 separate KDEs and dividing by 36. For each depth, eight quantiles (octiles) were calculated and displayed as lines on the KDE.[1]

Cell density estimation

Cell density at a given slice (z), having the unit "cells per cross-sectional area", is calculated by dividing the number of detected nuclei in this slice by the surface area of the region of interest $R_I(z)$ for that slice. The key difference between cell densities and the aforementioned probability densities is that cell densities are corrected for the ROI and, thus, give a measure of the physical cell density.

[1] Because of data circularity, the middle octile line does not represent the median angle.

Chapter 11

3D quantification of smooth muscle orientation in murine carotid arteries

The contents of this chapter are based on:

Bart Spronck,[1] Remco T.A. Megens,[1,2] Koen D. Reesink,[1] and Tammo Delhaas[1] (2016). A method for three-dimensional quantification of vascular smooth muscle orientation: application in viable murine carotid arteries. *Biomechanics and modeling in mechanobiology* 15:419–432.

[1] Department of Biomedical Engineering, CARIM School for Cardiovascular Diseases, Maastricht University, Maastricht, The Netherlands.
[2] Institute for Cardiovascular Prevention, Ludwig-Maximilians-Universität, Munich, Germany.

Abstract

When studying *in vivo* arterial mechanical behaviour using constitutive models, smooth muscle cells (SMCs) should be considered, while they play an important role in regulating arterial vessel tone. Current constitutive models assume a strictly circumferential SMC orientation, without any dispersion. We hypothesised that SMC orientation would show considerable dispersion in three dimensions and that helical dispersion would be greater than transversal dispersion. To test these hypotheses, we developed a method to quantify the 3D orientation of arterial SMCs. Fluorescently labelled SMC nuclei of left and right carotid arteries of ten mice were imaged using two-photon laser scanning microscopy. Arteries were imaged at a range of luminal pressures. 3D image processing was used to identify individual nuclei and their orientations. SMCs showed to be arranged in two distinct layers. Orientations were quantified by fitting a Bingham distribution to the observed orientations. As hypothesised, orientation dispersion was much larger helically than transversally. With increasing luminal pressure, transversal dispersion decreased significantly, whereas helical dispersion remained unaltered. Additionally, SMC orientations showed a statistically significant ($p < 0.05$) mean right-handed helix angle in both left and right arteries and in both layers, which is a relevant finding from a developmental biology perspective. In conclusion, vascular SMC orientation 1) can be quantified in 3D; 2) shows considerable dispersion, predominantly in the helical direction; and 3) has a distinct right-handed helical component in both left and right carotid arteries. The obtained quantitative distribution data are instrumental for constitutive modelling of the artery wall and illustrate the merit of our method.

11.1 Introduction

SMOOTH muscle cells (SMCs) play a crucial role in regulating arterial vessel tone. When an SMC contracts, it exerts a force along its long axis. Therefore, the orientation of SMCs within the artery wall is mechanically of importance. Several mechanical models of the artery wall include a smooth muscle component, e.g., (Masson et al. 2011; Spronck et al. 2015a; Zulliger et al. 2004b). To our knowledge, all currently available constitutive models assume SMC orientation to be strictly circumferential and ignore any dispersion in SMC orientation. In order to develop constitutive models that describe SMC orientation more realistically, knowledge on SMC orientation and its dispersion is essential.

The assumption in current constitutive models of strictly circumferentially oriented SMCs may have arisen from experimental studies (Peters et al. 1983; Walmsley 1983), stating that SMC orientation is circumferential. Other studies have shown a more disperse SMC orientation with two main orientations (Holzapfel et al. 2002), and have shown that SMCs are enveloped by collagen bundles, leading to a parallel orientation of collagen and SMCs in the media of rat aortas (O'Connell et al. 2008). In the aforementioned studies on SMC orientation, arteries were first fixed and subsequently histologically sectioned,

potentially causing artefacts. To overcome this problem, a method using intact arteries is required.

Previously, we developed a two-dimensional (2D) method to quantify SMC orientation in vessels using two-photon laser scanning microscopy (TPLSM) (Spronck et al. 2014b). This method, which was used in rat ureters, had the advantage over previous methods that it did not require sectioning. However, it only yielded 2D orientations, neglecting out-of-plane orientation. Clearly, using such a method, it is impossible to quantify transverse angles. In addition, due to the curvature of the wall, only a very limited part of the wall could be analysed, leading to inclusion of only a few SMCs per acquisition. To parameterise a constitutive model, ideally, three-dimensional (3D) orientation and dispersion information are available.

We hypothesised that SMC orientation would show considerable dispersion, based on recent published work assessing porcine aortic SMC orientation in 2D (Tonar et al. 2015). As we expected SMCs to be mainly oriented in the plane of the arterial wall (Peters et al. 1983), we further hypothesised SMC orientation dispersion in the helical direction to be greater than in the transversal direction. To test these hypotheses, we developed a method for quantification of 3D SMC orientation, applicable to viable, intact murine carotid arteries. This 3D method does allow for quantification of transverse angles and is suited for analysis of a much larger part of the acquired vessel wall than the previous 2D method (Spronck et al. 2014a; Spronck et al. 2014b). In the present study we used this 3D method to assess orientation and dispersion differences between left and right carotid arteries (potentially relevant from a developmental biology point of view). Additionally, we investigated the effect of increasing luminal pressure on 3D SMC orientation.

11.2 Methods

11.2.1 Animals and staining

Mice were sacrificed with an overdose of isoflurane (Forane, Baxter, Deerfield, IL). Left and right common carotid arteries of ten male C57BL/6JRj mice were excised, labelled at the proximal end, and carefully mounted between micropipettes (Fig. 11.1A) to maintain viability for a prolonged period of time ($>$ 2 hrs) as described previously (Megens et al. 2007). Carotid artery sections of 5 mm were mounted, yielding a length of 3 mm of artery usable for imaging (i.e., without imaging one of the pipettes). Calcium-free HEPES buffer was used as submersion medium. SMC nuclei were stained using 2.7 μM SYTO 13 (Life Technologies, Gaithersburg, MD) for 30 minutes. Arteries were maximally vasodilated by addition of nitroprusside (Sigma-Aldrich, St. Louis, MO) to a concentration of 10 μM, and were imaged at room temperature. Animals were checked for situs inversus totalis (SIT) by inspection of the location of the visceral organs; none of the animals showed SIT. All animal experiments were approved by the local authority and were performed in accordance with the ethical standards laid down in the 1964 Declaration of Helsinki and its later amendments.

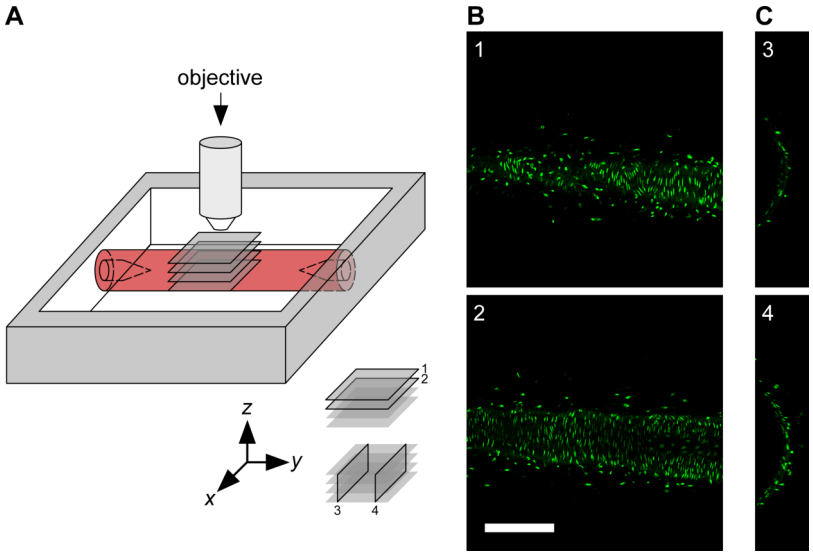

Figure 11.1: Data acquisition. **A**: Measurement set-up. The common carotid artery is mounted between glass micropipettes and imaged with an upright microscope. 1 and 2 indicate example x-y image slices in **B**, 3 and 4 indicate examples of reconstructed x-z image slices in **C**. **B**: Example x-y image slices acquired at increasing imaging depth, i.e., at decreasing z-coordinate (1: $z = 93\,\mu m$, 2: $z = 81\,\mu m$). Scale bar: 200 µm. **C**: Examples of reconstructed x-z image slices. Figure scale equal to scale in **B**.

11.2.2 Image acquisition

Viable mounted arteries were imaged using an upright TPLSM system (Leica TCS SP5II MP, Leica Microsystems, Mannheim, Germany) equipped with a Leica HCX APO L 20x/1.00W water dipping objective (Fig. 11.1A). Two-photon excitation was achieved using a pulsed Ti-Sapphire laser (Spectra Physics Mai Tai DeepSee, Newport, USA) tuned at 825 nm. Signal detection was performed using a descanned hybrid diode detector (GaAsP) between wavelengths of 510 and 555 nm. Image slices of 1480 × 1480 pixels were acquired with a pixel size of 0.5 × 0.5 µm^2, resulting in a field of view of 0.74 × 0.74 mm^2. Pixel dwell time was 1.1 µs, acquisition was performed at 12 bit precision. Acquisition of one slice took 2.6 s. Slice spacing was 0.5 µm, resulting in an effective voxel size of 0.5 × 0.5 × 0.5 µm^3. All subsequent image processing (see following section) was performed at this resolution; no downsampling was performed. Images slices formed stacks of 334 ± 30 slices (mean ± SD). Left carotid arteries were imaged at luminal pressures of 40, 80, and 100 mmHg, respectively. Right carotid arteries were imaged at 40 mmHg. At each luminal pressure, one image stack was acquired for each animal. Representative image slices are shown in Fig. 11.1B,C. All subsequent image processing was performed at full resolution, i.e., no downsampling was performed. All arteries were imaged directly after excision. A maximum of two hours were required to complete the imaging of the left and right arteries of one mouse. Previously, we have shown that in this time span, mounted arteries remain viable (Megens et al. 2007).

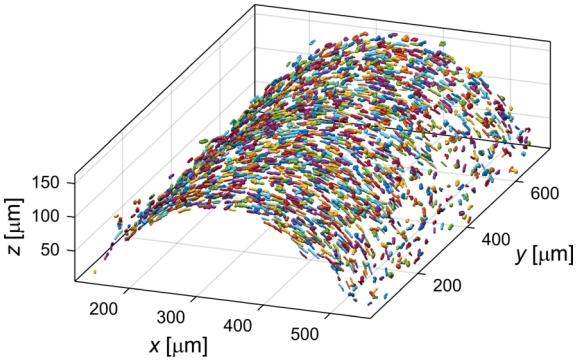

Figure 11.2: Isosurface plot showing detected SMC nuclei. Nuclei are randomly coloured for clarity. SMC, smooth muscle cell.

11.2.3 Image processing

Deconvolution and vesselness filtering

Raw image stacks were deconvolved using 10-pass adaptive blind 3D deconvolution (AutoQuant X2, MediaCybernetics, Bethesda, MD). Deconvolution of one stack took approximately 35 min on a modern computer (Intel i7-2670QM quad-core central processing unit (CPU) at 2.20 GHz and 16 GB of random access memory (RAM)). Further data processing and analysis were performed using MATLAB R2014b (MathWorks, Natick, MA). After deconvolution, the deconvolved data stack was 3D vesselness-filtered (Frangi et al. 1998) to enhance elongated structures. Note that in contrast to the approach described in our previous paper (Spronck et al. 2014b), filtering is performed in 3D on the image stack as a whole. A 3×3 Hessian matrix was calculated for each voxel using a Gaussian width of $\sigma_x = \sigma_y = \sigma_z = 1\,\mu\text{m}$. Hessian components were calculated by convolving the image stack with discretised Gaussian derivative kernels. The eigenvalues of the Hessian matrix ($\lambda_1 \leq \lambda_2 \leq \lambda_3$) were used for performing the vesselness filtering. Vesselness parameters were $\alpha = \beta = 0.5$ (Frangi et al. 1998). c was determined for each image stack as half the value of the maximum Hessian norm, as suggested by Frangi et al. (1998). Vesselness filtering of one stack took approximately 65 min on a modern computer (see above). All further image processing steps were completed in < 1 min per stack.

Clustering and cell orientation calculation

To separate cell nuclei from background, the vesselness stack was thresholded at a cut-off value of 0.01. Voxels were then clustered based on their 3D 6-connected neighbourhood (Gonzalez and Woods 2008). Clusters were included based on their volume using upper (320.1 μm^3) and lower (38.5 μm^3) thresholds calculated as mean $\pm$ 2SD from aortic SMC nucleus sizes (O'Connell et al. 2008). An example of a stack of clustered nuclei is given in Fig. 11.2. For each cluster, an inertia matrix was calculated (Jähne 1993; Vader et al. 2009). The eigenvector corresponding to the largest eigenvalue of this matrix represents the principal SMC orientation.

Coordinate transformation

To assess SMC orientations with respect to the vessel wall, a cylinder was least-squares fitted through the detected centroids as follows: First, a rough fit was obtained by fitting a cylinder through all centroids. Using the axis of this cylinder, the inner layer of centroids was detected by selecting the centroids closest to the axis in a moving 3D search window of 50 µm in axial and 10° in angular directions. Second, a cylinder was fitted through the detected inner layer of centroids. The axis of this cylinder was used as a reference to convert all centroid locations to cylindrical coordinates (ρ, θ, z_c, Fig. 11.3A). Subscript c in z_c is used to distinguish the axial cylindrical coordinate (z_c, Fig. 11.3A) from the vertical cartesian coordinate (z, Fig. 11.1 and 11.2). The orientations of the SMCs were expressed locally with respect to the vessel wall (Fig. 11.3B) and are represented as a point on a unit hemisphere (Fig. 11.3C). Orientations were quantified by a helix angle ($-90° \leq \theta_h < 90°$) and a transverse angle ($-90° \leq \theta_t < 90°$, Fig. 11.3C and D). Visual inspection of the detected cell nuclei (as exemplified in Fig. 11.2) shows that, from a certain imaging depth, the number of detected nuclei decreased. In order to assure that we imaged a region of sufficient image quality, centroids were selected from an angular region of interest of $-22.5° \leq \theta \leq 22.5°$. In order to prevent border effects, an axial window slightly smaller than the z_c-range was manually selected (704 ± 23 µm, mean ± SD). In 6 stacks, using this large axial window led to SMC layers getting merged during SMC layer detection (see following section) due to inhomogeneities in vessel diameter along the axial coordinate. In these cases, a smaller window of 379 ± 74 µm (mean ± SD) was used.

Smooth muscle layer separation

Cell density as a function of the radial coordinate (ρ) was calculated using kernel smoothing density estimation (KDE) (Silverman 1986). KDE allows for estimation and visualisation of the probability density from a set of data points. In our case, the KDE shows the density of SMCs at a certain radial coordinate (ρ). A Gaussian kernel with $\sigma = 1$ µm was used on the list of radial coordinates (ρ) of all included nuclei of one stack, yielding the initial kernel density estimate $f(\rho)[\mu m^{-1}]$. This estimate was converted to an absolute density $d(\rho)$ in cells per μm^3 via

$$d(\rho) = f(\rho)\frac{N}{r_\theta r_{z_c} \rho}\ , \tag{11.1}$$

with N the total number of detected nuclei, r_θ the angular region of interest in radians, and r_{z_c} the axial region of interest in µm. An example density plot is shown in Fig. 11.4A. SMCs showed to be concentrated in two distinct layers, as visible in the example. We analysed SMC orientation separately for these (inner and outer) layers. To separate the layers, we detected the two density maxima, the distance between which we defined as 2Δ. Each layer is taken to be centred around its maximum, with boundaries of $\pm\Delta$ on each side (Fig. 11.4A). The artery diameter (as reported in the Results section) is taken to be the middle between the inner and outer layer density maxima.

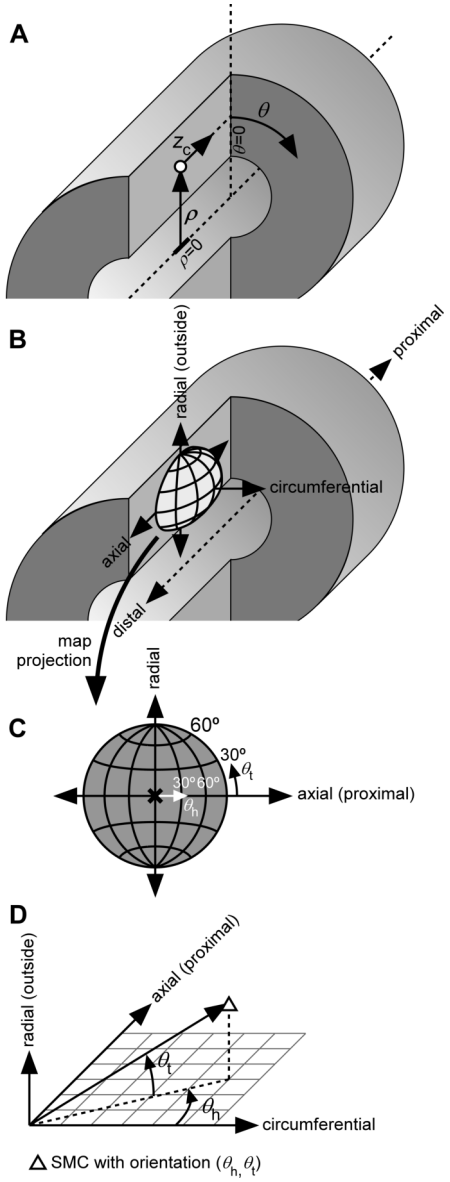

Figure 11.3: Coordinate and orientation definitions. **A**: Definition of cylindrical coordinate system using radial (ρ), angular (θ), and axial (z_c) coordinates. **B**, **C**: Orientations of SMCs can be visualised as points on a unit hemisphere. Panel **B** shows the orientation of such a hemisphere with respect to the vessel. Panel **C** shows the two spherical coordinates that are used to quantify SMC orientation. θ_h and θ_t are an SMC's helix and transverse angles, respectively. **D**: Exact definitions of θ_h and θ_t. θ_h is the angle that the orientation's projection on the axial-circumferential plane makes with the circumferential direction. θ_t is the angle that the orientation makes with the axial-circumferential plane. SMC, smooth muscle cell.

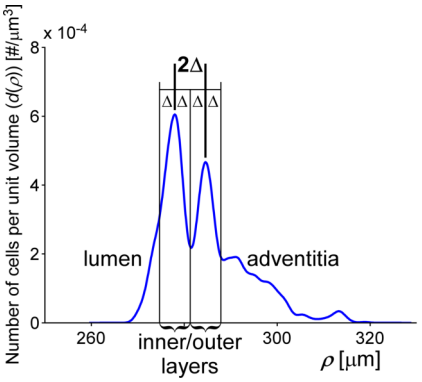

Figure 11.4: Representative example of SMC density as a function of the radial coordinate (ρ, Fig. 11.3A). Inner and outer layers of SMCs are clearly visible. Layers were detected by finding the two largest density maxima. The distance between those maxima was defined as 2Δ. SMCs are assumed to be part of the inner/outer layer if they are within a distance of Δ from their respective maximum. SMC, smooth muscle cell.

Orientations of SMC nuclei in detected layers

After smooth muscle layer separation, SMC orientations can be depicted on a projected hemisphere, as defined in Fig. 11.3C. A representative example of such a visualisation is given in Fig. 11.5A–C. The need for using a projection is elaborated on in Appendix 11.A1.

11.2.4 Orientation statistics

As our method yields orientations in 3D; appropriate, spherical statistics are required to accurately quantify our results (Fisher et al. 1993). In particular, the obtained orientations are undirected (i.e., axial data), requiring a 3D probability distribution that is antipodally symmetric (Mardia and Jupp 2000). One of the simplest distributions of this kind would be a (rotationally symmetric) Watson distribution (Mardia and Jupp 2000). However, this distribution requires data to be rotationally symmetric around the main direction. In the vessel wall, the largest spread in SMC direction will be in the axial-circumferential plane, whereas the spread in the radial-circumferential plane will be much smaller. The probability distribution used should be able to accommodate this non-rotationally-symmetric geometry. The Bingham distribution fulfills this requirement, while still being antipodally symmetric (Bingham 1964; Bingham 1974). The Bingham density function has the form (Bingham 1964):

$$\rho(\underset{\sim}{\mu_1}, \underset{\sim}{\mu_2}, \kappa_1, \kappa_2, \underset{\sim}{x}) = \frac{\exp\left(\kappa_1(\underset{\sim}{\mu_1}^T \underset{\sim}{x})^2 + \kappa_2(\underset{\sim}{\mu_2}^T \underset{\sim}{x})^2\right)}{K(\kappa_1, \kappa_2)}, \tag{11.2}$$

where κ_1 and κ_2 are two concentration parameters, $\underset{\sim}{\mu_1}$ and $\underset{\sim}{\mu_2}$ are two orthogonal unit vectors indicating the two spread directions of the distribution (corresponding to κ_1 and

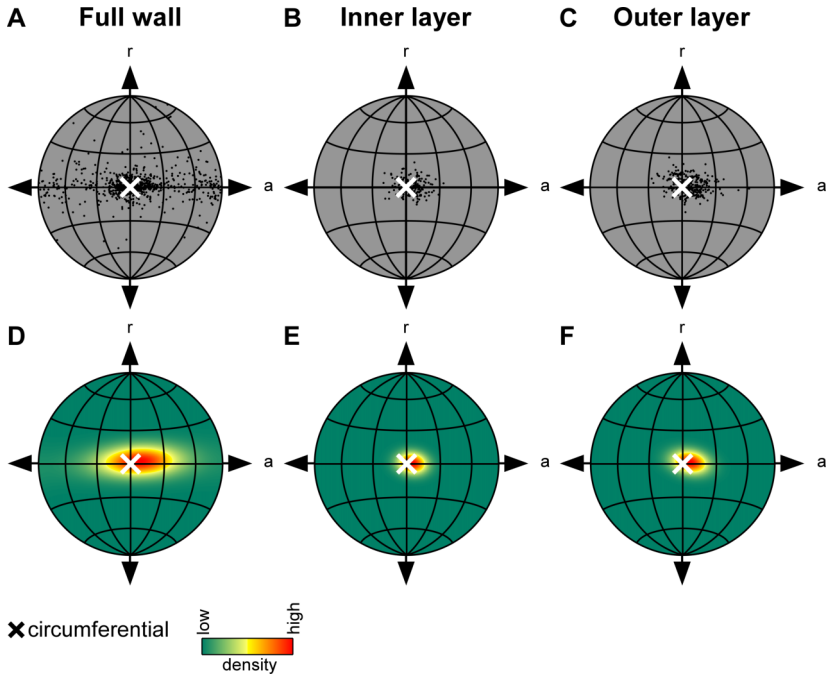

Figure 11.5: Representative examples of orientations of SMC nuclei in the artery wall. **A**, **B**, **C**: Orientations of detected nuclei, visualised using Lambert equal-area projection: **A** before layer separation, **B** for the inner layer, and **C** for the outer layer. The Lambert equal-area projection is elaborated on in Appendix 11.A1. **D**, **E**, **F**: Corresponding fitted Bingham distributions to orientations in panels **A**, **B**, **C**. The obtained Bingham distributions provide a quantification of the distribution of the individual orientations. The distribution parameters are explained in Fig. 11.6. SMC, smooth muscle cell; a, axial; r, radial.

κ_2), and $\underset{\sim}{x}$ the current local (Cartesian) coordinate on the unit sphere. The normalisation function $K(\kappa_1, \kappa_2)$ was evaluated by numerically solving the integral (Bingham 1964; Onstott 1980)

$$K(\kappa_1, \kappa_2) = \int_0^{2\pi} \int_0^{\pi} \exp\left(\left(\kappa_1 \cos^2\phi + \kappa_2 \sin^2\phi\right) \sin^2\theta\right) \sin\theta \, \mathrm{d}\theta \, \mathrm{d}\phi \ . \tag{11.3}$$

Fitting the Bingham distribution to our data was performed in two steps by using the moment method (Bingham 1964; Onstott 1980; Tanaka 1999). First, the local centroid orientations were converted to Cartesian coordinates

$$\underset{\sim}{x} = \begin{bmatrix} \cos\theta_t \cos\theta_h \\ \cos\theta_t \sin\theta_h \\ \sin\theta_t \end{bmatrix} , \tag{11.4}$$

and the following matrix was computed:

$$\underline{\underline{X}} = \left(\underset{\sim}{x}_1 \dots \underset{\sim}{x}_N \right) , \tag{11.5}$$

with N the number of detected centroids. $\underset{\sim}{\mu}_1$ and $\underset{\sim}{\mu}_2$ can now be obtained as the eigenvectors of $\underline{\underline{XX}}^T$ corresponding to the smallest and middle eigenvalues, respectively. $\underset{\sim}{\mu}_3$, corresponding to the largest eigenvalue, represents the distribution's centre. It is converted back to spherical coordinates ($\Theta_\mathrm{h}, \Theta_\mathrm{t}$, Fig. 11.6A) using

$$\Theta_\mathrm{h} = \arctan \frac{\mu_{3,y}}{\mu_{3,x}} \text{ , and} \tag{11.6}$$

$$\Theta_\mathrm{t} = \arctan \frac{\mu_{3,z}}{\sqrt{\mu_{3,x}^2 + \mu_{3,y}^2}} , \tag{11.7}$$

where $\mu_{3,x}$, $\mu_{3,y}$ and $\mu_{3,z}$ represent the x, y, and z components of $\underset{\sim}{\mu}_3$. Note the use of capital thetas, representing the orientation's centre. Θ_i is defined as the angle that $\underset{\sim}{\mu}_2$ makes with the xy-plane (Fig. 11.6B). The second step in fitting the Bingham distribution is finding κ_1 and κ_2. This is performed through maximisation of the log-likelihood function (Bingham 1964; Onstott 1980; Tanaka 1999)

$$F = -N \ln 4\pi - N \ln d(\kappa_1, \kappa_2) + \kappa_1 \tau_1 + \kappa_2 \tau_2 , \tag{11.8}$$

where τ_1 and τ_2 are the smallest and middle eigenvalues of $\underline{\underline{XX}}^T$. Maximisation was performed by minimisation of $-F$ using the MATLAB Optimization Toolbox FMINCON function and the interior-point algorithm, while constraining κ_1 and κ_2 to the interval $(-\infty, 0)$. Bingham distributions of the representative examples in Fig. 11.5A–C are shown in Fig. 11.5D–F.

11.3 Results

11.3.1 Qualitative results

Orientation plots for all arteries studied show a cloud of points that is approximately centred around the circumferential direction, as also visible in the representative example (Fig. 11.5A–C). Although these plots provide a good qualitative overview of the orientations of the SMC nuclei, it is hard to derive quantitative conclusions from them. Therefore, Bingham distributions were fitted to the acquired orientations, as exemplified in Fig. 11.5D–F, providing quantitative orientation data. These quantitative (Bingham parameter) results are discussed below.

11.3.2 Left versus right carotid arteries

Fig. 11.7 shows Bingham parameters and diameters for left ($n = 10$) and right ($n = 10$) carotid arteries at a luminal pressure of 40 mmHg. Left and right artery diameters are

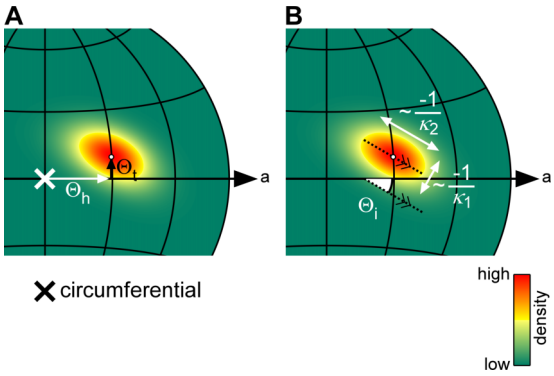

Figure 11.6: Definitions of Bingham distribution parameters. **A**: Parameters describing the distribution's centre. Θ_h and Θ_t are the centre's helix and transverse angles. **B**: Parameters describing the distribution's dispersion. κ_1 and κ_2 describe the distribution's concentration along two orthogonal directions. The more negative a κ is, the narrower the distribution is in the respective direction (Onstott 1980). Θ_i is the angle that the principal spread direction (corresponding to κ_2) makes with the axial-circumferential plane. In this example, $\Theta_h = 30°$, $\Theta_t = 10°$, $\kappa_1 = -30$, $\kappa_2 = -10$, and $\Theta_i = -25°$. a, axial.

nearly equal. As Θ_i is relatively close to zero, κ_1 represents dispersion in transversal direction and κ_2 represents dispersion in helical direction. The fact that κ_1 is more negative than κ_2 indicates that dispersion in helical direction is larger than in transversal direction. This holds for left as well as right arteries. Θ_h is positively different from zero in the right as well as the left arteries, in both the inner and outer layers (all $p < 0.05$), which is indicative of a right-handed helical pattern. No statistically significant differences were found between left and right arteries, except that only in the right arteries, Θ_h was significantly larger in the outer layer than in the inner layer. Θ_t shows the same pattern, being significantly different from zero in all cases. Please refer to the Discussion section for an interpretation of the latter finding.

11.3.3 Dependence of smooth muscle orientation on luminal pressure

As expected, artery diameter increased significantly with increasing luminal pressure, illustrating vessel deformation at macro-level (Fig. 11.8). Fig. 11.8 further shows Bingham parameters for the left carotid arteries ($n = 10$) at three luminal pressures (40, 80, and 100 mmHg). Θ_h and Θ_t are both again significantly different from zero in all cases. κ_1 shows a very consistent pattern in the inner layer, becoming more negative with increasing pressure, thereby indicating a decrease in SMC orientation dispersion. As mentioned above, because Θ_i is relatively close to zero, this decrease is approximately along the transversal direction. κ_2 increases with increasing luminal pressure from 40 to 100 mmHg in the inner layer, reflecting an increase in dispersion in helical direction. κ_1 and κ_2 show the same pattern with increasing luminal pressure in the outer layer, although it is not statistically significant here.

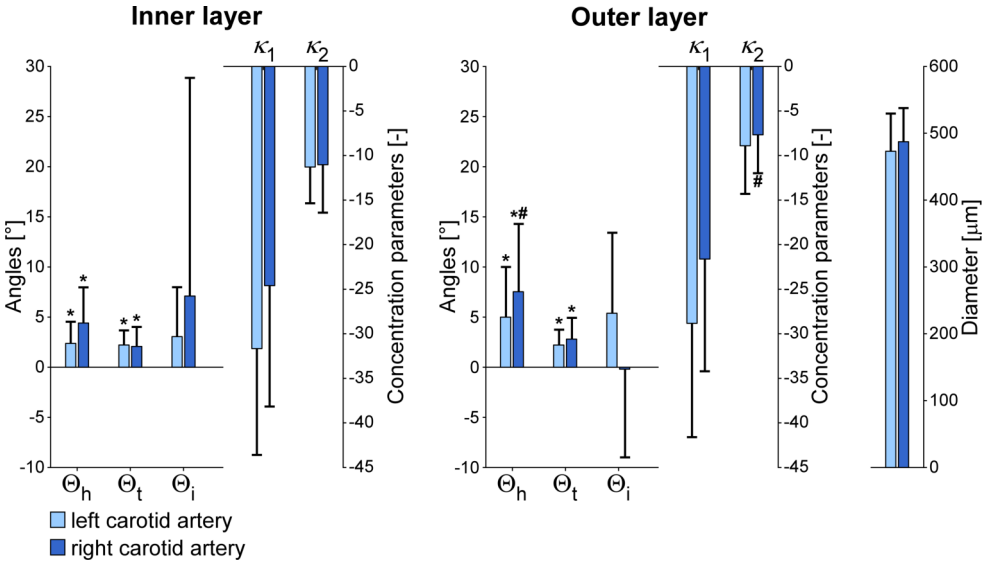

Figure 11.7: SMC orientations and diameters in left and right carotid arteries at 40 mmHg (circular mean ± circular SD for Θ_h, Θ_t, and Θ_i; arithmetic mean ± SD for κ_1, κ_2, and diameter). $^*p < 0.05$ vs. angle zero (Rayleigh test). $^\#p < 0.05$ inner vs. outer layer (Rayleigh or paired Student t-test). Θ_h, Θ_t, Θ_i, κ_1, and κ_2 are defined in Fig. 11.6. SD, standard deviation; SMC, smooth muscle cell.

11.3.4 Reproducibility

Reproducibility of our findings was assessed and is described in Appendix 11.A2.

11.4 Discussion

In this study, we quantified SMC orientation and dispersion in viable murine carotid arteries in full 3D. We found that SMCs are arranged in two layers, and we quantified SMC orientation and dispersion for each layer separately. Orientation dispersion in the helical direction was larger than in the transversal direction. We found a statistically significant right-handed helix in both left and right arteries, in both layers. With an increase in luminal pressure, the dispersion in transversal orientation was found to decrease.

The quantification method we developed in this study has three key advantages over previous methods: 1) arteries are mounted in their *in vivo* geometry and are kept viable (Megens et al. 2007); 2) by using TPLSM, 3D microscopic image stacks at large imaging depths (as compared to e.g., confocal laser scanning microscopy) can be acquired (Oheim et al. 2001); and 3) the present processing method analyses the full 3D image stack as a whole, instead of analysing data on a slice-by-slice basis as most other methods do (including our previous method (Spronck et al. 2014b)). As arteries are mounted in their *in vivo* geometry (point 1), artefacts that could potentially arise due to fixation (e.g., shrinking) and/or sectioning are absent. It has been shown that the present vessel

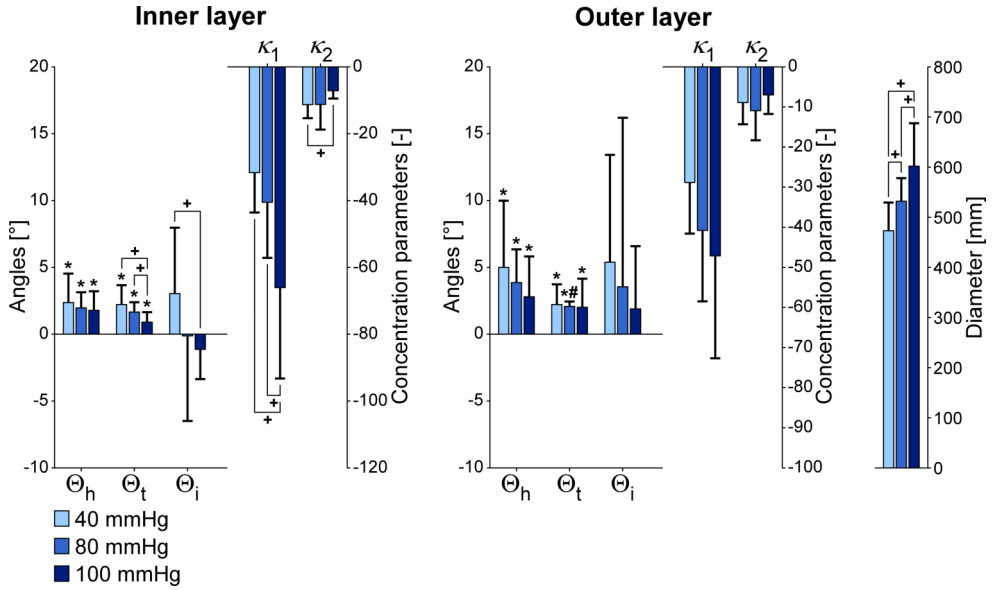

Figure 11.8: SMC orientations and arterial diameters in left carotid arteries at luminal pressures of 40, 80, and 100 mmHg (circular mean ± circular SD for Θ_h, Θ_t, and Θ_i; arithmetic mean ± SD for κ_1, κ_2, and diameter). $^{*}p < 0.05$ vs. angle zero (Rayleigh test). $^{\#}p < 0.05$ inner vs. outer layer (Rayleigh or paired Student t-test). $^{+}p < 0.05$ for parameter difference between pressures (Rayleigh or paired Student t-test). Θ_h, Θ_t, Θ_i, κ_1, and κ_2 are defined in Fig. 11.6. SD, standard deviation; SMC, smooth muscle cell.

mounting and TPLSM imaging setup (points 1,2) can be used to visualise both structural and functional properties of intact viable murine arteries. Its physiological relevance is demonstrated in various studies. Examples include the study of the endothelial glycocalyx (Reitsma et al. 2011; Slaaf and Van Zandvoort 2011), endothelial junctional adhesion molecule A (JAM-A) and its effect on monocyte or platelet recruitment (Karshovska et al. 2015; Schmitt et al. 2014), or the presence of smooth muscle progenitor cells (Subramanian et al. 2010) and proliferating endothelial cells (Schober et al. 2014) in healthy and atherosclerosis-prone arteries. Consequently, we believe that the results obtained in our study are relevant and well-translatable to an *in vivo* situation, albeit that we studied mouse and not human arteries. In a slice-by-slice analysis, *flat* image slices are acquired of a *curved* object, causing cells at various depths of the wall to end up in one image slice (Spronck et al. 2014b). This limitation is overcome in our present approach by analysing the acquired image stacks as a whole and using a curved (cylindrical) coordinate system (point 3), omitting the need for a small region of interest (Spronck et al. 2014b). Hence our 3D method allows a larger number of nuclei to be analysed and thus provides more robust results. Furthermore, transverse angles and dispersion therein can be analysed, whereas in a slice-by-slice analysis, out-of-plane information is lost.

Our results display statistically significant mean transverse and helix angles (Θ_t and Θ_h, Fig. 11.7 and 11.8). SMC orientation shows considerable dispersion in both helical

and transversal directions. To critically evaluate our findings, we performed the following two additional experiments for five left arteries at a luminal pressure of 40 mmHg: 1) we *digitally* rotated our image stack (after deconvolution) by 180° around the z-axis; and 2) we *physically* rotated the mounting chamber by 180° around the z-axis (i.e., around the objective axis). As compared to the non-rotated situation, both experiments should lead to a negation of Θ_t and Θ_i. Experiment 1 indeed led to these negations (data not shown) and did not affect Θ_h, κ_1, and κ_2. Experiment 2, on the contrary, still yielded positive Θ_t values (Fig. 11.A1). The observed significant average transverse angle (Θ_t) therefore seems to be a methodological artefact and not a true anatomical feature. We believe that this artefact results from inhomogeneities in image field brightness, slightly shifting the fitted cylinder axis and causing an artificially significant Θ_t value. The mean helix angle (Θ_h) observed in these two experiments remained positive, as would be theoretically expected. For the physically rotated acquisitions, we used the same imaging region as used in these arteries for the non-rotated acquisitions. We achieved this by measuring the distance between the non-rotated imaging region and the proximal pipette (measuring the movement of the calibrated microscope table). After rotation of the mounting chamber, imaging was performed at the same distance from the proximal pipette.

We further verified our helix angle findings by a third experiment, digitally *flipping* image stacks (after deconvolution) along the x-axis. Results were as expected: A negation of Θ_h and Θ_t, and Θ_i and both κ parameters remaining unaltered. Therefore, it is unlikely that our statistically significant average *helix* angle findings are artefactual.

Historically, SMC orientation has been studied in a variety of different species and arteries. Some authors described a spiralling orientation of medial smooth muscle (Benninghoff 1927; Pflieger and Goerttler 1970; Schultze-Jena 1939; Strong 1938), whereas others described smooth muscle orientation as circumferential (Pichler et al. 1953; Ushiwata and Ushiki 1990). Benninghoff described already in 1927 a spiralling smooth muscle orientation with a helix angle increase towards the periphery (Benninghoff 1927). In 1939, Schultze-Jena assessed the muscle spiral in a variety of arteries and found opposing-handed helices in left and right arm arteries (Schultze-Jena 1939). A subsequent work by Pichler et al. (1953) assessed the potential mechanical consequences of a helical orientation. Pichler concludes, based on measurements in helically-cut strips of carotid artery, cut at helix angles of +30° and −30°, that a single-helical structure is unlikely. Although these historical studies provide excellent qualitative anatomical insight, only limited quantitative conclusions can be drawn.

The results we obtained, indicating a significant right-handed helix, contradict the conclusion of most quantitative studies that SMC orientation is strictly circumferential. In human cerebral arteries, Walmsley (1983) found a statistically non-significant mean helix angle of $-0.2 \pm 2.4°$, in contrast to our angles of $2.4 \pm 2.2°$ (inner layer) and $5.0 \pm 5.0°$ (outer layer; mean ± SD; left carotid arteries at 40 mmHg). Peters et al. reported a "truly circumferential" smooth muscle orientation and an "inconsequential" left- or right-handedness of the helix (Peters et al. 1983) in human cerebral arteries, whereas we found a consistent, significant helix, however in viable carotid arteries of mice.

Some studies take a slightly different approach and consider the arterial (aortic) smooth muscle orientation to be a mixture of two or more distributions. Holzapfel et al., in their modelling paper in 2002, analysed SMC orientation in human aortas (Holzapfel et al. 2002). They implemented a method similar to our previous 2D method (Spronck et al.

2014b), but used histologically fixed instead of fresh tissue. Interestingly, Holzapfel et al. assumed the SMC orientation distribution to be centred around the circumferential direction, with two equally-weighted helical parts. Using this assumption, they argued for two helices with angles of ±8.4°. Tonar et al. (2015) assessed potential segmental differences in SMC orientation in porcine aortas, using a mixture of one to five Von Mises distributions. Their paper concludes that "The orientation of vascular smooth muscle was successfully fitted using two von Mises distributions in most of the samples…" and that "Only a minor fraction of samples required a tertiary von Mises component to describe the orientation…". We carefully studied Supplemental Material 1 of their paper. When assessing the $N_c = 2$ columns (i.e., the columns that correspond to two Von Mises distributions), one can count that in 55 out of 82 samples, one of the two Von Mises components was weak and/or redundant. Tonar et al. (2015) state this in Section 4.2 as "From a mathematical modelling point of view, this indicates that a structural model with a single vascular SMC system would be sufficient for most of our data". Another finding of Tonar et al. is a segmental difference in SMC orientation dispersion (not in main orientation) along the aortic tree. This may also be the case along the carotid artery, potentially explaining the spread in κ_1 and κ_2 parameters we measured (whiskers in Fig. 11.7 and 11.8), since we may not have imaged the exact same part of the common carotid artery in all mice.

In our study we analysed both left and right arteries and found a right-handed helix at both sites, violating left-right symmetry. Although very speculative, this may be explained by the intrinsic asymmetry of molecules, especially the proteins actin and myosin (Delhaas et al. 2008). As both molecules are arranged in a right-handed helix, when stretched, they will exhibit torsional motion. If a larger structure is built from such smaller helical components, an overall helicity may result. A more detailed discussion of this hypothesis can be found in (Delhaas et al. 2008) In our case, when this hypothesis would hold, one would *expect* left and right arteries to show the same helical handedness, as we observed. It may also be the case that this molecular asymmetry effect acts through the extracellular matrix. As smooth muscle cells have been shown to align with the extracellular matrix collagen (O'Connell et al. 2008), asymmetry of the extracellular matrix will presumably translate to asymmetry in SMC orientations as well.

Our study population of ten male C57BL/6JRj mice consisted of five young (age 8 weeks) and five older (age 23 weeks) individuals. We assessed whether age had an influence on orientations by comparing the results for the two age groups for left arteries at 40 mmHg (Fig. 11.A2) and found no statistically significant orientation parameter difference. We therefore decided to pool data from both age groups, yielding one group of $n = 10$.

Our study involved the use of lower and upper volume thresholds to exclude clusters that were too large or too small. The effect of this thresholding was analysed in a subset ($n = 5$) of samples at 40 mmHg (Fig. 11.A3). Thresholding excluded 26.8 ± 3.9 % (mean ± SD) of the clusters. The locations of these clusters are shown in Fig. 11.A3. The combination of vesselness filtering and subsequent cluster volume thresholding were aimed at excluding non-SMCs. It should be noted that the number of nuclei excluded by vesselness filtering is not visible in Fig. 11.A3. Calculating this number would require running the image analysis without vesselness filtering. However, vesselness filtering additionally functions as a means to convert the images from 12-bit grayscale ($[0, 4095]$)

values to continuous ($[0,1]$) values. Running the analysis without vesselness filtering, therefore, would require the definition of a new image threshold in the 12-bit domain, making comparison of the vesselness-filtered and -unfiltered results problematic.

Our finding of an arterial helix could have implications for the constitutive modelling of the artery wall. SMCs oriented in a slight net helix will create a slight torsion in the artery wall, which changes with SMC contraction. Such effects can and should be investigated using a constitutive modelling approach. Additionally, the fact that SMC orientation shows dispersion may have mechanical implications. An excellent example of the mechanical consequence of the inclusion of structural dispersion in constitutive models is given by the collagen modelling performed by Gasser et al. (2006). They found that, due to the dispersion of collagen, the recruitment of collagen fibres occurs at much lower stretches. In addition, when they excluded dispersion, collagen fibres showed larger-than-physiological rotations before bearing any load. Clearly, such effects also play a role in the modelling of SMC contraction in the artery wall.

Our study was limited in the sense that we assumed the orientation of the SMC nucleus to be representative of the orientation of the entire SMC. This assumption was also made in (Holzapfel et al. 2002; Peters et al. 1983; Walmsley 1983). Staining nuclei instead of entire cells has the advantage that it leads to more robust clustering results. Canham et al. (1982) studied the coalignment of the muscle cell and nucleus and found the upper limit on misalignment in three dimensions to be 2.4°. We used an aspecific nuclear dye, staining nuclei of all cells in the artery wall. Therefore, non-SMCs (e.g., fibroblasts) may have been included in our analyses. However, by applying vesselness filtering, the narrow layer separation, and nucleus volume thresholds, we assume to have filtered out the majority of non-SMCs.

11.4.1 Conclusions

We conclude that 1) vascular SMC orientation can be quantified in 3D; 2) SMC orientation shows considerable dispersion, predominantly in the helical direction, which decreases transversally with increasing luminal pressure; and 3) 3D quantification of SMC orientation reveals a distinct right-handed helical component in both left and right carotid arteries. These quantitative distribution data are essential to improve constitutive modelling of the artery wall.

11.5 Acknowledgements

We thank Paul Schiffers for providing calcium-free HEPES buffer. This study was supported by a Kootstra talent fellowship awarded to B. Spronck by Maastricht University. The two-photon laser scanning microscope used was supported by the Deutsche Forschungsgemeinschaft (DFG, INST409/97-1).

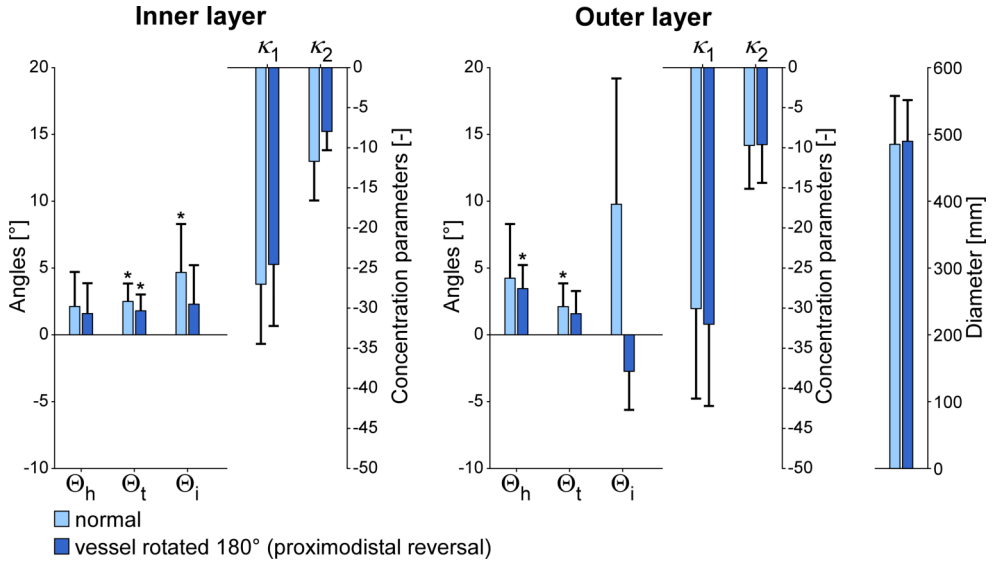

Figure 11.A1: SMC orientations and arterial diameters in normal and rotated left carotid arteries at a luminal pressure of 40 mmHg (circular mean ± circular SD for Θ_h, Θ_t, and Θ_i; arithmetic mean ± SD for κ_1, κ_2, and diameter). $^*p < 0.05$ vs. angle zero (Rayleigh test). Θ_h, Θ_t, Θ_i, κ_1, and κ_2 are defined in Fig. 11.6. SD, standard deviation; SMC, smooth muscle cell.

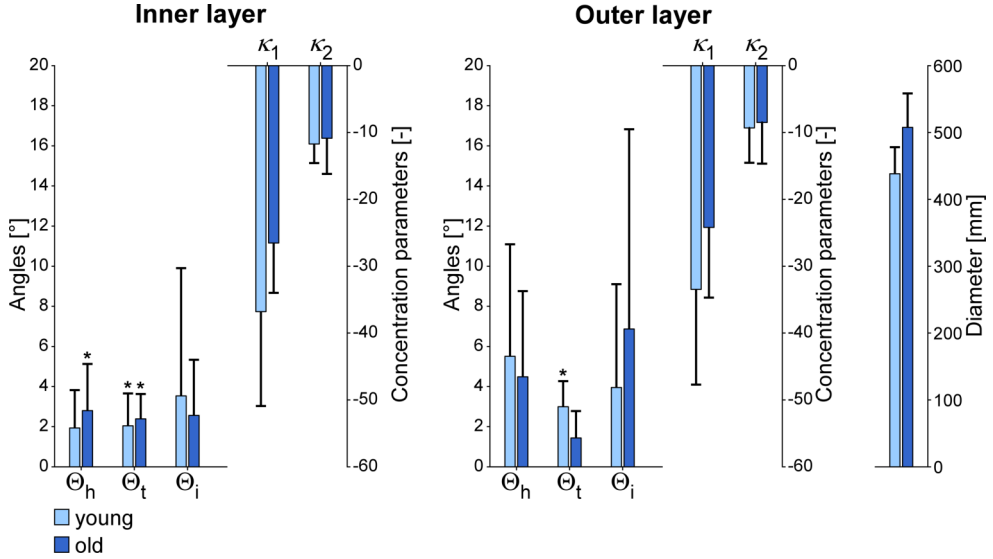

Figure 11.A2: SMC orientations and arterial diameters in left carotid arteries at a luminal pressure of 40 mmHg in young (age 8 weeks) and old (age 23 weeks) mice (circular mean ± circular SD for Θ_h, Θ_t, and Θ_i; arithmetic mean ± SD for κ_1, κ_2, and diameter). $^*p < 0.05$ vs. angle zero (Rayleigh test). Θ_h, Θ_t, Θ_i, κ_1, and κ_2 are defined in Fig. 11.6. SD, standard deviation; SMC, smooth muscle cell.

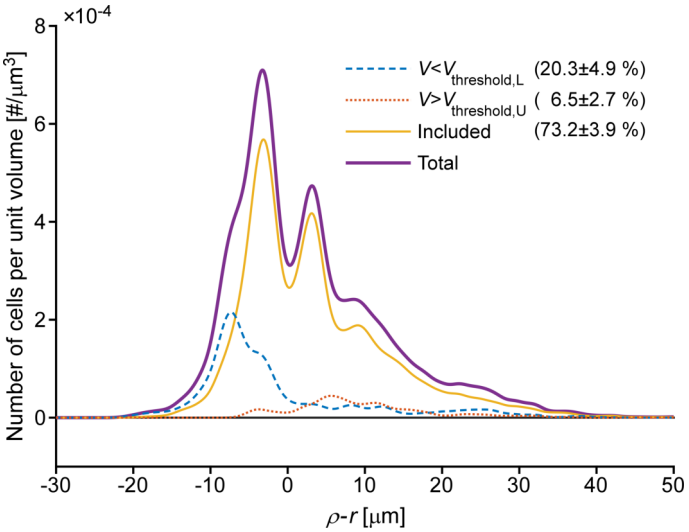

Figure 11.A3: Effect of cluster volume thresholding. Curves show SMC density as a function of the relative radial coordinate ($\rho - r$), where ρ is the radial coordinate as defined in Fig. 11.3**A** and r is half of the detected vessel diameter ($\frac{1}{2}D$). Pooled data of five samples at a luminal pressure of 40 mmHg are shown (those (non-rotated) samples that were also used for assessing reproducibility (Table 11.A1) and the effects of rotation (Fig. 11.A1)). The lower volume threshold ($V_{\text{threshold,L}}$, blue, dashed line) removed clusters mainly at the inner side of the wall, whereas the upper volume threshold ($V_{\text{threshold,U}}$, red, dotted line) removed clusters mainly at the outer side of the wall. Percentages pertain to the number of clusters in each stack that were excluded/included, respectively (mean ± SD). SD, standard deviation; SMC, smooth muscle cell.

11.A1 Appendix: Projecting orientations on a unit hemisphere

The reader of this paper may wonder why a map projection is used to visualise SMC orientations. In this section, we will explain why the use of projections is beneficial.

An orientation in 3D can be quantified by two spherical angles: an elevation and an azimuth. In our study, the elevation corresponds to the transverse angle (θ_t) and the azimuth corresponds to the helix angle (θ_h). One could choose to make a rectangular plot and plot θ_h vs. θ_t. Gasser et al. (2012) have chosen to construct histograms in this way (Fig. 4 in (Gasser et al. 2012)) and to depict an orientation density (Fig. 8 in (Gasser et al. 2012)). Although at first sight these representations appear feasible, they provide a deformed view of reality, for two (related) reasons:

1. Consider the surface element on the unit hemisphere spanning from θ_h to $\theta_h + \mathrm{d}\theta_h$ and θ_t to $\theta_t + \mathrm{d}\theta_t$. The area of this element is *not* $\mathrm{d}\theta_h \mathrm{d}\theta_t$, but $\mathrm{d}\theta_h \mathrm{d}\theta_t \cos\theta_t$. Consequently, visualising orientations by using a rectangular θ_h-versus-θ_t plot overemphasises orientations with large θ_t.
2. A related error occurs when trying to represent an orientation of $\theta_t = \pm 90°$. At

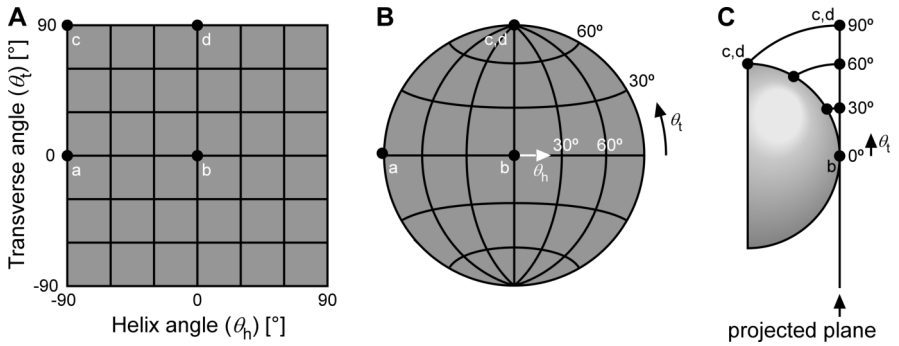

Figure 11.A4: Considerations for using map projections. **A**: Typical problem when representing a three-dimensional orientation without using a projection. Consider four points a, b, c, and d with indicated spherical coordinates. Points a and b clearly represent a different orientation that is 90° apart. Points c and d, however, appear to also represent a different orientation, whereas in reality, they are equal (they are both at the "top" of the hemisphere). **B**: The problem in **A** can be solved using a map projection. By representing the orientations using a projection, points c and d coincide. The projection used is the Lambert azimuthal equal area projection. **C**: A Lambert azimuthal equal area projection is created by using a plane tangential to the center point on the unit hemisphere (point b in this case). All points will be projected on this plane. From all points on the hemisphere, a circular arc is drawn to the projected plane that 1) ends perpendicular to the projected plane and 2) has point b as its centre.

what θ_h should this orientation be drawn? Clearly, for $\theta_t = \pm 90°$, θ_h is undefined.

These problems are illustrated in Fig. 11.A4A. A solution to this problem could be to display the hemisphere in 3D, as performed by Alastrué et al. (2010). Although correct, such 3D figures are, to our opinion, hard to interpret from a (2D) document.

The problem of displaying spherical information on a flat surface is not new and occurs for example when creating a 2D map of the 3D world. The transformation from latitudes and longitudes of locations on the surface of a sphere into locations of a plane is called a map projection (Snyder and Voxland 1989). A large number of map projections exist, all suited for a specific goal. Importantly, there is not one general "best" projection (Snyder 1987). For our application, we require the projection to be equal-area, tackling the aforementioned point 1 (Snyder 1987) and illustrated in Fig. 11.A4B. Many projections possess this property, but the one that is most often used to plot directional data is the Lambert azimuthal equal-area projection (Borradaile 2003). This is the projection used in this paper. Its geometrical construction is explained in Fig. 11.A4C. Mathematically, it is obtained via the following equations:

$$x = \sqrt{\frac{2}{1+\cos\theta_t \cos\theta_h}}\cos\theta_t \sin\theta_h \text{ , and} \tag{11.A1}$$

$$y = \sqrt{\frac{2}{1+\cos\theta_t \cos\theta_h}}\sin\theta_t \text{ .} \tag{11.A2}$$

11.A2 Appendix: Reproducibility

To evaluate our findings, in five arteries, we acquired a second image stack after physically rotated the mounting chamber by 180° around the z-axis (see Discussion section and Fig. 11.A1). As these rotated stacks were acquired at the same location as the corresponding non-rotated stacks, these data can be used to analyse the repeatability of our method.

In order to assess repeatability, we calculated three summary values of parameters $P_{ij} \in \{\Theta_{\mathrm{h},ij}, \kappa_{1,ij}, \kappa_{2,ij}, D_{ij}\}$, with D_{ij} representing diameter. Subscript $i \in \{\mathrm{N}, \mathrm{R}\}$ denotes non-rotated (N)/rotated (R) stacks; subscript $j \in \{1, 2, 3, 4, 5\}$ denotes animal number. The following summary values were computed:

1. The overall mean (μ):
$$\mu = M[m_1, m_2, \ldots, m_5] \ . \tag{11.A3}$$
2. The between-animal standard deviation (σ_μ):
$$\sigma_\mu = S[m_1, m_2, \ldots, m_5] \ . \tag{11.A4}$$
3. The reproducibility standard deviation (σ_r):
$$\sigma_\mathrm{r} = S[P_{\mathrm{N}1} - m_1, P_{\mathrm{R}1} - m_1, P_{\mathrm{N}2} - m_2, P_{\mathrm{R}2} - m_2, \ldots, P_{\mathrm{N}5} - m_5, P_{\mathrm{R}5} - m_5] \ . \tag{11.A5}$$

In these equations, M and S denote the circular mean and circular standard deviation operators for $P_{ij} = \Theta_{\mathrm{h},ij}$; and the arithmetic mean and standard deviation operators for $P_{ij} \in \{\kappa_{1,ij}, \kappa_{2,ij}, D_{ij}\}$, respectively. m_j is used as a short-hand notation of $M(P_{\mathrm{N}j}, P_{\mathrm{R}j})$.

Results are shown in Table 11.A1. In all cases, the reproducibility standard deviations were smaller than the between-animal standard deviations. Reproducibility of the helix angle (σ_r) was good at 0.76° (inner layer) and 1.37° (outer layer), respectively.

Table 11.A1: Reproducibility statistics

Parameter	Unit	μ		σ_μ		σ_r	
		I	O	I	O	I	O
Θ_h	°	1.85	3.85	2.32	2.83	0.76	1.37
κ_1	-	−25.80	−31.04	7.75	8.44	2.37	6.33
κ_2	-	−9.83	−9.66	3.42	4.68	2.56	1.90
D	µm	487		62		22	

μ, overall mean; σ_μ, between-animal standard deviation; σ_r, reproducibility standard deviation. See Appendix 11.A2 for details on computing these values. Θ_h, κ_1, and κ_2 are defined in Fig. 11.6. D, diameter; I and O, inner and outer layer, respectively.

Chapter 12

In vitro assessment of arteries under pulsatile conditions

The contents of this chapter are based on:

Bart Spronck,[1] Paulus J.M. Spronck,[2] Remco T.A. Megens,[1,3] Tammo Delhaas,[1] and Koen D. Reesink[1] (2016).
In vitro assessment of arteries under pulsatile conditions [in preparation].

[1] Department of Biomedical Engineering, CARIM School for Cardiovascular Diseases, Maastricht University, Maastricht, The Netherlands.
[2] Innovatech Holding B.V., Maastricht, The Netherlands.
[3] Institute for Cardiovascular Prevention, Ludwig-Maximilians-Universität, Munich, Germany.

Abstract

Arterial biomechanical behaviour under dynamic (pulsatile, *in vivo*) conditions may differ substantially from its behaviour under static conditions. Therefore, we propose that the arterial structure-function relationship should be characterised under dynamic conditions, reflecting *in vivo* mechanical behaviour as much as possible. In the present study, we aim to develop an integrated system for biomechanical assessment of murine arteries under pulsatile conditions. A custom-built set-up prototype was made to generate pulsatile pressure (pulse frequency 2–10 Hz) and to apply these pressure pulses to murine carotid arteries mounted between glass micropipettes. Pressure (P) was acquired both at the proximal and distal pipettes. Arterial diameter (D) was recorded using high-frequency ultrasound wall tracking; axial force was measured by means of a load cell. Pilot experiments using a single 22-week old C57BL/6JRj mouse carotid artery were performed under no-flow conditions. First, the artery was exposed to static pressure from 0 to 200 mmHg while recording diameter. Second, the artery was exposed to pressure pulses at 2, 5, and 10 Hz and to three different pressure ranges. Synchronisation of pressure and cross-sectional area ($A = \frac{1}{4}\pi D^2$) signals, and the effect of post hoc synchronisation by second derivative matching were assessed. Proximal pressure matched the A signal well whereas distal pressure was unexpectedly smoothed and did not show the detail that was present in the A signal. Without post hoc synchronisation, P-A loops plotted using proximal P ran clockwise (physically plausible) whereas loops plotted using distal P ran counterclockwise (physically impossible). This opposition in direction remained after post hoc synchronisation. Future directions for improving synchronisation and determining true, intraluminal P are given. We have demonstrated the feasibility of *ex vivo* mechanical assessment of murine carotid arteries under pulsatile conditions. In the future, the developed method could yield novel mechanical insights into physiological arterial wall mechanics in health and disease.

12.1 Introduction

STIFFENING of arteries poses a major threat to the present population. Whereas pulse wave velocity is clinically the gold standard method providing a measure of arterial stiffness, pulse wave velocity measurements generally do not yield insight into the *mechanisms* underlying the stiffening of the arteries.

A few studies have attempted to assess biomechanical arterial behaviour non-invasively in humans (for a short overview, see Spronck et al. 2015a). Though such studies provide a crucial, structural view on the biomechanics of the artery wall, they are limited in the sense that an artery can only be assessed at the human working pressure range. Furthermore, pressure (by applanation tonometry) and diameter (by echo-tracking) waveforms cannot be simultaneously acquired.

These limitations can be overcome by studying biomechanics in excised arteries, mounted between glass (micro)pipettes and pressurised and/or stretched. This approach al-

lows not only haemodynamical and mechanical measurements, but also structural imaging (Spronck et al. 2015a). Recorded data on pressure, diameter, length, axial force, and sometimes structure is typically integrated into a constitutive model of the artery wall to obtain detailed insight into the biomechanical behaviour of the artery. Mechanical characterisation of mounted murine arteries has been extensively performed by Humphrey and co-workers (e.g., Ferruzzi et al. 2013) and by Holzapfel et al. (Holzapfel and Ogden 2010a). A limitation of most of the experimental work that has been performed to date is that measurements are mostly performed under static conditions.

Because arterial biomechanical behaviour under dynamic (pulsatile, *in vivo*) conditions may differ substantially from its static behaviour (Holzapfel et al. 2002; Learoyd and Taylor 1966; Lichtenstein et al. 1998), we propose that the arterial structure-function relationship should be characterised under dynamic conditions, reflecting *in vivo* mechanical behaviour as much as possible.

Several studies have performed *ex vivo* dynamic assessment of arteries. An overview is given in Table 12.1. More than 50 years ago, Bergel (1961) already mounted dog aorta samples vertically and subjected them to sinusoidal pressure waves. Learoyd and Taylor (1966) followed roughly the same approach. More recently, Armentano et al. (2007) also performed pulsatile experiments on excised human common carotid arteries, stating that "Pressure and pumping rate levels were chosen to be similar to those observed in normotensive patients." It is unclear to us what pressure waveforms were actually used by Armentano et al. (2007) to distend the vessel.

Lichtenstein et al. (1998) did assess static as well as dynamic (pulsatile) mechanics in rat carotid arteries. The pulse waveforms that Lichtenstein et al. (1998) generated were sinusoidal and not physiologically shaped. Gleason et al. (2004), to our knowledge, are the only researchers who subjected *murine* carotid arteries to *pulsatile* pressure. Furthermore, their set-up allows for measurement of axial force in the mounted arteries. The pulsatile pressure waves in the set-up by Gleason et al. (2004) are sinusoidal. Furthermore, the sites of pressure acquisition are far away from the mounting pipettes, inducing a substantial difference in pressure as measured proximal and distal to the mounted artery. This complicates estimating pressure *inside* the artery.

Boutouyrie et al. (1997) assessed rat aortas under pulsatile pressure. Notably, they mimicked physiologically shaped pressure waveforms, containing a realistic systolic pressure rise time and a dicrotic notch. If a measurement set-up is able to subject the mounted artery to such pressure waveforms, its *in vivo* mechanical behaviour can be simulated. The advantage of performing such an experiment *in vitro* is that measurements of much higher precision than in the *in vivo* situation can be obtained. Furthermore, pressure, diameter, and axial force can be measured simultaneously.

In the present study, we aim to develop a measurement set-up for biomechanical characterisation of murine arteries under pulsatile conditions. The set-up will consist of a high-speed valve, allowing generation of pressure pulses at > 600 bpm (10 Hz, a typical mouse heart rate (Ho et al. 2011)), and a closed-loop artificial circulation. Axial force and pipette pressure will be measured using miniature pressure sensors at both pipettes and a load cell, respectively. Artery diameter will be tracked using high-frequency ultrasound.

Table 12.1: Previous studies investigating pulsatile behaviour of mounted vessels

Study	Species	Vessel	Wave shape	Base frequency
Bergel 1961	dog	thoracic and abdominal aorta, femoral and carotid arteries	sinusoidal	0–18 Hz
Learoyd and Taylor 1966	human	thoracic and abdominal aorta, iliac, femoral and carotid arteries	sinusoidal	0–10 Hz
Bauer et al. 1982	rat	abdominal aorta, carotid artery, and tail artery	sinusoidal	0–20 Hz
Boutouyrie et al. 1997	rat	aorta	physiological	*
Lichtenstein et al. 1998	rat	carotid artery	sinusoidal	5 Hz
Zanchi et al. 1998	rat	carotid artery	(nearly) sinusoidal	1–4 Hz
Gleason et al. 2004	mouse	carotid artery	sinusoidal	0–10 Hz
Bia et al. 2005	sheep	femoral artery, jugular vein	(nearly) sinusoidal**	110 bpm
Armentano et al. 2007	human	carotid artery	not specified	70 bpm
Zocalo et al. 2008	sheep	anterior vena cava, jugular and femoral veins	(nearly) sinusoidal	1.8 Hz
Valdez-Jasso et al. 2011	sheep	thoracic descending aorta, carotid artery	(nearly) sinusoidal	110 bpm

In Boutouyrie et al. 1997 and Armentano et al. 2007, axial mounting length was not specified. In all other studies, vessels were mounted at *in vivo* length. *After *in vivo* examination, the arterial segments were isolated, mounted, and subjected to resynthesised pressure waves identical to those recorded *in vivo* (Boutouyrie et al. 1997). **Bia et al. (2005) state that "…the device allows adjustments of heart rate, length of systolic and diastolic period for each cycle, pressure values, …". However, visually (Fig. 4 in Bia et al. 2005), the generated waveforms seem to (nearly) resemble sinusoids.

12.2 Methods

12.2.1 Set-up

A custom-built set-up prototype (Fig. 12.1) was made to generate pulsatile pressure that can be applied to murine carotid arteries (diameter ≈ 0.5 mm, length ≈ 1 cm) and other arteries of similar dimensions. The set-up is a closed-loop system, which enables it to run for a prolonged period of time while re-using fluid to repetitively distend the mounted artery. Below, a brief description is given of the main elements and functions of the set-up.

Fluid circuit

The majority of the system's fluid is contained in 1) the fluid reservoir, and 2) the vessel bath. Both containers are temperature-controlled. Fluid in the reservoir is pressurised using the laboratory air supply, the pressure of which is downregulated using a pressure regulator. Reservoir pressure is measured using a pressure sensor (P_0, Fig. 12.1). Fluid in the vessel bath is open to the air and hence unpressurised. From the reservoir, a short pipe leads to a high speed valve, consisting of a compliant tube and an indenter driven by a loudspeaker. If no electrical current is passed through the loudspeaker, the indenter presses on this tubing using a spring, closing the tube (state drawn in Fig. 12.1). If electrical current is passed through the loudspeaker, it will lift the indenter from the compliant tube (downwards in Fig. 12.1). This (partially) opens the tube, allowing pressurised fluid from the reservoir to pass generating a pulsed flow into the rest of the circuit. The fluid then flows into a hydraulic resistance-compliance (RC) circuit. The fluid resistance of this circuit (Fig. 12.1) is implemented by using a small valve that is nearly shut. Through this resistance, fluid flows into the vessel bath. Compliance essentially arises from the use of silicone tubing throughout the system. Extra compliance (Fig. 12.1) can be added by means of a 1 mL syringe in which a small air bubble is kept. The RC circuit is connected to the proximal pipette (indicated with a "p" in Fig. 12.1) via a flow-through pressure sensor (P_1, Fig. 12.1). The distal pipette ("d", Fig. 12.1) is connected to a flow-through pressure sensor (P_2), of which the outflow end is typically closed. If the fluid level in the reservoir drops below approximately 2/3, this will be detected by an optical level sensor, switching on the return pump. The return pump takes fluid from the vessel bath and returns it to the reservoir.

Vessel bath and ultrasound

Two glass micropipettes between which an artery can be mounted are submerged in the vessel bath. The proximal pipette ("p" in Fig. 12.1) is attached to a motorised slide, allowing automated setting of artery axial stretch using a stepper motor. The distal pipette ("d" in Fig. 12.1) is attached to a load cell, allowing measurement of axial force. The vessel bath is dimensioned such that a mounted artery can be imaged from the top using either

1. A high-frequency ultrasound transducer, or
2. A water-dipping microscope objective.

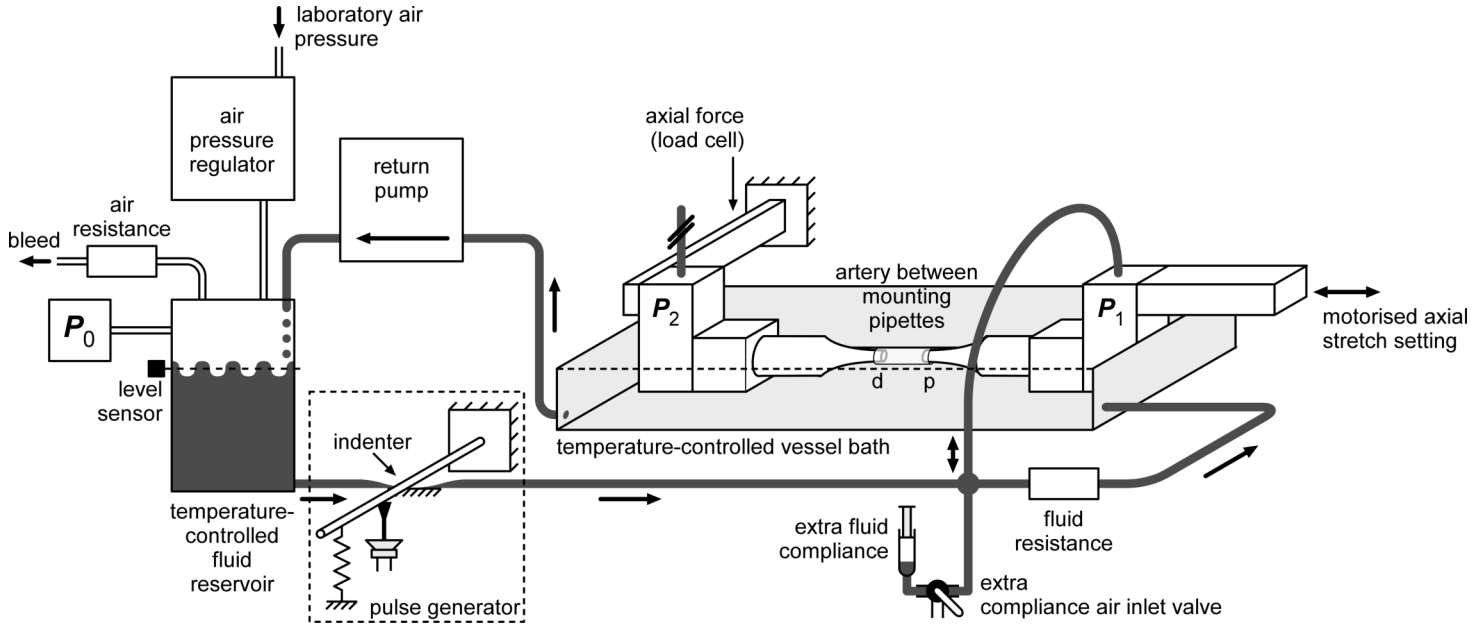

Figure 12.1: Prototype set-up used for biomechanical assessment of murine arteries under pulsatile conditions. p and d, proximal and distal pipettes, respectively; P_0, P_1, and P_2, reservoir, proximal, and distal pressure sensors, respectively. For further details, see text.

In the present study, a high-frequency ultrasound probe (MS700, FujiFilm VisualSonics Inc., Toronto, ON, Canada) connected to a VEVO 2100 system (FujiFilm VisualSonics Inc.) was used to image the artery under static and pulsatile conditions.

Control of indenter and motorised slide

The pulse generator and the stepper motor moving the proximal pipette are controlled by an Arduino UNO microcontroller board. The microcontroller also generates a synchronisation signal that will be used to synchronise the ultrasound image acquisition with the acquisition of the other signals (particularly pressure signals P_1 and P_2).

Signal acquisition and control

The following analog signals are acquired on a USB-6001 A/D-D/A converter (National Instruments Corporation, Austin, TX, USA) at a sampling rate of 2500 Hz: pressures P_0, P_1, and P_2; temperatures of reservoir and vessel bath; axial force; and the synchronisation signal. The level sensor is connected to a digital input. The heating circuits of the reservoir and vessel bath, and the pump are connected to three digital outputs. Signal acquisition and control are performed using LabVIEW 2013 (National Instruments Corporation). The synchronisation signal is also fed to the ECG input of the VEVO 2100 ultrasound system.

Ultrasound acquisition was performed in B-mode at maximal frame rate, which was 564 Hz. For each pulsatile experiment, 1000 frames were acquired.

12.2.2 Pilot experiments

Preparations

Before starting the experiments, in an empty set-up, all three pressure transducers (P_0, P_1, and P_2) were calibrated using a mercury column at pressures 0 and 100 mmHg. Subsequently, calcium-free HEPES buffer was added to the vessel bath, while the return pump (Fig. 12.1) was used to pump this fluid into the fluid reservoir. The indenter was temporarily opened, and the entire system was fluid filled. The dead end tubing of P_2 (Fig. 12.1) was also temporarily connected to the circulation to also fill the P_2 sensor.

Artery mounting

In the present study, we used an artery of a single 22-week old C57BL/6JRj mouse to perform our pilot experiments. The mouse was sacrificed with an overdose of carbon dioxide, after which the left common carotid artery was excised and labelled at the proximal end. The proximal and distal ends of the artery were carefully mounted between the proximal and distal micropipettes of the set-up ("p" and "d" in Fig. 12.1). When mounted in this way, arteries remain viable for a prolonged period of time ($>$ 2 hrs, Megens et al. 2007). A carotid artery section of $\approx$ 5 mm was mounted, yielding a length of approximately 3 mm of artery accessible for imaging. The artery was maximally vasodilated by addition of nitroprusside (Sigma-Aldrich, St. Louis, MO) to a concentration of 10 μM and was examined at 37°C. The experiment was approved by the local authority. No extra compliance (see Fig. 12.1) was used.

Adjusting axial stretch and pre-conditioning

Physiologically, it is known that if an artery is stretched to its *in vivo* length, distension due to pressure changes has only minimal effects on the axial force of the vessel (Avril et al. 2013; Brossollet and Vito 1995; Fung 1990; Humphrey 2002; Weizsäcker et al. 1983). If the artery is stretched to a lesser or greater extent than to this *in vivo* length, axial force fluctuations with pressure will increase. This physiological knowledge was used to determine the *in vivo* length of the artery: axial stretch was adjusted to have minimal changes in axial force with vessel distension over the cardiac cycle. This stretch is termed the *in vivo* axial stretch ratio. The *in vivo* axial stretch ratio for the mounted artery was determined by measuring axial force at luminal pressures of 0 and 100 mmHg and minimising the difference between those two force measurements. Subsequently, the artery was pre-conditioned to eliminate the excessive hysteresis found on first inflation (Bergel 1960; Learoyd and Taylor 1966; Remington 1955) by a set of 5 inflation-deflation cycles from 0 to 100 mmHg with a cycle time of approximately 5 s.

Static measurements

First, the artery was assessed statically by measuring diameter at small pressure increments. Pressure was increased from 0 to 200 mmHg in steps of 5 mmHg and then decreased back to 0 in steps of 5 mmHg. Time between steps taken was $\geq$ 10 s. This inflation-deflation experiment was repeated twice.

Dynamic measurements

Dynamic (pulsatile) measurements were performed using two protocols as illustrated in Fig. 12.2. Both protocols consist of nine combinations of pressures/frequencies. The protocols are started in the centre of the figure panels (Fig. 12.2).

Protocol A Protocol A is illustrated in Fig. 12.2A. Pulse frequency (f) is set to 5 Hz, and reservoir pressure P_0 and fluid resistance (R) are tuned such that systolic (maximum) and diastolic (minimum) pressures as recorded by P_2 read 100 and 60 mmHg, respectively. This is the "reference state" (REF). Subsequently, frequency is changed to 10 Hz and 2 Hz (vertical steps in Fig. 12.2A), keeping all other settings (notably, P_0 and R) constant. Due to haemodynamics, therefore, in general, pressures will not exactly equal 100/60 anymore. This completes the middle column in Fig. 12.2A. Subsequently, only P_0 is changed such that systolic pressure equals 60 mmHg (middle left block, Fig. 12.2A). Note that diastolic pressure was not adjusted (R was kept constant). Again, vertical steps were made from here by changing only frequency. Finally, f is set to 5 Hz and P_0 is changed such that systolic pressure equals 140 mmHg (middle right block, Fig. 12.2A). From here, again f is changed, keeping all other settings constant.

Protocol B Protocol A is illustrated in Fig. 12.2B. Again, $f = 5$ Hz and pressures are set to 100/60 mmHg. Protocol B differs from protocol A as follows: when f is adjusted (vertical steps in Fig. 12.2B), systolic pressure is adjusted as well, by means of varying P_0.

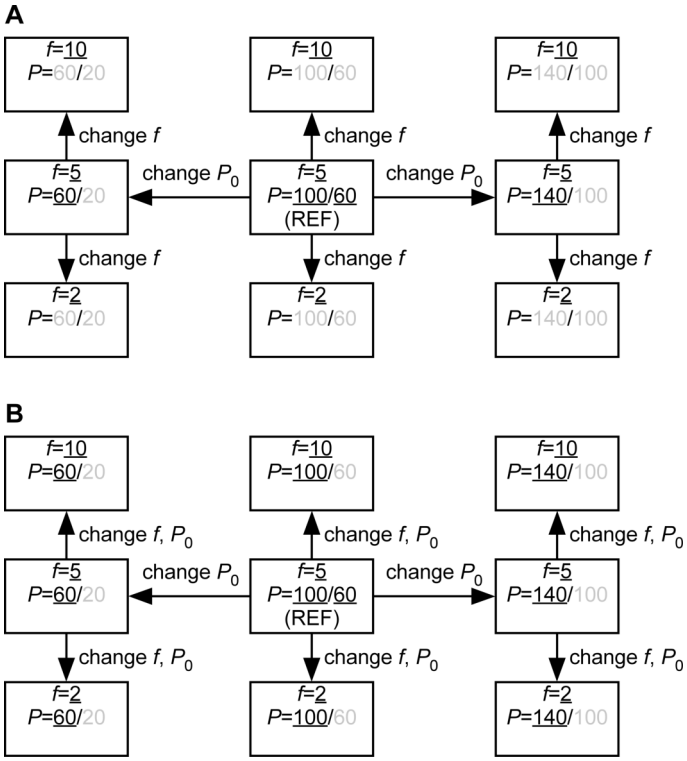

Figure 12.2: Experimental protocols used for assessment of murine arteries under pulsatile pressure. Both protocols consist of nine combinations of pressures/frequencies. Panels **A** and **B** correspond to protocols A and B, respectively. All pressures (P) are denoted as systolic/diastolic pressure, in mmHg; frequencies (f) are given in Hz. Underlined quantities are actually set, gray values are a resultant of system dynamics. REF, reference state; P_0, reservoir pressure. For details, see text.

This implies that in protocol B, systolic pressure is adjusted for all nine states. R is again only set at REF and remains unaltered.

Data processing

B-mode ultrasound images were processed using B-mode edge tracking as described by Steinbuch et al. (2016). Dynamic pressure and cross-sectional area signals were resampled off-line at 1000 Hz. Data were filtered using a 51-point Savitzky-Golay filter of order 8 ($N = 8$, $M = 25$), having a -3 dB cut-off frequency of 60 Hz (Schafer 2011). At a pulse frequency of 10 Hz, this leads to inclusion of the first six harmonics of the signals, yielding a reasonable representation of the actual signals (Moxham 2003; Nichols et al. 2011). Pressure and cross-sectional area signals were synchronised using the synchronisation signal that was acquired on both the ultrasound system and the A/D converter. We also used a further fine tuning of synchronisation, which was based on the acquired pressure and diameter signals. This post hoc synchronisation method involved calculat-

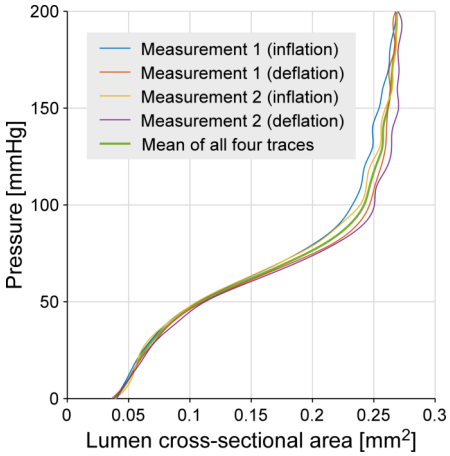

Figure 12.3: Static pressure-area relationships.

ing the second derivative of the pressure and diameter signals and detecting the maxima in these signals. Subsequently, the pressure signal was time-shifted such that the second derivative maxima of the pressure signal matched those of the diameter signal.

12.3 Results

The *in vivo* stretch ratio of our sample was determined to be $\lambda_z = 1.75$. All further experiments were performed at this stretch ratio.

12.3.1 Static measurements

Results of static inflation and deflation are shown in Fig. 12.3.

12.3.2 Dynamic (pulsatile) measurements

All dynamic experiments were performed in duplicate. Results shown in this section pertain to the first set of experiments performed.

Raw signals

Raw pressure and cross-sectional area signals of dynamic experiments are shown in Fig. 12.4. Signals for $f = 2\,\text{Hz}$ and $f = 5\,\text{Hz}$ are shown in appendix Fig. 12.A1 and Fig. 12.A2. Note the much smoother and lower-frequency shape of the distal pressure signal (P_2) as compared to the proximal pressure signal (P_1), at all three blood pressure conditions.

Influence of pressure acquisition site and of post hoc synchronisation on *P-A* curves

Fig. 12.5 shows representative *P-A* curves, generated using proximal (left column) as well as distal (right column) pressures for $f = 10\,\text{Hz}$. Curves for $f = 2\,\text{Hz}$ and $f = 5\,\text{Hz}$

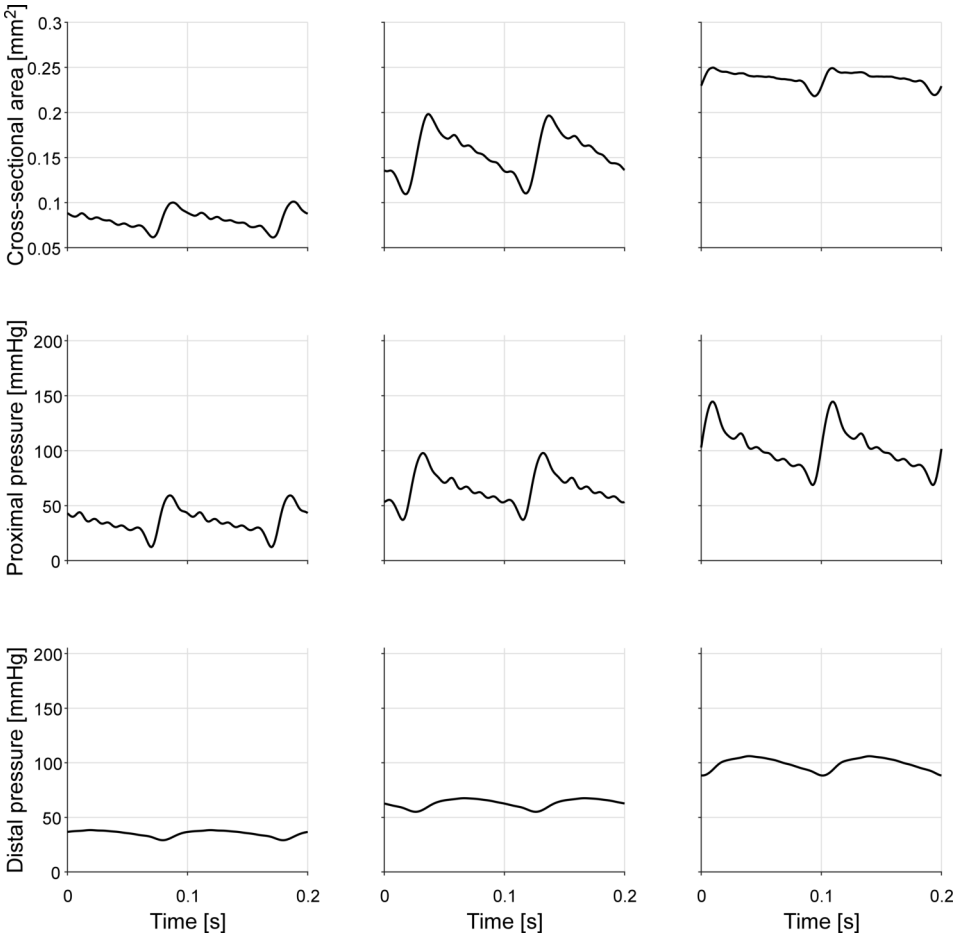

Figure 12.4: Raw acquired cross-sectional area and proximal (P_1) and distal (P_2) pressure signals, acquired at 10 Hz (protocol A, Fig. 12.2A) and systolic reference pressures (defined at 5 Hz, see protocol) of 60, 100, and 140 mmHg (left, middle, and right columns, respectively).

are shown in appendix Fig. 12.A3 and Fig. 12.A4. Note that *P-A* curves drawn using proximal pressures turn clockwise, indicating physically feasible dissipation of energy in the vessel wall. *P-A* curves drawn using distal pressures turn counter-clockwise, which is physically impossible when no signal distortion or misalignment are present (Hoeks et al. 2000). Signals used to generate the top row *P-A* curves were only synchronised based on the electrical synchronisation signals (see Methods section). Synchronisation of bottom-row signals was obtained by the post hoc synchronisation method. Notably, even after this synchronisation, the distal pressure-based *P-A* curves ran counter-clockwise. All following *P-A* curves are drawn using the proximal pressure signals and using post hoc synchronisation.

P-A curves at varying heart rates

We generated *P-A* curves for all three heart rates and blood pressure profiles as specified in our protocol (Fig. 12.2). Results are shown in Fig. 12.6. For both protocols, increased heart rate led to smaller *P-A* loop areas. However, note that in both protocols, with increasing heart rate, pulse pressures decreased (see Discussion section).

12.4 Discussion

In this study, we aimed to develop a measurement set-up for biomechanical characterisation of murine arteries under pulsatile conditions. We constructed a prototype set-up, and performed pilot measurements at different pulse rates and pressure profiles. Individual aspects of our development and future directions are outlined below.

12.4.1 Pilot measurement protocol

For our pilot measurements, we used two protocols as illustrated in Fig. 12.2. The pressures referred to in the protocol correspond to *distal* pressures. We made this choice, as we expected the distally measured pressure to be more reflective of the intravascular pressure than the proximally measured pressure. This assumption was based on the fact that the distal pressure transducer is at a "dead end" and is connected rigidly to the distal pipette. Theoretically, this would result in no flow across the distal pipette and therefore in no pressure drop across this pipette. Therefore, in our current set-up (Fig. 12.1), in theory, distal pipette pressure should follow intravascular pressure perfectly. However, a close look at the acquired raw signals in Fig. 12.4 reveals that in most cases, ripples that are present in the *A*-signal, are absent in the distal pressure signal. These ripples *are* present in the proximal pressure signal. This suggests that the ripples in the *A*-signal are a result of these proximal pressure ripples, and therefore, that intravascular pressure also shows these ripples. This implies that considering waveform shape, in our pilot data set, the proximal pressure signal better represents intravascular pressure than the distal pressure signal does.

The "smoothed" distal pressure signal that we recorded was unexpected. Additional experiments are required to reveal the source of this "oversmoothing". A possible cause of this finding may be an air bubble trapped near the distal pipette pressure transducer.

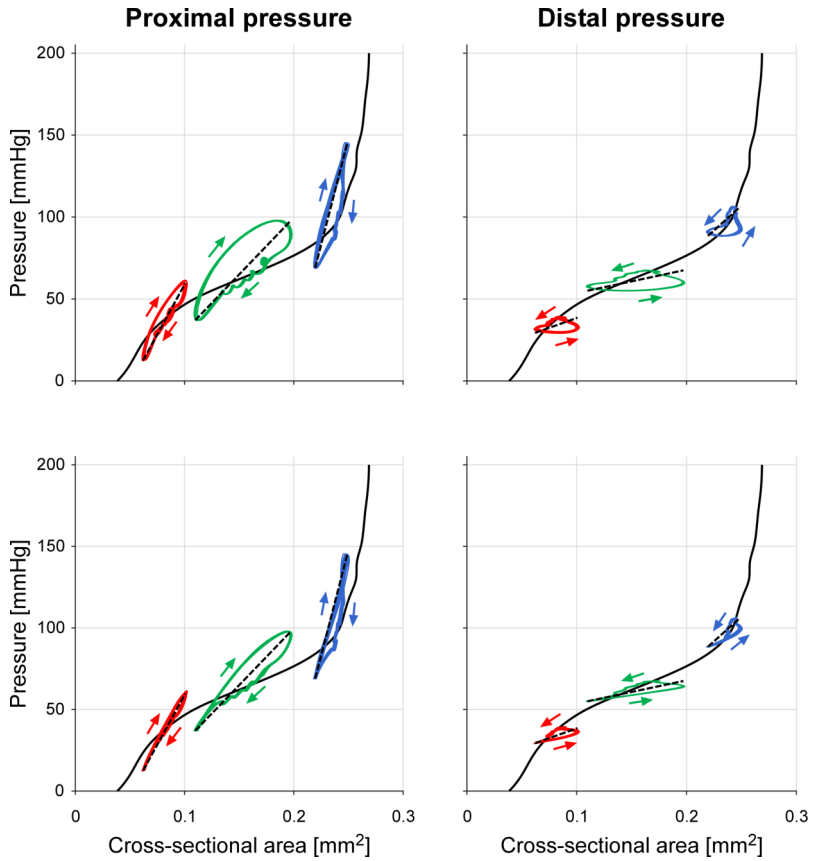

Figure 12.5: Effects of proximal (left column) versus distal (right column) pressure measurements and of post hoc pressure-area synchronisation (sync.) on resulting P-A relationships at a pulse rate of 10 Hz. Top row: no post hoc synchronisation; Bottom row: P-A synchronisation based on maximum of second-order derivative. Thick, solid line: average static P-A relationship. Dashed lines are drawn from $(P_{\min}, A_{\min})$ to $(P_{\max}, A_{\max})$, where subscripts min and max denote minimum and maximum, respectively. Signals acquired during protocol A (Fig. 12.2A).

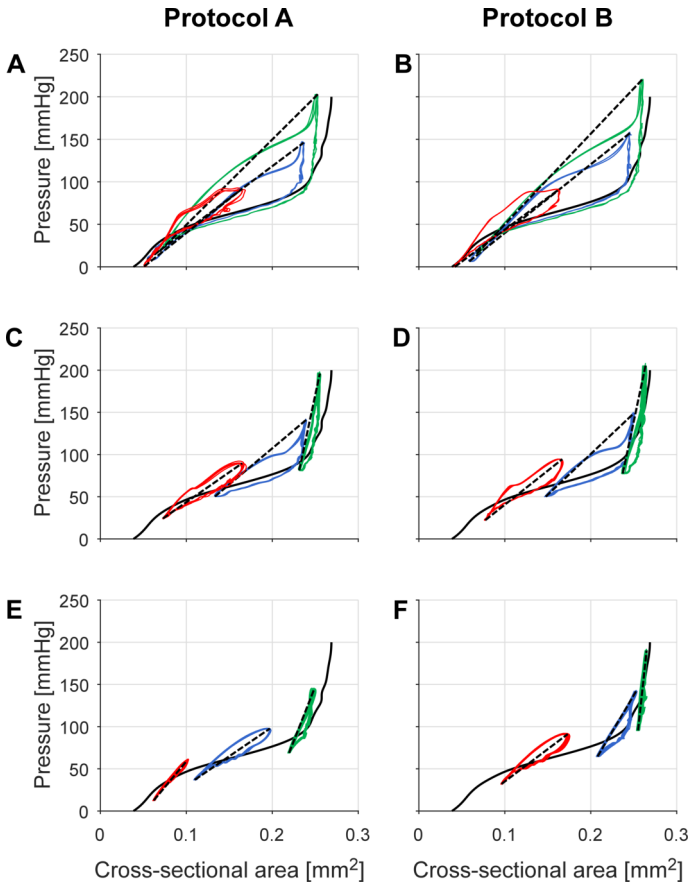

Figure 12.6: Dynamic pressure-area relationships acquired at 2 Hz (**A**, **B**), 5 Hz (**C**, **D**), and 10 Hz (**E**, **F**) using protocols A (left column, Fig. 12.2A) and B (right column, Fig. 12.2B). All loops run in clockwise direction.

The pressure transducer is attached to the set-up via a small silicone ring (not shown in Fig. 12.1). The edge of this ring could have bulged slightly into the set-up orifice, creating an irregularity behind which air bubbles could potentially get trapped.

12.4.2 Intravascular pressure

The previous section raises the question of what the actual intravascular pressure is. Although easily asked, this question has been proven hard to answer. One could possibly just fit a catheter tip pressure sensor through one of the pipettes, but this will inevitably fully or nearly fully occlude the lumen of this pipette, significantly altering the pressure drop across it. Another option could be to mount two ends of a carotid artery bifurcation between the pipettes and use the third end of the bifurcation to insert a catheter into and to measure pressure. Such an experiment could be performed to quantitatively assess the pressure drop across the pipettes. If this pressure drop is properly quantified in

terms of phase and magnitude, it can function as a reference for normal, straight artery experiments.

12.4.3 Shape of the applied pressure pulse

In our set-up, a sharply rising pressure pulse that is reasonably similar to an *in vivo* pressure wave is generated and applied to the artery, mimicking *in vivo* conditions. Performing the experiment *in vitro*, however, allows us to acquire simultaneous pressure, diameter, and axial force measurements at higher precision than possible *in vivo*. Other researchers have subjected the mounted arteries to sinusoidal pressure waves of various frequencies (for an overview, see Table 12.1). The advantage of this is that in general, such waves are more controllable. The obvious disadvantage is that when sinusoidal waves are used, the arteries are not directly studied under their *in vivo* conditions.

12.4.4 Application of flow

As this is a pilot study, we have deliberately chosen at this stage not to apply flow to the mounted vessel. However, this could be easily accomplished in our set-up by slightly modifying the fluid routing in Fig. 12.1. Note that, in order to simulate the effects of flow-induced shear stress on the arterial wall, the viscosity of the fluid used in the system should match the viscosity of blood.

12.4.5 Signal filtering

In our processing, we have chosen to use a Savitzky-Golay with a cut-off frequency of 60 Hz, corresponding to inclusion of the first six harmonics of the pressure and diameter signals at a pulse frequency of 10 Hz. Studies indicate that ideally, ten harmonics should be included to optimally reconstruct an arterial pressure signal (Moxham 2003; Nichols et al. 2011); twenty harmonics should be used to optimally reconstruct the second derivative of the pressure signal. Nevertheless, we have chosen to stick to six harmonics to limit the effects of non-physiological measurement noise.

Arterial diameter was tracked on a frame-by-frame basis and is therefore effectively sampled at the ultrasound frame rate (564 Hz). Pressure signals are acquired using mechanical transducers with a specified rise time of 1 ms, corresponding to a bandwidth of approximately 350 Hz (Sobering 1999). For a correct interpretation of *P*-*A* loops, it is essential that both *P* and *A* are recorded simultaneously, at the same location, and processed by circuitries having the same frequency characteristics (Hoeks et al. 2000). The use of a conservative filtering approach limits the potential problem of combining high-frequency diameter signals with lower-frequency pressure signals.

12.4.6 Constitutive modelling

In future, the data generated using the set-up presented can be used to characterise constitutive models of the artery wall (Holzapfel and Ogden 2010a). Such models can be used to *interpret* the obtained measurements, yielding insight into the mechanical behaviour of the individual wall components.

12.4.7 Conclusions

In the present study, we have demonstrated the feasibility of *ex vivo* mechanical assessment of murine carotid arteries under pulsatile conditions. Although still in a piloting stage, in the future, the developed method could yield novel mechanical insights into physiological arterial wall mechanics in health and disease. Engineering a phase consistent pulse wave generation circuit and signal processing system remains a true challenge.

12.5 Acknowledgements

Help from Arnold Hoeks on processing ultrasound images using wall tracking is gratefully acknowledged.

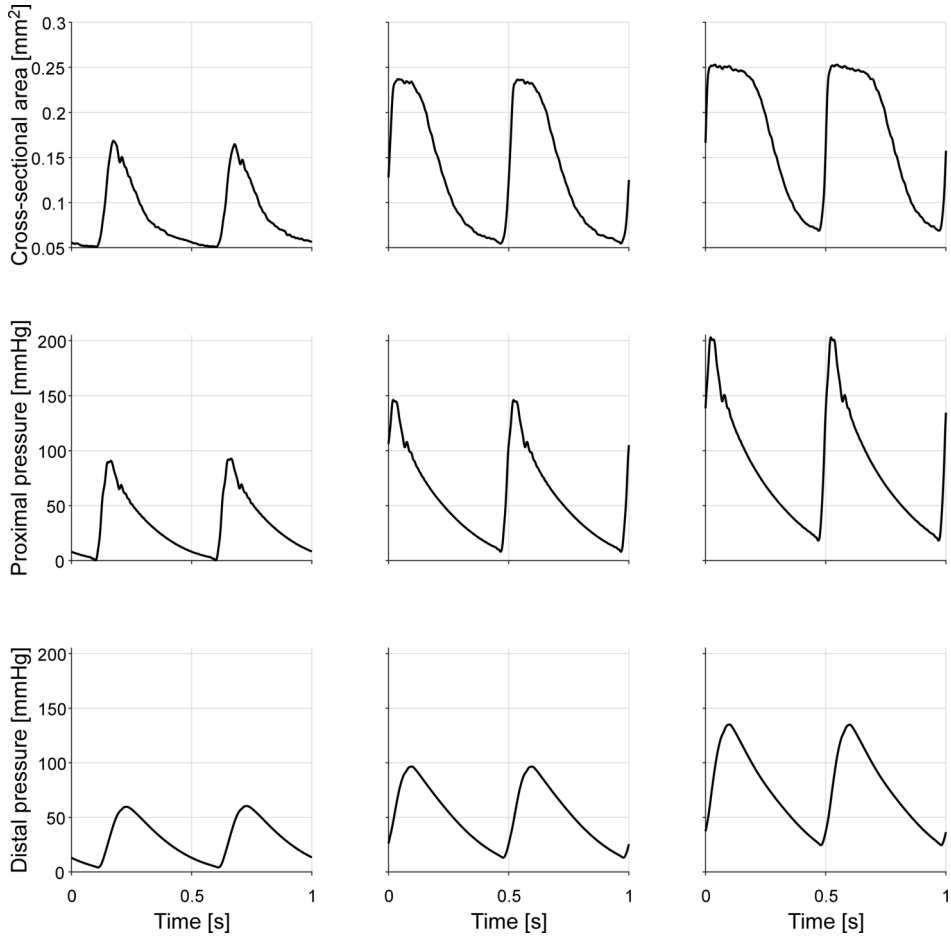

Figure 12.A1: Raw acquired cross-sectional area and proximal (P_1) and distal (P_2) pressure signals, acquired at 2 Hz (protocol A, Fig. 12.2A) and systolic reference pressures (defined at 5 Hz, see protocol) of 60, 100, and 140 mmHg (left, middle, and right columns, respectively).

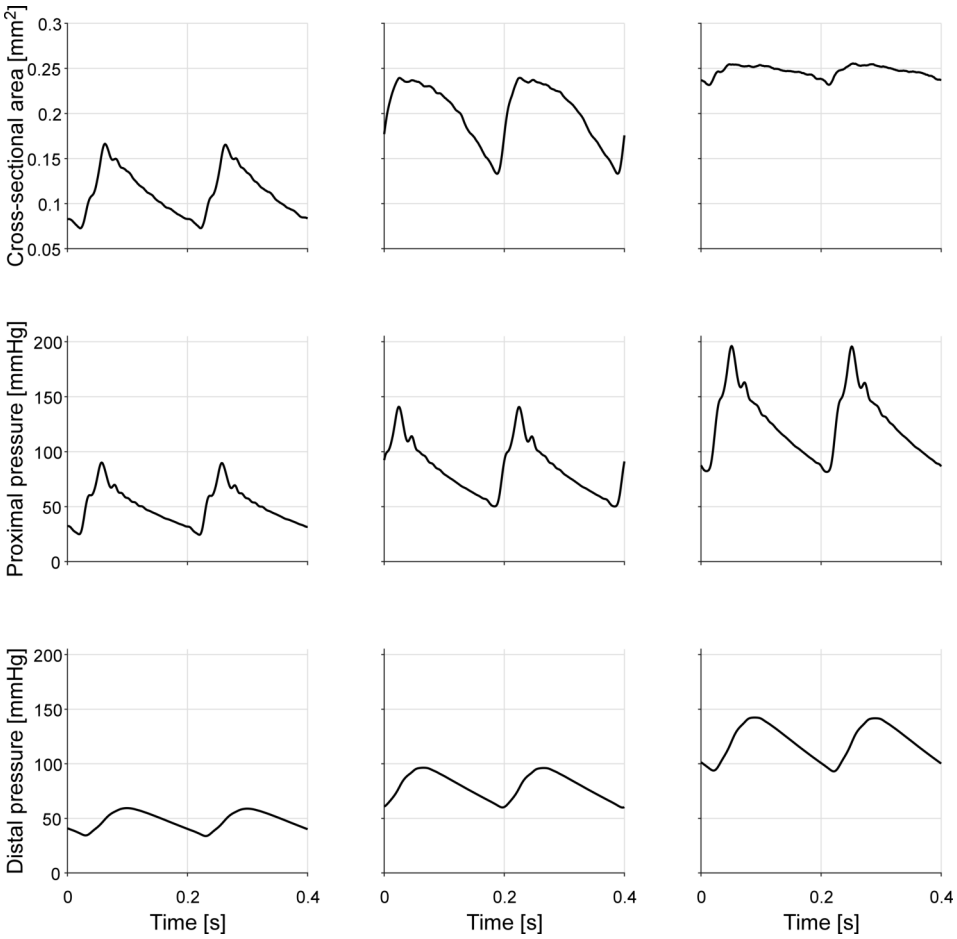

Figure 12.A2: Raw acquired cross-sectional area and proximal (P_1) and distal (P_2) pressure signals, acquired at 5 Hz (protocol A, Fig. 12.2A) and systolic reference pressures of 60, 100, and 140 mmHg (left, middle, and right columns, respectively).

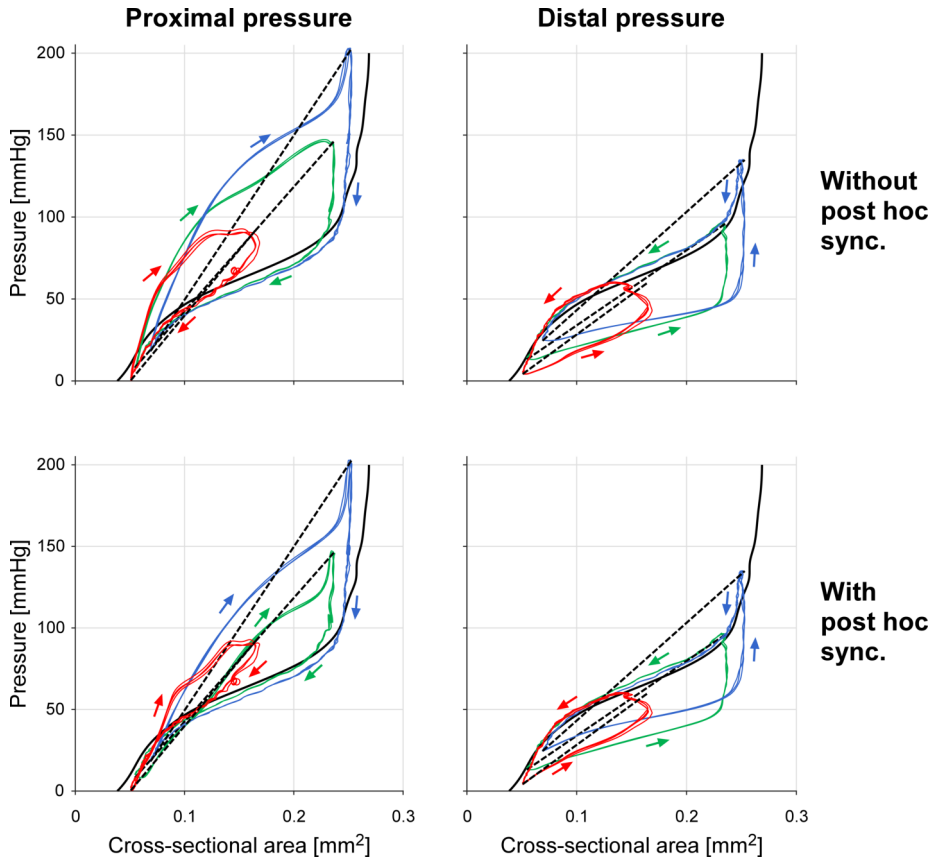

Figure 12.A3: Effects of proximal (left column) versus distal (right column) pressure measurements and of post hoc pressure-area synchronisation (sync.) on resulting *P*-*A* relationships at a pulse rate of 2 Hz. Top row: no post hoc synchronisation; Bottom row: *P*-*A* synchronisation based on maximum of second-order derivative. Thick, solid line: average static *P*-*A* relationship. Dashed lines are drawn from (P_{min}, A_{min}) to (P_{max}, A_{max}), where subscripts min and max denote minimum and maximum, respectively. Signals acquired during protocol A (Fig. 12.2A).

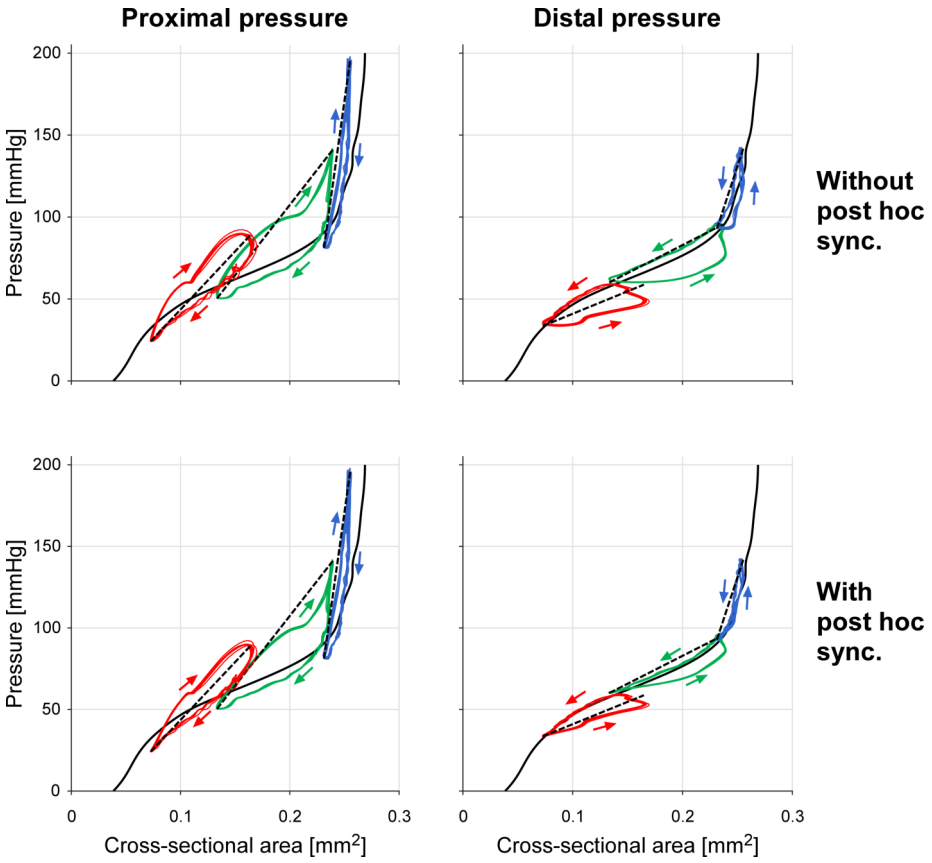

Figure 12.A4: Effects of proximal (left column) versus distal (right column) pressure measurements and of post hoc pressure-area synchronisation (sync.) on resulting *P*-*A* relationships at a pulse rate of 5 Hz. Top row: no post hoc synchronisation; Bottom row: *P*-*A* synchronisation based on maximum of second-order derivative. Thick, solid line: average static *P*-*A* relationship. Dashed lines are drawn from (P_{min}, A_{min}) to (P_{max}, A_{max}), where subscripts min and max denote minimum and maximum, respectively. Signals acquired during protocol A (Fig. 12.2A).

Chapter 13

General discussion

13.1 Introductory remarks

In this thesis, the topic of arterial stiffening has been approached from clinical as well as engineering perspectives. Significant efforts have been made to advance the *quantification* as well as the *interpretation* of arterial stiffening.

13.2 Advancing the quantification of arterial stiffness

The gold standard for assessing arterial stiffness is measuring the carotid-femoral pulse wave velocity (PWV, Laurent et al. 2006). The *Recommendations for Improving and Standardizing Vascular Research on Arterial Stiffness* by the American Heart Association have formulated several future needs in the field of arterial stiffness (Townsend et al. 2015). One of these needs is the development of therapeutic interventions to reduce arterial stiffness. Two potential interventions to reduce arterial stiffness are currently available:

1. Blood pressure-lowering drugs, acting indirectly on the arterial wall by reducing cyclical pressure load, and
2. Interventions that act directly on the arterial wall.

When assessing interventions of the first category, care should be taken since blood pressure is an intrinsic determinant of PWV. Therefore, the design as well as the results of studies investigating the effect of blood pressure-lowering drugs on the arterial wall require careful consideration of the intrinsic dependence of PWV on blood pressure. This emphasises that *independent quantification* of arterial stiffness is not trivial, and that a change in measured PWV can not be directly and unambiguously interpreted as a change in intrinsic arterial wall stiffness. We set out to quantitatively assess the physiological confounders of PWV (Townsend et al. 2015), investigating the *magnitude* of their effect and ways to correct for them. These confounders include blood pressure, heart rate, and axial stretch.

In this section of the discussion, we will first review these confounders. Subsequently, we will integrate the obtained insight into a set of recommendations for the optimal measurement of arterial stiffness.

13.2.1 Confounders of arterial stiffness

Blood pressure

Correction methods Current recommendations by the American Heart Association (Townsend et al. 2015) emphasise blood pressure and heart rate as confounders of PWV. PWV has long been known to change with actual blood pressure (Bramwell et al. 1923). We investigated and quantified the *intrinsic* relationship between blood pressure and PWV (**chapter 2**). Due to its substantial dependence on blood pressure, PWV must be corrected for blood pressure if one wishes to assess arterial stiffness independently.

In this thesis, five methods have been touched upon to address the blood pressure dependence of PWV:

1. Correcting PWV based on a blood pressure dependence derived from an exponential relationship between pressure (P) and cross-sectional area (A);

2. Correcting PWV for blood pressure on a statistical basis;
3. Using reference values or a rule of thumb to correct PWV;
4. Converting PWV to a blood pressure-independent measure such as cardio-ankle vascular index (CAVI) or stiffness index β; and
5. Assessing the blood pressure dependence of PWV by experimentally influencing blood pressure while recording the change in PWV.

Method 1 is presented in **chapter 2**, where it was used to correct local carotid PWVs. The method gives *direct* insight into the magnitude of the pressure dependence. We additionally used this method in a data set of subjects that were treated using anti-angiogenic drugs (**chapter 3**). In chapter 3, we also compared method 1 to a purely statistical approach (method 2). Numerical results of this approach were similar. However, a statistical approach is only applicable if a *population* or a group of subjects is studied, i.e., it is not applicable in individuals. A possible solution to this problem is to relate a PWV measurement to a reference value, e.g., from The Reference Values for Arterial Stiffness' Collaboration 2010 study. Nonetheless, as pointed out in the General Introduction, the values in this study represent both acute and remodelling effects of blood pressure on PWV. Therefore, the reference values from The Reference Values for Arterial Stiffness' Collaboration 2010 do not independently quantify the physiological confounding effect of blood pressure on PWV.

A very simple type of "reference value" is a rule of thumb. As presented in **chapter 2**, PWV changes with approximately 1 m/s per 10 mmHg change in diastolic blood pressure. Such a rule of thumb has the clear advantage of being easily applicable in the clinic. However, **chapter 2** also shows that the actual pressure dependence of PWV is patient-specific. A change in blood pressure from 120/80 to 160/90 leads to a change in PWV of 0.9 m/s in "young" subjects (mean age 41 years), but to a change of 1.3 m/s in "old" subjects (mean age 64 years). These numbers are slightly lower than those calculated from The Reference Values for Arterial Stiffness' Collaboration 2010 data. This difference could be caused by the remodelling effect of high blood pressure on arterial stiffness. Thus, if one aims to calculate the acute effect of blood pressure on PWV, our novel method (**chapter 2**) is to be preferred.

Blood pressure-independent measures Another method to control for blood pressure is to convert PWV to a blood pressure-independent measure (method 4). Cardio-ankle vascular index (CAVI) has been proposed to be such a measure (Shirai et al. 2006). Note that although named "cardio-ankle", the CAVI formula can equally well be applied to the carotid-femoral PWV. We have shown that, on a theoretical basis, the use of the standard CAVI equation as proposed by Shirai et al. (2006) does *not* yield a fully pressure-independent index (**chapter 4**). This also holds for stiffness index β, which is another suggested blood pressure-independent measure of arterial stiffness (Hirai et al. 1989). In a simulation study ($n = 161$), simulating the effects of blood pressure lowering medication on CAVI, we showed that the pressure dependence of CAVI can lead to erroneous conclusions and to the *suggestion* of an intrinsically de-stiffened wall. This finding is important, as CAVI is increasingly being used to assess blood pressure-independent effects on arterial stiffness (Saiki et al. 2015; Shirai et al. 2011). If CAVI is "trusted" to be 100% pressure-independent, wrong conclusions may be drawn.

To overcome the problem of CAVI's blood pressure dependence, we have derived an updated formula that does yield a pressure-independent CAVI index (**chapter 4**). Using this formula CAVI *can* be used as a blood pressure-independent measure.

Which blood pressure component to use for statistical correction? When correcting for blood pressure statistically, one has to choose which blood pressure component (diastolic, mean, systolic blood pressure or pulse pressure) to use for correction. Several studies have touched upon the question of which component determines PWV. Current recommendations state that mean arterial pressure should be taken into consideration when PWV data are analysed (Townsend et al. 2015). Kim et al. (2007), Stompor et al. (2003), and Tanaka et al. (1998) assessed the relationship between PWV and these blood pressure components cross-sectionally. They found a significant correlation of PWV with all measures *except* diastolic blood pressure. Sá Cunha et al. (1997) reported a correlation between PWV and systolic blood pressure for both genders, and a correlation between PWV and diastolic blood pressure only in women. In contrast, Nürnberger et al. (2003) only report a correlation between PWV and diastolic blood pressure. All these studies have in common that they assessed the association between PWV and blood pressure cross-sectionally. The relationship that is obtained in this way may not reflect the *acute* effect of blood pressure on PWV.

Acutely and *physically*, it can be shown that PWV varies with diastolic blood pressure (Bramwell et al. 1923; Nichols et al. 2011; Nye 1964; Willemet et al. 2015). This is due to the fact that a propagating pulse wave "sees" the diastolic pressure. In other words, the front of the pressure wave travelling to the periphery encounters an arterial section that is still at diastolic blood pressure.

As is clear from the above, the question of which blood pressure component to use for correction of PWV can be approached from 1) a cross-sectional, population side; or 2) an acute, mechanistic side. If one wishes to correct a measurement set on a statistical basis for the influence of blood pressure, mean blood pressure seems a good candidate. If, on the other hand, one wants to remove the acute effect of blood pressure on PWV, diastolic blood pressure is a well-founded choice.

Heart rate

The role of heart rate as a confounding factor of PWV has been controversial. In this thesis, we report the largest patient study investigating the direct effect of heart rate on carotid-femoral PWV (**chapter 5**). A limitation of previous studies on the heart rate effect on PWV was that many showed an increase in blood pressure with the increase in heart rate. We used our knowledge on blood pressure corrections (**chapters 2** and **3**) to correct for this blood pressure increase with heart rate. We corrected for blood pressure using methods 1 (correcting based on an exponential *P-A* relationship), 2 (statistically), and 5 (experimentally, influencing blood pressure by varying posture) described above. The resulting blood pressure-corrected effect of heart rate on PWV was on average 0.18 m/s per 10 bpm.

In the General Introduction, we pointed out the white-coat effect on heart rate (Mancia et al. 1983). Given the average increase in heart rate as reported by Mancia et al. (1983) (15.9 bpm) and our heart rate dependence of PWV, the white-coat increase in PWV due to heart rate would be 0.29 m/s. The diastolic blood pressure increase observed by Mancia

et al. (1983) (14.9 mmHg), given our rule of thumb of 1 m/s per 10 mmHg (**chapter 2**) corresponds to a white-coat PWV increase of 1.5 m/s. In total, the combined white-coat effect on PWV is roughly 1.8 m/s. Clearly, the blood pressure component of the white-coat effect appears much larger than the heart rate component.

In the measurement of carotid-femoral PWV, carotid applanation tonometry is performed to record the carotid artery pulse waveform. The substantial pressure applied locally to the carotid artery with applanation tonometry could potentially evoke a baroreceptor response, resulting in bradycardia and hypotension. In **chapter 6**, we assessed whether carotid artery applanation tonometry leads to baroreceptor activation. We found that, when performed by an experienced research nurse or clinician, carotid artery tonometry does not lead to substantial baroreceptor activation. Care should be taken not to occlude the carotid artery, and to keep the tonometer at a constant position relative to the artery. Furthermore, the potential influence of head rotation on PWV during carotid artery assessments should be taken into account. When local carotid artery PWV is measured, ultrasound wall tracking measurements are performed at the carotid artery (**chapters 2**, **3**, **7**, **8**, and **9**). During ultrasound measurements, however, the force applied to the carotid artery is negligible, and does not cause baroreceptor activation.

Axial stretch

Another, often ignored confounder of local arterial stiffness is the axial stretching of an artery. When local, carotid PWV is measured, the head is often tilted sidewards and backwards. This stretches the carotid artery. Consistent head rotation during a common carotid artery ultrasound assessment and the concomitant arterial stretch cause a significant and clinically relevant bias in carotid artery PWV measurements of 0.20 m/s on average (**chapter 7**). The impact of unstandardised use of head rotation in studies with carotid distensibility or PWV as an outcome measure should not be neglected, and, hence, standardisation is highly recommendable (see section 13.2.2).

Other confounders

Age is often considered a primary confounder of arterial stiffness (Cecelja and Chowienczyk 2009; Nürnberger et al. 2003). However, while blood pressure, heart rate, and axial stretch are *physiological confounders*, age is *not*. Physiological confounders have the effect that if one and the same artery is assessed under different conditions with respect to a physiological confounder, different PWVs will be *measured*. With age, however, arteries stiffen *physically* (**chapter 8**, O'Rourke and Hashimoto 2007).

Age acts as an "integrator" of several ongoing processes, including remodelling due to wear and tear of elastin, but also of latent disease processes. The inclusion of age as a variable in statistical analyses of arterial stiffness studies may be useful to ensure comparability of measured arterial stiffness between subjects of different age. However, it should be noted that this yields only a first order correction, as changes in arterial stiffness with age will inevitably be patient-specific.

There is also a substantial list of what Townsend et al. (2015) term *methodological confounders*. First, the measurement of carotid-femoral PWV requires a transit distance measure. A large number of distance formulae have been proposed. Those have been

compared by Huybrechts et al. (2011). The two most commonly used methods for obtaining travel distance are 1) the direct distance method, measuring the direct distance from the carotid to the femoral recording sites, or 2) the subtraction method, measuring the distance from the suprasternal notch to both these sites. In case 1, the direct distance is multiplied by 0.8 to obtain the "true" travel distance. In case 2, the carotid distance is subtracted from the femoral distance. According to Townsend et al. (2015), both these measures are acceptable, whereas Van Bortel et al. (2012) recommend the direct distance method. Huybrechts et al. (2011) compared these non-invasively measured distance estimates to a "reference distance" obtained by magnetic resonance imaging (MRI). This distance, presuming the same PWV in the thoracic aorta and the carotid artery, was calculated as the ascending aorta to femoral artery distance minus the ascending aorta to carotid artery distance. Huybrechts et al. (2011) found that the direct distance method, using the multiplication factor of 0.8, led to the smallest bias when compared to the reference distance. The subtraction method as well as other methods led to higher biases. From this finding, Huybrechts et al. (2011) concluded that the direct distance method "corresponds best with the real travelled aortic path length". However, they did not test whether this direct distance method yields the best *estimator* of the reference distance; in other words, they did not test whether the estimate from this method explains the largest amount of variance in the reference distance. Sugawara et al. (2016) did confirm that the direct distance method corresponds best with the real travelled aortic path length. Unlike previous studies (Huybrechts et al. 2011; Sugawara et al. 2008; Van Bortel et al. 2012; Weber et al. 2009), Sugawara et al. (2016) quantified the *correlations* between an MRI reference and both methods. Importantly, they statistically compared these correlations using the Meng-Rosenthal-Rubin method, and found that the correlation for the direct distance method was significantly larger than for the subtraction method. This, in our opinion, truly proves that the direct distance method is superior to the subtraction method. Regardless of the distance measurement method used, it should be identical in all subjects, and it should be clearly mentioned when reporting a study. Commonly, tape measures are used for the actual distance measurements. Calipers, however, better minimise the impact of body contours and therefore are recommended (Levi-Marpillat et al. 2013; Townsend et al. 2015).

Second, carotid-femoral PWV can be measured at either the left or the right body side. As the iliac bifurcation is anatomically located slightly to the left of the sagittal plane, the true travel distance for a right-sided PWV measurement is slightly larger than the distance for a left-sided measurement. Bossuyt et al. (2013) showed that, compared to measurements at the right side, measuring at the left side induces a 2.7% bias in measured PWV when using the direct distance method and a multiplication factor of 0.8. This underlines the importance of standardisation of measurement side (Van Bortel et al. 2016).

Third, PWV is sometimes not measured along the carotid-femoral arterial bed but e.g., along the brachial-ankle bed. The resulting PWV measures are not necessarily interchangeable. Results of studies showing prognostic value of carotid-femoral PWV do not directly apply to other PWV measures. Therefore, the methodology used to assess PWV should be clearly stated when reporting a study (Townsend et al. 2015).

Fourth, the use of different devices may yield different values of PWV for the same arterial bed, a difference that is often largely attributable to the algorithm used to detect the arterial foot (Millasseau et al. 2005). In **chapter 5** (Appendix 5.A2), when studying

the effect of heart rate on PWV, we also investigated the influence of using a different foot detection algorithm on the obtained PWVs. In our case, the timing algorithm used did not significantly influence the slope of the linear relationship between heart rate and carotid-femoral PWV.

In order to minimise the effects of these methodological confounders it is important that within one and the same study, a clear protocol is available, stating the exact method of transit distance measurement, the device used for PWV measurement, and the settings for the PWV measurement device.

13.2.2 Recommendations for the independent quantification of arterial stiffness: What (not) to do?

Using the findings presented above, we synthesised a set of recommendations for the independent assessment of acute arterial stiffness. Some of these recommendations are included in the current guidelines, while others do not. In our recommendations, we will indicate if our guidelines correspond to existing guidelines, as indicated by the following abbreviations:

TF3 Clinical Applications of Arterial Stiffness, Task Force III: Recommendations for User Procedures (Van Bortel et al. 2002).

EXC Expert consensus document on the measurement of aortic stiffness in daily practice using carotid-femoral pulse wave velocity (Van Bortel et al. 2012).

AHA Recommendations for Improving and Standardizing Vascular Research on Arterial Stiffness by the American Heart Association (Townsend et al. 2015).

Our recommendations should be regarded as an addition to the current guidelines, to optimise the *independent* assessment of arterial stiffness. They are *not* meant to replace the existing documents.

Preparations

- Ideally, take a 24-hour blood pressure recording before the subject visits the clinic for PWV measurement. This yields insight into the subject's resting heart rate as well as blood pressure. Alternatively, perform a 30-minute unattended blood pressure measurement, which may be more practical.
- Before starting a PWV measurement, make sure that the subject is at rest to prevent acute influences on heart rate and blood pressure (TF3, EXC, and AHA).

Measurements

- When measuring *local carotid PWV* or carotid distensibility, care should be taken to rotate each subject's head by a *fixed* amount (**chapter 7**). In our study, a total rotation angle of 50° was practical and yielded clear images of the carotid artery.
- When measuring *carotid-femoral PWV*, the amount of head rotation is of minor importance, as the potential local change in carotid artery stiffness will have only a minor contribution to overall PWV.

- Carotid tonometry measurements should be performed by an experienced research nurse (TF3, AHA), using only minimal applanation force, at a distance approximately 2 cm proximal to the carotid sinus (**chapter 6**).
- Blood pressure should be recorded twice directly before the PWV measurement. Of these measurements, the fist one is performed to allow settling of the BP cuff, while the second one is performed to obtain an actual and reliable BP reading. BP should again be measured directly after the PWV measurement. The latter two measurements should be averaged to obtain a representative blood pressure during PWV measurement (TF3, EXC, and AHA; all less explicit).
- Heart rate should be recorded during PWV measurement (AHA). Heart rate is generally given by the PWV device. Heart rate is also obtainable as pulse rate from an ultrasound distensibility recording.

Data processing

- Correct for the difference in the subject's heart rate during PWV measurement and his/her resting heart rate, using 0.18 m/s/(10 bpm) (**chapter 5**) as a correction factor.
- Account for blood pressure (TF3, AHA) in one of the following ways:
  - Correct PWV to a reference pressure of 120/80 mmHg using an exponential *P-A* relationship (**chapter 2**).
  - Convert PWV into a blood pressure-independent index measure (**chapter 4**).

This will yield an *acute*, independent measure of arterial stiffness. Failing to account for the confounding effects of heart rate and blood pressure may yield artificial increases in measured PWV of the order of 2 m/s (**chapters 2** and **5**, Mancia et al. 1983; Spronck et al. 2015b). To put this into perspective, a PWV increase of 2 m/s would correspond to a 78% increased all-cause mortality risk in end-stage renal disease patients (Blacher et al. 1999).

13.3 Advancing the interpretation of changes in arterial stiffness

The second aim of this thesis is to improve the *interpretation* of changes in arterial stiffness. Two aspects of this aim were addressed: *in vivo* quantification of constitutive properties and improving methods for *in vitro* mechanical characterisation of arteries.

13.3.1 *In vivo* quantification of constitutive properties

Ideally, any change in arterial stiffness as non-invasively measured in patients would be directly interpretable in terms of changes in the individual wall components.

In **chapter 8**, we fitted a constitutive model to non-invasively measured *P-A* data from the carotid artery. By using a combination of physiological constraints, we were able to obtain a stable model fit and interpret the change in *P-A* relationship with ageing. The model distinguished between changes in collagen and elastin stiffness, and smooth

muscle properties. Our study demonstrated that constitutive modelling can be used to study existing hypotheses and provide quantitative estimates of changes in constitutive properties.

The formulation of a clear *hypothesis* is important in this light. A common pitfall is to create very detailed models, incorporating large sets of model parameters. Such large sets of parameters can never be properly and uniquely quantified using the limited measurement data obtainable *in vivo*. Therefore, for application *in vivo*, models should be kept as simple as possible, and should be designed around the hypothesis.

In **chapter 9**, we used the confounding effect of axial stretch on arterial stiffness to our advantage, employing it to assess carotid artery mechanics at two axial stretch states. We fitted a constitutive model incorporating collagen and elastin to our data. Our new approach led to a 43% reduction in variance of the model parameter corresponding to collagen stiffness. Variance of the other two constitutive parameters (the collagen *P-A* shape parameter and elastin stiffness) remained equal. These results show that our method leads to a more accurate *in vivo* estimation of carotid artery wall properties.

13.3.2 An integrative set-up for *in vitro* mechanical characterisation of arteries

In **chapter 12**, we present a newly developed set-up for biomechanical assessment of murine arteries under pulsatile conditions. The set-up will be further developed in the near future, complementing the current approach with two additions. First, arteries mounted in the set-up will be imaged using two-photon laser scanning microscopy, which can be used to *structurally* assess the arteries. In **chapters 10** and **11**, we demonstrated the use of two-photon laser scanning microscopy to quantify the orientation of smooth muscle cells in tubular structures such as an artery. Second, functional and structural (previous point) data will be integrated using constitutive modelling. We will extend the constitutive modelling framework presented in **chapter 8** to incorporate dynamic (viscoelastic) behaviour, enabling the study of the effect of pulsatility on arterial mechanics. The combination of two-photon laser scanning microscopy with the functional assessment as presented in **chapter 12** will be a step forward in studying the structure-function relationship in the murine arterial wall.

Sáez et al. (2016) recently published a related study, combining microscopical study of collagen orientation with mechanical inflation testing. They were able to successfully combine the structural and mechanical data in a constitutive model. Our approach differs in several aspects from the approach by Sáez et al. (2016). First, our set-up allows us to study static *as well as dynamic* mechanical behaviour. Second, in our set-up, the artery can be imaged at microscopic and macroscopic scales in precisely the same configuration that was used for mechanical testing, potentially yielding a better correspondence between mechanical and structural data. Third, in our set-up, the mounted arteries remain viable (Megens et al. 2007), which allows us to not only study *passive* but also *active* mechanical behaviour, including smooth muscle contraction. Fourth, our *structural* information can be obtained under stressed conditions, at different pressures and axial stretch ratios, potentially improving the constitutive descriptions even further. Finally, we perform our measurements in murine carotid arteries, whereas Sáez et al. (2016) used porcine carotid arteries.

As discussed above, potential interventions for arterial stiffness include blood pressure lowering agents, but also agents that directly target the arterial wall (Smulyan et al. 2016; Townsend et al. 2015). In the development of these agents, the proposed set-up could yield in-depth insight into the structural *and* functional effects of those drugs on the stiffened arterial wall. Some future directions on this topic are given in section 13.4.

13.4 Limitations and future directions

13.4.1 True shape of the pressure-area relationship

The exponential relationship between pressure (P) and lumen cross-sectional area (A) is commonly used and accepted as a good representation of the true P-A relationship in the physiological blood pressure range. In several chapters, we made use of an exponential relationship between pressure and diameter or lumen cross-sectional area of the artery (**chapters 2**, **3**, **4**, **5**, **8**, and **9**). In these chapters, we aimed to provide clinically applicable blood pressure and heart rate correction methods.

If one wishes to correct "simple" PWV and blood pressure measurements using patient-specific representations of the P-A relationship, one cannot fit complicated P-A relationships. The number of parameters of such relationships would be too large to be fitted using only systolic and diastolic pressures and their corresponding diameters, or using these pressures and PWV. Nevertheless, the true P-A relationship is inevitably more complicated than a single exponential.

In **chapter 4**, we assessed the pressure (in)dependence of CAVI and stiffness index β. Based on the *assumption* that the pressure-diameter relationship is single-exponential, the original indices show pressure dependence. Furthermore, we were able to derive corrected indices that, based on the exponential assumption, are pressure-independent. Further research is required to assess the pressure dependence of our new indices given *measured*, non-approximated P-A relationships. Such research could strengthen our theoretical proof of the pressure dependence of CAVI and β.

13.4.2 Cause of the heart rate dependence of PWV

In **chapter 5**, we quantified the dependence of PWV on heart rate. The *cause* of this dependence cannot be concluded from our study. Potential causes include viscoelasticity of the arterial wall, changes in smooth muscle tone, artefacts induced by the foot detection algorithm, or blood flow effects. With respect to viscoelasticity, it should be noted that P-A loop area, commonly associated with viscoelastic behaviour, appears to be very small under human, physiological conditions (Hermeling et al. 2012a). The *slope* of the P-A relationship, also associated with viscoelasticity, appears to change with heart rate (**chapter 12**; Holzapfel et al. 2002; Lichtenstein et al. 1998). Blood flow potentially influences PWV because the arterial pulse wave is known to move relative to its medium (relative to the blood). This implies that when blood *flow* velocity increases, measured PWV also increases. An increased heart rate may well coincide with an increased cardiac output, on its turn increasing blood flow velocity and thereby PWV.

These hypotheses could be assessed using a combination of (animal) experiments and mathematical modelling. Viscoelasticity of the arterial wall could be studied by subjecting

murine arteries mounted in our novel set-up (**chapter 12**) to pressure pulses of different frequencies. The haemodynamic effect of blood flow velocity on PWV could be assessed using a mathematical (pulse wave propagation) model. Such a model, when performing realistic pressure waveforms, could also be used to assess the effect of the foot detection algorithm on PWV. An other option would be to perform *in vivo* animal experiments, changing heart rate by means of cardiac pacing (e.g., Tan et al. 2012), while continuously measuring blood flow velocity.

13.4.3 Studying the role of novel arterial stiffness treatments on the arterial wall

Several classes of drugs are proposed to have a direct effect on arterial wall stiffness. These include angiotensin-converting enzyme (ACE) inhibitors (Mallareddy et al. 2006; Ong et al. 2011; Shahin et al. 2012) as well as aldosterone inhibitors (Bénétos et al. 1997; Edwards et al. 2009). Inflammation may also play a role in arterial stiffness (Roman et al. 2005). In rheumatoid arthritis patients, reducing inflammation led to a significant reduction in arterial stiffness, either by anti–tumour necrosis factor-α (TNF-α) therapy (Mäki-Petäjä et al. 2006) or by statin therapy (Mäki-Petäjä et al. 2007).

Some drugs are proposed to lower arterial stiffness by directly targeting collagen or elastin in the arterial wall. Elastin fragmentation is thought to be one of the causes of arterial stiffening. This causes a larger amount of the arterial pressure load to be borne by the much stiffer collagen (**chapter 8**, O'Rourke and Hashimoto 2007). Increased arterial stiffness is associated with an increase in activity of matrix metalloproteinases (MMPs, Sun 2015). MMPs are enzymes (endopeptidases) that are capable of degrading numerous extracellular matrix proteins (Wang et al. 2012). MMP activation results in increased cellularity and thickening of the arterial intima, as well as causes elastin network fracture (Wang et al. 2012). In rats, inhibition of MMPs has been shown to preserve elastin integrity with hypertension (Wang et al. 2012).

Other drugs target the increased collagen cross-linking that is thought to partially cause arterial stiffening. Increased collagen cross-linking by advanced glycation end-products is associated with increased arterial stiffness (Llauradó et al. 2014; McNulty et al. 2007; Zieman and Kass 2004). Cross-link breakers could potentially reverse this cross-linking, improving arterial compliance and decreasing stiffness (Kass et al. 2001; Wolffenbuttel et al. 1998).

The modelling and *in vitro* quantification methods presented in this thesis could well be used to integrate structural and functional measurements, comparing treated and untreated arteries. The constitutive model presented in **chapter 8** could be extended to explicitly model collagen cross-linking (e.g., Sáez et al. 2014). Such a detailed model could subsequently be characterised with detailed measurement data acquired *in vitro* (**chapter 12**).

13.4.4 Closing the loop

In our *in vitro* set-up (**chapter 12**), we are able to assess local PWV and distensibility in mice using the same (ultrasound wall tracking) methodology that is used in patients. This allows us to directly translate our in-depth structural and mechanical findings to clinically

measurable stiffness parameters. *In vitro* local PWV measurements on murine arteries can also be compared to *in vivo* carotid-femoral pulse wave velocity measurements in mice (Leloup et al. 2014), which are up and running at our institute. When studying the role of novel arterial stiffness treatments on the arterial wall, these developments could prove a key advantage, allowing for a more direct estimation of the effect of such treatments on *in vivo* PWV.

13.5 Conclusions

Throughout this thesis, we have approached the assessment and interpretation of arterial stiffness from a medical engineering perspective.

We have rigourously identified and tackled blood pressure, heart rate, and axial stretch as confounders of arterial stiffness measurements. We believe that the developed methodology and concepts may ultimately contribute to a better understanding of the behaviour of the (diseased) arterial wall in a variety of clinical and scientific settings.

Furthermore, by building a novel set-up that enables integration of different modalities, we have taken a significant step to improve the understanding of arterial structure-function relationships at micro and macro scales.

Summary

EMERGING evidence exists that accelerated stiffening of the large arteries is a strong predictor of cardiovascular complications worldwide. The gold standard method for the assessment of arterial stiffness in patients is the measurement of pulse wave velocity (PWV), the velocity of the pressure pulse wave as it travels along the large arteries. Although PWV is positively related to arterial stiffness, this relationship is confounded by several factors. Furthermore, establishing whether an artery is stiffened or not does not inform a researcher or clinician on the *cause* of the stiffening. Therefore, this thesis is centred around two aims: 1) to advance the objective *quantification* of arterial stiffness; and 2) to advance the *interpretation* of observed differences and changes in arterial stiffness. Chapters 2 to 7 pertain to aim 1, chapters 8 to 12 pertain to aim 2.

Chapter 1 provides a general introduction to this thesis and introduces the reader to the problem of arterial stiffening and its relationship with hypertension.

In **chapter 2**, we studied the dependence of PWV on blood pressure (BP). We recorded carotid artery echo-tracking and tonometry waveforms in a group of hypertensive patients. Echo-tracking was used to measured the time course of the artery diameter and thereby cross-sectional area, whereas tonometry was used to measure the time course of local arterial pressure. These measurements were performed at baseline and after three months of anti-hypertensive treatment. The recorded waveforms at baseline were combined into exponential pressure-area curves for each subject. Using follow-up pressures and baseline curves, we predicted the follow-up decrease in local, carotid PWV after anti-hypertensive treatment. Follow-up measurements showed a near 1 m/s decrease in carotid PWV when compared to baseline, which fully agreed with our model prediction given the roughly 10 mmHg decrease in diastolic pressure. This implies that in this patient group, the measured decrease in local, carotid PWV is fully explained by the decrease in BP, and suggests no change in intrinsic arterial wall behaviour. Quantitatively, our findings are surprisingly similar to data from the "Reference Values for Arterial Stiffness' Collaboration" study, albeit that in this reference values study, carotid-femoral (transit time) PWVs were measured.

In **chapter 3**, we used the measurement and modelling methodology developed in chapter 2 to study the effects of anti-angiogenic drugs (AADs) on intrinsic arterial stiffness. AADs are increasingly used in anti-cancer therapy, with hypertension and an increased PWV as frequent side effects. PWVs and pressure-area curves were measured at baseline (before AAD treatment) and at four follow-up visits spaced two weeks apart. In this study, the measured change in carotid PWV with AAD treatment significantly exceeded the BP-predicted change, indicating structural changes in arterial wall behaviour. We compared our method to a traditional, statistical method of correction; results were quantitatively similar. However, our novel (chapter 2) methodology is applicable in individual patients, whereas a fully statistical method requires a patient cohort in order to be applied.

Chapter 4 assessed two indices of arterial stiffness: stiffness index β and cardio-ankle vascular index (CAVI). Both are used to quantify the intrinsic exponent (β_0) of the BP-diameter relationship, and are often presented to be BP-independent. CAVI and β assume an exponential relationship between pressure (P) and diameter (D). In this chapter, we demonstrated that, 1) under this assumption, β and CAVI as currently implemented are inherently BP-dependent; and 2) that this BP dependence can be readily corrected for. To substantiate the BP effect on CAVI in a typical follow-up study, we computer-simulated a patient cohort of 161 subjects before and following BP-lowering "treatment" (assuming no follow-up change in intrinsic β_0 and therefore in actual P-D relationship). Lowering BP from a hypertensive to a normotensive range resulted in a significant CAVI decrease, whereas our corrected CAVI measure ($CAVI_0$) showed no significant change.

Chapter 5 assessed the influence of heart rate on transit-time PWV. In this study, individuals with an *in situ* cardiac pacemaker or cardioverter defibrillator were paced at heart rates from 60 to 100 bpm. At each heart rate, BP and PWV were measured. As expected, both PWV and central aortic diastolic BP increased with heart rate. We corrected PWV for the influence of BP in three ways: 1) statistically, using a linear mixed model; 2) mathematically, using an exponential relationship between BP and cross-sectional lumen area (chapter 2); and 3) using the measured BP dependence of cfPWV derived from changes in BP induced by position changes (seated and supine) in a subset of subjects. All three methods yielded a similar, BP-independent heart rate dependence of PWV in the range of 0.16 to 0.20 m/s/(10 bpm).

In **chapter 6**, we assessed whether carotid artery applanation tonometry causes activation of the carotid baroreceptors. Such activation could cause fluctuations in heart rate and blood pressure. We studied this potential activation by comparing finger blood pressure-derived parameters during carotid and femoral applanation tonometry. 95%-confidence intervals were used to calculate the maximum absolute difference in heart rate and blood pressure between carotid and femoral tonometry. These differences were of such a small magnitude that we concluded that in our study, carotid artery applanation tonometry did not cause clinically significant baroreceptor activation.

During ultrasound distensibility assessment of the carotid artery, the patient's head is usually rotated sidewards and slightly upwards to optimise visibility of the carotid segment. This rotation may affect vessel length and thus the longitudinal arterial strain, which intrinsically influences circumferential mechanical measures such as diameter and distension. In **chapter 7**, we quantified the influence of head rotation on circumferential mechanics by performing ultrasound distensibility examinations with the head in two orientations: 1) the normal orientation, facing forwards; and 2) the rotated orientation, facing sidewards and slightly upwards. Additionally, we measured common carotid artery length in both orientations using magnetic resonance imaging (MRI) to assess whether indeed a change in length occurred with head rotation. MRI measurements showed a significant rotation-induced longitudinal strain that led to a significant decrease in absolute and relative distension with head rotation, respectively. From these measurements, we concluded that consistent head rotation during a common carotid artery ultrasound assessment causes a significant and clinically relevant bias in carotid artery distension measurements.

In **chapter 8**, we used the measurement data from chapter 2, which we divided into a "young" and an "old" group of subjects. We aimed to quantitatively interpret the ob-

served changes in wall behaviour with age using a constitutive modelling approach. We implemented a model of arterial wall biomechanics and fitted this to the group-averaged pressure-area (*P-A*) relationship of the "young" subgroup of our study population. Using this model as our take-off point, we assessed which parameters had to be changed to let the model describe the "old" subgroup's *P-A* relationship. Realistic conditions were enforced by adapting the following physiologically based assumptions: 1) we required wall stress to be homogeneously distributed over the arterial wall; 2) we assumed wall stress normalisation with age by keeping average "old" wall stress at the "young" level; and 3) we required axial force to remain constant over the cardiac cycle. Changing from "young" to "old", our simulations showed a shift in pressure load bearing from elastin to collagen, caused by a decrease in elastin stiffness and a considerable increase in collagen recruitment. Correspondingly, simulated diameter and wall thickness increased by about 20 % and 17 %, respectively. The latter compared well with a measured thickness increase of 21 %. This chapter showed that changes with age in arterial wall mechanics can be interpreted in terms of constitutive properties.

In **chapter 9**, we investigated whether we could improve the process of constitutive parameter estimation as proposed in chapter 8 by effectively increasing the amount of measurable mechanical information. To this end, we used measurement data from chapter 7 that was acquired at two levels of axial stretch. We compared the case of fitting our constitutive model to the "full" distensibility data set containing data from both levels of axial stretch, with the "normal" case of using only one level. In the case of using data from both levels, variability of the constitutive model parameter representing collagen stiffness reduced with 43% as compared to the case of using only one level. Sensitivity analysis revealed that in further reducing the uncertainty of estimated constitutive parameters, it is most beneficial to increase the accuracy of ultrasound-based measurements of arterial diameter, distension and wall thickness. This chapter demonstrated that constitutive model-based interpretation of stiffness measurements (as in chapter 8) can be improved by exploiting the dependence of distensibility measurements on head rotation (chapter 7).

In **chapter 10**, we developed a method to determine two-dimensional smooth muscle cell orientation in tubular structures. We extended this method to a three-dimensional method in **chapter 11**, and used it to quantify smooth muscle cell orientation in viable murine carotid arteries. In these arteries, mounted between micropipettes, smooth muscle cell nuclei were fluorescently labelled and imaged using two-photon laser scanning microscopy. After image processing, orientations were quantified by fitting a Bingham distribution to the observed orientations. We observed that the orientations were not only dispersed in the axial-circumferential plane (i.e., helically), but also in the radial-circumferential plane (i.e., transversally). Helical dispersion in orientation was much larger than transversal dispersion. Additionally, SMC orientations showed a statistically significant mean right-handed helix angle in both inner and outer smooth muscle layers of both left and right arteries.

Arterial biomechanical behaviour under dynamic (pulsatile, *in vivo*) conditions may differ substantially from its behaviour under static conditions. Therefore, in **chapter 12**, we developed an integrated system for biomechanical assessment of murine arteries under pulsatile conditions. In this system, murine carotid arteries are mounted between glass micropipettes. Subsequently, pulsatile pressure is generated (pulse frequency 2–

10 Hz) and applied to these arteries. We performed pilot measurements using this system, showing the feasibility of *ex vivo* mechanical assessment of murine carotid arteries under pulsatile conditions.

Chapter 13 concludes this thesis and discusses our most important findings and their clinical implications. In this chapter, also a set of clinical recommendations for the assessment of arterial stiffness are given. Furthermore, the limitations of our work are reviewed and directions for future research are suggested.

Samenvatting

Versnelde verstijving van de grote slagaders vergroot sterk de kans op hart- en vaatziekten. De gouden standaard om vaatstijfheid te meten is het bepalen van de polsgolfsnelheid, de snelheid waarmee de bloeddrukgolf zich beweegt langs de grote slagaders. De polsgolfsnelheid (pulse wave velocity, PWV) is weliswaar geassocieerd met vaatstijfheid, maar deze relatie wordt door een aantal factoren verstoord. Bovendien vertelt een PWV-meting een arts niets over de oorzaak van de vaatverstijving. Dit proefschrift heeft daarom twee hoofddoelen: 1) het verbeteren van de objectieve *kwantificatie* van vaatstijfheid, en 2) het verbeteren van de *interpretatie* van gemeten verschillen en veranderingen in vaatstijfheid.

Allereerst wordt in **hoofdstuk 1** een algemene inleiding tot dit proefschrift gegeven en introduceert dit hoofdstuk het probleem van vaatverstijving aan de lezer, alsmede de nauwe relatie tussen vaatverstijving en hoge bloeddruk.

Hoofdstukken 2 tot en met 7 richten zich op de kwantificatie van vaatstijfheid in patiënten. In **hoofdstuk 2** hebben we onderzocht hoe de PWV van de bloeddruk afhangt. In een groep patiënten met hoge bloeddruk hebben we met behulp van echografie en tonometrie metingen aan de halsslagader uitgevoerd. Met echografie maten we het diameterverloop over de tijd van het vat; met tonometrie konden we een inschatting maken van het lokale bloeddrukverloop in het vat. We hebben deze metingen uitgevoerd vóór- en nadat deze patiënten behandeld werden voor hun hoge bloeddruk. Met behulp van deze metingen hebben we in de uitgangssituatie de relatie (een curve) bepaald tussen bloeddruk en doorsneeoppervlakte van het vat, gedurende de hartperiode. Met deze curves kunnen we de invloed van een bloeddrukdaling op de doorsneeoppervlakte, maar ook op de PWV voorspellen. We doen dit door voor iedere individuele patiënt de druk-oppervlaktecurve vóór de hoge-bloeddrukbehandeling te bepalen, en van deze curve de oppervlakte af te lezen bij de bloeddruk van de patiënt ná behandeling. Op deze manier voorspelden we een PWV-verlaging van 1 m/s na een bloeddrukdaling van 10 mmHg diastolisch. Deze voorspelling kwam precies overeen met de gemeten PWV-verlaging. Dit betekent dat de gemeten PWV-verlaging in deze studie puur en alleen een bloeddrukeffect is, en dat de PWV-verlaging in dit geval niet duidt op veranderingen in de vaatwand. Getalsmatig is de door ons gevonden bloeddrukafhankelijkheid verrassend vergelijkbaar met de waarden uit de "Reference Values for Arterial Stiffness' Collaboration" studie. Hierbij moet worden opgemerkt dat in deze referentiewaardenstudie, carotis-femoralis-PWV werd gebruikt, terwijl wij in onze studie lokale, carotis-PWV's hebben gebruikt.

In **hoofdstuk 3** gebruiken we de methode uit hoofdstuk 2 om het effect van een bepaald type kankermedicijnen (angiogeneseremmers) op vaatstijfheid te bepalen. Van deze medicijnen is niet alleen bekend dat ze een verhoging in PWV veroorzaken, maar ook dat ze de bloeddruk verhogen. In een groep van patiënten met kanker hebben we PWV en druk-oppervlaktecurves gemeten vóór start van de kankerbehandeling en viermaal daarna, telkens met tussenpozen van twee weken. Omdat in deze studie de gemeten PWV-

veranderingen significant groter waren dan de voorspelde veranderingen, was er meer aan de hand dan alleen een bloeddruk-effect. In hoofdstuk 3 hebben we onze nieuwe druk-oppervlaktecurve-gebaseerde methode om PWV te corrigeren voor bloeddrukveranderingen, vergeleken met de gebruikelijke, statistische methode van bloeddrukcorrectie. De resultaten van beide methodes bleken vergelijkbaar. Echter, onze nieuwe methode (hoofdstuk 2) is toepasbaar op individuele patiënten, terwijl voor de gebruikelijke methode een hele patiëntengroep vereist is.

In **hoofdstuk 4** hebben we twee indices voor vaatstijfheid nader bekeken: stiffness index β en cardio-ankle vascular index (CAVI). Deze indices nemen allebei aan dat de relatie tussen bloeddruk en vaatdiameter (de druk-diametercurve) een exponentieel verloop heeft, waarbij deze indices de exponent van deze relatie kwantificeren. Bovendien worden beide indices vaak gepresenteerd als bloeddrukonafhankelijk. In dit hoofdstuk tonen we aan 1) dat β en CAVI, gegeven de aanname van een exponentiële druk-diametercurve, wél van de bloeddruk afhangen; en 2) dat deze drukafhankelijkheid makkelijk te corrigeren is. Om de impact van deze drukafhankelijkheid te illustreren hebben we een computersimulatiestudie uitgevoerd in 161 patiënten. Bij hen hebben we bloeddruk- en PWV-metingen gesimuleerd vóór- en nadat in deze patiënten de bloeddruk verlaagd werd. We namen hierbij expliciet aan dat door de bloeddrukverlaging de wandeigenschappen niet veranderden (met andere woorden: de druk-diametercurves bleven ongewijzigd). De gesimuleerde bloeddrukverlaging leidde tot een significante verlaging in CAVI, terwijl onze gecorrigeerde maat ($CAVI_0$) geen verandering vertoonde.

In **hoofdstuk 5** hebben we de invloed van de hartfrequentie op de carotis-femoralis-PWV onderzocht. In deze studie hebben we in pacemakerpatiënten de hartfrequentie gevarieerd tussen de 60 en 100 slagen per minuut. Bij iedere frequentie hebben we bloeddruk en PWV gemeten. Zoals verwacht stegen zowel de PWV als de diastole bloeddruk met de hartfrequentie. We hebben de gemeten PWV's op drie manieren gecorrigeerd voor bloeddruk: 1) op een statistische manier, 2) met behulp van de in hoofdstuk 2 beschreven curve-methode, en 3) door de bloeddrukafhankelijkheid direct af te leiden uit bloeddrukverschillen geïnduceerd door houdingsveranderingen (zitten versus liggen) in een deel van de patiëntengroep. Alle drie de methoden gaven een vergelijkbare hartfrequentie-afhankelijkheid van PWV, tussen 0.16 en 0.20 m/s per 10 slagen per minuut.

In **hoofdstuk 6** hebben we bekeken of tonometrie van de halsslagader leidt tot activatie van de in de hals gelegen baroreceptoren, en daarmee tot schommelingen in hartfrequentie en bloeddruk. We hebben dit onderzocht door bloeddrukmetingen tijdens tonometrie van de halsslagader te vergelijken met metingen tijdens tonometrie van de dijslagader. De gevonden verschillen waren dusdanig klein, dat we konden concluderen dat tonometrie van de halsslagader niet leidt tot baroreceptoractivatie.

Tijdens echografie wordt het hoofd van de patiënt vaak naar opzij en naar achteren gedraaid. Door zo'n hoofdrotatie wordt de slagader een klein beetje uitgerekt. Deze uitrekking heeft potentieel ook effect op de vaatmechanica in diameterrichting (lees: op de distensie van het bloedvat). In **hoofdstuk 7** hebben we bestudeerd hoe het draaien van het hoofd tijdens echografie van de halsslagader lokale stijfheidsmetingen beïnvloedt. We hebben dit gekwantificeerd door echografiemetingen te doen met het hoofd zowel in een neutrale als in een gedraaide stand. De verschillen in vaatlengte hebben we gekwantificeerd met behulp van magnetic resonance imaging (MRI). MRI toonde aan dat er een significante rek in lengterichting optreedt. Deze leidt ertoe dat zowel absolute als rela-

tieve distensie afnemen. We concluderen hieruit dat het draaien van het hoofd tijdens echografie leidt tot een onzuiverheid in het meten van distensie van de halsslagader.

Hoofdstukken 8 tot en met 12 richten zich op de interpretatie van vaatstijfheidsmetingen. In **hoofdstuk 8** hebben we de meetgegevens van hoofdstuk 2 gebruikt. We hebben de patiënten uit dit hoofdstuk onderverdeeld in een "jonge" en een "oude" groep. Hoofdstuk 8 had tot doel om de gemeten verschillen in wandgedrag tussen deze groepen te interpreteren in termen van de individuele wandcomponenten. We hebben hiertoe een computermodel van de slagaderwand geïmplementeerd, en dit model gefit op de meetgegevens van de jonge groep. Vervolgens hebben we bekeken welke modelparameters er veranderd moesten worden om dit "jonge" model te veranderen in een "oud" model. Hierbij hebben we een aantal fysiologisch onderbouwde aannames gemaakt: 1) de wandspanning werd vereist homogeen te zijn over de vaatwand, 2) de gemiddelde wandspanning in de "oude" groep werd geforceerd op de waarde van de "jonge" groep, en 3) axiale kracht werd constant verondersteld over de hartcyclus. Onze simulaties lieten van "jong" naar "oud" een verschuiving zien van elastine als grootste drager van de drukbelasting, naar collageen. Hierbij werd ook het percentage collageenvezels dat daadwerkelijk kracht droeg, groter. In het model nam door veroudering de wanddikte toe met 17%. Deze toename in het model kwam goed overeen met de gemeten diktetoename van 21%. Dit hoofdstuk laat zien dat een interpretatie van niet-invasieve stijfheidsmetingen mogelijk is.

In **hoofdstuk 9** hebben we bestudeerd of we de interpretatiemethode uit hoofdstuk 8 konden verbeteren door de metingen hiervoor te doen met het hoofd zowel in een neutrale als in een gedraaide stand (hoofdstuk 7). Door de gegevens van metingen in deze twee houdingen te combineren beschikken we effectief over tweemaal zoveel meetgegevens in dezelfde patiënt. We hebben onze nieuwe methode vergeleken met de "normale" methode waarbij slechts één houding van het hoofd gebruikt wordt. Door het gebruik van de nieuwe methode werd de spreiding in de collageenstijfheidsparameter van het model 43% lager dan bij de "normale" methode. Een sensitiviteitsanalyse wees uit dat verdere winst te behalen valt door de ultrageluidsparameters betrouwbaarder te meten (bijvoorbeeld door deze metingen een aantal maal te herhalen).

In **hoofdstuk 10** hebben we een methode ontwikkeld om in twee dimensies de richting van gladde spiercellen in buisvormige structuren te bepalen. In **hoofdstuk 11** hebben we deze methode uitgebreid tot een driedimensionale methode, waarna we deze gebruikt hebben om de gladde-spierceloriëntatie in muizenslagaders te bepalen. We hebben deze slagaders opgespannen tussen glazen micropipetten, en de celkernen hiervan aangekleurd met een fluorescente marker. Vervolgens hebben we van deze celkernen opnamen gemaakt met behulp van tweefotonmicroscopie. Na verwerking van de microscoopbeelden hebben we de gladde-spierceloriëntaties gekwantificeerd met behulp van Bingham-verdelingen. Door het gebruik van deze statistische methode konden we de spreiding in oriëntatie afzonderlijk kwantificeren in twee richtingen: in het axiaal-circumferentiële vlak (helicaal), maar ook in het radiaal-circumferentiële vlak (transversaal). De helicale spreiding bleek veel groter dan de transversale spreiding. Naast deze bevinding bleek dat de gladde-spierceloriëntaties een significante rechtshandige helix vertoonden in de binnenste én buitenste gladde-spiercellaag van zowel de linker als rechter halsslagader.

Omdat het mechanische gedrag van slagaders onder dynamische (pulsatiele, *in vivo*)

condities waarschijnlijk substantieel verschilt van het gedrag onder statische condities, hebben we een systeem ontwikkeld om muizenslagaders biomechanisch te testen onder statische én dynamische condities. Dit systeem beschrijven we in **hoofdstuk 12**. In dit systeem worden muizenslagaders opgespannen tussen micropipetten. Vervolgens wordt een pulsatiele druk gegenereerd met pulsfrequenties tussen 2 en 10 Hz, welke aan de binnenkant op de slagaders wordt aangebracht. We hebben met dit systeem proefmetingen uitgevoerd, en hebben zo laten zien dat het mogelijk is om *ex vivo* muizenslagaders te bestuderen onder pulsatiele condities.

Hoofdstuk 13 besluit dit proefschrift en bediscussieert onze belangrijkste bevindingen en de klinische implicaties hiervan. We formuleren in dit hoofdstuk ook een set van klinische aanbevelingen voor het meten van vaatstijfheid. Verder bespreken we de beperkingen van ons onderzoek, en doen we suggesties voor vervolgonderzoek.

Valorisation

Introductory remarks

ARTERIAL stiffening is a key aspect in the development of cardiovascular disease (Laurent et al. 2006). Cardiovascular disease was responsible for 27% of all deaths in the Netherlands in 2014 (Centraal Bureau voor de Statistiek 2016a), a percentage that is expected to rise in our ageing population (Centraal Bureau voor de Statistiek 2016b; Lakatta and Levy 2003a; Lakatta and Levy 2003b). Arterial stiffening makes the arteries less compliant. In a healthy individual, this compliance reduces the force required by the heart to eject its blood. In patients with reduced compliance, therefore, more force is required from the heart, potentially leading to heart failure. Therefore, accelerated stiffening is a strong predictor of cardiovascular complications (Ben-Shlomo et al. 2014; Laurent et al. 2001; Van Bortel et al. 2012).

In this chapter, we will address the valorisation potential of the arterial stiffness research as performed in this thesis. This chapter is structured according to two aspects of valorisation (Drooge et al. 2013): 1) making knowledge available and suitable for economic and social exploitation; and 2) translating this knowledge into products, services, processes and new business.

Making knowledge available and suitable for economic and societal exploration

Part of the work presented in this thesis is directly and clinically applicable. Chapter 2 on pressure dependence of pulse wave velocity (PWV) gives clinicians a direct handle to more realistically interpret arterial stiffness measurements. Instead of assuming PWV to be an independent marker for arterial stiffness, it can now be interpreted in the context of the actual blood pressure. This is relevant, as this directly influences the intensity of antihypertensive treatment. Economically, this potentially leads to less use of antihypertensive medications.

A first step in making knowledge available is sharing it among peers. In this context, the results from this thesis have been presented at numerous conferences, generating much interest by other researchers. In addition, the majority of the chapters are published in scientific journals, or are submitted for publication therein. As this thesis was written from a *medical* engineering perspective, we aimed to publish our work not only in engineering journals (e.g., chapter 11 in Biomechanics and Modeling in Mechanobiology), but also in medical journals (e.g., chapter 2 in Journal of Hypertension) in order to directly address both clinicians, but also researchers as our target groups. As the implications of the work presented may directly influence patient treatment, patients are also among the target

groups. Patients will benefit from this work through their clinicians' better understanding. These clinicians can now more specifically prescribe anti-hypertensive treatment.

Whereas we strongly feel that knowledge availability is important for *all* research findings, whether positive or negative, we would like to highlight two products of knowledge that emerge from this thesis. First, the research on the pressure dependence of pulse wave velocity that was presented in chapter 2 was performed with the aim of clinical applicability in mind. Instead of using very detailed models of arterial mechanics (like in chapter 8), we used a very simple, exponential model approach to assess pressure dependence. This has the advantage that our method can be readily applied to clinically available measurements. Indeed, our method has already been applied to data from two separate patient cohorts (chapters 2 and 3). When we presented these studies at clinical conferences, it was very well received. As an example, I gave an invited talk summarising our work on pressure dependence of arterial stiffness at the European Society for Hypertension 2016 meeting in Paris (see About The Author). Discussion after this talk has led to two new collaborations, in which our pressure correction approach is also going to be used. Second, in the General Discussion of this thesis, we formulated an updated set of recommendations for the assessment of arterial stiffness. These recommendations could be directly translated to clinical practice and thereby affect clinicians, but also patients.

Until now, pulse wave velocity was generally corrected for blood pressure by means of a statistical approach. However, in this thesis, we present an innovative approach that is applicable to individuals (chapter 2). We furthermore critically assessed a commercially available method (cardio-ankle vascular index, CAVI), that is presented as blood pressure-independent. During this assessment, we found, in the context of CAVI's intrinsic assumption of an exponential pressure-diameter relationship, that this method yields slightly pressure-*dependent* values of arterial stiffness. This finding is important for CAVI users, so that they are aware of possible blood pressure-induced changes in this measure.

The knowledge availability that this section pertains to will be planned and realised by disseminating and communicating our results in various ways. We will ensure that all knowledge becomes available through academic publication. Furthermore, we actively communicate our findings at scientific, medical conferences to ensure that we also reach our clinical target audience. Through our active membership of the European Society for Hypertension Working Group on Vascular Structure and Function, as well as of the European ARTERY society, we will ensure that our findings are taken into consideration when new guidelines for the treatment of hypertension are formulated.

Translating knowledge into products, services, processes, and new businesses

Chapters 8 to 12 are all targeted at the *interpretation* or *understanding* of changes in arterial stiffness. This aspect of arterial stiffness is relevant, as it may provide new insights into the causes of arterial stiffening, and thereby may also elucidate potential targets for anti-stiffness medication.

Target groups for translation include pharmaceutical companies, medical device companies, other groups performing pre-clinical research and companies producing labora-

tory equipment. In chapter 8, we presented a method to interpret *in vivo* arterial stiffness measurements in terms of the individual wall components: collagen, elastin, and smooth muscle cells. By this means, a pharmaceutical company can e.g., monitor non-invasively what effect anti-hypertensive/anti-stiffening medication has on the wall components. The aforementioned modelling framework could also be implemented in e.g., the software of an ultrasound scanner. This would equip such a scanner with the direct capability to disentangle arterial stiffness effects on-the-fly, directly in the clinic. Furthermore, in chapter 12, we presented a set-up for pulsatile characterisation of murine arteries. Such set-up may provide relevant novel insight to researchers at various groups who are currently studying murine arteries. In many cases, only arterial structure is studied (e.g., using histology), whereas quantification of function in those same arteries could significantly improve insights. Furthermore, this set-up is potentially interesting for laboratory equipment producers to commercially produce and sell.

The constitutive modelling framework that we present in chapter 8 is aimed at attributing a change in arterial stiffness to one of the individual wall components. When e.g., developing a new drug to target arterial stiffness, such a model (our product) can be used to assess which component of the artery wall is affected by the drug. This methodology is truly innovative as it potentially allows clinical stiffness measurements to be used as more than "just" a single stiffness number. Besides this methodology, in chapter 12, we presented a novel set-up to study artery mechanics under pulsatile conditions. This set-up provides a methodology to fundamentally study arterial mechanics in pre-clinical, murine studies. Currently available methods are limited in the sense that they only allow for static measurements. Therefore, dynamic assessment of arteries provides an important step to study arterial mechanics under physiologically more realistic conditions.

Although our modelling methodology is potentially a candidate for valorisation, we plan to first further elaborate it before valorisation. During my follow-up research, I will continue to scrutinise and improve this methodology to verify the robustness of the results. An essential aspect of this verification process is an elaborate sensitivity analysis (see chapter 9), a technique which will be employed to quantify the validity and certainty of our model predictions. After these verification analyses, contact can be sought with medical device companies, of which Esaote Benelux (Maastricht, The Netherlands) is a potential candidate. Esaote is a leading manufacturer of medical ultrasound machines, and is a company with which we closely collaborate. Esaote has in the past always been open to new approaches that were developed in the academic sector.

Our set-up for pulsatile characterisation of artery mechanics, which is currently under further development, will deliver a highly relevant methodology for a large number of research groups at Maastricht University. Eventually, our set-up will be moved from the Department of Biomedical Engineering to the CARIM Muroidean Facility (CARIM-MF). CARIM-MF employs a group of highly skilled technicians that are experienced in working with small rodent models. The addition of our set-up to their laboratory will ensure that our methodology becomes accessible to all researchers at the CARIM School for Cardiovascular Diseases. Furthermore, researchers at other universities have shown interest in our methodology. A notable example is Prof. Jo de Mey at University of Southern Denmark (Odense, Denmark), whose focus is on human, small, resistance-sized arteries. Although physiologically these vessels are markedly different from the large arteries that our set-up is developed for, geometrically they are of the same size. This collaboration ensures

further development of our set-up towards clinical application.

Our pulsatile set-up could finally be produced and transferred/sold to third parties. We work in close contact with Danish Myo Technology (DMT, Aarhus, Denmark), a company producing laboratory equipment, in particular pressure myographs. For DMT, our pulsatile *in vitro* set-up would be potentially of commercial interest. In order to protect intellectual property rights, we will formulate a commercialisation roadmap in collaboration with the Technology Transfer Office (Maastricht Valorisation Centre) at Maastricht University. This roadmap will pinpoint exploitable aspects of our set-up, and will help identifying target markets, business conditions, opportunities and potential pitfalls.

Dankwoord/Acknowledgements

Zo. Na lang zwoegen ligt er... een proefschrift! Hoewel de enkele naam op de kaft van mijn proefschrift misschien anders doet vermoeden, is de totstandkoming van mijn proefschrift een echte team effort geweest. Ik wil iedereen in dit team dan ook graag bedanken voor alle tijd en moeite. Zonder jullie was dit proefschrift er niet geweest!

Tammo, in het begin moest ik best wel aan jou wennen. Ik schrok vaak van je directe commentaar. Inmiddels, na meer dan vijf jaar, weet ik wel beter. Op jou als promotor kun je bouwen. Je bent altijd beschikbaar om te sparren en werkte tot laat in de avond om te zorgen dat we de deadline voor mijn proefschrift zouden halen. Tijdens onze BME-skivakanties was je altijd van de partij. Bedankt! **Koen**, hoe vaak ben ik niet bij jou binnen gelopen ("Vijf minuten...") om "even" een update te doen... Jij zorgde ervoor dat mijn promotie inhoudelijk voor mekaar kwam, maar dat ik ook bleef ademen. Je gaf me ook de ruimte om mijn eigen weg te bepalen tijdens mijn promotie. Van die ruimte heb ik veel geleerd. Bedankt voor al je steun, door dwars en dun! **Remco**, bij jou in Duitsland is het goed toeven. Muziek op het tweefotonlab, Riesenschnitzel in de buurt, wat wil je nog meer? We hebben altijd heel relaxt samen op het lab gezeten, van 's morgens vroeg tot soms 's avonds laat. Bedankt voor je relaxte maar toch zeker productieve manier van samenwerken!

Maarten, al vrij vroeg in je BMT-opleiding leerden we elkaar kennen. Voordat je goed en wel afgestudeerd was lagen er al meerdere co-publicaties van ons! Ik vind het nog steeds gaaf om met je samen te werken. Bedankt!

Beste leden van de beoordelingscommissie, Prof. **Harry** Struijker-Boudier, Prof. **Luc** van Bortel, Prof. **Casper** Schalkwijk, Prof. **Frans** van de Vosse en Prof. **Nico** Westerhof, bedankt dat jullie de tijd hebben genomen om dit lijvige proefschrift grondig te lezen. Prof. Struijker-Boudier, bedankt voor het vervullen van de voorzittersrol. Frans, met mijn afstuderen bij jou is het allemaal begonnen... Daarvóór was ik ervan overtuigd dat de wetenschap niets voor mij was, maar al na een aantal maanden begon ik bij te draaien. Fijn dat ik tijdens mijn afstuderen de ruimte kreeg om een Kootstra-aanvraag te schrijven!

Dear colleagues from Down Under; **Isabella**, I still remember when we met down under. I just arrived in Sydney at Macquarie University Village, and was completely jetlagged when you came to deliver some cooking utensils and a pillow. Your welcome, in a place where I knew nobody, was heart warming. I've really enjoyed the time that I spent with you and your family. Thank you, and thanks to William, Jon Jon and Vanessa! **Alberto**, when we met at conferences, you were always cheerful and enthusiastic. This, together with the research that you, Mark, and Isabella performed, made me decide to come over. Thank you very much for all your support. **Mark**, thanks for all your time. I really admire your perseverance when it comes to rat experiments! Thank you also for giving me my first beer brewing experience, and for inviting me over for Sinterklaas at your and CJ's place :-)! See you all again in November!

Dear Prof. Humphrey, dear **Jay**, I really look forward to working with you in the future. Thank you for our valuable meetings at conferences!

Anouk, bedankt voor onze samenwerking. Je herinnert je vast nog wel onze trip met Koen naar Parijs... Onze trein-en-dinerplanning was misschien iets te scherp, maarja, dan heb je wel wat om over te praten :-). **Pierre** and **Maureen**, thank you for your input from Paris! **Jo** and **Maria**, thanks for our Danish-Dutch collaboration, which we'll definitely pursue in the future.

Peter en **Sabine**, jullie zijn ook van die types die tijdens hun promotie hun vakantiedagen op krijgen... Bedankt voor jullie gastvrijheid in New York en in Bordeaux. We zien jullie wel verschijnen in Sydney! En Peter, ik ben benieuwd naar je looks in pinguïn-outfit... **Raf** en **Jeire**, bedankt voor de gezellige tripjes, verjaardagsfeesten en oudejaarsavonden! Jeire, het was gezellig met jou op het lab. Altijd als jij binnenkwam (of als ik binnenkwam en jij was er al) had je tijd voor een praatje. Dankjewel, ook voor je rol als paranimf! **Niek**, mede PINT-lid, dank voor alle (speciaal)bier-gerelateerde incentives.

Marieke, **Yvette** en **Jort**, jullie hoorden ook bij de "laboudsten". Marieke, gaaf dat ik je paranimf mocht zijn. Yvette, jij was een fijne achterbuurvrouw. Ik denk dat jij de eerste was die, tijdens de ski-trip in Corvara, doorkreeg dat Elien en ik aan het daten waren... Je hebt goed je mond weten te houden :-). Jort, mr. "hot global data meeting", dankjewel voor het leven dat jij in de brouwerij bracht! Ik vond het prachtig om een overbuurman te hebben waar ik zo tegen op kon kijken :-). **John**, jij bent iets vóór mij uit het lab verbannen. Ik ben je achterna gekomen! Ik bewonder hoe goed je in korte tijd Nederlands en zelfs Limburgs geleerd hebt. Bedankt voor de gezellige tijd. **Wilco** ("Enne Sjef?"), met jou ging ik naar mijn eerste congres, in Rotterdam, waar we belandden in een Monty Python-voorstelling... Bedankt voor je samenwerking en joligheid op het lab. **Joost**, wat een goed idee om je partner bij Fysiologie te zoeken. Bedankt voor alle discussies over sjroep/sjwrap, vès/vusj, tas/tèsj, kemissies/boodsjappe en meer van dit alles! **Lauren** and **Georgina**, thanks for bringing some internationality to our lab! It's good to see that also people who are not from Limburg or Brabant can survive here (which also holds for you, John). Verder wil ik ook de andere labgenoten (**Wouter**, **Alex**, **Sjeng**, **Ben**, **Frank** (2x), **Erik** en **Tommy**) bedanken voor het verzorgen van de nodige gezelligheid. **Jorrit** en **Christel**, bedankt voor de gezelligheid tijdens de skivakantie! Mijn dank gaat ook uit naar **Nico** en **Wouter H.**.

Jeroen, bedankt voor je hulp bij allerlei praktische zaken, zoals pipetten trekken, kabeltjes solderen, enz. enz.! **Claire**, middelpunt van de afdeling, bedankt voor alle hulp en voor het delen van je Afrika-ervaringen! **Peter L.**, wij gaan elkaar nog vaker zien op het CARIM-MF-lab. Bedankt voor je ondersteuning bij het ontwikkelen van mijn meetopstelling. **Wim**, mister tweefoton, jij vertrok ongeveer toen ik bij de afdeling kwam. Dankjewel voor onze nuttige en fascinerende gesprekken. **Timo**, bedankt voor je hulp. **Arnold**, bedankt voor je hulp bij het verwerken van vaatechobeelden en voor je uitgesproken ideeën over de wetenschap.

Aan alle co-auteurs (**Rob**, **Jos**, **Evelien**, **Bram**, **Floris**): bedankt voor jullie input, maar ook voor het vergaren/beschikbaar stellen van meetdata! **Annelies**, tijdens onze eerste BME-skivakanties mocht jij ook niet ontbreken. Bij de laatste wel, maar daar bleek een goede reden voor :-). Bedankt voor de gezelligheid, maar ook voor onze statistische samenwerking.

Alle vrienden van BMT-Eindhoven (**Anne**, **Anneloes**, **Ellen** (2x), **Esther**, **Germaine**,

Jelle, **Joke**, **Mark**, **Rob**, **Stijn**, **Stefan**), bedankt voor de gezellige etentjes en weekenden weg!

Paul en **Elly**, bedankt voor jullie steun door dik en dun. Jullie waren er altijd voor mij. Paul, er zijn niet veel vaders die dag en nacht, in de woonkamer, op de eettafel, werken aan een opstelling om muizenvaatjes te bestuderen. Avondeten moest maar ergens anders... Zonder jou was hoofdstuk 12 in dit proefschrift er echt niet geweest! **Hub** en **Gerry**, **Tim**, **Bart** en **Mirthe**: ik had me geen betere schoonfamilie kunnen wensen!

Elien. Ik vind het heerlijk met jou de wereld te verkennen! Ook in de afgelopen, hectische tijd van proefschriften (meervoud!) afronden en beursaanvragen schrijven was jij er voor me. Ik zie uit naar onze Australië- en US-avonturen, maar eigenlijk gewoon naar onze toekomst: Samen!

Bart

About the author

Biography

On October 4, 1987, I was born at the Sint Annadal hospital in Maastricht. At primary school, I was already intrigued by knowledge in a very broad sense. When I was asked to name my favourite book, I never mentioned a novel, but instead some sort of children's encyclopaedia. Physics, chemistry, biology and mathematics have always fascinated me. Therefore, after high school graduation in 06-2006, I went looking for a bachelor programme that integrated these subjects. That programme was Biomedical Engineering at Eindhoven University of Technology (TU/e, 09-2006–08-2009): an integrative field of education and research, combining specialisations instead of keeping them apart. I continued in this field, starting a Master in Medical Engineering at TU/e (09-2009–10-2011). During this Masters, I performed a three-month internship at Universitätsklinikum Aachen under supervision of Dr. Remco T.A. Megens and Prof. Marc A.M.J. van Zandvoort (10-2010–12-2010). After this internship, I finished my graduation project at the Department of Biomedical Engineering at Maastricht University (MU), supervised by Dr. Esther G.H.J Martens, Dr. Erik D. Gommer, and Prof. Frans N. van de Vosse. During this period, I also successfully applied for a Kootstra Talent Fellowship, that I used as a bridge (11-2011–10-2012) towards my PhD trajectory.

From 11-2012 until 06-2016 I worked as a PhD candidate under supervision of Prof. Tammo Delhaas, Dr. Koen D. Reesink, and Dr. Remco T.A. Megens. This resulted in the thesis you're currently reading. From 10-2015–12-2015, I visited the laboratory of Prof. Alberto P. Avolio (Macquarie University, Sydney, NSW, Australia), resulting in chapters 4 and 5 of this thesis. Work visits in 2013 and 2014 to the laboratory of Dr. Remco T.A. Megens (Ludwig-Maximilians Universität München, Germany) provided me with the experimental results presented in chapter 11. A collaborative project with Prof. Alun D. Hughes (University College London, United Kingdom) that resulted from a KNAW (Royal Netherlands Academy of Arts and Sciences) Ter Meulen Grant was started 02-2016 and is still ongoing. Collaboration with Prof. Pierre Boutouyrie (European Georges Pompidou Hospital, Paris, France) resulted in chapter 3.

Currently, I work as a postdoctoral researcher at the Department of Biomedical Engineering (MU), funded by a second Kootstra Talent Fellowship (06-2016–10-2016). In November, I will leave to Prof. Avolio's laboratory again on a six-month Endeavour Research Fellowship by the Australian Government. After this fellowship, I plan to join Prof. Jay D. Humphrey's laboratory (Yale University, CT, United States of America) as a postdoctoral researcher.

Grants and awards

10-2007 Professor Huson Award, by Eindhoven University of Technology (TU/e). Award for best first year Biomedical Engineering student at TU/e.

11-2007 Encouragement Award for Young Talents ("Aanmoedigingsprijs Jong Talent"), by the Royal Holland Society of Sciences and Humanities ("Koninklijke Hollandsche Maatschappij der Wetenschappen"). Award for best first year Biomedical Engineering student in the Netherlands.

10-2009 BEST/e (Biomedical Engineering Sciences & Technology Eindhoven) Grant, by BEST/e. Awarded to the five best TU/e Biomedical Engineering bachelor students.

08-2010 Erasmus Grant, by the European Union, to fund my internship at Institute for Molecular Cardiovascular Research (IMCAR), Universitätsklinikum Aachen, Aachen, Germany. IMCAR was at that time headed by Prof. Christian Weber.

06-2011 Kootstra Talent Fellowship: prospective talented PhD, by the Executive Board of Maastricht UMC+. Grant to perform one year of research as a bridge between the master programme and a PhD programme.

06-2012 2011's best master thesis at the TU/e Faculty of Biomedical Engineering, resulting a nomination for the TU/e Final Project Award 2011.

10-2012 Artery 12 Brigitte Laloux bursary to attend the Artery 12 conference. The two bursary applicants with the two best abstracts are awarded a Brigitte Laloux bursary.

10-2012 Artery 12 first poster prize.

06-2013 23rd European Meeting on Hypertension & Cardiovascular Protection accommodation grant.

10-2013 Artery 13 educational bursary to attend the Artery 13 conference.

11-2013 Runner-up for poster prize at the Dutch Physiological Society's 29th Papendal Symposium: Adaptive Physiology.

10-2014 Artery 14 second oral young investigator prize.

10-2014 Best oral presentation at the 3rd joint meeting of the Dutch Endothelial Biology Society and the Dutch Society for Microcirculation and Vascular Biology.

02-2015 Gert van Montfrans prize for the best Dutch young investigator journal paper on hypertension, by the Dutch Hypertension Society ("Nederlandse Hypertensievereniging") for the paper "Pressure-dependence of arterial stiffness: potential clinical implications" (Spronck et al. 2015b).

06-2015 Ter Meulen grant, by the Royal Netherlands Academy of Arts and Sciences ("Koninklijke Nederlandse Akademie van Wetenschappen") to perform three months of research on the project *Obesity-related differences in arterial structure and function in seventeen-year olds* at the group of Prof. Alun D. Hughes, Faculty of Population Health Sciences, University College London, United Kingdom.

11-2015 Endeavour Research Fellowship by the Australian Government to perform six months of research in 2016 at the laboratory of Prof. Alberto P. Avolio and Dr. Mark Butlin, Macquarie University, Sydney, NSW, Australia.

12-2015 Best oral presentation at the 5th Annual Macquarie BioFocus Research Conference.

06-2016 Kootstra Talent Fellowship: prospective talented postdoctoral researcher, by the Executive Board of Maastricht UMC+. Grant to perform one year of postdoctoral research, as a bridge to a prestigious longer-term postdoctoral position.

Publications in peer-reviewed journals

13.5.1 Published

1. Spronck B, Martens EGHJ, Gommer ED, and Van de Vosse FN (2012). A lumped parameter model of cerebral blood flow control combining cerebral autoregulation and neurovascular coupling. *Am J Physiol Heart Circ Physiol* 303:H1143–H1153.
2. Spronck B, Merken JJ, Reesink KD, Kroon W, and Delhaas T (2014). Ureter smooth muscle cell orientation in rat is predominantly longitudinal. *PLOS ONE* 9:e86207.
3. Spronck B, Heusinkveld MHG, Donders WP, De Lepper AGW, Op't Roodt J, Kroon AA, Delhaas T, and Reesink KD (2015). A constitutive modeling interpretation of the relationship between carotid artery stiffness, blood pressure and age in hypertensive subjects. *Am J Physiol Heart Circ Physiol* 308:H568–H582.
4. Spronck B, Heusinkveld MHG, Vanmolkot FH, Op 't Roodt J, Hermeling E, Delhaas T, Kroon AA, and Reesink KD (2015). Pressure-dependence of arterial stiffness: Potential clinical implications. *J Hypertens* 33:330–338.
5. Holtackers RJ, Spronck B, Heusinkveld MHG, Crombag G, op 't Roodt J, Delhaas T, Kooi ME, Reesink KD, and Hermeling E (2016). Head orientation should be considered in ultrasound studies on carotid artery distensibility. *J Hypertens* 34:1551–1555.
6. Schueth A, Spronck B, Van Zandvoort MAMJ, and Van Koeveringe GA (2016). Age-related changes in murine bladder structure and sensory innervation: a multiphoton microscopy quantitative analysis. *AGE* 38:1–11.
7. Spronck B, Avolio AP, Tan I, Butlin M, Reesink KD, and Delhaas T (2016). Arterial stiffness index beta and cardio-ankle vascular index inherently depend on blood pressure, but can be readily corrected. *J Hypertens* [accepted].
8. Spronck B, Delhaas T, Roodt JO, and Reesink KD (2016). Carotid artery applanation tonometry does not cause significant baroreceptor activation. *Am J Hypertens* 29:299–302.
9. Spronck B, Megens RTA, Reesink KD, and Delhaas T (2016). A method for three-dimensional quantification of vascular smooth muscle orientation: application in viable murine carotid arteries. *Biomech Model Mechanobiol* 15:419–432.
10. Spronck B, Walmsley J, Palau-Caballero G, Reesink KD, and Delhaas T (2016). Can significance of aortic sinus vortices be assessed using the assumptions in the model of Aboelkassem et al.? *J Theor Biol* 389:304–305.
11. Tan I, Spronck B, Kiat H, Barin E, Reesink KD, Delhaas T, Avolio AP, and Butlin M (2016). Heart rate dependency of large artery stiffness. *Hypertension* 68:236–242.
12. Walavalkar V, Evers E, Pujar S, Viralam K, Maiya S, Frerich S, John C, Rao S, Reddy C, Spronck B, Prinzen FW, Delhaas T, and Vanagt WY (2016). Preoperative sildenafil administration in children undergoing cardiac surgery: a randomized controlled preconditioning study. *Eur J Cardiothorac Surg* 49:1403–1410.

13.5.2 Under review

13. Schueth A, Spronck B, Van Zandvoort MAMJ, and Van Koeveringe GA. Computer-assisted three-dimensional tracking of sensory innervation in the murine urinary

bladder with two-photon laser scanning microscopy.
14. Spronck B, Delhaas T, De Lepper AGW, Giroux J, Goldwasser F, Boutouyrie P, Alivon M, and Reesink KD. Patient-specific blood pressure correction technique for arterial stiffness: Evaluation in a cohort on anti-angiogenic medication.
15. Van de Ven A, Spronck B, Van Asselt T, and Andriessen P. Een retrospectief onderzoek naar het vervoer van kritisch zieke neonaten in de regio zuidoost Brabant [in Dutch, English title: A retrospective study into the transport of critically-ill neonates in the region of Southeast Brabant].

13.5.3 In preparation

16. Bloksgaard M, Leurgans TM, Spronck B, Heusinkveld MHG, Rosenstand K, Nissen I, Brewer JR, Bagatolli LA, Rasmussen LM, Irmukhamedov A, Reesink KD, and De Mey JGR. Microarchitecture and biomechanics of elastin and collagen in pericardial resistance arteries.
17. Butlin M, Connolly K, Spronck B, Georgevsky D, McEneiry CM, Wilkinson IB, and Avolio AP. High salt diet increases aortic stiffness and pressure pulse amplification in rat.
18. Heusinkveld MHG, Quicken S, Holtackers RJ, Huberts WH, Reesink KD, Delhaas T, and Spronck B. Non-invasive estimation of carotid artery constitutive properties in human subjects using distensibility measurements acquired at two levels of axial stretch.
19. Spronck B, Spronck PJM, Megens RTA, Delhaas T, and Reesink KD. In vitro assessment of arteries under pulsatile conditions.

Proceedings in peer-reviewed journals

1. Spronck B, Megens RTA, Reesink KD, and Delhaas T (2014). Three-dimensional vascular smooth muscle orientation as quantitatively assessed by multiphoton microscopy: mouse carotid arteries do show a helix. In: *Conf Proc IEEE Eng Med Biol Soc*. Vol. 2014, pp. 202–205.

Oral conference presentations

I have authored a total of **21 oral conference presentations**. Of these, two were invited and four were award-winning:

13.5.4 Invited

1. Spronck B. Population based biomechanics: Model-based interpretation of clinically measurable parameters. Workshop Arterial Stiffness, Basic and Clinical Aspects (September 19, 2014, Odense, Denmark).
2. Spronck B. How to deal with pressure dependence? 26th European Meeting on Hypertension & Cardiovascular Protection (June 10 – 13, 2016, Paris, France).

13.5.5 Award-winning

1. Spronck B, Megens RTA, Reesink KD, and Delhaas T. Quantification of three-dimensional vascular smooth muscle orientation and its dispersion in murine carotid arteries. Artery 14 (October 9 – 11, 2014, Maastricht, The Netherlands); presentation winning second oral young investigator award.
2. Spronck B, Megens RTA, Reesink KD, and Delhaas T. Quantification of three-dimensional vascular smooth muscle orientation and its dispersion in murine carotid arteries. 3rd joint meeting of the Dutch Endothelial Biology Society and the Dutch Society for Microcirculation and Vascular Biology (October 30 – 31, 2014, Biezenmortel, The Netherlands); presentation winning best oral presentation prize.
3. Spronck B, Heusinkveld MHG, Vanmolkot FH, Op 't Roodt J, Hermeling E, Delhaas T, Kroon AA, and Reesink KD. Pressure-dependence of arterial stiffness: potential clinical implications. General meeting of the Dutch society for hypertension (ledenvergadering van de Nederlandse Hypertensievereniging) at the Dutch hypertension conference (Nationaal Hypertensie Congres) 2015 (February 5 – 7, 2015, Zeist, The Netherlands); winning the Gert van Montfrans prize for the best Dutch young investigator journal paper on hypertension.
4. Spronck B, Tan I, Reesink KD, Delhaas T, Butlin M, and Avolio AP. Heart rate dependence of arterial pulse wave velocity calculated using three blood pressure correction methods. 5th Annual Macquarie BioFocus Research Conference (December 15, 2015, Sydney, Australia); presentation winning best oral presentation prize.

Conference poster presentations

I have authored a total of **29 conference poster presentations**, of which two were award-winning. Of these award-winning posters, I presented one:

1. Spronck B, Merken JJ, Kroon W, Megens RTA, Reesink KD, and Delhaas T. Quantitative method to determine smooth muscle cell orientation in vital arteries. Artery 12 (October 18 – 20, 2012, Vienna, Austria); guided poster, winning first poster prize.

Bibliography

Alastrué V, Sáez P, Martínez M, and Doblaré M (2010). On the use of the Bingham statistical distribution in microsphere-based constitutive models for arterial tissue. *Mech Res Commun* 37:700–706.

Albaladejo P, Copie X, Boutouyrie P, Laloux B, Déclère AD, Smulyan H, and Bénétos A (2001). Heart rate, arterial stiffness, and wave reflections in paced patients. *Hypertension* 38:949–952.

Alghatrif M, Strait JB, Morrell CH, Canepa M, Wright J, Elango P, Scuteri A, Najjar SS, Ferrucci L, and Lakatta EG (2013). Longitudinal trajectories of arterial stiffness and the role of blood pressure: the Baltimore Longitudinal Study of Aging. *Hypertension* 62:934–941.

Alivon M, Giroux J, Briet M, Goldwasser F, Laurent S, and Boutouyrie P (2015). Large artery stiffness and hypertension after antiangiogenic drugs: influence on cancer progression. *J Hypertens* 33:1310–1317.

Antonov P, Antonova M, Nikolova N, Antonova N, Vlaskovska M, and Kasakov L (2008). Age dependent changes of arterial wall viscoelasticity. *Clin Hemorheol Microcirc* 39:63–68.

Aragona F, Artibani W, de Caro R, Pizzarella M, and Passerini G (1988). The morphological basis of ureteral peristalsis. *Int Urol Nephrol* 20:239–250.

Armentano RL, Barra JG, Pessana FM, Craiem DO, Graf S, Santana DB, and Sanchez RA (2007). Smart smooth muscle spring-dampers. *IEEE Eng Med Biol Mag* 26:62–70.

Armentano RL, Barra JG, Levenson J, Simon A, and Pichel RH (1995). Arterial wall mechanics in conscious dogs assessment of viscous, inertial, and elastic moduli to characterize aortic wall behavior. *Circ Res* 76:468–478.

Asmar RG, Bénétos A, Topouchian J, Laurent P, Pannier B, Brisac AM, Target R, and Levy BI (1995). Assessment of arterial distensibility by automatic pulse wave velocity measurement. Validation and clinical application studies. *Hypertension* 26:485–490.

Asmar RG, London GM, O'Rourke MF, Safar ME, and REASON Project Coordinators and Investigators (2001). Improvement in blood pressure, arterial stiffness and wave reflections with a very-low-dose perindopril/indapamide combination in hypertensive patient: a comparison with atenolol. *Hypertension* 38:922–926.

Åstrand H, Stålhand J, Karlsson J, Karlsson M, Sonesson B, and Länne T (2011). In vivo estimation of the contribution of elastin and collagen to the mechanical properties in the human abdominal aorta: effect of age and sex. *J Appl Physiol* 110:176–187.

Avolio AP, Chen SG, Wang RP, Zhang CL, Li MF, and O'Rourke MF (1983). Effects of aging on changing arterial compliance and left ventricular load in a northern chinese urban community. *Circulation* 68:50–58.

Avril S, Badel P, Gabr M, Sutton MA, and Lessner SM (2013). Biomechanics of porcine renal arteries and role of axial stretch. *J Biomech Eng* 135:081007.

Badel P, Avril S, Lessner S, and Sutton M (2012). Mechanical identification of layer-specific properties of mouse carotid arteries using 3D-DIC and a hyperelastic anisotropic constitutive model. *Comput Methods Biomech Biomed Engin* 15:37–48.

Baek EB and Kim SJ (2011). Mechanisms of myogenic response: Ca^{2+}-dependent and -independent signaling. *J Smooth Muscle Res* 47:55–65.

Balkestein EJ, Van Aggel-Leijssen DP, Van Baak MA, Struijker-Boudier HAJ, and Van Bortel LMAB (1999). The effect of weight loss with or without exercise training on large artery compliance in healthy obese men. *J Hypertens* 17:1831–1835.

Bauer RD, Busse R, and Schabert A (1982). Mechanical properties of arteries. *Biorheology* 19:409–424.

Bénétos A, Lacolley P, and Safar ME (1997). Prevention of aortic fibrosis by spironolactone in spontaneously hypertensive rats. *Arterioscler Thromb Vasc Biol* 17:1152–1156.

Bénétos A, Laurent S, Hoeks APG, Boutouyrie PH, and Safar ME (1993). Arterial alterations with aging and high blood pressure. A noninvasive study of carotid and femoral arteries. *Arterioscler Thromb Vasc Biol* 13:90–97.

Benninghoff A (1927). Über die Beziehungen zwischen elastischem Gerüst und glatter Muskulatur in der Arterienwand und ihre funktionelle Bedeutung. *Z Zellforch Microsk Anat* 6:348–396.

Ben-Shlomo Y, Spears M, Boustred C, May M, Anderson SG, Benjamin EJ, Boutouyrie P, Cameron J, Chen CH, Cruickshank JK, Hwang SJ, Lakatta EG, Laurent S, Maldonado J, Mitchell GF, Najjar SS, Newman AB, Ohishi M, Pannier B, Pereira T, Vasan RS, Shokawa T, Sutton-Tyrell K, Verbeke F, Wang KL, Webb DJ, Willum Hansen T, Zoungas S, McEniery CM, Cockcroft JR, and Wilkinson IB (2014). Aortic pulse wave velocity improves cardiovascular event prediction: an individual participant meta-analysis of prospective observational data from 17,635 subjects. *J Am Coll Cardiol* 63:636–646.

Bergel DH (1961). The dynamic elastic properties of the arterial wall. *J Physiol* 156:458–469.

Bergel DH (1960). The visco-elastic properties of the arterial wall. PhD thesis. University of London.

Bevan JA and Laher I (1991). Pressure and flow-dependent vascular tone. *FASEB J* 5:2267–2273.

Bia D, Armentano RL, Zócalo Y, Barmak W, Migliaro E, and Cabrera Fischer EI (2005). In vitro model to study arterial wall dynamics through pressure-diameter relationship analysis. *Latin Am Appl Res* 35:217–224.

Bingham C (1964). Distributions on the sphere and on the projective plane. PhD thesis. Yale University.

Bingham C (1974). An antipodally symmetric distribution on the sphere. *Ann Stat* 2:1201–1225.

Blacher J, Guerin AP, Pannier B, Marchais SJ, Safar ME, and London GM (1999). Impact of aortic stiffness on survival in end-stage renal disease. *Circulation* 99:2434–2439.

Bland JM and Altman DG (1996). Statistics notes: measurement error. *BMJ* 313:744.

Blokstra A, Over EAB, and Verschuren WMM (2015). Toekomstscenario's hart- en vaatziekten 2011-2040. In: *Hart- en vaatziekten in Nederland 2015, cijfers over heden, verleden en toekomst*. Ed. by Van Dis I, Buddeke J, Vaartjes I, Visseren F, and Bots M. Den Haag: Hartstichting.

Borradaile GJ (2003). *Statistics of earth science data: their distribution in time, space and orientation*. Berlin Heidelberg: Springer.

Bossuyt J, Van De Velde S, Azermai M, Vermeersch SJ, De Backer TLM, Devos DG, Heyse C, Filipovsky J, Segers P, and Van Bortel LMAB (2013). Noninvasive assessment of carotid-femoral pulse wave velocity: the influence of body side and body contours. *J Hypertens* 31:946–951.

Bots ML, Hofman A, and Grobbee DE (1997). Increased common carotid intima-media thickness. Adaptive response or a reflection of atherosclerosis? Findings from the Rotterdam study. *Stroke* 28:2442–2447.

Boutouyrie P, Bézie Y, Lacolley P, Challande P, Chamiot-Clerc P, Bénétos A, de la Faverie JFR, Safar M, and Laurent S (1997). In vivo/in vitro comparison of rat abdominal aorta wall viscosity influence of endothelial function. *Arterioscler Thromb Vasc Biol* 17:1346–1355.

Boutouyrie P, Boumaza S, Challande P, Lacolley P, and Laurent S (1998). Smooth muscle tone and arterial wall viscosity an in vivo/in vitro study. *Hypertension* 32:360–364.

Boutouyrie P, Bussy C, Hayoz D, Hengstler J, Dartois N, Laloux B, Brunner HR, and Laurent S (2000). Local pulse pressure and regression of arterial wall hypertrophy during long-term antihypertensive treatment. *Circulation* 101:2601–2606.

Boutouyrie P, Lacolley P, Briet M, Regnault V, Stanton A, Laurent S, and Mahmud A (2011). Pharmacological modulation of arterial stiffness. *Drugs* 71:1689–1701.

Bouvin MJ (1869). Over den bouw en de beweging der ureteres. PhD thesis. Hoogeschool te Utrecht.

Bramwell JC and Hill AV (1922a). The velocity of the pulse wave in man. *Proc R Soc Lond B* 93:298–306.

Bramwell JC and Hill AV (1922b). Velocity of transmission of the pulse-wave: and elasticity of arteries. *Lancet* 199:891–892.

Bramwell JC, McDowall RJS, and McSwiney BA (1923). The variation of arterial elasticity with blood pressure in man (part I). *Proc R Soc Lond B* 94:450–454.

Brasseur JG, Nicosia MA, Pal A, and Miller LS (2007). Function of longitudinal vs circular muscle fibers in esophageal peristalsis, deduced with mathematical modeling. *World J Gastroenterol* 13:1335–1346.

Brossollet LJ and Vito RP (1995). An alternate formulation of blood vessel mechanics and the meaning of the in vivo property. *J Biomech* 28:679–687.

Brunner-La Rocca HP (2010). Towards applicability of measures of arterial stiffness in clinical routine. *Eur Heart J* 31:2320–2322.

Butlin M, Hathway PJ, Kouchaki Z, Peebles K, and Avolio AP (2015). A simplified method for quantifying the subject-specific relationship between blood pressure and carotid-femoral pulse wave velocity. In: *Conf Proc IEEE Eng Med Biol Soc*. Vol. 2015, pp. 5708–5711.

Butlin M, Qasem A, and Avolio AP (2012). Estimation of central aortic pressure waveform features derived from the brachial cuff volume displacement waveform. In: *Conf Proc IEEE Eng Med Biol Soc*. Vol. 2012, pp. 2591–2594.

Butlin M, Qasem A, Battista F, Bozec E, McEniery CM, Millet-Amaury E, Pucci G, Wilkinson IB, Schillaci G, Boutouyrie P, and Avolio AP (2013). Carotid-femoral pulse wave velocity assessment using novel cuff-based techniques: comparison with tonometric measurement. *J Hypertens* 31:2237–2243.

Canham PB, Henderson RM, and Peters MW (1982). Coalignment of the muscle cell and nucleus, cell geometry and vv in the tunica media of monkey cerebral arteries, by electron microscopy. *J Microsc* 127:311–319.

Cao Y and Langer R (2010). Optimizing the delivery of cancer drugs that block angiogenesis. *Sci Transl Med* 2:15ps3.

Carallo C, Irace C, Pujia A, De Franceschi MS, Crescenzo A, Motti C, Cortese C, Mattioli PL, and Gnasso A (1999). Evaluation of common carotid hemodynamic forces. Relations with wall thickening. *Hypertension* 34:217–221.

Cardamone L, Valentin A, Eberth JF, and Humphrey JD (2009). Origin of axial prestretch and residual stress in arteries. *Biomech Model Mechanobiol* 8:431–446.

Cecelja M and Chowienczyk PJ (2009). Dissociation of aortic pulse wave velocity with risk factors for cardiovascular disease other than hypertension: a systematic review. *Hypertension* 54:1328–1336.

Centraal Bureau voor de Statistiek (2016a). *Statline: overledenen; belangrijke doodsoorzaken (korte lijst), leeftijd, geslacht*. URL: http://statline.cbs.nl/.

Centraal Bureau voor de Statistiek (2016b). *Statline: prognose bevolking; geslacht, leeftijd, herkomst en generatie, 2015-2060*. URL: http://statline.cbs.nl/.

Chiu YC, Arand PW, Shroff SG, Feldman T, and Carroll JD (1991). Determination of pulse wave velocities with computerized algorithms. *Am Heart J* 121:1460–1470.

Clark JM and Glagov S (1985). Transmural organization of the arterial media. The lamellar unit revisited. *Arteriosclerosis* 5:19–34.

Cnaan A, Laird NM, and Slasor P (1997). Using the general linear mixed model to analyse unbalanced repeated measures and longitudinal data. *Stat Med* 16:2349–2380.

Cohen ML and Berkowitz BA (1976). Vascular contraction: effect of age and extracellular calcium. *J Vasc Res* 13:139–154.

Courand PY, Feugier P, Workineh S, Harbaoui B, Bricca G, and Lantelme P (2014). Baroreceptor stimulation for resistant hypertension: first implantation in france and literature review. *Arch Cardiovasc Dis* 107:690–696.

Cowin SC and Humphrey JD (2001). *Cardiovascular Soft Tissue Mechanics*. New York: Kluwer Academic.

Cox RH (1975). Arterial wall mechanics and composition and the effects of smooth muscle activation. *Am J Physiol* 229:807–812.

De Hoon JNJM, Poppe KA, Thijssen HHW, Struijker-Boudier HAJ, and Van Bortel LMAB (2001). Dihydroergotamine: discrepancy between arterial, arteriolar and pharmacokinetic data. *Br J Clin Pharmacol* 52:45–51.

Delfino A, Stergiopulos N, Moore Jr JE, and Meister JJ (1997). Residual strain effects on the stress field in a thick wall finite element model of the human carotid bifurcation. *J Biomech* 30:777–786.

Delhaas T, Kroon W, Bovendeerd P, and Arts T (2008). Left ventricular apical torsion and architecture are not inverted in situs inversus totalis. *Prog Biophys Mol Biol* 97:513–519.

Denk W and Svoboda K (1997). Photon upmanship: why multiphoton imaging is more than a gimmick. *Neuron* 18:351–357.

Denk W, Strickler JH, and Webb WW (1990). Two-photon laser scanning fluorescence microscopy. *Science* 248:73–76.

Dernellis J and Panaretou M (2005). Aortic stiffness is an independent predictor of progression to hypertension in nonhypertensive subjects. *Hypertension* 45:426–431.

Disse J (1896). *Handbuch der Anatomie des Menschen; Band 7: Harn- und Geschlechtsorgane; Teil 1: Harnorgane*. Jena: Gustav Fischer.

Disselhorst R (1894). Der Harnleiter der Wirbeltiere. *Anatomische Hefte* 4:127–191.

Dobrin PB (1978). Mechanical properties of arteries. *Physiol Rev* 58:397–460.

Dodds WJ, Stewart ET, Hodges D, and Zboralske FF (1973). Movement of the feline esophagus associated with respiration and peristalsis. An evaluation using tantalum markers. *J Clin Invest* 52:1–13.

Drooge LV, Vandeberg R, Zuijdam F, Mostert B, der Meulen BV, and Bruins E (2013). *Valuable – indicators for valorisation*. National Valorisation Commission. URL: https://www.maastrichtuniversity.nl/about-um/units/maastricht-valorisation-centre.

Drzewiecki GM, Melbin J, and Noordergraaf A (1983). Arterial tonometry: review and analysis. *J Biomech* 16:141–152.

Duckles SP, Carter BJ, and Williams CL (1985). Vascular adrenergic neuroeffector function does not decline in aged rats. *Circ Res* 56:109–116.

Ebner VW (1902). *A. Koelliker's Handbuch der Gewebelehre des Menschen*. Leipzig: Wilhelm Engelmann.

Edwards NC, Steeds RP, Stewart PM, Ferro CJ, and Townend JN (2009). Effect of spironolactone on left ventricular mass and aortic stiffness in early-stage chronic kidney disease: a randomized controlled trial. *J Am Coll Cardiol* 54:505–512.

Engelen L, Bossuyt J, Ferreira I, Van Bortel LMAB, Reesink KD, Segers P, Stehouwer CDA, Laurent S, Boutouyrie P, and Reference Values for Arterial Measurements Collaboration (2015). Reference values for local arterial stiffness. Part a: carotid artery. *J Hypertens* 33:1981–1996.

Fay FS and Delise CM (1973). Contraction of isolated smooth-muscle cells–structural changes. *Proc Natl Acad Sci U S A* 70:641–645.

Ferruzzi J, Bersi MR, and Humphrey JD (2013). Biomechanical phenotyping of central arteries in health and disease: advantages of and methods for murine models. *Ann Biomed Eng* 41:1311–1330.

Fisher NI (1989). Smoothing a sample of circular data. *J Struct Geol* 11:775–778.

Fisher NI, Lewis T, and Embleton BJJ (1993). *Statistical analysis of spherical data*. Cambridge: Cambridge University Press.

Fisher NI (1995). *Statistical analysis of circular data*. Cambridge: Cambridge University Press.

Floyd RV, Borisova L, Bakran A, Hart CA, Wray S, and Burdyga TV (2008). Morphology, calcium signaling and mechanical activity in human ureter. *J Urol* 180:398–405.

Frangi A, Niessen W, Vincken K, and Viergever M (1998). Multiscale vessel enhancement filtering. In: *Medical Image Computing and Computer-Assisted Interventation - MICCAI'98*. Ed. by Wells W, Colchester A, and Delp S. Berlin: Springer, 130–137.

Fridez P, Zulliger MA, Bobard F, Montorzi G, Miyazaki H, Hayashi K, and Stergiopulos N (2003). Geometrical, functional, and histomorphometric adaptation of rat carotid artery in induced hypertension. *J Biomech* 36:671–680.

Fung YC (1990). *Biomechanics: Motion, Flow, Stress, and Growth*. New York: Springer.

Gasser TC, Gallinetti S, Xing X, Forsell C, Swedenborg J, and Roy J (2012). Spatial orientation of collagen fibers in the abdominal aortic aneurysm's wall and its relation to wall mechanics. *Acta Biomater* 8:3091–3103.

Gasser TC, Ogden RW, and Holzapfel GA (2006). Hyperelastic modelling of arterial layers with distributed collagen fibre orientations. *J R Soc Interface* 3:15–35.

Gelman A and Hill J (2006). *Data analysis using regression and multilevel/hierarchical models*. Cambridge: Cambridge University Press.

Gent AN (1996). A new constitutive relation for rubber. *Rubber Chem Technol* 69:59–61.

Giannattasio C, Failla M, Stella ML, Mangoni AA, Carugo S, Pozzi M, Grassi G, and Mancia G (1995). Alterations of radial artery compliance in patients with congestive heart failure. *Am J Cardiol* 76:381–385.

Gleason RL, Gray SP, Wilson E, and Humphrey JD (2004). A multiaxial computer-controlled organ culture and biomechanical device for mouse carotid arteries. *J Biomech Eng* 126:787–795.

Gonzalez RC and Woods RE (2008). *Digital Image Processing*. Upper Saddle River, New Jersey: Pearson Education, Inc.

Göppert-Mayer M (1931). Über Elementarakte mit zwei Quantensprüngen. *Ann Phys-New York* 401:273–294.

Gosling JA, Dixon JS, and Humpherson JR (1983). *Functional Anatomy of the Urinary Tract*. London: Gower Medical Publishing.

Haesler E, Lyon X, Pruvot E, Kappenberger L, and Hayoz D (2004). Confounding effects of heart rate on pulse wave velocity in paced patients with a low degree of atherosclerosis. *J Hypertens* 22:1317–1322.

Hahn C and Schwartz MA (2009). Mechanotransduction in vascular physiology and atherogenesis. *Nat Rev Mol Cell Biol* 10:53–62.

Hayashi K, Handa H, Nagasawa S, Okumura A, and Moritake K (1980). Stiffness and elastic behavior of human intracranial and extracranial arteries. *J Biomech* 13:175–184.

Hayes SC, Strosahl KD, and Wilson KG (1999). *Acceptance and Commitment Therapy*. New York: The Guilford Press.

Helmchen F and Denk W (2005). Deep tissue two-photon microscopy. *Nat Methods* 2:932–940.

Henle J (1866). *Handbuch der Systematischen Anatomie des Menschen. Zweiter band. Eingeweidelehre*. Braunschweig: Friedrich Vieweg und Sohn.

Hermeling E, Hoeks APG, Reneman RS, Segers P, and Reesink KD (2012a). Assessment of systolic and diastolic arterial stiffness. *J Hypertens* 30:1489–1491.

Hermeling E, Hoeks APG, Winkens MHM, Waltenberger JL, Reneman RS, Kroon AA, and Reesink KD (2010). Noninvasive assessment of arterial stiffness should discriminate between systolic and diastolic pressure ranges. *Hypertension* 55:124–130.

Hermeling E, Reesink KD, Reneman RS, and Hoeks APG (2007). Measurement of local pulse wave velocity: effects of signal processing on precision. *Ultrasound Med Biol* 33:774–781.

Hermeling E, Reesink KD, Reneman RS, and Hoeks APG (2008). Confluence of incident and reflected waves interferes with systolic foot detection of the carotid artery distension waveform. *J Hypertens* 26:2374–2380.

Hermeling E, Vermeersch SJ, Rietzschel ER, de Buyzere ML, Gillebert TC, Van de Laar RJ, Ferreira I, Hoeks APG, Van Bortel LMAB, Reneman RS, Segers P, and Reesink KD (2012b). The change in arterial stiffness over the cardiac cycle rather than diastolic stiffness is independently associated with left ventricular mass index in healthy middle-aged individuals. *J Hypertens* 30:396–402.

Hicks RM (1965). The fine structure of the transitional epithelium of rat ureter. *J Cell Biol* 26:25–48.

Hirai T, Sasayama S, Kawasaki T, and Yagi S (1989). Stiffness of systemic arteries in patients with myocardial infarction. A noninvasive method to predict severity of coronary atherosclerosis. *Circulation* 80:78–86.

Ho D, Zhao X, Gao S, Hong C, Vatner DE, and Vatner SF (2011). Heart rate and electrocardiography monitoring in mice. *Curr Protoc Mouse Biol* 1:123–139.

Hoeks APG, Brands PJ, Smeets FAM, and Reneman RS (1990). Assessment of the distensibility of superficial arteries. *Ultrasound Med Biol* 16:121–128.

Hoeks APG, Brands PJ, Willigers JM, and Reneman RS (1999). Non-invasive measurement of mechanical properties of arteries in health and disease. *P I Mech Eng H* 213:195–202.

Hoeks APG, Willekes C, Boutouyrie P, Brands PJ, Willigers JM, and Reneman RS (1997). Automated detection of local artery wall thickness based on M-line signal processing. *Ultrasound Med Biol* 23:1017–1023.

Hoeks APG, Hermeling E, and Reneman RS (2008). Artery wall mechanics determined by ultrasound. In: *Vascular Hemodynamics: Bioengineering and Clinical Perspectives*. Ed. by Yim PJ. Hoboken, NJ: John Wiley & Sons.

Hoeks APG, Willigers JM, and Reneman RS (2000). Effects of assessment and processing techniques on the shape of arterial pressure-distension loops. *J Vasc Res* 37:494–500.

Holtackers RJ, Spronck B, Heusinkveld MHG, Crombag G, op 't Roodt J, Delhaas T, Kooi ME, Reesink KD, and Hermeling E (2016). Head orientation should be considered in ultrasound studies on carotid artery distensibility. *J Hypertens* 34:1551–1555.

Holzapfel GA, Gasser TC, and Stadler M (2002). A structural model for the viscoelastic behavior of arterial walls: continuum formulation and finite element analysis. *Eur J Mech A-Solid* 21:441–463.

Holzapfel GA, Gasser TC, and Ogden RW (2000). A new constitutive framework for arterial wall mechanics and a comparative study of material models. *J Elasticity* 61:1–48.

Holzapfel GA and Ogden RW (2010a). Constitutive modelling of arteries. *Proc R Soc A* 466:1551–1597.

Holzapfel GA and Ogden RW (2010b). Modelling the layer-specific three-dimensional residual stresses in arteries, with an application to the human aorta. *J R Soc Interface* 7:787–799.

Hoyes AD, Bourne R, and Martin BG (1976). Ureteric vascular and muscle coat innervation in the rat. A quantitative ultrastructural study. *Invest Urol* 14:38–43.

Huberts W, Donders WP, Delhaas T, and Van de Vosse FN (2014). Applicability of the polynomial chaos expansion method for personalization of a cardiovascular pulse wave propagation model. *Int J Numer Meth Biomed Eng* 30:1679–1704.

Humphrey JD (2002). *Cardiovascular solid mechanics: cells, tissues, and organs*. New York: Springer Science & Business Media.

Humphrey JD, Harrison DG, Figueroa CA, Lacolley P, and Laurent S (2016). Central artery stiffness in hypertension and aging: a problem with cause and consequence. *Circ Res* 118:379–381.

Huybrechts SAM, Devos DG, Vermeersch SJ, Mahieu D, Achten E, De Backer TLM, Segers P, and Van Bortel LMAB (2011). Carotid to femoral pulse wave velocity: a comparison of real travelled aortic path lengths determined by MRI and superficial measurements. *J Hypertens* 29:1577–1582.

Hwang MH, Yoo JK, Kim HK, Hwang CL, Mackay K, Hemstreet O, Nichols WW, and Christou DD (2014). Validity and reliability of aortic pulse wave velocity and augmentation index determined by the new cuff-based SphygmoCor Xcel. *J Hum Hypertens* 28:475–481.

Imura T, Yamamoto K, Satoh T, Kanamori K, Mikami T, and Yasuda H (1990). In vivo viscoelastic behavior in the human aorta. *Circ Res* 66:1413–1419.

Jähne B (1993). *Spatio-Temporal Image Processing: Theory and Scientific Applications*. Berlin Heidelberg: Springer Berlin/Heidelberg.

Kaess BM, Rong J, Larson MG, Hamburg NM, Vita JA, Levy D, Benjamin EJ, Vasan RS, and Mitchell GF (2012). Aortic stiffness, blood pressure progression, and incident hypertension. *JAMA* 308:875–881.

Karalliedde J, Smith A, DeAngelis L, Mirenda V, Kandra A, Botha J, Ferber P, and Viberti G (2008). Valsartan improves arterial stiffness in type 2 diabetes independently of blood pressure lowering. *Hypertension* 51:1617–1623.

Karshovska E, Zhao Z, Blanchet X, Schmitt MM, Bidzhekov K, Soehnlein O, von Hundelshausen P, Mattheij NJ, Cosemans JM, Megens RTA, Koeppel TA, Schober A, Hackeng TM, Weber C, and Koenen RR (2015). Hyperreactivity of junctional adhesion molecule A-deficient platelets accelerates atherosclerosis in hyperlipidemic mice. *Circ Res* 116:587–599.

Kass DA, Shapiro EP, Kawaguchi M, Capriotti AR, Scuteri A, De Groof RC, and Lakatta EG (2001). Improved arterial compliance by a novel advanced glycation end-product crosslink breaker. *Circulation* 104:1464–1470.

Kawasaki T, Sasayama S, Yagi SI, Asakawa T, and Hirai T (1987). Non-invasive assessment of the age related changes in stiffness of major branches of the human arteries. *Cardiovasc Res* 21:678–687.

Kelly RP, Millasseau SC, Ritter JM, and Chowienczyk PJ (2001). Vasoactive drugs influence aortic augmentation index independently of pulse-wave velocity in healthy men. *Hypertension* 37:1429–1433.

Kim EJ, Park CG, Park JS, Suh SY, Choi CU, Kim JW, Kim SH, Lim HE, Rha SW, Seo HS, and Oh DJ (2007). Relationship between blood pressure parameters and pulse wave velocity in normotensive and hypertensive subjects: invasive study. *J Hum Hypertens* 21:141–148.

Kithas PA and Supiano MA (2010). Spironolactone and hydrochlorothiazide decrease vascular stiffness and blood pressure in geriatric hypertension. *J Am Geriatr Soc* 58:1327–1332.

Köllilker A (1859). *Handbuch der Gewebelehre des Menschen: Für Aertzte und Studirende*. Leipzig: Wilhelm Engelmann.

Kubozono T, Miyata M, Ueyama K, Nagaki A, Otsuji Y, Kusano K, Kubozono O, and Tei C (2007). Clinical significance and reproducibility of new arterial distensibility index. *Circ J* 71:89–94.

Lakatta EG and Levy D (2003a). Arterial and cardiac aging: major shareholders in cardiovascular disease enterprises: part I: aging arteries: a "set up" for vascular disease. *Circulation* 107:139–146.

Lakatta EG and Levy D (2003b). Arterial and cardiac aging: major shareholders in cardiovascular disease enterprises: part II: the aging heart in health: links to heart disease. *Circulation* 107:346–354.

Lang RJ, Takano H, Davidson ME, Suzuki H, and Klemm MF (2001). Characterization of the spontaneous electrical and contractile activity of smooth muscle cells in the rat upper urinary tract. *J Urol* 166:329–334.

Langewouters GJ, Wesseling KH, and Goedhard WJA (1980). A new model for the static elastic properties of the aging human aorta. In: *Cardiovascular Physiology: Heart, Peripheral Circulation and Methodology: Proceedings of the 28th International Congress of Physiological Sciences, Budapest, 1980*. Vol. 8, pp. 271–281.

Langewouters GJ, Wesseling KH, and Goedhard WJA (1984). The static elastic properties of 45 human thoracic and 20 abdominal aortas in vitro and the parameters of a new model. *J Biomech* 17:425–435.

Langewouters GJ, Zwart A, Busse R, and Wesseling KH (1986). Pressure-diameter relationships of segments of human finger arteries. *Clin Phys Physiol Meas* 7:43.

Langewouters GJ (1982). Visco-elasticity of the human aorta in vitro in relation to pressure and age. PhD thesis. Vrije Universiteit, Amsterdam.

Lantelme P, Mestre C, Lievre M, Gressard A, and Milon H (2002). Heart rate an important confounder of pulse wave velocity assessment. *Hypertension* 39:1083–1087.

Laurent S, Boutouyrie P, Asmar RG, Gautier I, Laloux B, Guize L, Ducimetiere P, and Bénétos A (2001). Aortic stiffness is an independent predictor of all-cause and cardiovascular mortality in hypertensive patients. *Hypertension* 37:1236–1241.

Laurent S, Cockcroft JR, Van Bortel LMAB, Boutouyrie P, Giannattasio C, Hayoz D, Pannier B, Vlachopoulos C, Wilkinson IB, and Struijker-Boudier HAJ (2006). Expert consensus document on arterial stiffness: methodological issues and clinical applications. *Eur Heart J* 27:2588–2605.

Laurent S, Katsahian S, Fassot C, Tropeano AI, Gautier I, Laloux B, and Boutouyrie P (2003). Aortic stiffness is an independent predictor of fatal stroke in essential hypertension. *Stroke* 34:1203–1206.

Learoyd BM and Taylor MG (1966). Alterations with age in the viscoelastic properties of human arterial walls. *Circ Res* 18:278–292.

Leloup AJA, Fransen P, Van Hove CE, Demolder M, De Keulenaer GW, and Schrijvers DM (2014). Applanation tonometry in mice: a novel noninvasive technique to assess pulse wave velocity and arterial stiffness. *Hypertension* 64:195–200.

Levi-Marpillat N, Desamericq G, Akakpo S, Affes-Ayadi H, Tropeano AI, Millasseau SC, and Macquin-Mavier I (2013). Crucial importance of using a sliding calliper to measure distance for carotid-femoral pulse wave velocity assessment. *J Hypertens* 31:940–945.

Liang YL, Gatzka CD, Du XJ, Cameron JD, and Kingwell BA (1999). Effects of heart rate on arterial compliance in men. *Clin Exp Pharmacol Physiol* 26:342–346.

Liao D, Arnett DK, Tyroler HA, Riley WA, Chambless LE, Szklo M, and Heiss G (1999). Arterial stiffness and the development of hypertension. The ARIC study. *Hypertension* 34:201–206.

Lichtenstein O, Safar ME, Mathieu E, Poitevin P, and Levy BI (1998). Static and dynamic mechanical properties of the carotid artery from normotensive and hypertensive rats. *Hypertension* 32:346–350.

Lim J, Pearman M, Park W, Alkatan M, Machin DR, and Tanaka H (2015). Impact of blood pressure perturbations on arterial stiffness. *Am J Physiol Regul Integr Comp Physiol* 309:R1540–R1545.

Llauradó G, Ceperuelo-Mallafré V, Vilardell C, Simo R, Gil P, Cano A, Vendrell J, and González-Clemente JM (2014). Advanced glycation end products are associated with arterial stiffness in type 1 diabetes. *J Endocrinol* 221:405–413.

Lundberg MS and Crow MT (1999). Age-related changes in the signaling and function of vascular smooth muscle cells. *Exp Gerontol* 34:549–557.

Maier R (1881). Die Ganglien in den harnabführenden Wegen des Menschen und einiger Thiere. *Virchows Archiv* 85:49–70.

Mäki-Petäjä KM, Booth AD, Hall FC, Wallace SML, Brown J, McEniery CM, and Wilkinson IB (2007). Ezetimibe and simvastatin reduce inflammation, disease activity, and aortic stiffness and improve endothelial function in rheumatoid arthritis. *J Am Coll Cardiol* 50:852–858.

Mäki-Petäjä KM, Hall FC, Booth AD, Wallace SML, Bearcroft PWP, Harish S, Furlong A, McEniery CM, Brown J, and Wilkinson IB (2006). Rheumatoid arthritis is associated with increased aortic pulse-wave velocity, which is reduced by anti-tumor necrosis factor-α therapy. *Circulation* 114:1185–1192.

Mallareddy M, Parikh CR, and Peixoto AJ (2006). Effect of angiotensin-converting enzyme inhibitors on arterial stiffness in hypertension: systematic review and meta-analysis. *J Clin Hypertens (Greenwich)* 8:398–403.

Mancia G, Bertinieri G, Grassi G, Parati G, Pomidossi G, Ferrari A, Gregorini L, and Zanchetti A (1983). Effects of blood-pressure measurement by the doctor on patient's blood pressure and heart rate. *Lancet* 2:695–698.

Mancia G, De Backer G, Dominiczak A, Cifkova R, Fagard R, Germano G, Grassi G, Heagerty AM, Kjeldsen SE, Laurent S, Narkiewicz K, Ruilope L, Rynkiewicz A, Schmieder RE, Struijker-Boudier HAJ, and Zanchetti A (2007). 2007 guidelines for the management of arterial hypertension: the task force for the management of arterial hypertension of the European Society of Hypertension (ESH) and of the European Society of Cardiology (ESC). *J Hypertens* 25:1105–1187.

Mancia G, Fagard R, Narkiewicz K, Redón J, Zanchetti A, Böhm M, Christiaens T, Cifkova R, De Backer G, Dominiczak A, Galderisi M, Grobbee DE, Jaarsma T, Kirchhof P, Kjeldsen SE, Laurent S, Manolis AJ, Nilsson PM, Ruilope LM, Schmieder RE, Sirnes PA, Sleight P, Viigimaa M, Waeber B, and Zannad F (2013). 2013 ESH/ESC guidelines for the management of arterial hypertension: the task force for the management of arterial hypertension of the European Society of Hypertension (ESH) and of the European Society of Cardiology (ESC). *J Hypertens* 31:1281–1357.

Mangoni AA, Mircoli L, Giannattasio C, Ferrari AU, and Mancia G (1996). Heart rate-dependence of arterial distensibility in vivo. *J Hypertens* 14:897–901.

Mardia KV and Jupp PE (2000). *Directional Statistics*. Chichester, United Kingdom: John Wiley & Sons, Ltd.

Masson I, Beaussier H, Boutouyrie P, Laurent S, Humphrey JD, and Zidi M (2011). Carotid artery mechanical properties and stresses quantified using in vivo data from normotensive and hypertensive humans. *Biomech Model Mechanobiol* 10:867–882.

Masson I, Boutouyrie P, Laurent S, Humphrey JD, and Zidi M (2008). Characterization of arterial wall mechanical behavior and stresses from human clinical data. *J Biomech* 41:2618–2627.

Matsumoto T and Hayashi K (1994). Mechanical and dimensional adaptation of rat aorta to hypertension. *J Biomech Eng* 116:278–283.

Matsumoto T and Hayashi K (1996). Stress and strain distribution in hypertensive and normotensive rat aorta considering residual strain. *J Biomech Eng* 118:62–73.

McNulty M, Mahmud A, and Feely J (2007). Advanced glycation end-products and arterial stiffness in hypertension. *Am J Hypertens* 20:242–247.

Megens RTA, Reitsma S, Schiffers PHM, Hilgers RHP, De Mey JGR, Slaaf DW, oude Egbrink MGA, and Van Zandvoort MAMJ (2007). Two-photon microscopy of vital murine elastic and muscular arteries. *J Vasc Res* 44:87–98.

Meinders JM and Hoeks APG (2004). Simultaneous assessment of diameter and pressure waveforms in the carotid artery. *Ultrasound Med Biol* 30:147–154.

Millasseau SC, Stewart AD, Patel SJ, Redwood SR, and Chowienczyk PJ (2005). Evaluation of carotid-femoral pulse wave velocity: influence of timing algorithm and heart rate. *Hypertension* 45:222–226.

Milnor WR (1989). *Hemodynamics*. Baltimore.

Mitchell GF (2014). Arterial stiffness and hypertension: chicken or egg? *Hypertension* 64:210–214.

Moré JJ and Sorensen DC (1983). Computing a trust region step. *SIAM J Sci and Stat Comput* 4:553–572.

Moxham I (2003). Physics of invasive blood pressure monitoring. *South Afr J Anaesth Analg* 9:33–38.

Murnaghan GF (1957). Experimental investigation of the dynamics of the normal and dilated ureter. *Br J Urol* 29:403–409.

Nichols WW, O'Rourke MF, and Vlachopoulos C (2011). *McDonald's blood flow in arteries: theoretical, experimental and clinical principles*. London: CRC Press.

Noble MIM, Trenchord D, and Guz A (1966). Effect of changing heart rate on cardiovascular function in the conscious dog. *Circ Res* 19:206–213.

Nürnberger J, Dammer S, Saez AO, Philipp T, and Schäfers RF (2003). Diastolic blood pressure is an important determinant of augmentation index and pulse wave velocity in young, healthy males. *J Hum Hypertens* 17:153–158.

Nye ER (1964). The effect of blood pressure alteration on the pulse wave velocity. *Br Heart J* 26:261–265.

Obersteiner H (1871). Die Harnblase und die Ureteren. In: *Handbuch der Lehre von den Geweben des Menschen und der Thiere*. Ed. by Stricker S. Leipzig: Wilhelm Engelmann.

O'Connell MK, Murthy S, Phan S, Xu C, Buchanan J, Spilker R, Dalman RL, Zarins CK, Denk W, and Taylor CA (2008). The three-dimensional micro- and nanostructure of the aortic medial lamellar unit measured using 3D confocal and electron microscopy imaging. *Matrix Biol* 27:171–181.

Ogden RW (1972). Large Deformation Isotropic Elasticity: On the Correlation of Theory and Experiment for Compressible Rubberlike Solids. *Proc R Soc A* 328:567–583.

Ogden RW, Saccomandi G, and Sgura I (2004). Fitting hyperelastic models to experimental data. *Comput Mech* 34:484–502.

Oheim M, Beaurepaire E, Chaigneau E, Mertz J, and Charpak S (2001). Two-photon microscopy in brain tissue: parameters influencing the imaging depth. *J Neurosci Methods* 111:29–37.

Ong KT, Delerme S, Pannier B, Safar ME, Bénétos A, Laurent S, and Boutouyrie P (2011). Aortic stiffness is reduced beyond blood pressure lowering by short-term and long-term antihypertensive treatment: a meta-analysis of individual data in 294 patients. *J Hypertens* 29:1034–1042.

Onstott TC (1980). Application of the bingham distribution function in paleomagnetic studies. *J Geophys Res* 85:1500–1510.

O'Rourke MF and Hashimoto J (2007). Mechanical factors in arterial aging: a clinical perspective. *J Am Coll Cardiol* 50:1–13.

Papadopoulou DN, Mendrinos E, Mangioris G, Donati G, and Pournaras CJ (2009). Intravitreal ranibizumab may induce retinal arteriolar vasoconstriction in patients with neovascular age-related macular degeneration. *Ophthalmology* 116:1755–1761.

Parati G and Valentini M (2007). Do we need out-of-office blood pressure in every patient? *Curr Opin Cardiol* 22:321–328.

Patel DJ, Fry DL, and Janicki JS (1969). The elastic symmetry of arterial segments in dogs. *Circ Res* 24:1–8.

Peñáz J (1973). Photoelectric measurement of blood pressure, volume and flow in the finger. In: *Digest 10th Int Conf Med Biol Eng*. Vol. 104, pp. 162–164.

Perkins GM, Owen A, Swaine IL, and Wiles JD (2006). Relationships between pulse wave velocity and heart rate variability in healthy men with a range of moderate-to-vigorous physical activity levels. *Eur J Appl Physiol* 98:516–523.

Pernot M, Fujikura K, Fung-Kee-Fung SD, and Konofagou EE (2007). ECG-gated, mechanical and electromechanical wave imaging of cardiovascular tissues in vivo. *Ultrasound Med Biol* 33:1075–1085.

Perret-Guillaume C, Joly L, and Bénétos A (2009). Heart rate as a risk factor for cardiovascular disease. *Prog Cardiovasc Dis* 52:6–10.

Peters MW, Canham PB, and Finlay HM (1983). Circumferential alignment of muscle cells in the tunica media of the human brain artery. *Blood Vessels* 20:221–233.

Pflieger H and Goerttler Kl (1970). Konstruktionsprinzipien der Aortenwand im Ursprungsbereich der interkostalen, intestinalen und renalen Aortenäste. *Arch Kreislaufforsch* 62:223–248.

Pichler E, Lazarini W, and Filippi R (1953). Über schraubenförmige Struktur von Arterien. *Naunyn-Schmiedebergs Arch Pharmacol* 219:420–439.

Pinheiro J, Bates D, DebRoy S, and Sarkar D (2014). *nlme: linear and nonlinear mixed effects models. R package version 3.1-117*. R Core Team. URL: https://cran.r-project.org/package=nlme.

Protopopow S (1897). Beiträge zur Anatomie und Physiologie der Ureteren (Anatomisch-experimentelle Untersuchnng). *Pflugers Arch* 66:1–113.

Pruett JD, Bourland JD, and Geddes LA (1988). Measurement of pulse-wave velocity using a beat-sampling technique. *Ann Biomed Eng* 16:341–347.

Qiu H, Zhu Y, Sun Z, Trzeciakowski JP, Gansner M, Depre C, Resuello RR, Natividad FF, Hunter WC, Genin GM, Elson EL, Vatner DE, Meininger GA, and Vatner SF (2010). Short communication: vascular smooth muscle cell stiffness as a mechanism for increased aortic stiffness with aging. *Circ Res* 107:615–619.

R Core Team (2014). *R: A language and environment for statistical computing*. R Foundation for Statistical Computing. URL: http://www.R-project.org/.

Rachev A and Hayashi K (1999). Theoretical study of the effects of vascular smooth muscle contraction on strain and stress distributions in arteries. *Ann Biomed Eng* 27:459–468.

Reitsma S, oude Egbrink MGA, Vink H, Van den Berg BM, Passos VL, Engels W, Slaaf DW, and Van Zandvoort MAMJ (2011). Endothelial glycocalyx structure in the intact carotid artery: a two-photon laser scanning microscopy study. *J Vasc Res* 48:297–306.

Remington JW (1955). Hysteresis loop behavior of the aorta and other extensible tissues. *Am J Physiol* 180:83–95.

Reneman RS, Meinders JM, and Hoeks APG (2005). Non-invasive ultrasound in arterial wall dynamics in humans: what have we learned and what remains to be solved. *Eur Heart J* 26:960–966.

Rhee MY, Kwon NY, Kim JD, Song SH, Yoon YW, Lee MY, and Kim YK (2004). Do acute changes in heart rate by isoproterenol affect aortic stiffness in patients with hypertension? *Korean J Intern Med* 19:33–37.

Rhodin JA (1967). The ultrastructure of mammalian arterioles and precapillary sphincters. *J Ultrastruct Res* 18:181–223.

Roccabianca S, Figueroa CA, Tellides G, and Humphrey JD (2014). Quantification of regional differences in aortic stiffness in the aging human. *J Mech Behav Biomed Mater* 29:618–634.

Roman MJ, Devereux RB, Schwartz JE, Lockshin MD, Paget SA, Davis A, Crow MK, Sammaritano L, Levine DM, Shankar BA, Moeller E, and Salmon JE (2005). Arterial stiffness in chronic inflammatory diseases. *Hypertension* 46:194–199.

Sá Cunha R, Pannier B, Bénétos A, Siché JP, London GM, Mallion JM, and Safar ME (1997). Association between high heart rate and high arterial rigidity in normotensive and hypertensive subjects. *J Hypertens* 15:1423–1430.

Sáez P, García A, Peña E, Gasser TC, and Martínez MA (2016). Microstructural quantification of collagen fiber orientations and its integration in constitutive modeling of the porcine carotid artery. *Acta Biomater* 33:183–193.

Sáez P, Peña E, and Martíinez MA (2014). A structural approach including the behavior of collagen cross-links to model patient-specific human carotid arteries. *Ann Biomed Eng* 42:1158–1169.

Saiki A, Sato Y, Watanabe R, Watanabe Y, Imamura H, Yamaguchi T, Ban N, Kawana H, Nagumo A, Nagayama D, Ohira M, Endo K, and Tatsuno I (2015). The role of a novel arterial stiffness parameter, cardio-ankle vascular index (CAVI), as a surrogate marker for cardiovascular diseases. *J Atheroscler Thromb* [in press].

Saini A, Berry C, and Greenwald S (1995). Effect of age and sex on residual stress in the aorta. *J Vasc Res* 32:398–405.

Saltelli A, Ratto M, Andres T, Campolongo F, Cariboni J, Gatelli D, Saisana M, and Tarantola S (2008). *Global sensitivity analysis: the primer*. Chichester, United Kingdom: John Wiley & Sons.

Saltelli A, Tarantola S, Campolongo F, and Ratto M (2004). *Sensitivity analysis in practice: a guide to assessing scientific models*. Chichester, United Kingdom: John Wiley & Sons.

Salvi P, Magnani E, Valbusa F, Agnoletti D, Alecu C, Joly L, and Bénétos A (2008). Comparative study of methodologies for pulse wave velocity estimation. *J Hum Hypertens* 22:669–677.

Sappey PC (1873). *Traité D'Anatomie Descriptive: Tome Quatrième, Première partie: Splanchnologie - Appareil de la Digestion*. Vol. 4. Paris: Adrien Delahaye.

Satani Y (1919). Histologic study of the ureter. *J Urol* 3:247–267.

Schafer RW (2011). What is a Savitzky-Golay filter? *IEEE Signal Process Mag* 28:111–117.

Schillaci G, Pucci G, Pirro M, Settimi L, Hijazi R, Franklin SS, and Mannarino E (2011). Combined effects of office and 24-h blood pressure on aortic stiffness in human hypertension. *J Hypertens* 29:869–875.

Schmitt MMN, Megens RTA, Zernecke A, Bidzhekov K, Van den Akker NM, Rademakers T, Van Zandvoort MAMJ, Hackeng TM, Koenen RR, and Weber C (2014). Endothelial junctional adhesion molecule-a guides monocytes into flow-dependent predilection sites of atherosclerosis. *Circulation* 129:66–76.

Schneider W (1938). Die Muskulatur der oberen harnableitenden Wege. *Anat Embryol (Berl)* 109:187–196.

Schober A, Nazari-Jahantigh M, Wei Y, Bidzhekov K, Gremse F, Grommes J, Megens RTA, Heyll K, Noels H, Hristov M, Wang S, Kiessling F, Olson EN, and Weber C (2014). MicroRNA-126-5p promotes endothelial proliferation and limits atherosclerosis by suppressing Dlk1. *Nat Med* 20:368–376.

Schueth A, Spronck B, Van Zandvoort MAMJ, and Van Koeveringe GA (2016). Age-related changes in murine bladder structure and sensory innervation: a multiphoton microscopy quantitative analysis. *AGE* 38:1–11.

Schultze-Jena BS (1939). Über die schraubenförmige Struktur der Arterienwand. *Gegenbauers Morphol Jahrbuch* 83:230–246.

Schulze-Bauer CAJ and Holzapfel GA (2003). Determination of constitutive equations for human arteries from clinical data. *J Biomech* 36:165–169.

Schweitzer P and Teichholz LE (1985). Carotid sinus massage. Its diagnostic and therapeutic value in arrhythmias. *Am J Med* 78:645–654.

Seow CY (2000). Response of arterial smooth muscle to length perturbation. *J Appl Physiol* 89:2065–2072.

Shahin Y, Khan JA, and Chetter I (2012). Angiotensin converting enzyme inhibitors effect on arterial stiffness and wave reflections: a meta-analysis and meta-regression of randomised controlled trials. *Atherosclerosis* 221:18–33.

Shirai K, Song M, Suzuki J, Kurosu T, Oyama T, Nagayama D, Miyashita Y, Yamamura S, and Takahashi M (2011). Contradictory effects of β1- and α1-aderenergic receptor blockers on cardio-ankle vascular stiffness index (CAVI). *J Atheroscler Thromb* 18:49–55.

Shirai K, Utino J, Otsuka K, and Takata M (2006). A novel blood pressure-independent arterial wall stiffness parameter; cardio-ankle vascular index (CAVI). *J Atheroscler Thromb* 13:101–107.

Shotton DM (1989). Confocal scanning optical microscopy and its applications for biological specimens. *J Cell Sci* 94:175–206.

Silver FH, Snowhill PB, and Foran DJ (2003). Mechanical behavior of vessel wall: a comparative study of aorta, vena cava, and carotid artery. *Ann Biomed Eng* 31:793–803.

Silverman BW (1986). *Density Estimation for Statistics and Data Analysis*. London: Chapman & Hall.

Slaaf DW and Van Zandvoort MAMJ (2011). Endothelial glycocalyx thickness and platelet-vessel wall interactions during atherogenesis. *Thromb Haemostasis* 106:939–946.

Smulyan H, Mookherjee S, and Safar ME (2016). The two faces of hypertension: role of aortic stiffness. *J Am Soc Hypertens* 10:175–183.

Snyder JP and Voxland PM (1989). *An album of map projections*. Washington: USGPO.

Snyder JP (1987). *Map projections–A working manual*. Washington: USGPO.

Sobering TJ (1999). *Bandwidth and Risetime*. Technical report. SDE Consulting.

Sobol IM (1967). On the distribution of points in a cube and the approximate evaluation of integrals. *Zhurnal Vychislitel'noi Matematiki i Matematicheskoi Fiziki* 7:784–802.

Sommer G and Holzapfel GA (2012). 3D constitutive modeling of the biaxial mechanical response of intact and layer-dissected human carotid arteries. *J Mech Behav Biomed Mater* 5:116–128.

Sommer G, Regitnig P, Költringer L, and Holzapfel GA (2010). Biaxial mechanical properties of intact and layer-dissected human carotid arteries at physiological and supraphysiological loadings. *Am J Physiol Heart Circ Physiol* 298:H898–H912.

Spronck B, Megens RTA, Reesink KD, and Delhaas T (2014a). Three-dimensional vascular smooth muscle orientation as quantitatively assessed by multiphoton microscopy: mouse carotid arteries do show a helix. In: *Conf Proc IEEE Eng Med Biol Soc*. Vol. 2014, pp. 202–205.

Spronck B, Delhaas T, Roodt JO, and Reesink KD (2016b). Carotid artery applanation tonometry does not cause significant baroreceptor activation. *Am J Hypertens* 29:299–302.

Spronck B, Heusinkveld MHG, Donders WP, De Lepper AGW, Op't Roodt J, Kroon AA, Delhaas T, and Reesink KD (2015a). A constitutive modeling interpretation of the relationship between carotid artery stiffness, blood pressure and age in hypertensive subjects. *Am J Physiol Heart Circ Physiol* 308:H568–H582.

Spronck B, Heusinkveld MHG, Vanmolkot FH, Op 't Roodt J, Hermeling E, Delhaas T, Kroon AA, and Reesink KD (2015b). Pressure-dependence of arterial stiffness: Potential clinical implications. *J Hypertens* 33:330–338.

Spronck B, Martens EGHJ, Gommer ED, and Van de Vosse FN (2012). A lumped parameter model of cerebral blood flow control combining cerebral autoregulation and neurovascular coupling. *Am J Physiol Heart Circ Physiol* 303:H1143–H1153.

Spronck B, Megens RTA, Reesink KD, and Delhaas T (2016c). A method for three-dimensional quantification of vascular smooth muscle orientation: application in viable murine carotid arteries. *Biomech Model Mechanobiol* 15:419–432.

Spronck B, Merken JJ, Reesink KD, Kroon W, and Delhaas T (2014b). Ureter smooth muscle cell orientation in rat is predominantly longitudinal. *PLOS ONE* 9:e86207.

Spronck B, Walmsley J, Palau-Caballero G, Reesink KD, and Delhaas T (2016d). Can significance of aortic sinus vortices be assessed using the assumptions in the model of Aboelkassem et al.? *J Theor Biol* 389:304–305.

Stålhand J (2009). Determination of human arterial wall parameters from clinical data. *Biomech Model Mechanobiol* 8:141–148.

Stålhand J and Klarbring A (2005). Aorta in vivo parameter identification using an axial force constraint. *Biomech Model Mechanobiol* 3:191–199.
Stålhand J and Klarbring A (2006). Parameter identification in arteries using constraints. In: *Mechanics of Biological Tissue*. Berlin: Springer.
Stålhand J, Klarbring A, and Karlsson M (2004). Towards in vivo aorta material identification and stress estimation. *Biomech Model Mechanobiol* 2:169–186.
Stefanadis C, Vlachopoulos C, Karayannacos P, Boudoulas H, Stratos C, Filippides T, Agapitos M, and Toutouzas P (1995). Effect of vasa vasorum flow on structure and function of the aorta in experimental animals. *Circulation* 91:2669–2678.
Stefanadis C, Dernellis J, Tsiamis E, Stratos C, Kallikazaros I, and Toutouzas P (1998). Aortic function in patients during intra-aortic balloon pumping determined by the pressure-diameter relation. *J Thorac Cardiovasc Surg* 116:1052–1059.
Stefanadis C, Dernellis J, Vlachopoulos C, Tsioufis C, Tsiamis E, Toutouzas K, Pitsavos C, and Toutouzas P (1997). Aortic function in arterial hypertension determined by pressure-diameter relation: effects of diltiazem. *Circulation* 96:1853–1858.
Steinbuch J, Hoeks APG, Hermeling E, Truijman MTB, Schreuder FHBM, and Mess WH (2016). Standard B-mode ultrasound measures local carotid artery characteristics as reliably as radiofrequency phase tracking in symptomatic carotid artery patients. *Ultrasound Med Biol* 42:586–595.
Stevens A and Lowe J (1992). *Histology*. New York: Gower Medical Publishing.
Stewart AD, Millasseau SC, Kearney MT, Ritter JM, and Chowienczyk PJ (2003). Effects of inhibition of basal nitric oxide synthesis on carotid-femoral pulse wave velocity and augmentation index in humans. *Hypertension* 42:915–918.
Stompor T, Rajzer M, Sułowicz W, Dembińska-Kieć A, Janda K, Kawecka-Jaszcz K, Wojcik K, Tabor B, Zdzienicka A, and Janusz-Grzybowska E (2003). An association between aortic pulse wave velocity, blood pressure and chronic inflammation in ESRD patients on peritoneal dialysis. *Int J Artif Organs* 26:188–195.
Strong KC (1938). A study of the structure of the media of the distributing arteries by the method of microdissection. *Anat Rec* 72:151–167.
Subramanian P, Karshovska E, Reinhard P, Megens RTA, Zhou Z, Akhtar S, Schumann U, Li X, Van Zandvoort MAMJ, Ludin C, Weber C, and Schober A (2010). Lysophosphatidic acid receptors LPA1 and LPA3 promote CXCL12-mediated smooth muscle progenitor cell recruitment in neointima formation. *Circ Res* 107:96–105.
Sudret B (2008). Global sensitivity analysis using polynomial chaos expansions. *Reliab Eng Syst Safe* 93:964–979.
Sudret B (2015). Polynomials chaos expansions and stochastic finite element methods. In: *Risk and Reliability in Geotechnical Engineering*. Boca Raton, FL: CRC Press.
Sugawara J, Hayashi K, and Tanaka H (2016). Arterial path length for arterial stiffness: methodological consideration. *Am J Hypertens* [in press].
Sugawara J, Hayashi K, Yokoi T, and Tanaka H (2008). Age-associated elongation of the ascending aorta in adults. *JACC Cardiovasc Imaging* 1:739–748.
Sun Z (2015). Aging, arterial stiffness, and hypertension. *Hypertension* 65:252–256.
Takamizawa K and Hayashi K (1987). Strain energy density function and uniform strain hypothesis for arterial mechanics. *J Biomech* 20:7–17.

Takino M, Takino Y, and Sugahara K (1964). Apparatus and method for measurement of digital pressure applied to carotid sinus for causing carotid sinus syndrome. *Acta Neuroveg (Wien)* 26:93–103.

Tan I, Butlin M, Liu YY, Ng K, and Avolio AP (2012). Heart rate dependence of aortic pulse wave velocity at different arterial pressures in rats. *Hypertension* 60:528–533.

Tan I, Spronck B, Kiat H, Barin E, Reesink KD, Delhaas T, Avolio AP, and Butlin M (2016). Heart rate dependency of large artery stiffness. *Hypertension* 68:236–242.

Tanaka H (1999). Circular asymmetry of the paleomagnetic directions observed at low latitude volcanic sites. *Earth Planets Space* 51:1279–1286.

Tanaka H, DeSouza CA, and Seals DR (1998). Absence of age-related increase in central arterial stiffness in physically active women. *Arterioscler Thromb Vasc Biol* 18:127–132.

The Reference Values for Arterial Stiffness' Collaboration (2010). Determinants of pulse wave velocity in healthy people and in the presence of cardiovascular risk factors: 'establishing normal and reference values'. *Eur Heart J* 31:2338–2350.

Todd ME, Laye CG, and Osborne DN (1983). The dimensional characteristics of smooth muscle in rat blood vessels. a computer-assisted analysis. *Circ Res* 53:319–331.

Toldt C (1877). *Lehrbuch der Gewebelehre mit Vorzugsweiser Berücksichtigung der Menschlichen Körpers*. Stuttgart: Ferdinand Enke.

Tonar Z, Kochova P, Cimrman R, Perktold J, and Witter K (2015). Segmental differences in the orientation of smooth muscle cells in the tunica media of porcine aortae. *Biomech Model Mechanobiol* 14:315–332.

Toutouzas K, Stefanadis C, Tsiamis E, Vlachopoulos C, Tousoulis D, Tsioufis C, and Toutouzas P (2000). Aortic pressure-diameter relation in patients with non-insulin dependent diabetes mellitus: new insights. *Diabetologia* 43:1070–1075.

Townsend RR, Wilkinson IB, Schiffrin EL, Avolio AP, Chirinos JA, Cockcroft JR, Heffernan KS, Lakatta EG, McEniery CM, Mitchell GF, Najjar SS, Nichols WW, Urbina EM, and Weber T (2015). Recommendations for improving and standardizing vascular research on arterial stiffness: a scientific statement from the American Heart Association. *Hypertension* 66:698–722.

Tsamis A and Stergiopulos N (2007). Arterial remodeling in response to hypertension using a constituent-based model. *Am J Physiol Heart Circ Physiol* 293:H3130–H3139.

Tuttle RS (1966). Age-related changes in the sensitivity of rat aortic strips to norepinephrine and associated chemical and structural alterations. *J Gerontol* 21:510–516.

Ushiwata I and Ushiki T (1990). Cytoarchitecture of the smooth muscles and pericytes of rat cerebral blood vessels. *J Neurosurg* 73:82–90.

Vader D, Kabla A, Weitz D, and Mahadevan L (2009). Strain-induced alignment in collagen gels. *PLOS ONE* 4:e5902.

Valdez-Jasso D, Bia D, Zócalo Y, Armentano RL, Haider MA, and Olufsen MS (2011). Linear and nonlinear viscoelastic modeling of aorta and carotid pressure-area dynamics under in vivo and ex vivo conditions. *Ann Biomed Eng* 39:1438–1456.

Van Bortel LMAB, Spek JJ, Balkestein EJ, Sardina M, and Struijker-Boudier HAJ (1999). Is it possible to develop drugs that act more selectively on large arteries? *J Hypertens* 17:701–705.

Van Bortel LMAB, Vanmolkot FH, Van der Heijden-Spek JJ, Bregu M, Staessen JA, and Hoeks APG (2001). Does B-mode common carotid artery intima-media thickness differ from M-mode? *Ultrasound Med Biol* 27:1333–1336.

Van Bortel LMAB, Balkestein EJ, Van der Heijden-Spek JJ, Vanmolkot FH, Staessen JA, Kragten JA, Vredeveld JW, Safar ME, Struijker-Boudier HAJ, and Hoeks APG (2001). Non-invasive assessment of local arterial pulse pressure: comparison of applanation tonometry and echo-tracking. *J Hypertens* 19:1037–1044.

Van Bortel LMAB, De Backer TLM, and De Buyzere M (2011). How to treat arterial stiffness beyond blood pressure lowering? *J Hypertens* 29:1051–1053.

Van Bortel LMAB, De Backer TLM, and Segers P (2016). Standardization of arterial stiffness measurements make them ready for use in clinical practice. *Am J Hypertens* [in press].

Van Bortel LMAB, Duprez D, Starmans-Kool MJ, Safar ME, Giannattasio C, Cockcroft JR, Kaiser DR, and Thuillez C (2002). Clinical applications of arterial stiffness, task force III: recommendations for user procedures. *Am J Hypertens* 15:445–452.

Van Bortel LMAB, Laurent S, Boutouyrie P, Chowienczyk PJ, Cruickshank JK, De Backer TLM, Filipovsky J, Huybrechts S, Mattace-Raso FUS, Protogerou AD, Schillaci G, Segers P, Vermeersch S, and Weber T (2012). Expert consensus document on the measurement of aortic stiffness in daily practice using carotid-femoral pulse wave velocity. *J Hypertens* 30:445–448.

Van Gorp AW, Van Ingen Schenau DS, Hoeks APG, Struijker-Boudier HAJ, De Mey JGR, and Reneman RS (2000). In spontaneously hypertensive rats alterations in aortic wall properties precede development of hypertension. *Am J Physiol Heart Circ Physiol* 278:H1241–H1247.

Van Loon P (1976). Length-force and volume-pressure relationships of arteries. *Biorheology* 14:181–201.

Van Zandvoort MAMJ, Engels W, Douma K, Beckers L, Oude Egbrink MGA, Daemen M, and Slaaf DW (2004). Two-photon microscopy for imaging of the (atherosclerotic) vascular wall: a proof of concept study. *J Vasc Res* 41:54–63.

Virmani R, Avolio AP, Mergner WJ, Robinowitz M, Herderick EE, Cornhill JF, Guo SY, Liu TH, Ou DY, and O'Rourke MF (1991). Effect of aging on aortic morphology in populations with high and low prevalence of hypertension and atherosclerosis. Comparison between Occidental and Chinese communities. *Am J Pathol* 139:1119–1129.

Von Möllendorff W and Schröder R (1930). *Handbuch der Mikroskopischen Anatomie des Menschen; Siebenter Band: Harn- und Geschlechtsapparat; Erster Teil: Exkretionsapparat und Weibliche Genitalorgane*. Ed. by von Möllendorff W. Berlin: Julius Springer.

Wagenseil JE and Mecham RP (2012). Elastin in large artery stiffness and hypertension. *J Cardiovasc Transl Res* 5:264–273.

Walavalkar V, Evers E, Pujar S, Viralam K, Maiya S, Frerich S, John C, Rao S, Reddy C, Spronck B, Prinzen FW, Delhaas T, and Vanagt WY (2016). Preoperative sildenafil administration in children undergoing cardiac surgery: a randomized controlled preconditioning study. *Eur J Cardiothorac Surg* 49:1403–1410.

Walmsley JG (1983). Vascular smooth muscle orientation in straight portions of human cerebral arteries. *J Microsc* 131:361–375.

Walmsley JG and Canham PB (1979). Orientation of nuclei as indicators of smooth muscle cell alignment in the cerebral artery. *Blood Vessels* 16:43–51.

Wang M, Zhang J, Telljohann R, Jiang L, Wu J, Monticone RE, Kapoor K, Talan M, and Lakatta EG (2012). Chronic matrix metalloproteinase inhibition retards age-associated arterial proinflammation and increase in blood pressure. *Hypertension* 60:459–466.

Wang R, Raykin J, Li H, Gleason Jr RL, and Brewster LP (2014). Differential mechanical response and microstructural organization between non-human primate femoral and carotid arteries. *Biomech Model Mechanobiol* 13:1041–1051.

Watton PN, Ventikos Y, and Holzapfel GA (2009). Modelling the mechanical response of elastin for arterial tissue. *J Biomech* 42:1320–1325.

Weber T, Ammer M, Rammer M, Adji A, O'Rourke MF, Wassertheurer S, Rosenkranz S, and Eber B (2009). Noninvasive determination of carotid-femoral pulse wave velocity depends critically on assessment of travel distance: a comparison with invasive measurement. *J Hypertens* 27:1624–1630.

Weissler AM, Peeler RG, and Roehll WH (1961). Relationships between left ventricular ejection time, stroke volume, and heart rate in normal individuals and patients with cardiovascular disease. *American heart journal* 62:367–378.

Weizsäcker HW, Lambert H, and Pascale K (1983). Analysis of the passive mechanical properties of rat carotid arteries. *J Biomech* 16:703–715.

Wesseling KH, Jansen JR, Settels JJ, and Schreuder JJ (1993). Computation of aortic flow from pressure in humans using a nonlinear, three-element model. *J Appl Physiol* 74:2566–2573.

Wessling A and Boethius G (1990). Measurement of drug use in a defined population. *Eur J Clin Pharmacol* 39:207–210.

Westerhof N, Stergiopulos N, and Noble MIM (2010). *Snapshots of hemodynamics: an aid for clinical research and graduate education*. New York: Springer.

Wilkinson IB, Mohammad NH, Tyrrell S, Hall IR, Webb DJ, Paul VE, Levy T, and Cockcroft JR (2002). Heart rate dependency of pulse pressure amplification and arterial stiffness. *Am J Hypertens* 15:24–30.

Willekes C, Hoeks APG, Bots ML, Brands PJ, Willigers JM, and Reneman RS (1999). Evaluation of off-line automated intima-media thickness detection of the common carotid artery based on M-line signal processing. *Ultrasound Med Biol* 25:57–64.

Willemet M, Chowienczyk PJ, and Alastruey J (2015). A database of virtual healthy subjects to assess the accuracy of foot-to-foot pulse wave velocities for estimation of aortic stiffness. *Am J Physiol Heart Circ Physiol* 309:H663–H675.

Wolf Jr JS, Humphrey PA, Rayala HJ, Gardner SM, Mackey RB, and Clayman RV (1996). Comparative ureteral microanatomy. *J Endourol* 10:527–531.

Wolffenbuttel BH, Boulanger CM, Crijns FRL, Huijberts MSP, Poitevin P, Swennen GNM, Vasan S, Egan JJ, Ulrich P, Cerami A, and Lévy BI (1998). Breakers of advanced glycation end products restore large artery properties in experimental diabetes. *Proc Natl Acad Sci U S A* 95:4630–4634.

Wolinsky H (1972). Long-term effects of hypertension on the rat aortic wall and their relation to concurrent aging changes: morphological and chemical studies. *Circ Res* 30:301–309.

Wolinsky H and Glagov S (1964). Structural basis for the static mechanical properties of the aortic media. *Circ Res* 14:400–413.

Wolinsky H and Glagov S (1967). A lamellar unit of aortic medial structure and function in mammals. *Circ Res* 20:99–111.

Woodburne RT (1965). The ureter, ureterovesical junction, and vesical trigone. *Anat Rec* 151:243–249.

Wu S, Chen JJ, Kudelka A, Lu J, and Zhu X (2008). Incidence and risk of hypertension with sorafenib in patients with cancer: a systematic review and meta-analysis. *Lancet Oncol* 9:117–123.

Zanchi A, Stergiopulos N, Brunner HR, and Hayoz D (1998). Differences in the mechanical properties of the rat carotid artery in vivo, in situ, and in vitro. *Hypertension* 32:180–185.

Zieman SJ and Kass DA (2004). Advanced glycation end product cross-linking: pathophysiologic role and therapeutic target in cardiovascular disease. *Congest Heart Fail* 10:144–151.

Zocalo Y, Bia D, Lluberas S, and Armentano RL (2008). Regional differences in veins wall viscosity, compliance, energetics and damping: analysis of the pressure-diameter relationship during cyclical overloads. *Biol Res* 41:227–233.

Zulliger MA, Fridez P, Hayashi K, and Stergiopulos N (2004a). A strain energy function for arteries accounting for wall composition and structure. *J Biomech* 37:989–1000.

Zulliger MA, Kwak NTMR, Tsapikouni T, and Stergiopulos N (2002). Effects of longitudinal stretch on VSM tone and distensibility of muscular conduit arteries. *Am J Physiol Heart Circ Physiol* 283:H2599–H2605.

Zulliger MA, Rachev A, and Stergiopulos N (2004b). A constitutive formulation of arterial mechanics including vascular smooth muscle tone. *Am J Physiol Heart Circ Physiol* 287:H1335–H1343.

Zulliger MA and Stergiopulos N (2007). Structural strain energy function applied to the ageing of the human aorta. *J Biomech* 40:3061–3069.

Zuur A, Ieno EN, Walker N, Saveliev AA, and Smith GM (2009). *Mixed effects models and extensions in ecology with R*. New York: Springer Science & Business Media.